

Statistical Mechanics of Soft Core Fluid Mixtures

Andrew John Archer

H. H. Wills Physics Laboratory
University of Bristol

A thesis submitted to the University of Bristol in
accordance with the requirements of the degree of
Ph.D. in the Faculty of Science

August 2003

Abstract

In this thesis we investigate the statistical mechanics of binary mixtures of soft-core fluids. The soft-core pair potentials between the fluid particles are those obtained by considering the effective potential between polymers in solution. The effective pair potential between the centers of mass of polymers is well approximated by a repulsive Gaussian potential. A binary mixture of Gaussian particles can phase separate, and we calculate the phase diagrams for various size ratios of the two species. Using a simple mean field density functional theory (DFT), which generates the random phase approximation for the bulk pair direct correlation functions, we calculate the surface tension and density profiles for the free interface between the demixed fluid phases. We find that the asymptotic decay of the interfacial profiles into bulk can be oscillatory on *both* sides of the interface. We also calculate density profiles for the binary Gaussian core model (GCM) adsorbed at a planar wall and find a wetting transition from partial to complete wetting for certain purely repulsive wall potentials. By applying a general DFT approach for calculating the force between two big particles immersed in a solvent of smaller ones we calculate the solvent mediated (SM) potential between two big Gaussian core particles in the phase separating binary mixture of smaller GCM particles. We show that the theory for calculating the SM potential captures effects of thick adsorbed films surrounding the big solute particles and we find extremely attractive, long ranged SM potentials between the big particles whose range is determined by the film thickness. In the region of the solvent critical point we also find extremely attractive SM potentials whose range is now set by the bulk correlation length in the binary solvent.

In addition to the GCM, we also consider the effective potential between the central monomers on each polymer chain; this potential features a weak (logarithmic) divergence as the particle separation $r \rightarrow 0$. A binary mixture of these particles can also phase separate and displays many features in common with the binary GCM.

*To my family:
Sarah, Mum, Dad and Alice.*

Acknowledgments

First, and foremost, I would like to thank my supervisor, Bob Evans, for all his support, encouragement and patience, as well as his wisdom in suggesting the topics in this thesis for me to study. When I started out, I had a suspicion that doing physics could be fun. Working with Bob has proved to me that my inkling was right: physics is a lot of fun and to a great extent this has been due to Bob's enthusiasm.

There are also others I would like to thank: Joe Brader, who answered many of my questions at the beginning and helped me to get started. Christos Likos and Roland Roth: great scientists, good collaborators; they are both people I admire and like a lot.

I would also like to acknowledge the Bristol theory group, for providing a good working atmosphere and for being a friendly group. I mention especially the other PhD students – my friends and peers: Joe, Ben, Mark, Jorge, Dan, Denzil, Danny, David, Jamie, Maria and Emma.

Last, but not least, I mention my family: Sarah, my wife, for all her love and support, and my parents for the same. When, as an 18 year old, I asked my parents what I should study at university, they encouraged me to do whatever I enjoyed. I have been grateful for that advice many times.

Authors Declaration

I declare that the work in this thesis was carried out in accordance with the regulations of the University of Bristol. The work is original except where indicated by special reference in the text and no part of the thesis has been submitted for any other degree. Any views expressed in the thesis are those of the author and in no way represent those of the University of Bristol. The thesis has not been presented to any other University for examination either in the United Kingdom or overseas.

“...what seems so easy—namely, that the god must be able to make himself understood—is not so easy if he is not to destroy that which is different.”

Søren Kierkegaard, *Philosophical Fragments*, edited and translated by H.V. Hong and E.H Hong, (Princeton, Princeton University Press, 1985).

*“He had no beauty or majesty to attract us to him,
nothing in his appearance that we should desire him.”*

Isaiah 53:2.

This thesis is based partly on the following papers:

Chapter 5

A.J. Archer and R. Evans,

Binary Gaussian core model: Fluid-fluid phase separation and interfacial properties,
Phys. Rev. E **64** 041501 (2001).

Chapter 6

A.J. Archer and R. Evans,

Wetting in the binary Gaussian core model,
J. Phys.: Condens. Matter **14** 1131 (2002).

Chapter 7

A.J. Archer, R. Evans and R. Roth,

Microscopic theory of solvent mediated long range forces: Influence of wetting,
Europhys. Lett. **59** 526 (2002).

and

A.J. Archer and R. Evans,

Solvent mediated interactions and solvation close to fluid-fluid phase separation: A density
functional treatment,

J. Chem Phys. **118** 9726 (2003).

Chapter 8

A.J. Archer, C.N. Likos and R. Evans,

Binary star-polymer solutions: bulk and interfacial properties,
J. Phys.: Condens. Matter **14**, 12031 (2002).

Contents

1	Introduction	1
2	Background: Theory of Classical Fluids	5
2.1	Classical fluids	5
2.2	The Ornstein Zernike equation	10
2.3	Density functional theory: an introduction	11
3	A Simple Approach to Inhomogeneous Fluids and Wetting	17
3.1	Landau theory for simple fluids	18
3.2	Inhomogeneous fluid order parameter profiles	20
3.3	Thermodynamics of interfaces	22
3.4	Wetting: near to coexistence	23
3.5	Landau theory for wetting	24
3.6	Wetting transitions	27
3.7	Incorporating fluctuations	34
4	The One Component Gaussian Core Model	37
4.1	Introduction: effective interactions	37
4.2	A simple model for polymers in solution	38
4.3	Properties of the one-component GCM fluid	40
4.4	Solid phases of the GCM	43
4.5	DFT theory for the solid phases of the GCM	46
5	Binary GCM: Fluid-Fluid Phase Separation and Interfacial Properties	53
5.1	Demixing in binary fluids	54
5.2	The model mixture and its phase diagram	56

5.3	Properties of the fluid-fluid interface	61
5.3.1	Density profiles	62
5.3.2	Surface tension	66
5.4	Asymptotic decay of correlation functions	71
5.5	Discussion	75
6	Wetting in the Binary Gaussian Core Model	79
6.1	Introduction	79
6.2	The model mixture and choice of wall-fluid potentials	80
6.3	Results of calculations	83
6.3.1	First-order wetting transition	83
6.3.2	Thickness of the wetting film	86
6.4	Concluding remarks	89
7	Solvent Mediated Interactions Close to Fluid-Fluid Phase Separation	93
7.1	Introduction	94
7.2	Theory of the solvent mediated potential	98
7.2.1	General formalism	98
7.2.2	Application of the RPA functional	99
7.3	Results for a one-component solvent	101
7.3.1	Solvent radial distribution function by test-particle route	101
7.3.2	Density profile of small GCM particles around a single big GCM particle	102
7.3.3	The SM potential	107
7.3.4	The excess chemical potential of the big particle	109
7.4	Results for the binary mixture solvent	113
7.4.1	Phase diagram of the binary solvent	113
7.4.2	Density profiles of the binary mixture around a single big GCM particle	115
7.4.3	SM potentials for the binary mixture solvent	120
7.4.4	The excess chemical potential of the big particle immersed in the binary mixture	123
7.4.5	The SM potential in the vicinity of the binary mixture critical point	126
7.5	Test particle versus OZ route to the SM potential	130

7.6	Concluding remarks	133
8	Binary star-polymer solutions: bulk and interfacial properties	143
8.1	Introduction	143
8.2	The model mixture	146
8.3	Bulk structure and phase diagram	147
8.4	The free fluid-fluid interface	157
8.5	Star-polymers at a hard wall: wetting behaviour	162
8.6	Summary and concluding remarks	167
9	Final Remarks	169
A	DFT and the Einstein Model	173
B	Details of the binary GCM Pole Structure	181
C	Derivation of Eq. (7.3.37) for the excess chemical potential	185
D	Wetting on Curved Substrates and the Pre-Wetting line	187
E	Fourier Transform of the Star Polymer Pair Potential	191
	Bibliography	193

List of Figures

2.1	Radial distribution function for a Lennard-Jones fluid	9
3.1	A typical (wetting) density profile for a fluid at a wall	23
3.2	Excess surface grand potential $\omega_{ex}(l)$, at a continuous wetting transition . .	29
3.3	Excess surface grand potential $\omega_{ex}(l)$, at a first order wetting transition . .	30
3.4	Equilibrium adsorbed film thickness along paths above, intersecting and below the pre-wetting line	32
4.1	The ‘colloid’ approach to polymers in solution	39
4.2	$g(r)$ for the GCM at various densities	40
4.3	The HNC $g(r)$ for the GCM near freezing	42
4.4	Phase diagram for the one component GCM	45
4.5	Helmholtz free energy for an fcc lattice as a function the localization parameter	49
4.6	Phase diagram of the one component GCM	50
5.1	The phase diagram for a mixture of Gaussian particles, equivalent to a mixture of two polymers with length ratio 2:1	58
5.2	The phase diagram for a mixture of Gaussian particles, equivalent to a mixture of two polymers with length ratio 3:1	59
5.3	The phase diagram for a mixture of Gaussian particles, equivalent to a mixture of two polymers with length ratio 5:1	60
5.4	The phase diagram for a mixture of Gaussian particles, equivalent to a mixture of two polymers with length ratio 1.46:1	61
5.5	The phase diagram for a symmetric mixture of Gaussian particles	62
5.6	Density profiles at the planar interface	64
5.7	Free interface density profiles for the symmetric GCM fluid	65

5.8	The surface tension at the planar interface	67
5.9	The surface tension at the planar interface for the symmetric GCM binary mixture	68
5.10	Plots of the surface segregation and $(\omega(z) + P)$ at the free interface	69
5.11	$(\omega(z) + P)$ for the symmetric mixture	70
5.12	The RPA and HNC radial distribution function for the GCM	74
6.1	Wetting phase diagram for the binary GCM	82
6.2	Density profiles at a planar wall, for a path in the phase diagram intersecting the pre-wetting line	85
6.3	Density profiles at a planar wall, for a path in the phase diagram below the pre-wetting line	86
6.4	The adsorption of species 1	87
6.5	The pre-factor l_0 of the wetting film thickness ($l \sim -l_0 \ln(x - x_{coex.})$) versus the wall potential decay length λ	90
7.1	The density profile of small GCM particles around a single big GCM particle located at the origin	105
7.2	The SM potential between two big GCM particles in a pure solvent of small GCM particles	108
7.3	Phase diagram for a binary mixture of small GCM particles showing the thin-thick adsorption transition around a single big GCM particle	114
7.4	The density profiles of a binary solvent of small GCM particles around a single big GCM test particle, calculated on a path below the thin-thick adsorbed film transition line	117
7.5	The density profiles of a binary solvent of small GCM particles around a single big GCM test particle, calculated on a path above the thin-thick adsorbed film transition line	118
7.6	The density profiles of a binary solvent of small GCM particles around a single big GCM test particle, calculated on a path intersecting the thin-thick adsorbed film transition line	119
7.7	The SM potential between two big GCM particles in a binary solvent of small GCM particles calculated on a path in the phase diagram below the thin-thick adsorbed film transition line	120

7.8	The SM potential between two big GCM particles in a binary solvent of small GCM particles calculated on a path in the phase diagram intersecting the thin-thick adsorbed film transition line	121
7.9	The excess chemical potential of a big GCM particle in a binary solvent of small GCM particles	124
7.10	density profiles of a binary mixture of small GCM particles around a big GCM test particle calculated on a path in the phase diagram approaching the bulk critical point	128
7.11	SM potential between two big GCM particles in a binary solvent of small GCM particles, calculated on a path in the phase diagram approaching the bulk critical point	129
7.12	SM potentials calculated using $g_{bb}(r)$ obtained from the RPA closure to the OZ equations	132
7.13	The pair correlation functions calculated by the test particle route for a ternary mixture of GCM particles	134
8.1	The partial structure factors, calculated along two different thermodynamic paths in the (x, ρ) -plane of the star polymer mixture obtained from the HNC and RPA	149
8.2	The HNC radial distribution functions $g_{ii}(r)$ of the minority phases at high total densities	151
8.3	The RPA-spinodal and binodal lines for the star-polymer mixture along with the HNC-binodal	153
8.4	Comparison of the HNC- and RPA-results for the partial chemical potentials	156
8.5	The fluid-fluid interface density profiles	159
8.6	The surface tension at the planar free interface	161
8.7	Density profiles of a binary star-polymer fluid adsorbed at a wall	163
8.8	Binary star-polymer phase diagram showing the location of the pre-wetting line	164
8.9	Adsorption of species 1 at planar wall, for paths in the phase diagram near and intersecting the pre-wetting line	166
8.10	Adsorption of species 1 at planar wall, for paths in the phase diagram below the pre-wetting line	167

B.1	Imaginary part of the poles	182
B.2	Real part of the poles	183
D.1	Binary GCM density profiles on a curved substrate	188
D.2	Pre-wetting line on a curved substrate	189

Chapter 1

Introduction

“We all agree that your theory is crazy, but is it crazy enough?”

Niels Bohr

The subject of the theory of classical fluids is now well-established. The bulk structure and thermodynamics of simple (atomic) fluids is reasonably well understood [1], and can usually be described theoretically with the machinery of integral equations or perturbation theory. However, the complexity of liquid state problems increases hugely when one is interested in inhomogeneous fluids, i.e. the fluid in the presence of confining potentials or at interfaces. These types of problems can often be tackled within density functional theory (DFT) or simulation, but there is still much to understand, particularly when there are phenomena such as wetting, associated with phase separation, or bulk criticality involved.

Some of the focus in the field of liquid-state physics has shifted recently towards complex, colloidal fluids, and this too is the subject of the present thesis. The philosophy of our approach is to develop *simple* models for complex soft matter systems that capture the essential physics. These models then become interesting in their own right, from a statistical mechanics viewpoint, and often exhibit surprisingly rich features which do not have direct counterparts for simple (atomic) fluids. One then asks, in turn, whether what emerges from the models is relevant for real complex fluids. Since it is often possible to ‘tune’ the interactions in complex fluids, for example by the addition of non-adsorbing polymers or ions to a suspension of colloidal particles, the features emerging from the simple models are indeed often relevant for real complex fluids.

The particular focus of this thesis concerns simple models of binary polymer solutions where the interactions between the individual polymer chains are treated using an effective pair potential between the centers of mass, i.e. a Gaussian pair potential. Sometimes we consider the effective potential between the central monomers of each polymer (chapter 8). The results from the latter model also pertain to star-polymer solutions. These model fluids display many novel features arising from the soft (penetrable) cores of the particles. For example, mean-field theories become increasingly accurate as the density increases.

We have used DFT to calculate various properties for bulk and inhomogeneous binary mixtures of these model fluids. The binary mixture separates into two phases if the solution is sufficiently concentrated. Using DFT we have calculated the surface tension and density profiles of the two species at the interface between the two demixed fluid phases. The decay of the one-body density profiles at this fluid-fluid interface can be either monotonic or damped oscillatory; the type of decay is determined by the location of the state point in the phase diagram relative to the Fisher-Widom line [2]. The system is of particular interest since, unlike the liquid-gas interface in simple fluids, pronounced oscillations in the one-body density profiles can occur on *both* sides of the interface.

We calculated the density profiles of the binary Gaussian fluid at purely repulsive planar walls and found that for state points close to phase separation, complete wetting films of the coexisting fluid phase can develop at the wall – see Ch. 6. In addition we found that there is a wetting transition – i.e. for some state points at bulk coexistence the thickness of the fluid film adsorbed at the wall is finite, but as the total fluid density is decreased, staying at coexistence, there is a transition to a macroscopic thick adsorbed film. This transition can be first or second order, depending on the form of the wall potential, however, in this thesis we focus on the first-order transition regime. We use a fully microscopic fluid theory, the results from which can be used to test other mesoscopic (effective interfacial Hamiltonian) descriptions of the wetting transition. Our results support the general scheme of using effective interfacial Hamiltonians. We have also examined the phenomenology for a different model fluid: the central-monomer (star-polymer) effective potential.

A separate aspect of the work with Gaussian particles was to use the same simple model to implement a general DFT method for calculating solvent mediated (SM) potentials. This is a powerful way of treating multi-component fluids. One is attempting to determine an effective interaction potential between particles of one species in a solution of

another or several, generally smaller, species of particles. Much of the motivation for calculating effective SM potentials in complex (multi-component) fluids is that a theoretical treatment of the full mixture is often prohibitively difficult, particularly when there is a big size asymmetry between the different species of particles in the fluid. This difficulty is especially pronounced when one is interested in inhomogeneous systems. Formally the aim is to integrate out the degrees of freedom of the small particles in the system, describing their effect by means of an effective solvent (small particle) mediated potential between the big particles. Roth, Evans and collaborators [3, 4] introduced a general DFT scheme within which one can calculate solvent mediated potentials. This proved very effective for hard sphere fluids where the solvent mediated potential is termed the depletion potential. What is of particular interest is whether this (mean-field) theory can include effects such as a wetting film of the small particles around the big particle, or critical fluctuations in the small particle solvent fluid. Moreover these effects can result in long ranged SM potentials, which are important when considering segregation and the stability of multi-component fluid mixtures. When these long ranged SM potentials are attractive they can provide a mechanism for flocculation in colloidal suspensions. These effective SM potentials can be measured directly in colloidal systems by trapping a pair of colloids close together with optical tweezers, and using video-microscopy to obtain the SM potential from the averaged motion of the colloids in the traps – see for example Ref. [5]. Using the mean-field DFT for the Gaussian core model fluid of polymers in solution, we were able to include the effects of thick (wetting) films of the small solvent particles around the big particles and take account of critical solvent fluctuations, in determining the SM potential between the large particles. Because of the simplicity of the model Gaussian fluid we were able to find an analytic approximation to the SM potential in some particular cases, thereby gaining much insight into the general method.

This thesis proceeds as follows: In chapters 2 and 3 we provide the background theory that the rest of the thesis is built upon. Ch. 2 is a general introduction to liquid state theory, with a particular focus on DFT. In Ch. 3 we demonstrate (within Landau theory) some of the phenomenology of inhomogeneous fluids, with a strong emphasis on wetting and wetting transitions. In Ch. 4 we introduce the Gaussian core model – both the fluid and solid phases. In Ch. 5 we introduce the binary Gaussian core model, which can phase separate into two fluid phases at sufficiently high densities, and in this chapter we calculate phase diagrams and various properties of the interface between the demixed

phases, including interfacial density profiles and the surface tension. In Ch. 6 we calculate the density profiles for the binary Gaussian fluid at a planar wall, where we find a wetting transition from partial to complete wetting for certain purely repulsive wall potentials. Ch. 7 is where we determine the SM potential between two big Gaussian particles, immersed in a binary solvent of smaller Gaussian particles. In Ch. 8 we consider the central-monomer effective pair potential model for a binary polymer solution and show that this exhibits features very similar to those described in Chs. 5 and 6 for the binary Gaussian core model. In Ch. 9 we make a few final remarks.

Chapter 2

Background:

Theory of Classical Fluids

In this chapter we briefly introduce the theory of classical fluids, composed of spherically symmetric particles. We will describe some methods for calculating bulk thermodynamic quantities and correlation functions and subsequently provide a brief introduction to density functional theory, a formalism within which one can calculate properties of inhomogeneous fluids. This theory focuses on calculating the fluid density profile in the presence of an external potential such as a confining wall.

2.1 Classical fluids

Classical fluids are those where the quantum mechanical nature of the underlying subatomic particle interactions can be neglected and the interactions between the fluid particles can be treated in a purely classical way. This approximation is a good one for atomic fluids if the atoms are sufficiently massive and the temperature is sufficiently high. For example, liquid argon can be treated as a classical fluid with great success, whereas liquid helium cannot. A good indicator for when quantum mechanical effects can be neglected is if the thermal de Broglie wavelength $\Lambda \ll d$, where

$$\Lambda = \sqrt{\frac{2\pi\beta\hbar^2}{m}}. \quad (2.1.1)$$

$\beta = 1/k_B T$ is the inverse temperature, m is the mass of the atom and d is the average separation between the atoms, which in a liquid is normally of order the diameter of the

atoms. Colloidal fluids are also well described within a classical treatment.

The following discussion of classical fluids largely follows the standard presentation of the subject, e.g. Hansen and McDonald [1]. The starting point for the theory is defining the effective interaction potential between the particles in the fluid, $\Phi(\mathbf{r}^N)$, where $\mathbf{r}^N = \{\mathbf{r}_1, \mathbf{r}_2, \dots, \mathbf{r}_N\}$ denotes the set of position coordinates for the N particles in the system. The effective potential between the particles includes all the underlying interactions such as the Coulomb forces between the electrons and ions of the atoms. The Hamiltonian for such a system is

$$\mathcal{H}(\mathbf{p}^N, \mathbf{r}^N; N) = \sum_{i=1}^N \frac{\mathbf{p}_i^2}{2m} + \Phi(\mathbf{r}^N) + \sum_{i=1}^N V(\mathbf{r}_i), \quad (2.1.2)$$

where \mathbf{p}_i denotes the momentum of and $V(\mathbf{r}_i)$ the one-body external potential acting on the i^{th} particle. A further approximation often made is the assumption that the effective potential between the particles is pairwise additive, i.e.

$$\Phi(\mathbf{r}^N) = \frac{1}{2} \sum_{j \neq i} \sum_{i=1}^N v(|\mathbf{r}_i - \mathbf{r}_j|), \quad (2.1.3)$$

where $v(r)$ is the potential between a pair of particles separated by a distance r . An example of such an effective pair potential is the Lennard-Jones potential which provides a good approximation for the effective potential between the atoms in a simple fluid such as liquid argon [1]. The Lennard-Jones potential is

$$v(r) = 4\epsilon \left(\left(\frac{\sigma_{LJ}}{r} \right)^{12} - \left(\frac{\sigma_{LJ}}{r} \right)^6 \right), \quad (2.1.4)$$

where σ_{LJ} is roughly the atomic diameter and ϵ is a parameter which measures the strength of the attractive part of the potential. The r^{-12} term models the repulsive core, which arises from the Pauli repulsion between the atomic electrons and the attractive r^{-6} term arises from the induced dipole-induced dipole interaction between the atoms at larger separations.

Having specified the form of the interactions between the particles, the Hamiltonian is fully determined and equilibrium thermodynamic quantities and correlation functions can, in principle, be calculated. The equilibrium value of a phase function $\mathcal{O}(\mathbf{p}^N, \mathbf{r}^N; N)$ in the Grand canonical ensemble is given by

$$\langle \mathcal{O} \rangle = \sum_{N=0}^{\infty} \int d\mathbf{r}^N \int d\mathbf{p}^N \mathcal{O}(\mathbf{p}^N, \mathbf{r}^N; N) f(\mathbf{p}^N, \mathbf{r}^N; N), \quad (2.1.5)$$

where $f(\mathbf{p}^N, \mathbf{r}^N; N)$ is the probability density for a given configuration of the system coordinates $(\mathbf{p}^N, \mathbf{r}^N)$ and we denote the product $d\mathbf{r}_1 d\mathbf{r}_2 \dots d\mathbf{r}_N$ by $d\mathbf{r}^N$. For example, the internal energy is

$$U = \sum_{N=0}^{\infty} \int d\mathbf{r}^N \int d\mathbf{p}^N \mathcal{H}(\mathbf{p}^N, \mathbf{r}^N; N) f(\mathbf{p}^N, \mathbf{r}^N; N). \quad (2.1.6)$$

The idea behind this approach, due to Gibbs, is that the equilibrium state of the system can be determined by considering an ensemble of identical systems. By summing (integrating) over the probabilities of each of the different configurations that occur, one can determine equilibrium quantities. The form of f depends upon which ensemble of systems one is considering. In the Grand canonical ensemble one fixes the volume V , temperature T and chemical potential μ of the system. One can consider other ensembles, but in the thermodynamic limit, $V, N \rightarrow \infty$, they are all equivalent. In the Grand canonical ensemble

$$f(\mathbf{p}^N, \mathbf{r}^N; N) = \frac{h^{-3N}}{N!} \frac{\exp[\beta N \mu - \beta \mathcal{H}(\mathbf{p}^N, \mathbf{r}^N; N)]}{\Xi(\mu, V, T)}, \quad (2.1.7)$$

where the Grand partition function $\Xi(\mu, V, T)$ is

$$\begin{aligned} \Xi(\mu, V, T) &= \sum_{N=0}^{\infty} \frac{h^{-3N}}{N!} \int d\mathbf{r}^N \int d\mathbf{p}^N \exp[\beta N \mu - \beta \mathcal{H}(\mathbf{p}^N, \mathbf{r}^N)] \\ &= \text{Tr}_{\text{cl}} \exp[\beta N \mu - \beta \mathcal{H}(\mathbf{p}^N, \mathbf{r}^N; N)]. \end{aligned} \quad (2.1.8)$$

We have used Tr_{cl} to denote the classical trace in Eq. (2.1.8). The partition function is a key quantity in statistical mechanics, and it forms a link to thermodynamics because the grand potential of the system is simply

$$\Omega = -k_B T \ln \Xi. \quad (2.1.9)$$

The integral in Eq. (2.1.8) over the momentum degrees of freedom is straightforward, so the partition function can be expressed as just an integral over the configurational (position) degrees of freedom:

$$\Xi = \sum_{N=0}^{\infty} \frac{z^N}{N!} \int d\mathbf{r}^N \exp[-\beta \Phi(\mathbf{r}^N) - \beta \sum_{i=1}^N V(\mathbf{r}_i)], \quad (2.1.10)$$

where the activity $z = \Lambda^{-3} \exp(\beta \mu)$. Starting from Eq. (2.1.10), if we only perform a partial trace over the configurational degrees of freedom, we can generate a hierarchy of particle distribution functions:

$$\rho^{(n)}(\mathbf{r}^n) = \frac{1}{\Xi} \sum_{N \geq n}^{\infty} \frac{z^N}{(N-n)!} \int d\mathbf{r}^{(N-n)} \exp[-\beta \Phi(\mathbf{r}^N) - \beta \sum_{i=1}^N V(\mathbf{r}_i)]. \quad (2.1.11)$$

If we consider the homogeneous situation, where the external potential $V(\mathbf{r}_i) = 0$, then the first member of the hierarchy, $\rho^{(1)}(\mathbf{r})$ is then simply the one-body density of the fluid, which is a constant:

$$\rho^{(1)}(\mathbf{r}) = \frac{\langle N \rangle}{V} = \rho. \quad (2.1.12)$$

We will now focus on the second member of the hierarchy, the two-body distribution function $\rho^{(2)}(\mathbf{r}_1, \mathbf{r}_2)$. This is proportional to the probability of finding another particle at \mathbf{r}_2 , given there is already a particle at \mathbf{r}_1 . For a fluid of spherically symmetric particles in the bulk, where the external potential is zero, translational invariance demands $\rho^{(2)}(\mathbf{r}_1, \mathbf{r}_2) = \rho^{(2)}(|\mathbf{r}_1 - \mathbf{r}_2|) = \rho^{(2)}(r_{12})$. It is also useful to introduce the radial distribution function, $g(r) = \rho^{(2)}(r)/\rho^2$. When the particles in the fluid are far apart, $r \rightarrow \infty$, then their positions are uncorrelated, and $g(r) \rightarrow 1$. However, in a dense fluid, when the separation between the particles is only a few particle diameters, $g(r)$ can be highly structured. A typical plot of $g(r)$ for a dense liquid well away from the critical point is plotted in Fig. 2.1. This was calculated using the Percus-Yevick closure to the Ornstein-Zernike equation (details in the next section) for a fluid of particles which interact via the Lennard-Jones potential, Eq. (2.1.4), at a temperature $k_B T/\epsilon = 2.0$ and density $\rho\sigma_{LJ}^3 = 0.8$. In a dense fluid, when r is only a few σ_{LJ} , $g(r)$ can be highly oscillatory due to the packing of the hard cores of the particles.

There are several reasons for focusing on the radial distribution function. Firstly, the Fourier transform of the radial distribution function, the fluid structure factor, $S(\mathbf{k})$, is a quantity that is directly accessible in diffraction experiments (normally neutron or x-ray scattering, although if the particles are larger (colloids), then one can also use light scattering). The liquid structure factor is given by

$$S(\mathbf{k}) = 1 + \rho \int d\mathbf{r} (g(\mathbf{r}) - 1) \exp(i\mathbf{k} \cdot \mathbf{r}). \quad (2.1.13)$$

Another reason for focusing on the radial distribution function is that once it is known, one can use it to calculate thermodynamic quantities. For example, the $\mathbf{k} \rightarrow 0$ limit of $S(\mathbf{k})$ is related to the isothermal compressibility χ_T by the *compressibility equation*

$$\chi_T \equiv \frac{1}{\rho} \left(\frac{\partial \rho}{\partial P} \right)_T = \frac{S(0)}{\rho k_B T}. \quad (2.1.14)$$

For a system in which particles interact solely via a pairwise potential, $v(r)$, (see Eq. (2.1.3)), the internal energy of the system, Eq. (2.1.6), can be simplified to yield the

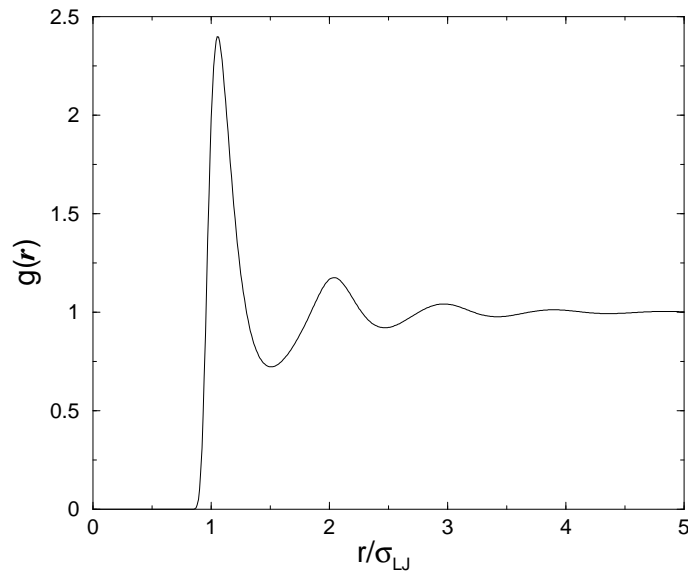


Figure 2.1: The radial distribution function for a Lennard-Jones fluid, at a reduced temperature $k_B T/\epsilon = 2.0$ and fluid density $\rho\sigma_{LJ}^3 = 0.8$, calculated using the Percus-Yevick closure to the Ornstein-Zernike equation.

internal energy per particle in terms of an integral involving only $g(r)$:

$$\frac{U}{N} = \frac{3}{2}k_B T + \frac{\rho}{2} \int d\mathbf{r} g(r) v(r). \quad (2.1.15)$$

This is known as the *energy equation*. Similarly, one can derive an equation for the pressure, known as the *virial equation* [1]:

$$P = \rho k_B T - \frac{\rho^2}{6} \int d\mathbf{r} g(r) r \frac{dv(r)}{dr}. \quad (2.1.16)$$

The radial distribution function for a particular model fluid can be determined in several ways. One way is to perform a computer simulation of the fluid. This could either be done by solving Newton's equations, a *molecular dynamics* simulation, or by generating random fluid configurations and calculating the Boltzmann weight for each configuration – this is a *Monte Carlo* simulation. Another approach is that based on perturbation theories. Here the idea is to split the pair potential of the fluid into two parts, the reference part (normally the harshly repulsive core part) and the perturbation. The correlations in the fluid due to the core part can be modeled by, for example, those of a hard sphere potential. There is much known about this system and the hard-sphere radial distribution function is well-known. One then calculates the full $g(r)$ by perturbing about the hard-sphere result

[1]. Another approach, which is the basis of many successful theories for $g(r)$ in a bulk fluid, is that based on closure approximations to the Ornstein-Zernike equation.

2.2 The Ornstein Zernike equation

In bulk, the radial distribution function for an ideal gas, $g(r) = 1$ for all values of r , i.e. there are no correlations between the particles. For a real fluid, one can define a total correlation function, $h(r)$, as the deviation of $g(r)$ from the ideal gas result, i.e. $h(r) = g(r) - 1$. The Ornstein Zernike (OZ) approach to calculating $h(r)$ is to split up the correlations present in $h(r)$ into a ‘direct’ part, which will include the correlations over a range of order the range of the pair potential, and an ‘indirect’ part, i.e. the rest. This idea is the basis of the OZ integral equation:

$$h(r) = c^{(2)}(r) + \rho \int d\mathbf{r}' c^{(2)}(|\mathbf{r} - \mathbf{r}'|) h(r'), \quad (2.2.1)$$

where $c^{(2)}(r)$ is the direct pair correlation function, which is generally less structured than $h(r)$ and has the range of the pair potential. Eq. (2.2.1) as it stands does not enable us to calculate $h(r)$; we have merely shifted the problem from calculating $h(r)$ to calculating $c^{(2)}(r)$. Eq. (2.2.1) can be viewed as an equation *defining* $c^{(2)}(r)$. In order to solve Eq. (2.2.1) we also need a closure relation, an additional equation relating $c^{(2)}(r)$ to $h(r)$, which we can use with the OZ equation, Eq. (2.2.1), to solve for $h(r)$. The exact closure equation can generally not be determined, and so one is forced to resort to making an approximation. The usual route is to make a diagrammatic expansion for the correlation functions and truncate the (infinite) series at some point or perform a re-summation [1]. For example, the Percus-Yevick closure relation [1], which was used to calculate $g(r)$ in Fig. 2.1, is

$$c_{PY}^{(2)}(r) = (1 - \exp[\beta v(r)])(1 + h(r)). \quad (2.2.2)$$

This closure is particularly good for fluids with short ranged potentials and sharply repulsive cores. Another closure relation is the hypernetted chain (HNC), given by [1]

$$c_{HNC}^{(2)}(r) = -\beta v(r) + h(r) - \ln(1 + h(r)). \quad (2.2.3)$$

This closure turns out to be particularly good for soft-core, purely repulsive pair potentials, such as the Coulomb potential (the one component classical plasma consisting of point particles in a neutralizing background), and in particular the Gaussian core model (GCM),

where the particles interact via a repulsive Gaussian potential. These particles are the subject of this thesis. What is even more striking is that for the GCM, when the fluid density is high, then a particularly simple closure, the random phase approximation (RPA), is also reasonably accurate:

$$c_{RPA}^{(2)}(r) = -\beta v(r), \quad \text{for all } r. \quad (2.2.4)$$

We shall return to this subject in the next section where we will describe how the OZ equation arises naturally in the context of density functional theory.

2.3 Density functional theory: an introduction

The discussion in this section is drawn mainly from the articles by Evans [6, 7]. The focus of density functional theory (DFT) is the one body density profile, $\rho^{(1)}(\mathbf{r})$, the first member of the hierarchy of particle distribution functions, defined by Eq. (2.1.11). DFT is therefore a theory for inhomogeneous fluids. If we introduce the particle density operator

$$\hat{\rho}(\mathbf{r}) = \sum_{i=1}^N \delta(\mathbf{r} - \mathbf{r}_i), \quad (2.3.1)$$

then we can express the partition function, Eq. (2.1.10), in terms of the particle density operator:

$$\Xi = \sum_{N=0}^{\infty} \frac{\Lambda^{-3N}}{N!} \int d\mathbf{r}^N \exp[-\beta\Phi(\mathbf{r}^N) + \beta \int d\mathbf{r} \hat{\rho}(\mathbf{r})u(\mathbf{r})], \quad (2.3.2)$$

where $u(r) = \mu - V(\mathbf{r})$. The logarithm of the partition function is the Grand potential Ω (see Eq. (2.1.9)), and so the functional derivative of Ω with respect to $u(\mathbf{r})$ is simply $-\langle \hat{\rho}(\mathbf{r}) \rangle$, which is the first member of the hierarchy of particle distribution functions, Eq. (2.1.11):

$$\frac{\delta\Omega}{\delta u(\mathbf{r})} = -\langle \hat{\rho}(\mathbf{r}) \rangle = -\rho^{(1)}(\mathbf{r}). \quad (2.3.3)$$

A second derivative yields the density-density correlation function

$$\beta^{-1} \frac{\delta^2\Omega}{\delta u(\mathbf{r}_2)\delta u(\mathbf{r}_1)} = G(\mathbf{r}_1, \mathbf{r}_2) = \langle \hat{\rho}(\mathbf{r}_1)\hat{\rho}(\mathbf{r}_2) \rangle - \rho^{(1)}(\mathbf{r}_1)\rho^{(1)}(\mathbf{r}_2), \quad (2.3.4)$$

from which we can obtain the second member of the hierarchy of particle distribution functions $\rho^{(2)}(\mathbf{r}_1, \mathbf{r}_2)$ (see Eq. (2.1.11)), since

$$\rho^{(2)}(\mathbf{r}_1, \mathbf{r}_2) = \langle \hat{\rho}(\mathbf{r}_1)\hat{\rho}(\mathbf{r}_2) \rangle - \langle \hat{\rho}(\mathbf{r}_1) \rangle \delta(\mathbf{r}_1 - \mathbf{r}_2). \quad (2.3.5)$$

Further differentiation yields the higher order particle distribution functions. It should be emphasized that Eq. (2.3.3) is exact and does not just apply to fluids interacting via pairwise additive potentials Eq. (2.1.3). The one body density, which we will now denote $\rho(\mathbf{r})$, is therefore a functional of $u(\mathbf{r})$. It can be shown that, for a given $\Phi(\mathbf{r}^N)$, μ and β , $\rho(\mathbf{r})$ is uniquely determined by the external potential $V(\mathbf{r})$ [6, 8]. Similarly the equilibrium probability density f (see Eq. (2.1.7)) is also a functional of the density $\rho(\mathbf{r})$. We can therefore construct a quantity

$$\mathcal{F}[\rho] = \text{Tr}_{\text{cl}}[f(\mathcal{H} - \int d\mathbf{r} \hat{\rho}(\mathbf{r})V(\mathbf{r}) + \beta^{-1} \ln f)], \quad (2.3.6)$$

which is a unique functional of the one-body density [6, 7]. From this functional is constructed a second functional:

$$\Omega_V[\rho'] = \mathcal{F}[\rho'] - \int d\mathbf{r} \rho'(\mathbf{r})[\mu - V(\mathbf{r})]. \quad (2.3.7)$$

When the density in Eq. (2.3.7), $\rho'(\mathbf{r})$, is the *equilibrium* density profile, $\rho(\mathbf{r})$, then $\Omega_V[\rho]$ is equal to the grand potential Ω [6] and the total Helmholtz free energy is

$$F = \mathcal{F}[\rho] + \int d\mathbf{r} \rho(\mathbf{r})V(\mathbf{r}), \quad (2.3.8)$$

and we identify $\mathcal{F}[\rho]$ as the intrinsic Helmholtz free energy. The fact that the equilibrium density profile $\rho(\mathbf{r})$ minimizes the functional $\Omega_V[\rho]$ results in the following variational principle:

$$\left. \frac{\delta \Omega_V[\rho']}{\delta \rho'(\mathbf{r})} \right|_{\rho'=\rho} = 0 \quad (2.3.9)$$

and

$$\Omega_V[\rho] = \Omega. \quad (2.3.10)$$

Inserting Eq. (2.3.7) into Eq. (2.3.9) yields:

$$\mu = V(\mathbf{r}) + \frac{\delta \mathcal{F}[\rho]}{\delta \rho(\mathbf{r})}. \quad (2.3.11)$$

If the fluid is at equilibrium, then the chemical potential μ is a constant throughout the inhomogeneous fluid and the term $\delta \mathcal{F}[\rho]/\delta \rho(\mathbf{r})$ in Eq. (2.3.11) is the *intrinsic* contribution to the chemical potential.

When the fluid is an ideal gas, then the intrinsic Helmholtz free energy functional is simply

$$\mathcal{F}_{id}[\rho] = \beta^{-1} \int d\mathbf{r} \rho(\mathbf{r}) [\ln \Lambda^3 \rho(\mathbf{r}) - 1]. \quad (2.3.12)$$

For a real fluid we can then divide the intrinsic Helmholtz free energy into an ideal gas part, Eq. (2.3.12), and an excess part, which takes into account the correlations between the particles in the fluid, i.e. $\mathcal{F}[\rho] = \mathcal{F}_{id}[\rho] + \mathcal{F}_{ex}[\rho]$. Eq. (2.3.11) therefore becomes

$$\Lambda^3 \rho(\mathbf{r}) = \exp[\beta u(\mathbf{r}) + c^{(1)}(\mathbf{r})] \quad (2.3.13)$$

where we have used $\delta \mathcal{F}_{id} / \delta \rho(\mathbf{r}) = \beta^{-1} \ln \Lambda^3 \rho(\mathbf{r})$, the ideal gas contribution to the intrinsic chemical potential and $c^{(1)}(\mathbf{r})$ is the excess (over ideal) term:

$$c^{(1)}(\mathbf{r}) \equiv -\beta \frac{\delta \mathcal{F}_{ex}[\rho]}{\delta \rho(\mathbf{r})}. \quad (2.3.14)$$

$c^{(1)}(\mathbf{r})$ is the one-body *direct correlation function* and is itself a functional of $\rho(\mathbf{r})$. Further differentiation with respect to the density generates the direct correlation function hierarchy [6, 7]:

$$c^{(n)}(\mathbf{r}^n) = \frac{\delta c^{(n-1)}(\mathbf{r}^{n-1})}{\delta \rho(\mathbf{r}_n)}. \quad (2.3.15)$$

Of particular interest is the two-body direct correlation function:

$$c^{(2)}(\mathbf{r}_1, \mathbf{r}_2) = \frac{\delta c^{(1)}(\mathbf{r}_1)}{\delta \rho(\mathbf{r}_2)} = -\beta \frac{\delta^2 \mathcal{F}_{ex}[\rho]}{\delta \rho(\mathbf{r}_2) \delta \rho(\mathbf{r}_1)}. \quad (2.3.16)$$

We have thus identified the direct pair correlation function, $c^{(2)}(\mathbf{r}_1, \mathbf{r}_2)$, for an *inhomogeneous* fluid. We introduced this function in the context of the OZ equation, Eq. (2.2.1), for homogeneous fluids in the previous section. This identification is proved as follows: If we insert Eq. (2.3.13) into Eq. (2.3.16), we find

$$c^{(2)}(\mathbf{r}_1, \mathbf{r}_2) = \frac{\delta(\mathbf{r}_1 - \mathbf{r}_2)}{\rho(\mathbf{r}_1)} - \beta \frac{\delta u(\mathbf{r}_1)}{\delta \rho(\mathbf{r}_2)} \quad (2.3.17)$$

The second term on the right hand side of Eq. (2.3.17) is the functional inverse, $G^{-1}(\mathbf{r}_1, \mathbf{r}_2)$, of the density-density correlation function (see Eq. (2.3.4)). A functional inverse is defined by

$$\int d\mathbf{r}_3 G^{-1}(\mathbf{r}_1, \mathbf{r}_3) G(\mathbf{r}_3, \mathbf{r}_2) = \delta(\mathbf{r}_1 - \mathbf{r}_2). \quad (2.3.18)$$

Substituting Eqs. (2.3.4), (2.3.5) and (2.3.17) into Eq. (2.3.18) and defining the inhomogeneous fluid total correlation function $h(\mathbf{r}_1, \mathbf{r}_2)$ by $\rho(\mathbf{r}_1)\rho(\mathbf{r}_2)h(\mathbf{r}_1, \mathbf{r}_2) = \rho^{(2)}(\mathbf{r}_1, \mathbf{r}_2) - \rho(\mathbf{r}_1)\rho(\mathbf{r}_2)$, we obtain the OZ equation for an inhomogeneous fluid [6, 7]:

$$h(\mathbf{r}_1, \mathbf{r}_2) = c^{(2)}(\mathbf{r}_1, \mathbf{r}_2) + \int d\mathbf{r}_3 h(\mathbf{r}_1, \mathbf{r}_3)\rho(\mathbf{r}_3)c^{(2)}(\mathbf{r}_3, \mathbf{r}_2). \quad (2.3.19)$$

When the fluid density is a constant, $\rho(\mathbf{r}) = \rho$, then this reduces to Eq. (2.2.1), the homogeneous fluid OZ equation.

As was the case for the homogeneous OZ equation, there are very few model fluids for which the inhomogeneous direct pair correlation function, $c^{(2)}(\mathbf{r}_1, \mathbf{r}_2)$, is known. However, DFT provides a formalism within which controlled approximations can be made for $c^{(2)}(\mathbf{r}_1, \mathbf{r}_2)$ and hence for $c^{(1)}(\mathbf{r})$. These approximations, together with Eq. (2.3.13), provide a prescription for calculating the inhomogeneous fluid density profile, $\rho(\mathbf{r})$. Such approximations are generally mean field in nature and so these DFT theories exhibit the mean field critical exponents for diverging quantities, such as the bulk correlation length, near the bulk critical point. They will also generate mean-field exponents for diverging interfacial thermodynamic quantities and correlation lengths – see Ch. 3. One route used to generate approximations for \mathcal{F}_{ex} , is to start from a functional integration of Eq. (2.3.16) [6, 7] and then focus on making an approximation for $c^{(2)}(\mathbf{r}_1, \mathbf{r}_2)$. An alternative route for determining \mathcal{F}_{ex} (a route limited to fluids where the potential function is pairwise additive – i.e. Eq. (2.1.3) holds) is as follows: One can recast the potential energy term in the Hamiltonian, Eq. (2.1.3), as [7]:

$$\Phi(\mathbf{r}^N) = \frac{1}{2} \int d\mathbf{r}_1 \int d\mathbf{r}_2 v(|\mathbf{r}_1 - \mathbf{r}_2|) \hat{\rho}(\mathbf{r}_1) (\hat{\rho}(\mathbf{r}_2) - \delta(\mathbf{r}_1 - \mathbf{r}_2)). \quad (2.3.20)$$

Inserting this expression into the partition function, Eq. (2.3.2), we find that on differentiating the partition function with respect to the pair potential $v(\mathbf{r}_1, \mathbf{r}_2)$ we arrive at the following equation:

$$\begin{aligned} \frac{\delta\Omega}{\delta v(\mathbf{r}_1, \mathbf{r}_2)} &= \frac{1}{2} (\langle \hat{\rho}(\mathbf{r}_1) \hat{\rho}(\mathbf{r}_2) \rangle - \langle \hat{\rho}(\mathbf{r}_1) \rangle \delta(\mathbf{r}_1, \mathbf{r}_2)) \\ &= \frac{1}{2} \rho^{(2)}(\mathbf{r}_1, \mathbf{r}_2), \end{aligned} \quad (2.3.21)$$

where we used Eq. (2.3.5) to obtain the second equality. Inserting Eq. (2.3.7) into Eq. (2.3.21), one obtains

$$\frac{\delta\mathcal{F}[\rho]}{\delta v(\mathbf{r}_1, \mathbf{r}_2)} = \frac{1}{2} \rho^{(2)}(\mathbf{r}_1, \mathbf{r}_2). \quad (2.3.22)$$

This equation can be integrated using a ‘charging’ parameter, α , to go from a reference fluid $\alpha = 0$, at the same temperature and with the same density profile, $\rho(\mathbf{r})$, but where particles interact via a pairwise potential $v_r(\mathbf{r}_1, \mathbf{r}_2)$, to the full system by means of the pair potential

$$v_\alpha(\mathbf{r}_1, \mathbf{r}_2) = v_r(\mathbf{r}_1, \mathbf{r}_2) + \alpha v_p(\mathbf{r}_1, \mathbf{r}_2) \quad 0 \leq \alpha \leq 1. \quad (2.3.23)$$

$\alpha = 1$ is the final system when the part of the pair potential, v_p , treated as the perturbation is fully ‘turned on’. The resulting intrinsic Helmholtz free energy is [7]:

$$\mathcal{F}[\rho] = \mathcal{F}_r[\rho] + \frac{1}{2} \int_0^1 d\alpha \int d\mathbf{r}_1 \int d\mathbf{r}_2 \rho^{(2)}(\mathbf{r}_1, \mathbf{r}_2; v_\alpha) v_p(\mathbf{r}_1, \mathbf{r}_2) \quad (2.3.24)$$

where \mathcal{F}_r is the free energy for the reference ($\alpha = 0$) fluid. Eq. (2.3.24) forms the basis for the perturbation theories mentioned earlier. Usually, the reference fluid would be the repulsive part of the pair potential, often modeled by the hard-sphere potential. However, if we simply use the ideal gas as the reference system, so that $v_r = 0$, then $v_p = v$, the full pair potential. If in addition we make a simple approximation, $\rho^{(2)}(\mathbf{r}_1, \mathbf{r}_2; v_\alpha) \simeq \rho(\mathbf{r}_1)\rho(\mathbf{r}_2)$, we arrive at the following intrinsic Helmholtz free energy functional:

$$\mathcal{F}[\rho] = \mathcal{F}_{id}[\rho] + \frac{1}{2} \int d\mathbf{r}_1 \int d\mathbf{r}_2 \rho(\mathbf{r}_1)\rho(\mathbf{r}_2)v(\mathbf{r}_1, \mathbf{r}_2). \quad (2.3.25)$$

This approximation assumes that the pair distribution function $\rho^{(2)}(\mathbf{r}_1, \mathbf{r}_2; v_\alpha)$ in the system subject to a pair potential v_α is simply the product of one-body densities $\rho(\mathbf{r}_1)\rho(\mathbf{r}_2)$, i.e. correlations are completely ignored for all coupling strengths α . Clearly this constitutes a gross mean-field-like approximation. Taking two derivatives of Eq. (2.3.25) with respect to $\rho(\mathbf{r})$, (see Eq. (2.3.16)) we find that (2.3.25) is the functional which generates the same RPA closure in bulk, Eq. (2.2.4), for the direct pair correlation function:

$$c_{RPA}^{(2)}(\mathbf{r}_1, \mathbf{r}_2) = -\beta v(\mathbf{r}_1, \mathbf{r}_2) = -\beta v(|\mathbf{r}_1 - \mathbf{r}_2|). \quad (2.3.26)$$

Note that (2.3.26) applies to all types of inhomogeneity. This particularly simple approximation turns out, as we shall see, to be a good approximation (at least for homogeneous fluids) when the pair potential $v(\mathbf{r}_1, \mathbf{r}_2)$ corresponds to a repulsive Gaussian. Eq. (2.3.25) forms the basis for much of the work in this thesis concerning the Gaussian core model.

Chapter 3

A Simple Approach to Inhomogeneous Fluids and an Introduction to Wetting

In this chapter we provide a brief introduction to certain aspects of inhomogeneous fluids. We employ a simple (Landau) free energy to describe inhomogeneous fluid density profiles with planar symmetry, and use these results to introduce the subject of wetting and wetting transitions and to describe some of the basic interfacial phenomena involved.

In the previous chapter we described a particular (RPA) approximation that can be made for the excess Helmholtz free energy functional of a simple fluid. The simplest approximation that can be made for the Helmholtz free energy functional of an inhomogeneous fluid is to make an expansion in powers of the gradient of the density profile around the bulk free energy of the fluid [6]:

$$\mathcal{F}[\rho] = \int d\mathbf{r} [f_0(\rho(\mathbf{r})) + f_2(\rho(\mathbf{r}))|\nabla\rho(\mathbf{r})|^2 + \mathcal{O}(\nabla\rho)^4], \quad (3.0.1)$$

where $f_0(\rho)$ is the Helmholtz free energy density for the homogeneous fluid of density ρ and for small deviations (within linear response) $f_2(\rho)$ can be shown to be [6]:

$$f_2(\rho(\mathbf{r})) = \frac{1}{12\beta} \int d\mathbf{r} r^2 c^{(2)}(\rho; r), \quad (3.0.2)$$

where $c^{(2)}(\rho; r)$ is the direct pair correlation function in a bulk fluid of density ρ . The first term in (3.0.1) is clearly a local density contribution. If we take two derivatives of Eq.

(3.0.1) with respect to $\rho(\mathbf{r})$, (see Eq. (2.3.16)) then we find that the direct pair correlation function generated is

$$c^{(2)}(\mathbf{r}_1, \mathbf{r}_2) = \left(-\beta \frac{\partial^2 f_0(\rho(\mathbf{r}_1))}{\partial \rho^2} + \frac{1}{\rho(\mathbf{r}_1)} - 2\beta f_2(\rho(\mathbf{r}_1)) \nabla^2 \right) \delta(\mathbf{r}_1 - \mathbf{r}_2). \quad (3.0.3)$$

This result, that the direct pair correlation function is a delta-function, means that the functional (3.0.1) is unable to incorporate the algebraic decay in the inhomogeneous fluid density profiles that one finds when the fluid pair potentials decay algebraically, such as for a Lennard-Jones fluid [7]. The Helmholtz free energy functional, Eq. (3.0.1), is strictly valid for fluids which interact via short ranged pair potentials (decaying exponentially or faster) and when the density profiles are slowly changing; one should not expect Eq. (3.0.1) to be able to incorporate the oscillatory density profiles that one finds for a fluid close to a strongly repulsive or hard wall.

3.1 Landau theory for simple fluids

We can simplify the square gradient Helmholtz free energy functional, Eq. (3.0.1), even further by assuming that f_2 can be taken to be a constant, i.e. that it is only weakly dependent on the density of the fluid in the region of the phase diagram we are interested in. Moreover we expand $f_0(\rho)$ around its value for a fluid with density ρ_c . We are seeking density profiles for the fluid with temperature T and chemical potential μ of a state near to the liquid-gas phase boundary, so we choose ρ_c such that $\rho_l > \rho_c > \rho_g$, where ρ_l and ρ_g are the coexisting liquid and gas densities. We expand in powers of the (dimensionless) order parameter,

$$\phi(\mathbf{r}) = L^3(\rho(\mathbf{r}) - \rho_c), \quad (3.1.1)$$

where L is a constant with the dimensions of a length. We can choose ρ_c so that there are no odd powers up to $\mathcal{O}(\phi^4)$ in the expansion [9], and in this case we find that Eq. (3.0.1) takes the form

$$\mathcal{F}[\rho] \simeq \int d\mathbf{r} (f_0(\rho_c) + a\phi^2(\mathbf{r}) + b\phi^4(\mathbf{r}) + \frac{g}{2}|\nabla\phi(\mathbf{r})|^2), \quad (3.1.2)$$

Where a and b are constants which can be determined from the expansion of the bulk Helmholtz free energy, $f_0(\rho)$, and g is a constant proportional to f_2 . In Eq. (3.1.2) we have kept only terms up to $\mathcal{O}(\phi^4)$ and $\mathcal{O}(\nabla\phi)^2$. Equation (3.1.2) is simply the Landau free energy for an Ising magnet, where ϕ corresponds to the magnetization.

We shall be using the Landau free energy, Eq. (3.1.2), in this chapter to calculate the order parameter profiles for a fluid wetting a planar wall. Our introduction to wetting is close to that found in Ref. [10] (see also Ref. [11]). Before moving on to discussing wetting within Landau theory, we shall recall some of the basic properties of the functional in Eq. (3.1.2). In the bulk of a fluid, where the order parameter is a constant, $\phi(\mathbf{r}) = \phi_b$, Eq. (3.1.2) yields the bulk free energy, $\mathcal{F}_b = V(f_0(\rho_c) + a\phi_b^2 + b\phi_b^4)$, where V is the volume of the fluid. The coefficient $a \rightarrow 0$ at the fluid critical point – i.e. $a \propto (T - T_c)$, where T_c is the temperature at the critical point. The coefficient $b > 0$, so that the global minimum of the free energy is at a finite value of the order parameter, ϕ_b . The equilibrium value of the order parameter corresponds to $\partial\mathcal{F}_b/\partial\phi_b = 0$, and when $a < 0$ and $b > 0$ there are two minima, $\pm\phi_b$, with $\phi_b^2 = -a/2b$. We will choose the value of L in Eq. (3.1.1) so that $|\phi_b| = 1$, and therefore $b = -a/2$ in Eq. (3.1.2). The two equilibrium values of the order parameter, $+\phi_b$ and $-\phi_b$, correspond to the coexisting liquid and gas phases respectively. We can also calculate the correlation functions generated by Eq. (3.1.2) in each of the bulk phases. If we substitute $\phi(\mathbf{r}) = \phi_b + \psi(\mathbf{r})$ into Eq. (3.1.2), where $\psi(\mathbf{r})$ is a small fluctuation in the order parameter, $\phi(\mathbf{r})$, from its bulk value, ϕ_b , then we find that from Eq. (3.1.2) we obtain

$$\mathcal{F}_{\phi_b} \simeq \int d\mathbf{r} (f_0(\rho_c) + \frac{a}{2} - 2a\psi^2(\mathbf{r}) + \frac{g}{2}|\nabla\psi(\mathbf{r})|^2), \quad (3.1.3)$$

where we have neglected terms of $\mathcal{O}(\psi)^3$ and higher. Taking two functional derivatives of Eq. (3.1.3) one obtains

$$\frac{\delta^2\mathcal{F}_{\phi_b}}{\delta\psi(\mathbf{r}')\delta\psi(\mathbf{r})} = (-4a - g\nabla^2)\delta(\mathbf{r} - \mathbf{r}'). \quad (3.1.4)$$

The functional inverse of the density-density correlation function, $G^{-1}(\mathbf{r}, \mathbf{r}')$, is obtained by taking two derivatives of the Helmholtz free energy, with respect to the fluid density profile:

$$G^{-1}(\mathbf{r}, \mathbf{r}') = \beta \frac{\delta^2\mathcal{F}[\rho]}{\delta\rho(\mathbf{r}')\delta\rho(\mathbf{r})} \quad (3.1.5)$$

(see Eqs. (2.3.4), (2.3.16) and (2.3.18)). From this and Eqs. (3.1.4) and (3.1.1) one finds that $G^{-1}(\mathbf{r}, \mathbf{r}') = \beta L^6(-4a - g\nabla^2)\delta(\mathbf{r} - \mathbf{r}')$. Fourier transforming this result into k -space one obtains the simple result

$$\hat{G}^{-1}(k) = \beta L^6 g(\xi^{-2} + k^2), \quad (3.1.6)$$

where \hat{G}^{-1} is the Fourier transform of G^{-1} and $\xi^{-2} = -4a/g$. In Fourier space Eq. (2.3.18) has a particularly simple form and one finds that the Fourier transform of the density-density correlation function has the (classical) Ornstein-Zernike form $\hat{G}(k) \sim 1/(\xi^{-2} + k^2)$. We can invert the Fourier transform $\hat{G}(k)$ in order to obtain the bulk density-density correlation function in 3 dimensions:

$$\begin{aligned} G(r) &= \frac{1}{(2\pi)^3} \frac{1}{\beta L^6 g} \int d\mathbf{k} \frac{\exp(i\mathbf{k}\cdot\mathbf{r})}{(\xi^{-2} + k^2)} \\ &= \frac{1}{4\pi\beta L^6 g} \frac{\exp(-r/\xi)}{r}. \end{aligned} \quad (3.1.7)$$

One therefore identifies ξ as the bulk correlation length. Note that within this simple Landau theory based on Eq. (3.1.2), one finds that the bulk correlation length is the same in both the liquid and gas phases – this is because Eq. (3.1.2) corresponds to the Landau free energy for an Ising magnet, where there is a symmetry between the ‘up’ spins and the ‘down’ spins. For all real fluids this result, that ξ is the same in both the liquid and the gas phases, is not generally true. Note also that the density-density correlation function given by Eq. (3.1.7) clearly does not incorporate the oscillations one often finds in $G(r) = \rho^2 h(r) + \rho\delta(r)$ in the bulk liquid phase for $r \sim \sigma$, the diameter of the fluid particles, nor does it incorporate the oscillatory asymptotic decay that $G(r)$ can exhibit in certain portions of a fluid phase diagram. (The asymptotic decay of $G(r)$, or equivalently $h(r)$, can cross over from damped oscillatory to monotonic, of the form in Eq. (3.1.7); the cross over line between these two regimes is the Fisher-Widom line [2], and we shall return to this topic in Ch. 5). This, as we anticipated earlier, means that one is unable to obtain oscillatory inhomogeneous fluid order parameter profiles for a fluid in a monotonic external potential $V(\mathbf{r})$, which minimize Eq. (3.1.2), something which one could expect in a more accurate theory for the density profile of a liquid at a strongly repulsive wall.

3.2 Inhomogeneous fluid order parameter profiles

In order to calculate the inhomogeneous fluid order parameter profiles due to an external potential $V(\mathbf{r})$, for a fluid whose Helmholtz free energy is approximated by Eq. (3.1.2), we must minimize the following grand potential functional:

$$\Omega = \int d\mathbf{r} \left[\omega(\rho'_c) + a\phi^2(\mathbf{r}) + b\phi^4(\mathbf{r}) + \frac{g}{2} |\nabla\phi(\mathbf{r})|^2 + V(\mathbf{r})\phi(\mathbf{r}) \right], \quad (3.2.1)$$

where $\omega(\rho'_c)$ is the grand potential density when the bulk fluid density is ρ'_c ¹. We must simply minimize Eq. (3.2.1) subject to the boundary condition $\phi(\infty) = -\phi_b$, i.e. we assume that $V(\mathbf{r})$ decays to zero as $\mathbf{r} \rightarrow \infty$. If $V(\mathbf{r})$ has planar symmetry, i.e. $V(\mathbf{r}) = V(z)$ as is appropriate to a planar wall, then from Eq. (3.2.1) we obtain the grand potential per unit area

$$\omega \equiv \frac{\Omega}{A} = \int_{-\infty}^{\infty} dz \left[\omega(\rho'_c) + a\phi^2(z) + b\phi^4(z) + \frac{g}{2} \left(\frac{d\phi(z)}{dz} \right)^2 + V(z)\phi(z) \right]. \quad (3.2.2)$$

The order parameter profile which minimizes this equation satisfies the Euler-Lagrange equation

$$2a\phi(z) + 4b\phi^3(z) - g \frac{d^2\phi(z)}{dz^2} + V(z) = 0. \quad (3.2.3)$$

When $V(z) = 0$ (the wall has vanishing effect) the solution to this differential equation is

$$\phi(z) = -\phi_b \tanh \left(\frac{z-l}{2\xi} \right), \quad (3.2.4)$$

where l is an undetermined constant; there is an infinite number of solutions. In this case, when the external potential $V(z) = 0$, the order parameter profile, Eq. (3.2.4), is that for the free-interface between the gas phase, $\phi(\infty) = -\phi_b$, and the liquid phase, $\phi(-\infty) = \phi_b$. The interface is located at $z = l$, and noting the denominator inside the tanh in (3.2.4), the length 2ξ determines the width of the interface. The intrinsic interfacial width takes this value because the bulk correlation length ξ is the same in both the gas and the liquid phase. More generally one would expect the width of the interface to be determined by $\xi_l + \xi_g$, where ξ_l and ξ_g are the correlation lengths in the coexisting liquid and gas phases respectively.

Having demonstrated how one can calculate the order parameter profile for the free interface between coexisting liquid and gas phases within Landau theory, we can consider the order parameter profile at a planar wall. However, before proceeding, we will briefly review some of the thermodynamic quantities that are relevant for studying wetting and interfaces.

¹Note we have chosen the reference density $\rho'_c \neq \rho_c$ in order to eliminate all odd powers of ϕ up to $\mathcal{O}(\phi^4)$, that would otherwise arise due to the $-\mu\phi(\mathbf{r})$ term in (3.2.1) [9]. This in turn changes our values for L , a and b but, of course, not quantities such as ξ .

3.3 Thermodynamics of interfaces

For a more detailed introduction to the thermodynamics of interfaces we refer the reader to Refs. [10, 12, 13]. Here we shall only introduce some of the ideas we will need for this thesis. In order to describe the thermodynamics of an interface, it is useful to consider the excess (over bulk) part of the different thermodynamic potentials. For example, one can consider the excess grand potential

$$\Omega_{ex} = \Omega - \Omega_b, \quad (3.3.1)$$

where Ω is the total grand potential of the system and Ω_b is the grand potential for a bulk fluid without the interface. In order to implement this, one has to define a Gibbs dividing surface which defines the volume over which Ω_b is calculated, since Ω_b is extensive in the volume of the system. When considering a fluid at a planar wall the natural choice for the Gibbs dividing surface is the point z_0 at which the external potential $V(z \rightarrow z_0) \rightarrow \infty$.

Having defined the excess grand potential, Ω_{ex} , one can also consider other excess quantities such as the excess number of particles:

$$N_{ex} = N - \rho_b V, \quad (3.3.2)$$

where N is the total number of particles in the system of volume V and ρ_b is the bulk density of the fluid at the given chemical potential μ and temperature T . Similarly one can define the excess surface entropy, S_{ex} . The second law of thermodynamics then leads to

$$d\Omega_{ex} = -S_{ex}dT - N_{ex}d\mu. \quad (3.3.3)$$

It is often more useful to work with excess quantities per unit area of the wall such as $s_{ex} = S_{ex}/A$, $\gamma = \Omega_{ex}/A$ and $\Gamma = N_{ex}/A$, which leads to

$$d\gamma = -s_{ex}dT - \Gamma d\mu. \quad (3.3.4)$$

Here we have introduced the surface tension γ , which is the surface excess grand potential per unit area, and the adsorption Γ . These are important quantities for analyzing adsorption and wetting phenomena. One can use Eq. (3.3.4) in the usual Gibbsian way to obtain results such as

$$\Gamma = - \left(\frac{\partial \gamma}{\partial \mu} \right)_T, \quad (3.3.5)$$

the *Gibbs adsorption equation*, as well as generating surface Maxwell relations [10, 12, 13].

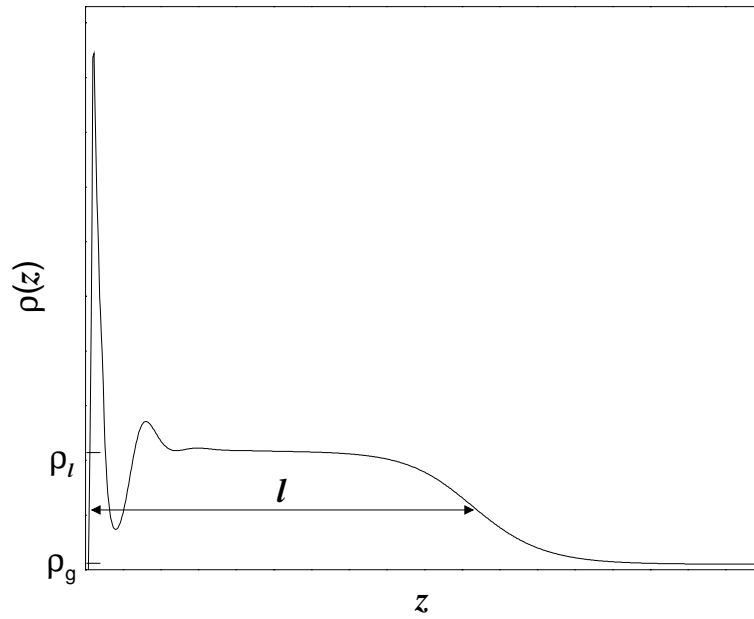


Figure 3.1: A typical wetting density profile for a fluid at a wall. z is the perpendicular distance from the wall. The bulk fluid (gas phase with density ρ_g) has a chemical potential, μ , near to that for liquid-gas coexistence, μ_{sat} . The liquid phase wetting the wall has a density ρ_l . For complete wetting the film thickness $l \rightarrow \infty$ as $\mu \rightarrow \mu_{sat}$.

3.4 Wetting: near to coexistence

Wetting of the interface between the fluid and the wall of a container can occur for any fluid that exhibits liquid-gas phase separation. Wetting can occur when the bulk fluid, say the gas phase, is in a state near to bulk coexistence. Then a thick adsorbed (wetting) film of the coexisting liquid phase can be found adsorbed at the wall. Similarly, when the bulk fluid is the liquid phase, near to coexistence, the interface of the liquid with a different (repulsive) wall can be wet by the gas phase – this is complete drying. In the complete wetting regime the thickness of the wetting film increases as the temperature of the bulk fluid $T \rightarrow T_{sat}$, the temperature at which the bulk fluid condenses. Alternatively, as one changes the chemical potential $\mu \rightarrow \mu_{sat}$, the chemical potential at which the fluid condenses, one finds that a thick wetting film can develop at the interface. One describes the interface between the substrate and the bulk fluid as completely wet by the other (coexisting) fluid phase if the thickness of the adsorbed layer of the latter at the wall, l , diverges – i.e. $l \rightarrow \infty$ as $\mu \rightarrow \mu_{sat}$.

In Fig. 3.1 is displayed a typical density profile for a liquid wetting a planar wall located at $z = 0$. For a planar structureless wall, the average density profile of the fluid in contact with that wall, $\rho(\mathbf{r})$, will depend only on the distance z from the wall, i.e. $\rho(\mathbf{r}) = \rho(z)$. From the microscopic density profile we can calculate the Gibbs adsorption,

$$\Gamma = \int_0^\infty dz [\rho(z) - \rho(\infty)]. \quad (3.4.1)$$

Eq. (3.4.1) provides a link between any microscopic theory for the density profile, and the surface thermodynamics (see Eq. (3.3.5)). The adsorbed film thickness l is proportional to the adsorption at the wall, Γ , since when the adsorbed film thickness is large,

$$\Gamma \simeq l(\rho_l - \rho_g), \quad (3.4.2)$$

where ρ_l and ρ_g are the coexisting liquid and gas densities. The adsorbed film thickness (or equivalently the adsorption) is a good order parameter for describing wetting phenomena. We shall pursue this idea in the next section.

3.5 Landau theory for wetting

In Sec. 3.2 we introduced some of the basic concepts associated with inhomogeneous fluids within a simple Landau theory approach. We will now develop some of those ideas further in order to introduce the subject of wetting and wetting transitions, and to derive an expression for the excess surface grand potential as a function of the adsorbed film thickness. This approach follows that of Ref. [10]. The approximate Landau free energy used in Sec. 3.2, Eq. (3.1.2), describes two equilibrium coexisting bulk phases with order parameter $\phi = \pm\phi_b$, where $\phi_b^2 = -a/2b$, and in each of the coexisting phases the bulk correlation length ξ is the same, with $\xi^{-2} = -4a/g$. The grand potential per unit area for an external potential with planar symmetry is given by Eq. (3.2.2). We are interested in the case when the external potential is of the form:

$$V(z) = \begin{cases} \infty & z < 0 \\ V_>(z) & z \geq 0. \end{cases} \quad (3.5.1)$$

We shall consider the case when the bulk phase $z \rightarrow \infty$ is the gas phase, with order parameter $\phi = -\phi_b$, and the wall is wet by the coexisting liquid phase, with order parameter

$\phi = \phi_b$. We shall focus on the excess grand potential per unit area which is given by (see Eqs. (3.2.2) and (3.3.1)):

$$\omega_{ex} = \int_0^\infty dz \left[a(\phi^2(z) - \phi_b^2) + b(\phi^4(z) - \phi_b^4) + \frac{g}{2} \left(\frac{d\phi(z)}{dz} \right)^2 + V_>(z)\phi(z) \right], \quad (3.5.2)$$

when the fluid is at coexistence, i.e. the chemical potential $\mu = \mu_{sat}$. The order parameter profile for $z > 0$ which minimizes Eq. (3.5.2) satisfies the Euler-Lagrange equation (3.2.3). When $V_>(z) = 0$, as we saw in Sec. 3.2, the order parameter profile is given by Eq. (3.2.4). If $V_>(z) = \epsilon\delta(z)$, i.e. a delta function, then the wall potential will provide a boundary condition at $z = 0$ and the order parameter profile for $z > 0$ will be given by Eq. (3.2.4). In this case we will write the excess grand potential as

$$\omega_{ex} = \int_0^\infty dz \left[a(\phi^2(z) - \phi_b^2) + b(\phi^4(z) - \phi_b^4) + \frac{g}{2} \left(\frac{d\phi(z)}{dz} \right)^2 \right] + \epsilon\phi(0) + c\phi^2(0). \quad (3.5.3)$$

The additional phenomenological term, $c\phi^2(0)$, where $c > 0$ is a constant, is added to take into account of the fact that the mean number of bonds between the particles located near the wall is smaller than in the bulk [10]. The order parameter profile for $z > 0$ satisfies the Euler-Lagrange equation

$$g \frac{d^2\phi(z)}{dz^2} = 2a\phi(z) + 4b\phi^3(z), \quad (3.5.4)$$

which on integration with respect to ϕ yields:

$$\frac{g}{2} \left(\frac{d\phi(z)}{dz} \right)^2 = a(\phi^2(z) - \phi_b^2) + b(\phi^4(z) - \phi_b^4). \quad (3.5.5)$$

If we substitute this into Eq. (3.5.3) we obtain:

$$\begin{aligned} \omega_{ex} &= \int_0^\infty dz g \left(\frac{d\phi(z)}{dz} \right)^2 + \epsilon\phi(0) + c\phi^2(0) \\ &= g \int_{\phi(0)}^{\phi(\infty)=-\phi_b} d\phi' \left(\frac{d\phi'}{dz} \right) + \epsilon\phi(0) + c\phi^2(0). \end{aligned} \quad (3.5.6)$$

Since the set of order parameter profiles which satisfy the Euler-Lagrange equation (3.5.4), are of the form: $\phi(z) = -\phi_b \tanh[(z-l)/2\xi]$, where l is yet to be determined, we will assume this form, and we therefore find $\partial\phi/\partial z = -(\phi_b^2 - \phi^2)/2\xi\phi_b$. Substituting this into Eq. (3.5.6) and then performing the simple integration, we obtain

$$\omega_{ex} = \frac{g}{2\xi\phi_b} \left[\frac{2\phi_b^3}{3} + \phi_b^2\phi(0) - \frac{\phi^3(0)}{3} \right] + \epsilon\phi(0) + c\phi^2(0). \quad (3.5.7)$$

When the interface between the wetting phase and the bulk phase is far from the wall ($l \rightarrow \infty$), then $\phi(0) = -\phi_b \tanh(-\infty) = \phi_b$, the bulk value of the order parameter for the wetting phase, and Eq. (3.5.7) yields

$$\omega_{ex}(l \rightarrow \infty) = \frac{2g\phi_b^2}{3\xi} + \epsilon\phi_b + c\phi_b^2. \quad (3.5.8)$$

The first term on the right hand side of Eq. (3.5.8) is simply the excess grand potential per unit area for the interface between the liquid and gas phases: the interfacial (gas-liquid) surface tension $\gamma_{lg} = 2g\phi_b^2/3\xi$. The final two terms are the wall-liquid surface tension, $\gamma_{wl} = \epsilon\phi_b + c\phi_b^2$. We have arrived at the general result that when the wetting film is (infinitely) thick then the wall-bulk-gas total surface tension,

$$\omega_{ex}(l \rightarrow \infty) \equiv \gamma_{wg} = \gamma_{lg} + \gamma_{wl}. \quad (3.5.9)$$

This result can also be obtained from Young's equation,

$$\gamma_{wg} = \gamma_{wl} + \gamma_{lg} \cos \theta \quad (3.5.10)$$

by taking $\theta \rightarrow 0$, where θ is the contact angle. Young's equation is obtained by a simple mechanical argument: one considers a drop of liquid on a surface and by balancing the forces at the contact line between the liquid-gas interface and the wall-liquid interface one arrives at Young's equation [11]. Returning to Eq. (3.5.7), when l (which has yet to be determined) is large one can expand $\phi(0) = -\phi_b \tanh(-l/2\xi)$ in powers of $\exp(-l/\xi)$, giving $\phi(0) = \phi_b - 2\phi_b \exp(-l/\xi) + 2\phi_b \exp(-2l/\xi) - 2\phi_b \exp(-3l/\xi) + \mathcal{O}(\exp(-4l/\xi))$. Substituting this into Eq. (3.5.7) one obtains the following result for the excess grand potential, when there is a wetting film of thickness l :

$$\begin{aligned} \omega_{ex}(l) = & \gamma_{wl} + \gamma_{lg} + A(T) \exp(-l/\xi) + B(T) \exp(-2l/\xi) \\ & + C(T) \exp(-3l/\xi) + \mathcal{O}(\exp(-4l/\xi)), \end{aligned} \quad (3.5.11)$$

where $A(T) = -2\phi_b(2c\phi_b + \epsilon)$, $B(T) = 2\phi_b(\epsilon + 4c\phi_b - g\phi_b/\xi)$ and $C(T) = 2\phi_b(8g\phi_b/3\xi - 6c\phi_b - \epsilon)$. The form of Eq. (3.5.11) demonstrates an important idea in the physics of liquids at interfaces: for fluids composed of particles interacting via short ranged pair potentials wetting a wall, it is the tail of the liquid-gas interfacial profile, which decays exponentially with decay length ξ , the bulk correlation length, interacting with the wall which determines the wetting film thickness. In the present (Ising) Landau treatment the bulk correlation length is the same in the two coexisting phases, however for a real

fluid, where the bulk correlation length is not the same in the two coexisting phases, it is the bulk correlation length in the phase wetting the wall, ξ_w , which should appear in the exponential terms in Eq. (3.5.11).

3.6 Wetting transitions

A wetting transition is a surface phase transition which occurs for example on the wall of a container which is enclosing a fluid. If the fluid in the container is in the gas phase near to but above the boiling temperature, then the liquid phase can wet the walls of the container, preceding the condensation in the bulk of the fluid. The wetting film grows in thickness as the boiling temperature is approached while keeping the pressure, p , in the bulk reservoir constant. This is not particularly surprising. However for some fluids there is a wetting transition, i.e. depending on the pressure there can be a thick wetting film adsorbed at the wall as bulk coexistence is approached, but for other (lower) pressures the adsorbed film thickness remains finite. Thus along the coexistence line $p_{sat}(T)$ there can be a transition from a thin to thick adsorbed layer. This transition can be either first order or continuous [11]. Not all (model) fluids exhibit a wetting transition, but of those that do, there are some that can display either a first order wetting transition or a continuous one, depending on the form of the wall-fluid potential.

We can use Eq. (3.5.11) to understand the origin of wetting transitions [11]. Eq. (3.5.11) was derived for the case when the bulk fluid is exactly at coexistence. The equilibrium adsorbed film thickness l_{eq} is obtained by minimizing (3.5.11) with respect to l , i.e. l_{eq} is the solution to

$$\left(\frac{\partial \omega_{ex}(l)}{\partial l} \right)_{l=l_{eq}} = 0. \quad (3.6.1)$$

If the coefficients $A(T)$, $B(T)$ and $C(T)$ in (3.5.11) are all positive, which is the situation one typically finds on the liquid-gas coexistence line near to the bulk critical point of the fluid, then it is the leading order term, $A(T) \exp(-l/\xi)$, which dominates the expression for $\omega_{ex}(l)$ for a large film thickness l and the equilibrium film thickness obtained is $l_{eq} = \infty$, i.e. the wall is wet by a macroscopically thick adsorbed film. However, if $A(T) < 0$ and $B(T) > 0$ in Eq. (3.5.11), which can occur as one moves to a point on the liquid-gas coexistence line further away from the bulk critical point, then the equilibrium film thickness obtained using Eqs. (3.5.11) and (3.6.1) is $l_{eq} \simeq \xi \ln[-2B(T)/A(T)] < \infty$; the adsorbed film thickness is finite. There is therefore a wetting transition between a thin (l is

finite) and thick (l is infinite) adsorbed film, which occurs when $A(T) = 0$. This transition is continuous, i.e. as one moves along the liquid-gas coexistence line, starting in the low temperature region, the thickness of the adsorbed film is finite in the low temperature ($A(T) < 0$) regime, but as we move along the coexistence line towards the critical point, increasing in temperature, the film thickness $l \rightarrow \infty$ continuously as $A(T) \rightarrow 0$, diverging at the wetting temperature, T_w , at which $A(T_w) = 0$. In Fig. 3.2 (see also Fig. 3.2 in Ref. [11]) we plot the excess surface grand potential $\omega_{ex}(l)$ as a function of l , for both $T > T_w$ and $T < T_w$, the wetting temperature. For $T > T_w$ the minimum (equilibrium) is at $l = \infty$, however for $T < T_w$ there is a minimum at a finite value of l .

We have seen how a continuous (second order) wetting transition can occur. A first order wetting transition is also possible. This can happen when the coefficients $A(T)$ and $C(T)$ in Eq. (3.5.11) are both positive and when the coefficient $B(T)$ becomes sufficiently negative. In Fig. 3.3 we plot (following Ref. [11]) the excess surface grand potential, $\omega_{ex}(l)$, as a function of l for three different temperatures, $T < T_w^1$, $T = T_w^1$ and $T > T_w^1$, the wetting temperature for the first order transition. In this situation, if one moves along the liquid-gas coexistence line towards the bulk fluid critical point, then for low temperatures, $T < T_w^1$, the equilibrium adsorbed film thickness is finite. However at the wetting temperature, T_w^1 , the finite and infinitely thick film have equal grand potential and the adsorbed film thickness jumps and becomes infinite, i.e. the film thickness diverges discontinuously at T_w^1 .

In all the discussion so far we have only considered the case when the bulk fluid is at liquid-gas coexistence, with chemical potential μ_{sat} . This begs the question: what is the equilibrium adsorbed film thickness when the the bulk fluid is off coexistence, i.e. the bulk fluid has chemical potential $(\mu_{sat} - \delta\mu)$, with $\delta\mu > 0$? In this situation there will be an extra term in Eq. (3.5.11) to take into account the fact that the bulk fluid is off-coexistence. From Eq. (3.3.4) we can expect that when $\delta\mu$ is small, the additional term in Eq. (3.5.11) will be $\Gamma\delta\mu$. Using Eq. (3.4.2), Eq. (3.5.11) becomes:

$$\begin{aligned} \omega_{ex}(l) = & \gamma_{wl} + \gamma_{lg} + l(\rho_l - \rho_g)\delta\mu + A(T) \exp(-l/\xi) \\ & + B(T) \exp(-2l/\xi) + \mathcal{O}(\exp(-3l/\xi)). \end{aligned} \quad (3.6.2)$$

If one minimizes this expression with respect to the adsorbed film thickness, l , when $\delta\mu \neq 0$, the equilibrium adsorbed film thickness is always finite. For example, in the regime where at coexistence ($\delta\mu = 0$) the equilibrium film thickness $l_{eq} = \infty$, i.e. in the

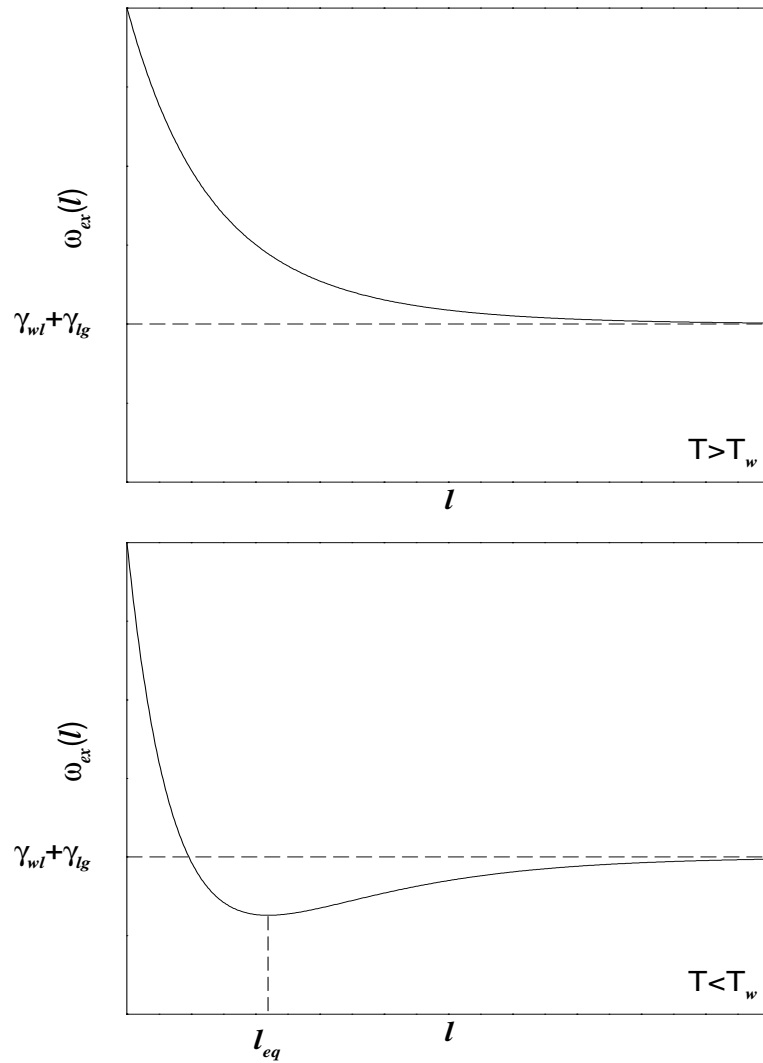


Figure 3.2: Plot of the excess surface grand potential per unit area $\omega_{ex}(l)$ at bulk coexistence as a function of l , the adsorbed wetting film thickness, for both $T > T_w$ and $T < T_w$, the wetting temperature. When $T > T_w$ the equilibrium adsorbed film thickness $l_{eq} = \infty$, however when $T < T_w$ one finds $l_{eq} < \infty$ is finite. As $T \rightarrow T_w$, $l_{eq} \rightarrow \infty$, this gives a continuous wetting transition.

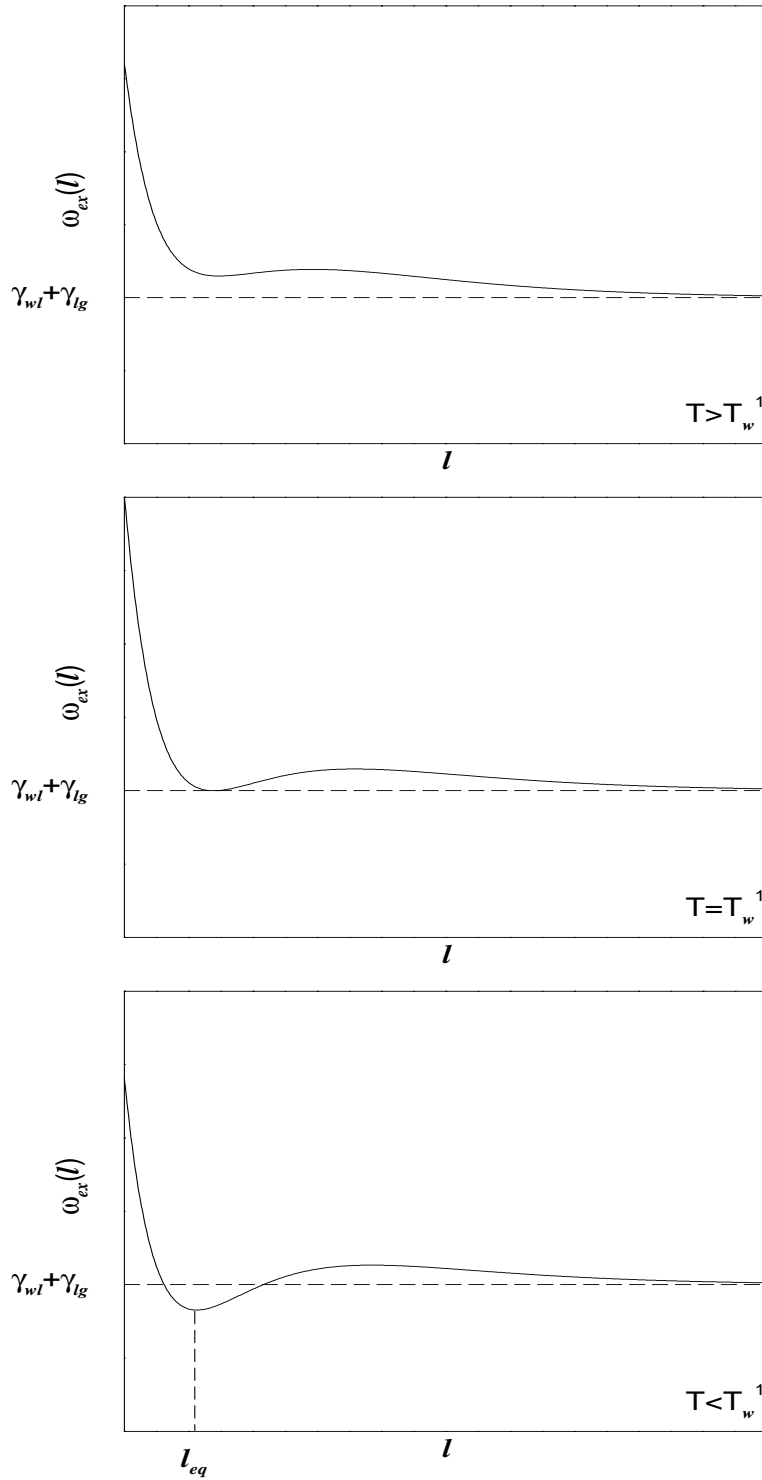


Figure 3.3: The excess surface grand potential per unit area, $\omega_{ex}(l)$ at bulk coexistence as a function of l , the adsorbed wetting film thickness, for three different temperatures, $T < T_w^1$, $T = T_w^1$ and $T > T_w^1$, the wetting temperature. When $T < T_w^1$ the equilibrium adsorbed film thickness l_{eq} is finite, whereas for $T > T_w^1$, $l_{eq} = \infty$. At T_w^1 the equilibrium wetting film thickness diverges discontinuously to infinity.

regime where both $A(T)$ and $B(T)$ in Eq. (3.6.2) are positive, then one finds that for small $\delta\mu$, l_{eq} is given by

$$l_{eq} \simeq -\xi \ln \left(\frac{\xi(\rho_l - \rho_g)\delta\mu}{A(T)} \right). \quad (3.6.3)$$

Thus as one approaches coexistence at constant temperature, the adsorbed film thickness diverges: $l \sim -\xi \ln \delta\mu$. This result, which applies for fluids interacting via short ranged pair potentials and short-ranged wall-fluid potentials, is not just a feature of the present Landau treatment of wetting. The same result appears in more sophisticated (albeit still mean-field) treatments, for example in DFT treatments of wetting [11].

When the wetting transition is first order we saw that there was a discontinuous jump (divergence) in the adsorbed film thickness at the wetting transition. This jump also manifests itself off-coexistence: For a first order wetting transition one finds a *pre-wetting line*. This line starts at the wetting transition point, $T = T_w^1$, and extends away from the liquid-gas coexistence line, ending in a critical point at a higher temperature $T_{wcp} > T_w^1$. If one considers a path approaching the liquid-gas coexistence line, at the point where this path intersects the pre-wetting line the adsorption at the wall is discontinuous. The adsorbed film thickness jumps from one finite value to another larger but finite value (both values are finite since neither state points are on the bulk liquid-gas coexistence line). The pre-wetting line is therefore a line of first order (thin-thick adsorbed film) surface phase transitions. It meets the bulk coexistence line tangentially at $T = T_w^1$. In Fig. 3.4 (see also Fig. 2.2 in Ref. [11]) we plot the adsorbed film thickness, l_{eq} , for three different paths (at three temperatures), intersecting the liquid-gas coexistence line at chemical potential μ_{sat} . In the inset is plotted a typical pre-wetting line (end-points marked with filled circles), on the phase diagram for the fluid in the chemical potential-temperature, (μ, T) , plane. For a temperature $T < T_w^1$, the wetting temperature, (path A) the adsorbed film thickness remains finite right up to coexistence. On path B, intersecting the pre-wetting line, there is a discontinuity in the adsorbed film thickness at the point where this path intersects the pre-wetting line. On path B and on path C, at a temperature above T_{wcp} , the pre-wetting line critical point, the adsorbed film thickness diverges continuously as $\mu \rightarrow \mu_{sat}^-$.

Another issue we have not addressed in this introduction to wetting of fluids composed of particles interacting via short ranged forces is what is the effect of wall potentials that are not delta function-like, as we assumed so far? If we set the external potential in Eq. (3.5.2) to be of the form $V_{>}(z) = \epsilon\delta(z) + \nu \exp(-z/\lambda)$, where λ is the wall potential decay

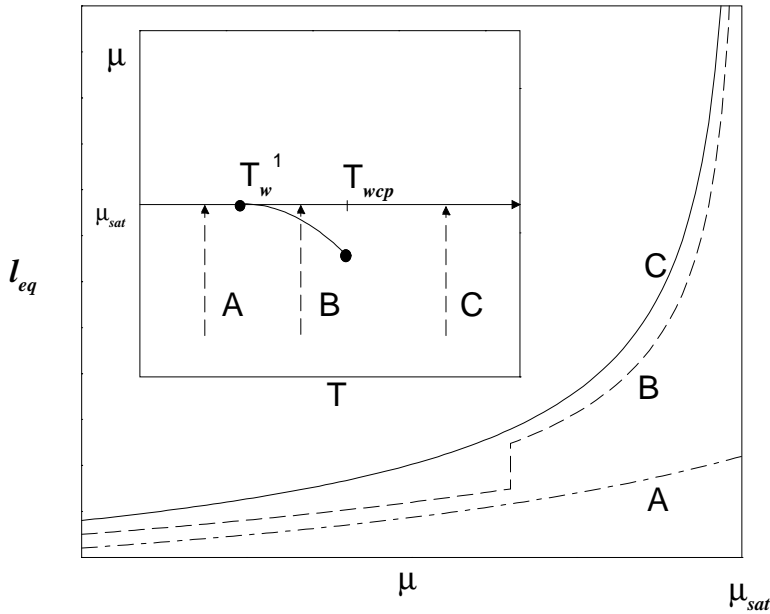


Figure 3.4: The equilibrium film thickness l_{eq} for three different paths at three different temperatures. The paths are marked in the fluid phase diagram in the inset. Path A is at a temperature $T < T_w^1$, below the wetting temperature T_w . On this path the adsorbed film thickness remains finite right up to coexistence. On path B, intersecting the pre-wetting line (filled circles at the ends), the film thickness is discontinuous at the point where this path intersects the pre-wetting line. On path B, $l_{eq} \rightarrow \infty$ as $\mu \rightarrow \mu_{sat}^-$. On path C, l_{eq} also diverges as $\mu \rightarrow \mu_{sat}^-$. However for this temperature, $T > T_{wcp}$, above the pre-wetting line critical point temperature, there is no jump at lower values of μ . Note that for simplicity we have assumed that the bulk coexistence value of the chemical potential μ_{sat} is independent of temperature.

length, this will add a term

$$\nu L^{-3} \int_0^\infty dz \exp(-z/\lambda) \phi(z) \quad (3.6.4)$$

to w_{ex} in Eq. (3.5.3). When the adsorbed wetting film thickness is large, then this will just add terms $\simeq A_{wall}(T) \exp(-l/\lambda) + \mathcal{O}(\exp(-2l/\lambda))$ to Eq. (3.6.2):

$$\begin{aligned} \omega_{ex}(l) = & \gamma_{wl} + \gamma_{lg} + l(\rho_l - \rho_g)\delta\mu + A(T) \exp(-l/\xi) + B(T) \exp(-2l/\xi) \\ & + A_{wall}(T) \exp(-l/\lambda) + \mathcal{O}[\exp(-3l/\xi), \exp(-2l/\lambda)]. \end{aligned} \quad (3.6.5)$$

In this situation there are now three competing length scales, λ , ξ and $\xi/2$. This can affect the type of wetting transition and can give rise to non-universal exponents for critical

wetting [14, 15, 11]. The competing length scales can also influence how the wetting film thickens as liquid-gas coexistence is approached. For example if $\lambda > \xi$, then the adsorbed film thickness diverges as $l \sim -\lambda \ln \delta\mu$, rather than with the prefactor to the logarithm equal to ξ , which is the case in Eq. (3.6.3) [11]. If the wall potential decays faster than an exponential, then when the adsorbed film thickness is sufficiently large, the exponential terms in Eq. (3.6.2) will dominate any wall terms in $\omega_{ex}(l)$. However, if the wall potential decays slower than exponential, the wall term will always dominate the terms in Eq. (3.6.2) which are powers of $\exp(-l/\xi)$, and will determine the equilibrium adsorbed film thickness, when l is large.

We should also mention the situation pertaining when the fluid particles interact via pair potentials which decay algebraically such as the Lennard-Jones potential, which decays $\sim r^{-6}$ as $r \rightarrow \infty$. In this case the surface excess grand potential, Eq. (3.6.5), should be replaced by

$$\omega_{ex}(l) = \gamma_{wl} + \gamma_{lg} + l(\rho_l - \rho_g)\delta\mu + A(T)l^{-\sigma} + B(T)l^{-\kappa} + \dots \quad (3.6.6)$$

where the indices σ and κ are determined by the power with which the fluid pair potentials decay, and we have ordered $\sigma < \kappa < \dots$. As one might expect, if the wall potential also decays algebraically, this can also add extra power law terms to Eq. (3.6.6) [11]. In the situation where the excess grand potential is given by Eq. (3.6.6), then in the regime where the liquid completely wets the wall, i.e. $l \rightarrow \infty$ when $\delta\mu \rightarrow 0$, then the equilibrium adsorbed film thickness diverges $l_{eq} \sim \delta\mu^{-1/(\sigma+1)}$ as $\delta\mu \rightarrow 0$ (c.f. Eq. (3.6.3)). Thus the equilibrium film thickness divergence is a power law

$$l_{eq} \sim \delta\mu^{-\beta_s^{co}}, \quad (3.6.7)$$

on approaching coexistence, where the critical exponent $\beta_s^{co} = (\sigma+1)^{-1}$, depends explicitly on σ , the power of the leading term in l^{-1} in the surface excess grand potential (3.6.6). For non-retarded van der Waals (dispersion) forces $\sigma = 2$ [11].

The surface excess grand potential, which can be either of the form (3.6.5) or (3.6.6), is in general of the form [16]:

$$\omega_{ex}(l) = \gamma_{wl} + \gamma_{lg} + \gamma_s(l, \delta\mu), \quad (3.6.8)$$

where γ_s is the extra contribution, which at coexistence, $\delta\mu \rightarrow 0$, and when there is complete wetting, must vanish: $\gamma_s \rightarrow 0$. γ_s has a ‘singular’ (non-analytic) contribution,

γ_{sing} , for $\delta\mu \rightarrow 0$, approaching liquid-gas coexistence. For example, when there are short ranged forces, then $l \sim -\ln \delta\mu$. Substituting this result back into Eq. (3.6.5), we find that $\gamma_{sing} \sim \delta\mu \ln \delta\mu$. For long-ranged forces we find that γ_{sing} has a power law dependence on $\delta\mu$. If one goes beyond the present mean-field approach, incorporating the effects fluctuations in the wetting film interface, then in general

$$\gamma_{sing} \sim \delta\mu^{2-\alpha_s^{co}}, \quad (3.6.9)$$

where the value of the surface heat capacity exponent, α_s^{co} , depends on the form of the wall-fluid and fluid-fluid pair potentials, even within a mean-field calculation [11].

3.7 Incorporating fluctuations

In this section we shall describe how one begins to incorporate the effects of fluctuations in a description of wetting phenomena. So far in this introduction to wetting all the results presented have been mean-field in nature, i.e. we have calculated the equilibrium position, l_{eq} , of the interface between the wetting film and the bulk fluid, but we have not considered the effects of fluctuations of the interface. We can expect the location of the interface to wander around l_{eq} due to thermal fluctuations – these are *capillary waves*. In order to go beyond mean-field we can consider small fluctuations in the location l of the interface between the wetting film and the bulk fluid. If we think of the interface between the wetting film and the bulk fluid as a fluctuating membrane, then the work required to produce a distortion in the height of the membrane, $l(\mathbf{R})$, at position \mathbf{R} in the membrane (\mathbf{R} is a two dimensional position vector in the plane of the interface) will be equal to the change in surface area of the membrane times the interfacial surface tension, γ_{lg} . This will contribute a term

$$\Delta F_1 = \gamma_{lg} \int d\mathbf{R} [\sqrt{1 + (\nabla_{\mathbf{R}} l(\mathbf{R}))^2} - 1], \quad (3.7.1)$$

to the free energy. In addition to this term, since we are considering a state off-coexistence, there will be a term due to the fact that the interface is bound to the wall. For small fluctuations we can incorporate this if we Taylor expand the surface excess grand potential, which in general is of the form (3.6.8), around its minimum value $\omega_{ex}(l_{eq})$. One obtains [10]:

$$\omega_{ex}(l) \simeq \omega_{ex}(l_{eq}) + \frac{1}{2} \gamma_{lg} \xi_{\parallel}^{-2} (l - l_{eq})^2 \quad (3.7.2)$$

where

$$\gamma_{lg} \xi_{\parallel}^{-2} = \left(\frac{\partial^2 \omega_{ex}(l)}{\partial l^2} \right)_{l=l_{eq}}. \quad (3.7.3)$$

The full interfacial free energy functional (or effective interfacial Hamiltonian) is thus

$$\Delta F = \frac{1}{2} \gamma_{lg} \int d\mathbf{R} [(\nabla_{\mathbf{R}} l)^2 + \xi_{\parallel}^{-2} (l - l_{eq})^2], \quad (3.7.4)$$

where we have linearised the square root in the contribution from Eq. (3.7.1) and we have ignored the constant $\omega_{ex}(l_{eq})$. We consider the correlation function,

$$C(\mathbf{R}) \equiv \langle (l(\mathbf{R}) - l_{eq})(l(0) - l_{eq}) \rangle, \quad (3.7.5)$$

which is the correlation function for fluctuations in the interface between the wetting film and the bulk fluid. Since Eq. (3.7.4) has a similar form to Eq. (3.1.3) (the difference between the two being the dimensionality of the order parameter) which was found to generate a correlation function with the (classical) Ornstein-Zernike form (see Eqs. (3.1.4) – (3.1.7)), it is not surprising that the Fourier transform of $C(\mathbf{R})$ is

$$\hat{C}(Q) \sim \frac{1}{\xi_{\parallel}^{-2} + Q^2}, \quad (3.7.6)$$

and thus

$$C(\mathbf{R}) \sim \int d\mathbf{R} \frac{\exp(i\mathbf{Q}\cdot\mathbf{R})}{\xi_{\parallel}^{-2} + Q^2}. \quad (3.7.7)$$

We can therefore identify ξ_{\parallel} as the correlation length for fluctuations in the plane of the interface (one can also define ξ_{\perp} , the interfacial thermal roughness). From Eq. (3.7.3) we can see that as bulk coexistence is approached, $\delta\mu \rightarrow 0$, then $l_{eq} \rightarrow \infty$ and therefore $\xi_{\parallel} \rightarrow \infty$ [10, 11]. The divergence of ξ_{\parallel} as $\delta\mu \rightarrow 0$ is a power-law:

$$\xi_{\parallel} \sim \delta\mu^{-\nu_{\parallel}^{co}}, \quad (3.7.8)$$

where the critical exponent ν_{\parallel}^{co} is dependent on the form with which the wall-fluid and fluid-fluid pair potentials decay [10, 11]. If we want to go beyond the Gaussian approximation for the interfacial Hamiltonian, Eq. (3.7.4), we must consider the Hamiltonian (see Ref. [16] and references therein):

$$H[l(\mathbf{R})] = \int d\mathbf{R} \left[\frac{\Sigma}{2} (\nabla_{\mathbf{R}} l(\mathbf{R}))^2 + W(l(\mathbf{R})) \right], \quad (3.7.9)$$

where Σ is the interfacial stiffness. To a first approximation $\Sigma \simeq \gamma_{lg}$, but in general Σ is dependent on l . The binding potential $W(l) \equiv \omega_{ex}(l) - \gamma_{wl} - \gamma_{lg}$ (see Eq. (3.6.8)). One

finds generally that in a renormalization group treatment of fluctuation effects in (3.7.9) that the critical exponents β_s^{co} , α_s^{co} and ν_{\parallel}^{co} can be altered from their mean-field values. However, for complete wetting in 3 dimensions one finds that the critical exponent values are unchanged by fluctuations but the critical amplitudes depend upon the value of the dimensionless parameter

$$\omega = \frac{k_B T}{4\pi\Sigma\xi^2}, \quad (3.7.10)$$

which controls the strength of interfacial fluctuations [11, 16].

The exponents β_s^{co} , α_s^{co} and ν_{\parallel}^{co} which characterize the approach to complete wetting can be related to one another using the Gibbs adsorption equation (3.3.5), plus other surface sum rules and scaling relations. This is analogous to methods used to derive the relations between the exponents characterizing bulk critical phenomena [11, 16]. From the Gibbs adsorption equation

$$1 - \alpha_s^{co} = -\beta_s^{co}, \quad (3.7.11)$$

while from a susceptibility sum rule [17, 16]

$$2\nu_{\parallel}^{co} = \alpha_s^{co}. \quad (3.7.12)$$

There is also a surface hyperscaling relation

$$2 - \alpha_s^{co} = (d - 1)\nu_{\parallel}^{co}, \quad (3.7.13)$$

where d is the dimensionality of the system. Within a mean-field treatment, for short ranged forces, the critical exponents are:

$$\alpha_s^{co} = 1, \quad \beta_s^{co} = 0 \text{ (ln)}, \quad \nu_{\parallel}^{co} = \frac{1}{2} \quad (3.7.14)$$

in $d = 3$. There is also a set of (different) exponents characterizing the wetting transition point, however these are beyond the scope of the present basic introduction to wetting, and we refer the reader to the literature – see Refs. [11, 16, 18], and references therein.

Chapter 4

The One Component Gaussian Core Model

The Gaussian core model (GCM) is a simple model for polymers in a good solvent. The effective pair potential between the centers of mass of the polymers is modeled by a repulsive Gaussian potential. In this chapter we provide a brief introduction to some of the existing results for the structure and thermodynamics of this model fluid. Since the GCM pair potential is purely repulsive, the one-component fluid does not exhibit liquid-gas phase separation, however the GCM does freeze and we present a simple theory for the phase diagram of the one-component GCM.

4.1 Introduction: effective interactions

The GCM consists of a set of classical particles each interacting with a repulsive pairwise potential given by:

$$v(r) = \epsilon \exp(-r^2/R^2), \quad (4.1.1)$$

where $\epsilon > 0$ and R is a length scale determining the size of the particles. In the next section we will describe briefly some simulation results which form the basis for viewing the GCM as a simple model for polymers dissolved in an athermal solvent, with Eq. (4.1.1) representing the effective interaction between the centers of mass of the individual polymer chains. This ‘colloid’ approach to polymers [19, 20, 21] represents a significant simplification in the description of a polymer solution. Formally one would calculate the effective potential between the polymers by integrating over the internal (monomeric)

degrees of freedom in the partition function, so that the partition function is in the form of a trace over the Boltzmann factor of an effective Hamiltonian which is only a function of the center of mass coordinates. In doing this, the effective Hamiltonian no longer contains just pairwise terms, even when the underlying monomer-monomer interactions are pairwise. In general the effective Hamiltonian is made up of a sum of terms, the first of which does not depend on the polymer coordinates; the second is a one body quantity which is a function of a single polymer coordinate; the third is a pairwise term, involving pairs of the polymer center of mass coordinates; the fourth is a three-body term and so on, with each successive term depending on increasing numbers of particle coordinates [22, 23, 24]. This sum is often truncated at the pair terms in order to render the system tractable. Although the GCM is not derived in such a manner, the Gaussian potential is an approximation at the pairwise level for the effective interaction between the centers of mass of the polymers in solution¹.

4.2 A simple model for polymers in solution

When a polymer is in solution, each polymer chain is free to move around. If the solvent is a poor solvent, i.e. when the attraction between the monomers, which make up the polymer chain, is stronger than the attraction between the solvent molecules and the monomers, then each polymer chain tends to collapse and to form a dense bundle, as it minimizes the contact with the solvent. However in a good solvent, the polymer chain opens up, to maximize the contact with the solvent molecules [22, 25]. In fact there is an effective repulsion between the monomers of the polymer, and the chain statistics can be well modeled by a self avoiding random walk. In a good solvent, each polymer chain can, on a coarse grained length scale and on time scales greater than that associated with the fluctuations of the polymer coils, be modeled as a ‘blob’, characterized by a mean position (the center of mass of the polymer) and by a typical size, the radius of gyration – see Fig. 4.1. This is the view of polymer solutions that we shall take in this thesis.

A Gaussian effective potential for polymers was first proposed by Flory and Krigbaum [26], and most recently, it is this aspect of the model that has generated the most interest.

¹One is not restricted to using the center of mass coordinates for the position of the polymer. One could, for example, use the coordinates of the central monomer in the polymer chains. In fact this approach is more fruitful for star-polymers – this is the approach we take in chapter 8.

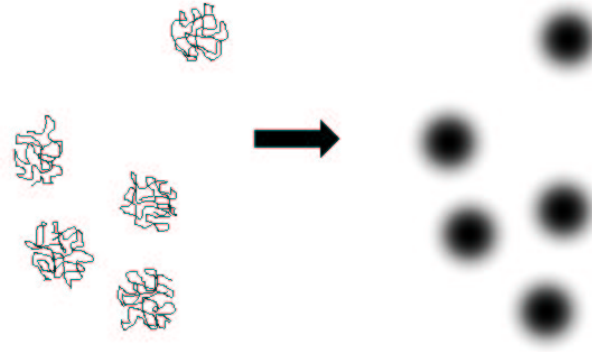


Figure 4.1: The ‘colloid’ approach to polymers in solution, where the interaction between the polymer chains is modeled by an effective pair potential between the centers of mass.

In order to determine the effective potential between a pair of polymer chains, the early (Monte-Carlo) simulation studies centered on the dilute regime, focusing on the effective potential between an isolated pair of polymer chains. These studies include both lattice simulations [27] and more realistic models such as the ‘pearl necklace model’ (hard spheres connected by hard, freely rotating rods) [28, 29]. For a complete description of the different simulation models used see Ref. [22] and references therein. In the study of Dautenhahn and Hall [30] the authors use a square well potential to model the interaction between the individual monomers. They find that the depth of the attractive well can be changed to mimic the effect of the solvent quality: a more attractive well corresponding to a poor quality solvent. The picture that emerges from these studies is that in an athermal solvent, the effective potential between a pair of polymers is well represented by the Gaussian form, Eq. (4.1.1) with $\epsilon \simeq 2k_B T$ (k_B is Boltzmann’s constant and T is the temperature) and R roughly equal to the radius of gyration of the polymer². However, a more significant result to emerge from the most recent simulation study, of not just two, but several chains, is that the Gaussian effective pair potential, Eq. (4.1.1), continues to be a reasonable approximation even when the polymer concentration is such that the polymers are overlapping [19, 20, 21, 34].

²A Gaussian effective pair potential also provides a good approximation for the interactions between dendrimers in solution. However, for these more compact molecules, $\epsilon \simeq 8 - 10k_B T$ [31, 32, 33].

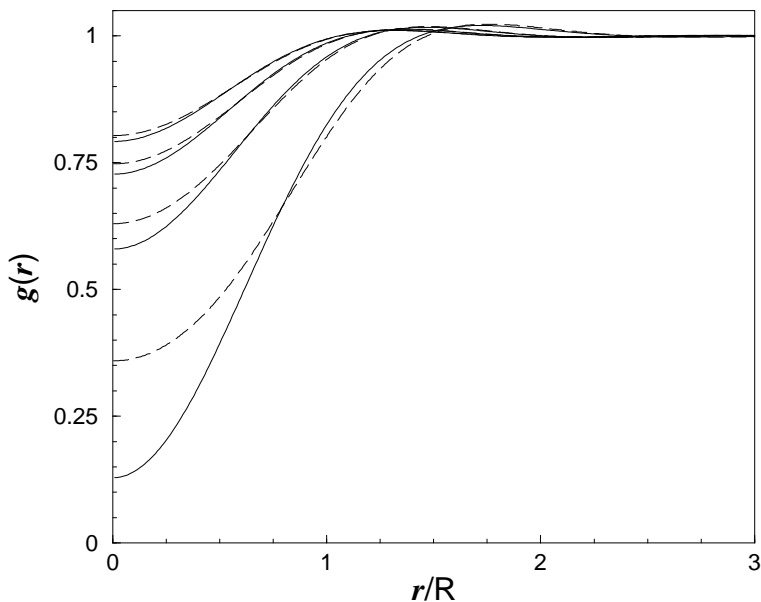


Figure 4.2: The radial distribution function, $g(r)$, for the GCM with $\epsilon^* = 2$ calculated using the quasi-exact (when compared with simulations) HNC closure to the OZ equation (dashed line) and with the RPA closure (solid line). These are calculated for fluid densities $\rho R^3 = 0.5, 2, 4$ and 6 (from bottom to top). Note that the RPA closure provides an increasingly accurate approximation for $g(r)$ as the density is increased. $g(r)$ displays a deep correlation hole, for $r \rightarrow 0$, at the lower densities, but as $\rho R^3 \rightarrow \infty$, then $g(r) \rightarrow 1$ for all values of r .

4.3 Properties of the one-component GCM fluid

An excellent review of the properties of the GCM can be found in Ref. [22] but for completeness we shall mention some of the properties here. The GCM was introduced in the mid-seventies by Stillinger [35], and was of interest because the GCM can yield a negative thermal expansion coefficient in the liquid phase [36]. The phase behaviour of the GCM is rather well established [22, 36, 37]; in the temperature-density (T, ρ) plane there is a region below $k_B T / \epsilon \simeq 0.01$ where increasing ρ leads to freezing into a fcc phase, followed by a fcc-bcc transition and then melting so that the fluid is stable at high densities. For $\epsilon^* \equiv \beta \epsilon < 100$, where $\beta = (k_B T)^{-1}$, the fluid is stable at *all* densities. Recently Lang *et al.* [37, 38] and Louis *et al.* [39] have studied the fluid region of the phase diagram using Monte Carlo simulations and integral equation theories. What emerges is that for high densities the hypernetted-chain (HNC) approximation provides an excellent account

of the Monte Carlo results for the radial distribution function $g(r)$, structure factor $S(q)$ and the equation of state and therefore the HNC approximation is viewed as being quasi-exact for the GCM. In the limit $\rho R^3 \rightarrow \infty$ it is argued that the HNC closure should become exact [37, 38]. Particularly striking is the observation that a very simple closure, the random phase approximation (RPA) which sets the pair direct correlation function $c^{(2)}(r) = -\beta v(r)$, becomes very accurate for very high densities: $\rho R^3 \gtrsim 5$ [37, 38, 39]³. This implies that the GCM behaves as a ‘mean-field fluid’ over a very wide density and temperature range. In Fig. 4.2 we plot the results for $g(r)$ from the HNC and RPA closures to the OZ equation. One can see that as the density increases the correlation hole at small values of r is reduced and $g(r) \rightarrow 1$, for all separations of the particles. Such behaviour is very different from that of fluids with hard-cores, where short-ranged (packing induced) correlations always persist [1]. For this soft-core model in the limit $\rho R^3 \rightarrow \infty$, the mean inter-particle separation $\rho^{-1/3}$ becomes $\ll R$ and a central particle interacts with a very large number of neighbours – a classic mean-field situation. However, for low temperatures and densities, this picture does not hold, the particle interactions become increasingly hard-sphere like as the temperature $T \rightarrow 0$ and the correlation functions for the GCM are well approximated by those of a hard-sphere fluid [22, 36]. The reason for this behaviour is as follows: In the partition function the pair potential appears as a Boltzmann factor. The Boltzmann factor of the GCM pair potential is

$$B(r, \beta) = \exp[-\beta\epsilon \exp(-r^2/R^2)]. \quad (4.3.1)$$

B is a monotonic function of the interparticle distance r . The separation r^* at which $B = \frac{1}{2}$ is

$$r^*(\beta) = R \sqrt{\ln \left(\frac{\beta\epsilon}{\ln 2} \right)}, \quad (4.3.2)$$

and the gradient of the Boltzmann factor at this point is:

$$\left(\frac{dB}{dr} \right)_{r=r^*} = \frac{\ln 2}{R^2} r^*(\beta), \quad (4.3.3)$$

so as $\beta \rightarrow \infty$, both r^* and $(dB/dr)_{r=r^*}$ diverge; i.e. the Gaussian particles behave more and more like hard-spheres as the temperature is decreased, with an effective hard-sphere radius equal to r^* [22, 36]. This argument, of course, only applies in the regime where the

³By making comparison with simulations C.N. Likos *et al.* [38] have established the validity of the RPA at high densities for bounded, positive definite pair potentials in general.

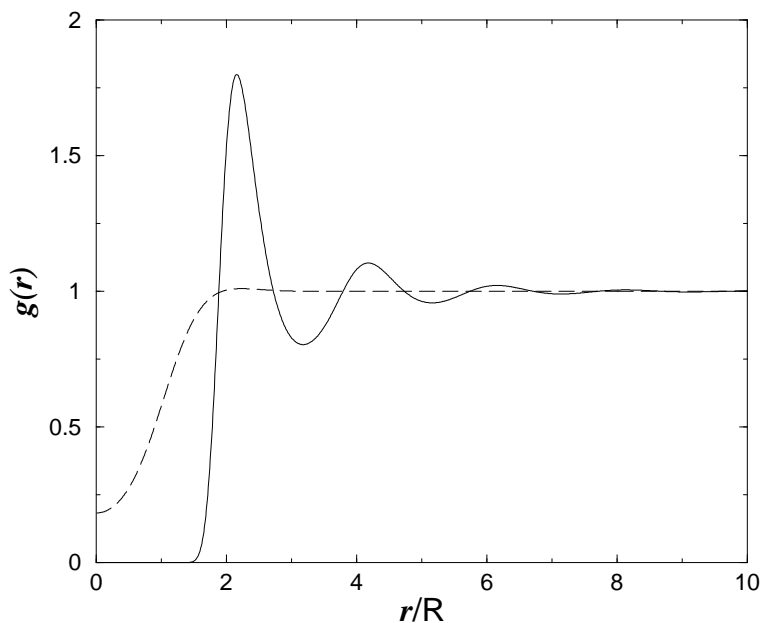


Figure 4.3: The radial distribution function, $g(r)$, calculated using the HNC closure to the OZ equation for a GCM fluid with density $\rho R^3 = 0.1$ at a temperature $k_B T/\epsilon = 0.01$ (solid line) and at $k_B T/\epsilon = 0.5$ (dashed line). Note that $g(r)$ at low temperatures resembles that of a hard-sphere fluid, whereas at higher temperatures $g(r)$ is completely different and is much less structured.

GCM fluid density is less than that at which hard-spheres of radius r^* close pack. In Fig. 4.3 we display the radial distribution function, $g(r)$, calculated using the HNC closure to the OZ equation for a GCM fluid with density $\rho R^3 = 0.1$ at a temperature $k_B T/\epsilon = 0.01$ (solid line) and at $k_B T/\epsilon = 0.5$ (dashed line). In the low temperature and density regime $g(r)$ is much more structured; the fluid is near to freezing and $g(r)$ is similar to that for a hard-sphere fluid. However at higher densities and/or temperatures, the particle cores overlap and $g(r)$ is much less structured. It is in this overlap regime that the RPA is a good approximation to make for the fluid correlation functions.

Since the RPA is accurate over such a large range of bulk densities it is tempting to argue [22, 37, 39] that the simple mean-field Helmholtz free energy functional, Eq. (2.3.25), should yield a realistic description of the *inhomogeneous* GCM fluid, provided the one-body density $\rho(\mathbf{r})$ does not acquire very small values. The density functional (2.3.25) *generates* the RPA: $c^{(2)}(r) = -\beta v(r)$. Physically one is arguing that the excess (over the ideal gas \mathcal{F}_{id}) free energy of the fluid can be approximated by the internal energy with the pairwise

distribution function $\rho^{(2)}(\mathbf{r}_1, \mathbf{r}_2)$ replaced by its uncorrelated limit $\rho(\mathbf{r}_1)\rho(\mathbf{r}_2)$. Louis *et al.* used the functional (2.3.25) to investigate the density profiles of GCM particles adsorbed at a hard wall. Their results agree closely with results from Monte Carlo simulations and with the results from the HNC DFT [39, 7] for the GCM with $\epsilon^* = 2$, both for a hard planar wall (i.e. the wall potential $V_{ext}(z) = \infty$ for $z < 0$ and $V_{ext}(z) = 0$ for $z > 0$) and also for an external potential of the form $\beta V_{ext} = \exp(-z)/z$, at three bulk densities $\rho R^3 = 1, 0.5, 0.1$, confirming that the GCM does behave as a ‘mean-field fluid’ – at least for this type of inhomogeneity [39].

4.4 Solid phases of the GCM

By performing lattice sums to determine the free energy for candidate solid phases of the GCM, and by molecular dynamics simulations, Stillinger and co-workers were able to determine the form of the GCM phase diagram [35, 36, 40, 41, 42, 43]. They found that there are two equilibrium solid phases: fcc at lower densities and bcc at higher densities. They also established a novel feature of the GCM: that the solid undergoes re-entrant melting, i.e. if one fixes the temperature, for example choose $k_B T/\epsilon = 0.004$, then as one increases the density, the fluid first freezes, but then as the density is further increased the crystal melts again and there are no further freezing transitions. This scenario is particular to some soft core systems, where the equilibrium phase at high densities is a liquid, rather than a solid. Note also that a solid with multiple occupancies on each lattice site is not the equilibrium phase for the GCM.

More recently Lang *et al.* [37] used a different method for calculating the GCM phase diagram. They adopted an Einstein-model approach [44], based on the Gibbs-Bogoliubov inequality, which relates the Helmholtz free energy F of a system with Hamiltonian \mathcal{H} , to that of a reference system, F_0 , with Hamiltonian \mathcal{H}_0 :

$$F \leq F_0 + \langle \mathcal{H} - \mathcal{H}_0 \rangle_0. \quad (4.4.1)$$

For the reference system, Lang *et al.* [37] used the Einstein model of a solid, which has the following Hamiltonian:

$$\mathcal{H}_0 = \sum_{i=1}^N \left[\frac{\mathbf{p}_i^2}{2m} + \alpha(\mathbf{r}_i - \mathbf{R}_i)^2 \right], \quad (4.4.2)$$

where i labels the particles, each of which has mass m , position \mathbf{r}_i and momentum \mathbf{p}_i . Each particle is bound by a harmonic potential to a lattice site at \mathbf{R}_i . The ‘spring constant’

α for the harmonic potential is treated as a variational parameter. The Helmholtz free energy for the Einstein solid is simply (see Appendix A)

$$F_0 = 3Nk_B T \ln \left(\frac{\phi \Lambda}{\sqrt{\pi} R} \right) \quad (4.4.3)$$

where the dimensionless parameter

$$\phi = \sqrt{\beta \alpha R^2} \quad (4.4.4)$$

and F_0 is, of course, independent of the length scale R . Within the Einstein model the one body density is simply a sum of Gaussian profiles, each centered on the lattice sites:

$$\rho_E(\mathbf{r}) = \sum_i \frac{\phi^3}{\pi^{3/2} R^3} e^{-\phi^2 |\mathbf{r} - \mathbf{R}_i|^2 / R^2}, \quad (4.4.5)$$

and the two-body density is a sum of products of Gaussians:

$$\rho_E^{(2)}(\mathbf{r}, \mathbf{r}') = \sum_{i \neq j} \frac{\phi^6}{\pi^3 R^6} e^{-\phi^2 |\mathbf{r} - \mathbf{R}_i|^2 / R^2} e^{-\phi^2 |\mathbf{r}' - \mathbf{R}_j|^2 / R^2}. \quad (4.4.6)$$

From the Gibbs-Bogoliubov inequality (4.4.1) one obtains the following upper bound for the Helmholtz free energy [1, 44]

$$F \leq F_0 + \frac{1}{2} \int d\mathbf{r} \int d\mathbf{r}' \rho_E^{(2)}(\mathbf{r}, \mathbf{r}') v(|\mathbf{r} - \mathbf{r}'|) - \frac{3}{2} N k_B T. \quad (4.4.7)$$

The final term is obtained simply by applying the equipartition theorem for the three potential energy (configurational) degrees of freedom in reference Hamiltonian (4.4.2). On substituting Eq. (4.4.6) into (4.4.7), one can perform the simple integrals, since the GCM pair potential $v(r)$ in Eq. (4.4.7) is a Gaussian, and one obtains:

$$F \leq \tilde{F} \equiv F_0 + \frac{N \epsilon \phi^3}{2(\phi^2 + 2)^{3/2}} \sum_{\nu} m_{\nu} \exp \left(-\frac{a_{\nu}^2}{R^2(1 + 2/\phi^2)} \right) - \frac{3}{2} N k_B T, \quad (4.4.8)$$

where the index ν denotes a sum over lattice vectors $\mathbf{a}_{\nu} = \mathbf{R}_i - \mathbf{R}_j$, with magnitude $|\mathbf{a}_{\nu}| = a_{\nu}$. m_{ν} is an integer denoting the number of lattice vectors of length a_{ν} belonging to a shell. The only parameter in Eq. (4.4.8) is the width parameter ϕ of the Gaussian density peaks, which is treated as a variational parameter, to be determined from the minimization condition $\partial \tilde{F} / \partial \phi = 0$, and one assumes that $F = \min \tilde{F}$. One can therefore calculate the Helmholtz free energy for any trial crystal structure; one simply inputs the sets of m_{ν} and $a_{\nu}(\rho)$ for the particular lattice structure into Eq. (4.4.8) and then minimizes with respect to ϕ . Lang *et al.* [37] calculated the free energy for various crystal structures

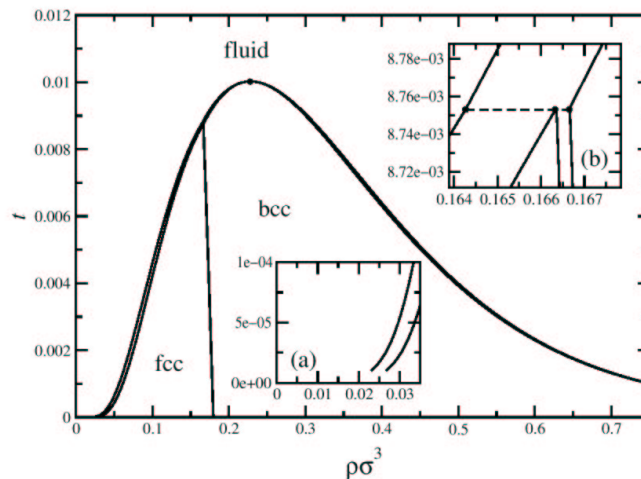


Figure 4.4: The phase diagram for the one component GCM calculated by Lang *et al.* [37] (taken with kind permission), plotted in the reduced temperature $t = k_B T / \epsilon$ versus density ρ plane (note: $\sigma \equiv R$). The two insets (a) and (b) show details of the phase diagram. The low density equilibrium solid phase is the fcc crystal, and at higher densities it is the bcc crystal. On increasing the temperature or the density, the fluid is the equilibrium phase.

and found, as one would expect based on the results of Stillinger and co-workers [35], that the only equilibrium crystal phases for the GCM were those with the fcc and bcc lattices.

In order to calculate the fluid free energy Lang *et al.* [37] used the HNC virial route. In order to implement this approach one uses the HNC closure to the OZ equation to calculate the radial distribution function for the fluid, $g(r)$, along a path at constant temperature in the phase diagram, starting from the point with density $\rho = 0$ and ending at the point with density ρ in the phase diagram, where the fluid free energy is required. One then inputs the HNC $g(r)$ to the virial equation (2.1.16) to calculate the pressure of the fluid, P . By integrating the thermodynamic relation $P = -(\partial F / \partial V)_T$ along the path in the phase diagram, one can determine the fluid free energy $F_{fluid}(\rho)$. In order to calculate the coexisting densities between any two phases (either the fluid, or the bcc and fcc solid phases) the common-tangent construction was performed between the F_{fluid}/V and F_{solid}/V curves. Their resulting phase diagram is displayed in Fig. 4.4. Note that the thermodynamic state point of the fluid or solid is completely determined by the average density of the system $\langle \rho(\mathbf{r}) \rangle = \rho = N/V$ and by the reduced temperature $k_B T / \epsilon$. The low density equilibrium solid phase is the fcc crystal, and at higher densities, $\rho R^3 \gtrsim 0.17$, it is

the bcc crystal that is the equilibrium solid phase. On increasing the temperature or the density, the fluid is the equilibrium phase. The difference in density between the coexisting phases are all relatively small – see the insets to Fig. 4.4. For example the difference in density between the coexisting fcc and bcc solid phases is independent of temperature, $(\rho_{bcc} - \rho_{fcc})R^3 = 3.6 \times 10^{-4}$ [37].

4.5 DFT theory for the solid phases of the GCM

Here we present a simple alternative (DFT) method for determining an approximate phase diagram for the one component GCM. The RPA excess Helmholtz free energy functional

$$\mathcal{F}[\rho] = \mathcal{F}_{id}[\rho] + \frac{1}{2} \int d\mathbf{r} \int d\mathbf{r}' \rho(\mathbf{r}) \rho(\mathbf{r}') v(|\mathbf{r} - \mathbf{r}'|), \quad (4.5.1)$$

where the ideal gas part of the free energy functional is

$$\mathcal{F}_{id}[\rho] = k_B T \int d\mathbf{r} \rho(\mathbf{r}) [\ln(\Lambda^3 \rho(\mathbf{r})) - 1], \quad (4.5.2)$$

provides an accurate approximation for the fluid free energy when the fluid is at temperatures and densities such that the soft cores of the particles are overlapping. However, as we have seen, the RPA functional generates correlation functions which fail to describe correctly the correlations in the fluid when it is near to freezing. The approximation leading to Eq. (4.5.1) assumes that there are multiple overlaps between the particles. However, in the regime where the particles freeze the repulsion between the GCM particles is sufficient for the correlations between the particles to be better approximated by particles with hard (impenetrable) cores – see Fig. 4.3. We therefore expect Eq. (4.5.1) to provide a poor approximation to the free energy of the GCM liquid in this region of the phase diagram. However, perhaps surprisingly, we find that an RPA-like approximation provides a good approximation for the Helmholtz free energy of the solid phases.

When in the fluid state, the one-body density is a constant, $\rho(\mathbf{r}) = \rho$. However, when the system freezes into a solid, the density is periodic, i.e. the symmetry breaks and $\rho(\mathbf{r}) = \rho(\mathbf{r} - \mathbf{R}_i)$, where \mathbf{R}_i is a lattice vector for the solid phase. An approximation that is often made in DFT studies of freezing [45, 22], is to assume that the density profile of the solid is made up of Gaussian peaks, of the form in Eq. (4.4.5). This density profile assumes a normalization condition: i.e. there is one particle per lattice site. This assumption need not necessarily be true. We can expect to find vacancies in the crystal, and indeed for the

present soft core system we may find another type of defect: double occupancy, since the particle cores can overlap. However, we expect the proportion of defects to be small, and assume therefore a perfect crystal. In fact, at high densities, where there is a tendency towards double occupancy, we find that for the present soft core system there is re-entrant melting: at high densities the fluid is the stable phase rather than a multiple occupied solid.

If we assume the crystal density is of the form given by Eq. (4.4.5), with ϕ taking a value sufficiently large that the overlap between the Gaussian density peaks on neighbouring lattice sites can be assumed to be negligible, then the ideal gas part of the Helmholtz free energy, Eq. (4.5.2), is simply

$$F_{id}^{solid}(\rho, \phi) = Nk_B T \left[3 \ln \left(\frac{\Lambda \phi}{\sqrt{\pi R}} \right) - \frac{5}{2} \right], \quad (4.5.3)$$

which is independent of R . It is interesting to note that this differs from the free energy of the Einstein solid, Eq. (4.4.3), solely by a (ϕ independent) amount, $\frac{5}{2}Nk_B T$, this is discussed further in Appendix A. We approximate the mean-field Helmholtz free energy by:

$$F(\rho) = F_{id}^{solid}(\rho, \phi) + \frac{\phi^6}{2\pi^3 R^6} \sum_{i \neq j} \int d\mathbf{r} \int d\mathbf{r}' e^{-\phi^2 |\mathbf{r} - \mathbf{R}_i|^2 / R^2} e^{-\phi^2 |\mathbf{r}' - \mathbf{R}_j|^2 / R^2} v(|\mathbf{r} - \mathbf{r}'|). \quad (4.5.4)$$

Note that this result is not exactly that which would arise from inserting the profile Eq. (4.4.5) into the RPA functional Eq. (4.5.1); we have omitted from the sum over lattice sites all the terms where the index $i = j$. The result can be viewed as an RPA-like approximation derived from Eq. (2.3.24) by assuming that the two body density is of the form in Eq. (4.4.6) for all values of the charging parameter α in Eq. (2.3.24).

The integrals in Eq. (4.5.4) are exactly the same as those in Eq. (4.4.7), and so we obtain:

$$F_{solid}(\rho, \phi) = F_{id}^{solid}(\rho, \phi) + \frac{N\epsilon\phi^3}{2(\phi^2 + 2)^{3/2}} \sum_{\nu} m_{\nu} \exp \left(-\frac{a_{\nu}^2}{R^2(1 + 2/\phi^2)} \right). \quad (4.5.5)$$

This expression is almost the same as that obtained in the previous section using a theory based on the Einstein model for the free energy of the solid phases, except the expression in Eq. (4.4.8) and that in Eq. (4.5.5) differ by $Nk_B T$. This difference originates from the presence of the $1/N!$ indistinguishability factor in the partition function that formed the (liquid state theory) basis for Eqs. (4.5.1) and (4.5.2), from which Eq. (4.5.5) is derived.

By contrast, in the Einstein model the particles are fixed to the lattice sites and are therefore distinguishable – see Appendix A for a more detailed discussion of these issues. However, for our present purposes this (ϕ independent) difference has no effect, because in the present approach all solid phases have this additional term, and we use a Lindemann criterion to calculate the solid melting curves, rather than compare our solid free energy with that of the liquid, which is the situation in which this term would matter.

We approximate Eq. (4.5.5) by truncating the sum over lattice vectors to a sum over nearest neighbours and next nearest neighbours only. The only parameter in Eq. (4.5.5) is the width of the Gaussian density peaks ϕ and, as in the previous section, we treat this as a variational parameter, determined from the minimization condition $\partial F_{solid}/\partial\phi = 0$. Based on information from earlier studies [22, 36, 37] for the phase diagram of the GCM, we calculated only the free energy for the bcc and fcc crystal structures. Some typical plots of the free energy as a function of ϕ are displayed in Fig. 4.5. We find that the free energy always has a minimum at $\phi = 0$, this corresponds to the fluid state, where the particles are completely delocalized. However, for some points in the phase diagram the free energy has a second minimum at some other (non-zero) value of ϕ , and this is the value we use to calculate the free energy.

The usual procedure for determining the phase diagram, once the free energy density for all the trial phases has been calculated, is to perform the common tangent construction (which is equivalent to equating chemical potentials and pressures in the coexisting phases) in order to find the coexisting state points between the different phases. We find, as did Lang *et al.* [37], that the free energy for the fcc solid is lower than that for the bcc at low densities ($\rho R^3 \lesssim 0.16$). We could therefore perform the common tangent construction between these two free energies and determine the coexisting densities. However, due to the soft core nature of the present system, the density change at the transition is very small – see the inset to Fig. 4.4 and Ref. [37], and since we are mostly interested in providing a simple theory which accounts for the topology of the phase diagram, we simply determined the density at which the Helmholtz free energy of the bcc equals that of the fcc structure for a given temperature. The resulting line is plotted in Fig. 4.6.

In order to calculate the fluid-solid coexistence we should calculate the fluid Helmholtz free energy density and perform the common tangent construction between this and the solid phase free energy. However, the integral equation procedure used by Lang *et al.* [37] is numerically intensive, and at the low temperatures and densities at which the GCM

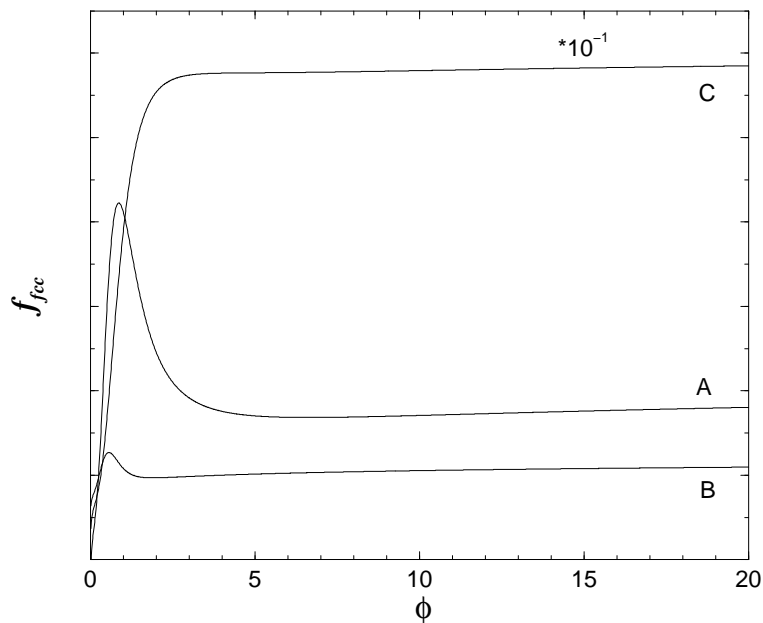


Figure 4.5: The Helmholtz free energy (in arbitrary units) for an fcc lattice as a function of ϕ , the localization parameter. Results are calculated at $\rho R^3 = 0.12$ and $k_B T/\epsilon = 0.004$ (labeled *A*), at $\rho R^3 = 0.04$ and $k_B T/\epsilon = 0.004$ (*B*) and at $\rho R^3 = 0.7$ and $k_B T/\epsilon = 0.01$ (*C*). Note that *C* is multiplied by a factor 10^{-1} . *A* has a minimum at $\phi = 6.63$, *B* a minimum at $\phi = 1.89$ and for *C* there is no minimum at all (except the trivial minimum at $\phi = 0$ which denotes a solution where the particles are completely delocalized). *A* is calculated at a state point inside the region where we expect the fcc to be the equilibrium phase, whereas *B* and *C* correspond to points where the fluid is the equilibrium phase.

freezes, we are unable to use the RPA Helmholtz free energy, since it provides a very poor estimate for the free energy of the fluid in this region of the phase diagram. It greatly over estimates the fluid free energy.

Here we will use a different method to determine the melting temperature of the solid, namely the Lindemann criterion: the crystal melts when the ratio of the root-mean-square displacement, $\sigma \equiv (\langle r^2 \rangle - \langle r \rangle^2)^{1/2}$, of the particle about its equilibrium position is roughly 10% of the nearest neighbour distance, a_1 . This is simple to implement for the Gaussian profile, Eq. (4.5.5) which gives $\sigma = \sqrt{\frac{3}{2}} \left(\frac{R}{\phi}\right)$. For the fcc crystal $a_1^{fcc} = 2^{1/6} \rho^{-1/3}$, and we choose the (somewhat arbitrary)⁴ Lindemann criterion for when the fcc melts to be

⁴In Ref. [43], Stillinger and Weber used molecular dynamics simulations to determine the temperature when the GCM fluid with density $\rho R^3 = 0.2$ melts. Their Lindemann ratio was $\sigma/a_1 = 0.16$. This value

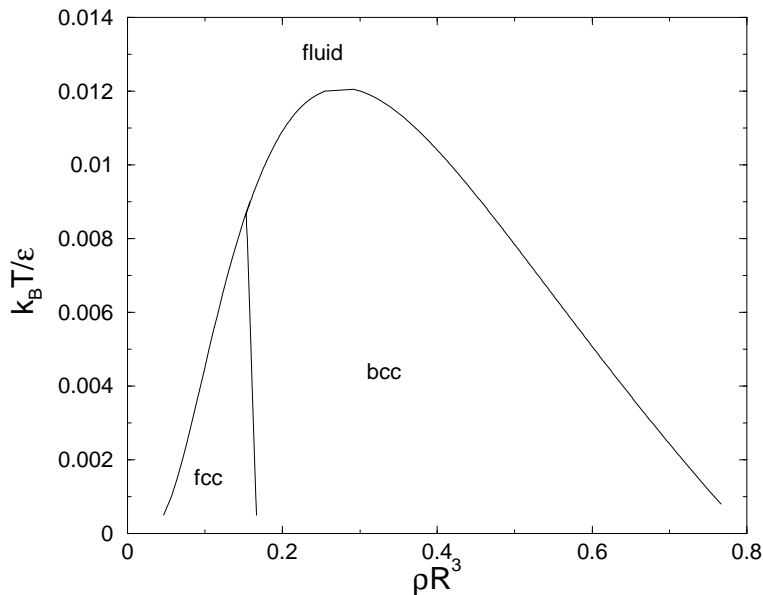


Figure 4.6: The phase diagram of the one component GCM. Rather than calculate the phase boundaries by performing the common tangent construction between the free energy densities of the competing solid phases, the fcc-bcc transition line is given by the locus of points where the Helmholtz free energies of the two phases are equal. The melting boundaries are determined using the Lindemann criterion – see the text.

$\phi a_1^{fcc}/R = 12.2$ (i.e. when $\sigma/a_1^{fcc} = 0.100$). Similarly for bcc $a_1^{bcc} = 2^{-2/3}\sqrt{3}\rho^{-1/3}$ and we choose the Lindemann criterion for when the bcc melts to be $\phi a_1^{bcc}/R = 11.8$ (i.e. when $\sigma/a_1^{bcc} = 0.104$). This second (slightly different) value for the bcc Lindemann criterion is chosen so that the melting lines for the bcc and fcc phases form a continuous boundary line between the fluid and solid phases. The plot of the resulting phase diagram is displayed in Fig. 4.6. Remarkably, all the transitions in Fig. 4.6 are located within 20% of the locations found in the more sophisticated approach of Lang *et al.* [37] – see Fig. 4.4. The main difference between Fig. 4.6, and the more accurate phase diagram in Fig. 4.4 is in the location of the bcc-solid melting transition line. This is because as the GCM density increases our approximation of truncating the sum over lattice vectors after nearest and next nearest neighbour contributions only in Eq. (4.5.5), becomes increasingly inaccurate.

is larger than the criterion we use here. Within the present theory there is not always a minimum of Eq. (4.5.5) for $\sigma/a_1 = 0.16$. It is well known that DFT theories for solids often under-estimate the value of the Lindemann ratio [46].

This can be seen particularly in the tail of the fluid-bcc boundary for densities $\rho R^3 > 0.6$. In order to improve the theory one should include further terms in the sum in Eq. (4.5.5). However, our main purpose in truncating the sum was to construct a simple theory and also to demonstrate that it is the nearest and next nearest neighbour contributions in Eq. (4.5.5) which dominate this expression for the Helmholtz free energy of the solid phases of the GCM. Another criterion that we used for determining the melting curves was to calculate the locus of points where there is no longer a solution $\phi \neq 0$ to the equation $\partial F_{solid}/\partial \phi = 0$, still using Eq. (4.5.5) to determine F_{solid} . This results in a phase diagram with the same topology as Fig. 4.6, but is, of course, a much less accurate method than that based on the Lindemann criterion.

Having given a brief overview of some of the properties of a one component fluid of GCM particles, in the next chapter we shall describe some of the properties of a binary fluid of GCM particles, the main topic of this thesis.

Chapter 5

The Binary Gaussian Core Model: Fluid-Fluid Phase Separation and Interfacial Properties

Using a mean-field equation of state we calculate the density-concentration phase diagrams for a binary mixture of repulsive Gaussian core particles over a range of size ratios. A simple RPA mean-field DFT approach is used to calculate the surface tension and density profiles of the interface between the demixed fluid phases of the binary mixture. For certain coexisting states oscillations are found in the density profiles on both sides of the interface, i.e. approaching both bulk phases. The form of the oscillations is determined by the asymptotic decay of the bulk total pairwise correlations and the onset of oscillations in the interfacial density profiles is linked to the location of the crossover line (Fisher-Widom line) in the bulk phase diagram where the asymptotic decay changes from monotonic to damped oscillatory. For certain particle size ratios we find a new crossover line which separates a region of the phase diagram where the longest range decay of the pairwise correlations is damped oscillatory from a region where the longest range decay is damped oscillatory but with a different wavelength. We argue that many of the predictions of the simple DFT approach should remain valid in more refined treatments.

Given the success of the simple mean-field RPA Helmholtz free energy functional (2.3.25) in describing the pure fluid it is natural to ask what the corresponding theory yields for a binary mixture of repulsive Gaussian core particles. This question was addressed partially in Refs. [39, 47] and the authors showed that for certain choices of the

energy and range parameters fluid-fluid demixing is predicted by the mean-field (RPA) approach. Although it is not clear that this phase separation mimics that which is found in polymer blends [39], the observation that a system with purely repulsive inter-particle potentials can separate into two fluid phases is of intrinsic interest. Recall that the pure GCM exhibits only a single fluid phase.

5.1 Demixing in binary fluids

Before considering demixing in binary fluids, we shall remind the reader about phase separation in one-component fluids. A simple one-component fluid can separate into two coexisting phases, a liquid and a gas. For these two phases to coexist the chemical potential μ and the pressure P must be equal in the two phases – i.e. the two phases must be in chemical and mechanical equilibrium. In any theory for a fluid, phase separation manifests itself as a convex portion in the Helmholtz free energy curve, i.e. the free energy per particle $f = F/N$, as a function of the volume per particle $v = V/N$ has a convex portion. If $f(v)$ is convex, then the fluid with density $\rho = 1/v$, will be unstable to density fluctuations, since in this region the isothermal compressibility χ_T , given by Eq. (2.1.14), will be negative. The boundary to this unstable region is the spinodal and is defined as the locus of points where $\chi_T^{-1} = 0$, i.e. where

$$\frac{\partial^2 f}{\partial v^2} = 0. \quad (5.1.1)$$

One finds that the two points on the curve $f(v)$, corresponding to the coexisting liquid and gas, are outside the unstable region, one either side. These points are determined as follows: The pressure in the fluid is given by

$$P(v) = - \left(\frac{\partial F}{\partial V} \right)_N = - \left(\frac{\partial f}{\partial v} \right) \quad (5.1.2)$$

and the chemical potential

$$\mu(v) = \left(\frac{\partial F}{\partial N} \right)_V = f(v) - v \left(\frac{\partial f}{\partial v} \right). \quad (5.1.3)$$

If the densities of the coexisting liquid and gas phases are v_l^{-1} and v_g^{-1} respectively, then from the conditions of mechanical equilibrium $P(v_l) = P(v_g)$ and of chemical equilibrium $\mu(v_l) = \mu(v_g)$ one obtains:

$$\left. \frac{\partial f}{\partial v} \right|_{v_l} = \left. \frac{\partial f}{\partial v} \right|_{v_g} = \frac{f(v_l) - f(v_g)}{v_l - v_g}, \quad (5.1.4)$$

which geometrically corresponds to the common tangent construction on the curve $f(v)$. The locus of points in the phase diagram defined by (5.1.4) is known as the binodal. The binodal meets the spinodal at a single point (temperature), the bulk critical point. This is the only point in the fluid phase diagram where there is an equilibrium phase with the compressibility $\chi_T = \infty$.

Extending the above ideas to a binary fluid is now straight-forward. A fluid composed of two different species of particles (labeled 1 and 2) can separate into two demixed phases, A and B , one rich in species 1 and the other poor in species 1. For phases A and B to be in equilibrium, the chemical potentials μ_i and the pressure P of the two phases must be equal, i.e. $\mu_{i,A} = \mu_{i,B}$ for $i = 1, 2$ and $P_A = P_B$. The variables we work with are the total density ρ and a composition variable x , such that the bulk densities of the two species are $\rho_1^b = (1 - x)\rho$ and $\rho_2^b = x\rho$. In terms of $v = 1/\rho$, the volume per particle, the chemical potentials and pressure are:

$$\mu_1 = f - v \left(\frac{\partial f}{\partial v} \right)_x - x \left(\frac{\partial f}{\partial x} \right)_v \quad (5.1.5)$$

$$\mu_2 = f - v \left(\frac{\partial f}{\partial v} \right)_x + (1 - x) \left(\frac{\partial f}{\partial x} \right)_v \quad (5.1.6)$$

$$P = - \left(\frac{\partial f}{\partial v} \right)_x. \quad (5.1.7)$$

The calculation of the binodal is simpler to perform in the ensemble where the pressure is the independent variable instead of the total density $\rho = 1/v$. We Legendre transform to $g = f + Pv$ where $g(x, P)$ is the Gibbs free energy per particle. In this ensemble the conditions of equal chemical potential and pressure lead to the common tangent construction on g :

$$\left(\frac{\partial g}{\partial x} \right)_P \Big|_{x_A} = \left(\frac{\partial g}{\partial x} \right)_P \Big|_{x_B} = \frac{g(x_A, P) - g(x_B, P)}{x_A - x_B} \quad (5.1.8)$$

where x_A and x_B are the concentrations of species 2 in phases A and B respectively. The spinodal is now the locus of points at which

$$\left(\frac{\partial^2 g}{\partial x^2} \right)_P = 0. \quad (5.1.9)$$

Note that all derivatives are performed at constant temperature T .

5.2 The model mixture and its phase diagram

The GCM binary mixture is specified by the pair potentials between particle species i and j . These are given by the two component generalisation of Eq. (4.1.1):

$$v_{ij}(r) = \epsilon_{ij} \exp(-r^2/R_{ij}^2) \quad (5.2.1)$$

where $\epsilon_{ij} > 0$ denotes the energy and R_{ij} determines the range of the ij interaction; $1 \leq i, j \leq 2$. Thinking of the particles as representing polymers, R_{ii} is roughly the radius of gyration of species i .

We use the multicomponent generalisation of Eq. (2.3.25) for the intrinsic Helmholtz free energy functional of the inhomogeneous mixture:

$$\mathcal{F}[\{\rho_i\}] = \mathcal{F}_{id}[\{\rho_i\}] + \frac{1}{2} \sum_{ij} \int d\mathbf{r}_1 \int d\mathbf{r}_2 \rho_i(\mathbf{r}_1) \rho_j(\mathbf{r}_2) v_{ij}(|\mathbf{r}_1 - \mathbf{r}_2|) \quad (5.2.2)$$

where

$$\mathcal{F}_{id}[\{\rho_i\}] = \frac{1}{\beta} \sum_i \int d\mathbf{r} \rho_i(\mathbf{r}) [\ln(\Lambda_i^3 \rho_i(\mathbf{r})) - 1], \quad (5.2.3)$$

is the ideal gas part of the free energy functional. Recalling that the two-body direct correlation functions are given by (see Eq. (2.3.16))

$$c_{ij}^{(2)}(\mathbf{r}_1, \mathbf{r}_2) = -\frac{\beta \delta^2(\mathcal{F}[\{\rho_i\}] - \mathcal{F}_{id}[\{\rho_i\}])}{\delta \rho_i(\mathbf{r}_1) \delta \rho_j(\mathbf{r}_2)} \quad (5.2.4)$$

it follows that

$$c_{ij}^{(2)}(\mathbf{r}_1, \mathbf{r}_2) = c_{ij}^{(2)}(|\mathbf{r}_1 - \mathbf{r}_2|) = -\beta v_{ij}(|\mathbf{r}_1 - \mathbf{r}_2|) \quad (5.2.5)$$

which is the random phase approximation (RPA) for the mixture. In the bulk mixture the densities are constants, $\rho_i(\mathbf{r}) = \rho_i^b$. Writing these in terms of the total density ρ and the concentration of species 2, x , we can write the bulk Helmholtz free energy per particle f , as [39]

$$f(\rho, x) = f_{id}(\rho, x) + \frac{1}{2} \rho \hat{V}_0(x) \quad (5.2.6)$$

βf_{id} contains the ideal free energy of mixing, $x \ln(x) + (1-x) \ln(1-x)$ as well as an irrelevant ρ dependent term. The mean field interaction term is

$$\hat{V}_0(x) = (1-x)^2 \hat{v}_{11}(0) + 2x(1-x) \hat{v}_{12}(0) + x^2 \hat{v}_{22}(0) \quad (5.2.7)$$

where $\hat{v}_{ij}(0)$ is the $q = 0$ limit of the Fourier transform (FT) of the pair potential (the $\hat{}$ denotes a FT with respect to wave vector q):

$$\hat{v}_{ij}(0) = \int d\mathbf{r} v_{ij}(r) = \pi^{3/2} \epsilon_{ij} R_{ij}^3 \quad (5.2.8)$$

Since the free energy (5.2.6) has the simple mean-field form the thermodynamic stability conditions for the binary mixture also take a very simple form and Louis *et al.* [39] showed that fluid-fluid phase separation is possible at constant volume provided

$$\beta^{-1}\chi \equiv 2\hat{v}_{12}(0) - [\hat{v}_{11}(0) + \hat{v}_{22}(0)] > 0 \quad (5.2.9)$$

or at constant pressure provided

$$\beta^{-2}\Delta \equiv [\hat{v}_{12}(0)]^2 - \hat{v}_{11}(0)\hat{v}_{22}(0) > 0. \quad (5.2.10)$$

This condition is obtained when we calculate the spinodal from (5.2.6) and (5.1.9). Within the present simple mean-field approximation the density along the spinodal can be determined analytically [39]:

$$\rho_s(x) = \frac{\hat{V}_1(x) + \sqrt{\hat{V}_1(x)^2 + 4x(1-x)\Delta}}{2x(1-x)\Delta} \quad (5.2.11)$$

where

$$\hat{V}_1(x) = (1-x)\beta\hat{v}_{11}(0) + x\beta\hat{v}_{22}(0). \quad (5.2.12)$$

In order to observe phase separation we must choose parameters ϵ_{ij} and R_{ij} so that these conditions are satisfied. The choice of parameters can be restricted further by making contact with simulation studies of binary solutions of self-avoiding polymer coils at infinite dilution [30] in which it was suggested that the effective potentials between the polymer centers of mass could be modeled quite well by the GCM, defined by Eq. (5.2.1), with

$$\epsilon_{12} \leq \epsilon_{11} = \epsilon_{22} \quad (5.2.13)$$

and

$$R_{12}^2 = \frac{1}{2}(R_{11}^2 + R_{22}^2). \quad (5.2.14)$$

Relation (5.2.13), which reflects the fact that the energy penalty is lower for smaller polymers to sit inside the coils of a larger one than if they are of the same size, clearly favours mixing; the energy penalty is lower if unlike species are neighbours. It is relation (5.2.14) that favours demixing since it implies $R_{12} > (R_{11} + R_{22})/2$, which corresponds to positive non-additivity, known to drive demixing in hard sphere mixtures [48].

The majority of our calculations for interfacial properties will be for a mixture with $\beta\epsilon_{11} \equiv \epsilon_{11}^* = \epsilon_{22}^* = 2$, $\epsilon_{12}^* = 1.888$, $R_{22}/R_{11} = 0.665$ and R_{12} given by Eq. (5.2.14). (Henceforward we use R_{11} , the radius of gyration of the longer polymer, as the length

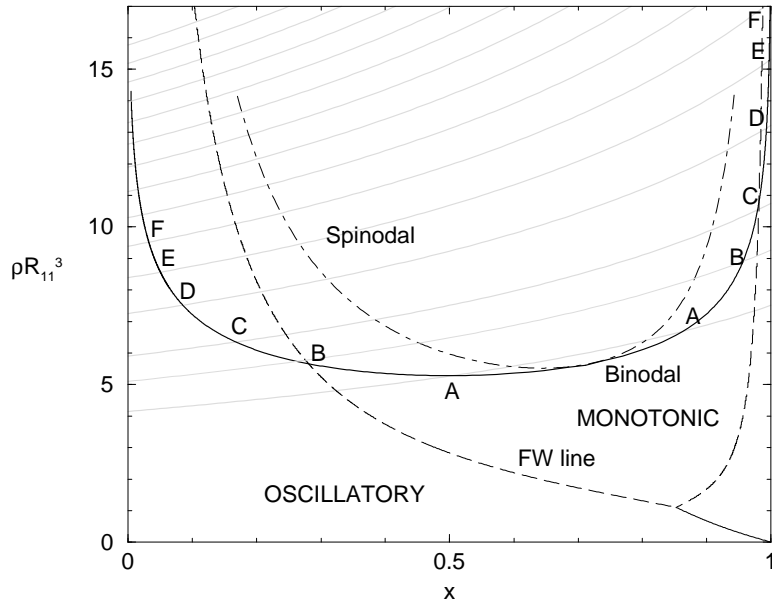


Figure 5.1: The bulk phase diagram for a binary mixture of Gaussian particles with $\epsilon_{12}/\epsilon_{11} = 0.944$ and $R_{22}/R_{11} = 0.665$ which is equivalent to a mixture of two polymers with length ratio 2:1. ρ is the total density and x is the concentration of the smaller species 2. The gray lines are lines of constant pressure; the lowest is at reduced pressure $P\beta R_{11}^3 = 100$, the next at $P\beta R_{11}^3 = 150$, then 200 and the subsequent ones increase in increments of 100. The points marked A-F are the points where the gray lines intersect the binodal (solid line). The density profiles for the corresponding fluid-fluid interfaces are shown in Fig. 5.6. The dashed line denotes the Fisher-Widom (FW) line where the asymptotic decay of the bulk pairwise correlation functions crosses over from oscillatory to monotonic. The solid line in the bottom right corner denotes a new line of crossover from asymptotic oscillatory decay with a certain wavelength to a similar oscillatory decay but with a different wavelength – see section 5.4.

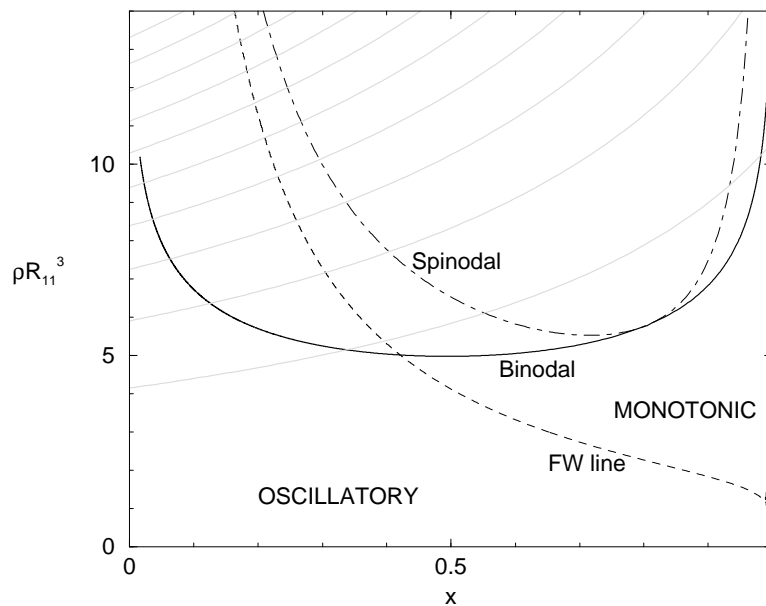


Figure 5.2: As in Fig. 5.1 but now $\epsilon_{12}/\epsilon_{11} = 0.825$ and $R_{22}/R_{11} = 0.524$ which is equivalent to a mixture of two polymers with length ratio 3:1. The gray lines are lines of constant pressure; the lowest is at reduced pressure $P\beta R_{11}^3 = 100$ and the others increase in increments of 100. The right hand branch of the FW line (dashed line) lies close to the $x = 1$ axis but the solid line in the bottom right corner denoting oscillatory-oscillatory crossover is still present for these parameters.

scale in our analysis.) This choice of parameters was motivated by the study of Louis *et al.* [39] where the R_{ij} were chosen to model a mixture of self-avoiding polymers with $L = 200$ (species 1) and $L = 100$ (species 2) monomers. The radius of gyration $R_g \sim L^\nu$, where $\nu \simeq 0.588$ is the Flory exponent.

For $\epsilon^* = 2$ the pure GCM remains fluid for all densities – see Fig. 4.4. If the mixture is treated within the present mean-field approximation the temperature scales out of the free-energy in Eq. (5.2.6) and the phase behaviour is that of an athermal system [39], depending only on the ratios $\epsilon_{12}/\epsilon_{11}$ and R_{22}/R_{11} . We chose $\epsilon_{12}/\epsilon_{11}$ so that the critical point of the fluid-fluid demixing was the same as that in the mixture considered in Ref. [39], i.e. at $x_c = 0.70$, $\rho_c R_{11}^3 = 5.6$. In Fig. 5.1 we plot the phase diagram for this particular choice of parameters. The spinodal (dash-dot line) and binodal (solid line) are obtained as described in section 5.1.

The gray lines in Fig. 5.1 denote lines of constant pressure in the (ρ, x) phase diagram.

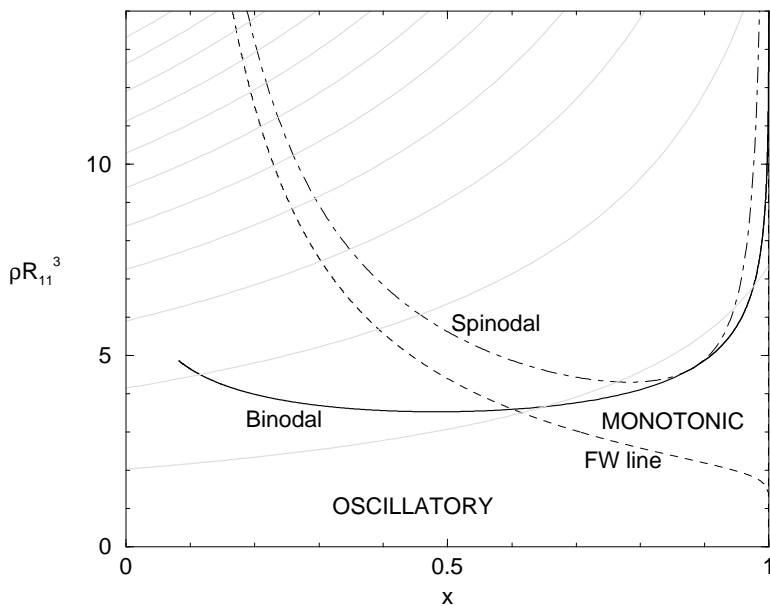


Figure 5.3: As in Fig. 5.1 but now $\epsilon_{12}/\epsilon_{11} = 0.70$ and $R_{22}/R_{11} = 0.388$ which is equivalent to a mixture of two polymers with length ratio 5:1. The gray lines are lines of constant pressure; the lowest is at reduced pressure $P\beta R_{11}^3 = 25$, the next at $P\beta R_{11}^3 = 100$ and then increasing in increments of 100. It becomes increasingly difficult to determine the binodal as P is increased; the coexisting phase to the right is almost pure species 2 ($x = 1$) and the total density ρ becomes very high. The right hand branch of the FW line and the oscillatory-oscillatory crossover cannot be seen due to their proximity to the $x = 1$ axis.

Also plotted is the Fisher-Widom (FW) line to which we shall return later. Other representative phase diagrams are shown in Figs. 5.2 – 5.4. These are obtained from the same mean field free energy but correspond to different choices of R_{22}/R_{11} , i.e. different length ratios. In each case $\epsilon_{12}/\epsilon_{11}$ is chosen to keep the (total) critical density at a similar value to that of the original mixture. As R_{22}/R_{11} is reduced the critical concentration x_c shifts to higher values and the shape of the FW line is altered significantly.

Finally in Fig. 5.5 we consider a different class of mixture described by the parameters $\epsilon_{11}^* = \epsilon_{22}^* = 2$, $\epsilon_{12}^* = 2.07$ and $R_{11} = R_{22} = R_{12}$. Now the demixing occurs not because of the non-additivity of the R_{ij} but because there is a lower energy penalty when like species are neighbours. The phase diagram is symmetrical about $x = 0.5$. We shall find that several of the interfacial properties are quite different in this class of mixture from those in the former class.

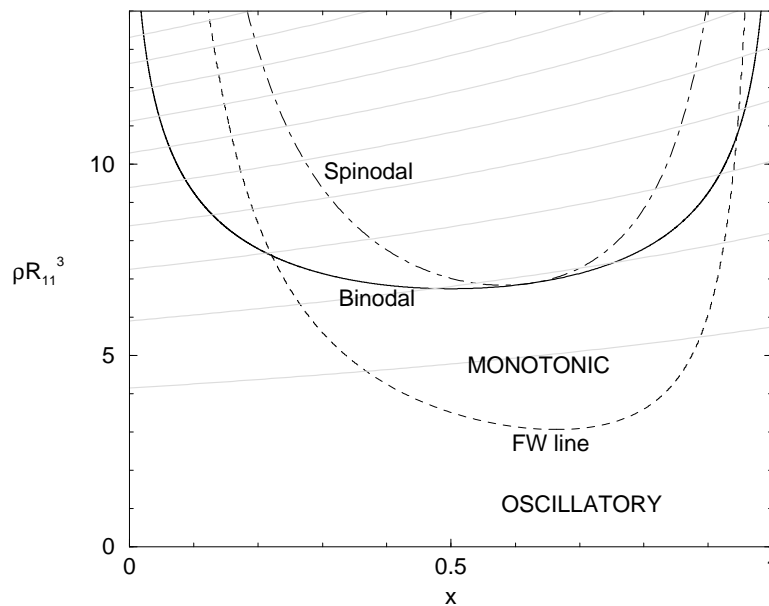


Figure 5.4: As in Fig. 5.1 but now $\epsilon_{12}/\epsilon_{11} = 1.0$ and $R_{22}/R_{11} = 0.8$ which is equivalent to a mixture of two polymers with length ratio 1.46:1. The gray lines are lines of constant pressure; the lowest is at reduced pressure $P\beta R_{11}^3 = 100$ and the others increase in increments of 100. For these parameters there is no crossover line between two types of oscillatory decay and no cusp in the FW line.

5.3 Properties of the fluid-fluid interface

In this section we investigate the one-body density profiles $\rho_i(z)$, $i = 1, 2$, and the surface tension γ for the planar interfaces which arise between coexisting fluid phases in the GCM. Since our approach is based on the mean-field free energy functional (5.2.2) effects of capillary-wave fluctuations are omitted and (away from the critical point) the interfacial width remains finite in vanishing gravitational field. Thus we work with the grand potential functional

$$\Omega_V[\{\rho_i\}] = \mathcal{F}[\{\rho_i\}] - \sum_{i=1}^2 \int d\mathbf{r} (\mu_i - V_i(\mathbf{r})) \rho_i(\mathbf{r}), \quad (5.3.1)$$

which is the two component generalisation of Eq. (2.3.7). Taking from the outset the external potentials $V_i(\mathbf{r}) = V_i(z) = 0$, this procedure yields well-defined planar density profiles $\rho_i(z)$, with z normal to the surface, from which the surface tension can be calculated.

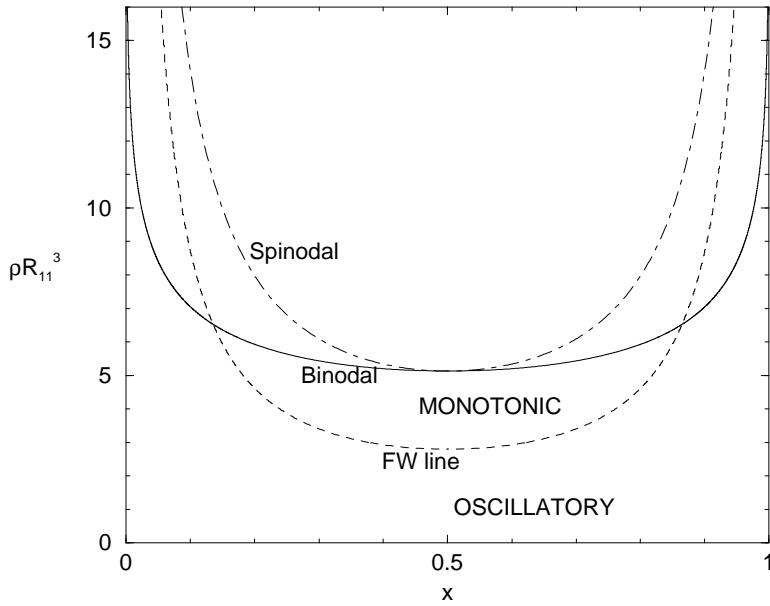


Figure 5.5: As in Fig. 5.1 but now $\epsilon_{12}/\epsilon_{11} = 1.035$ and $R_{22}/R_{11} = 1.0$. In this symmetrical case there is no crossover line between two types of oscillatory decay and no cusp in the FW line. Note the perfect symmetry about the line $x = 0.5$. The tie lines are horizontal in this case.

5.3.1 Density profiles

In order to calculate the equilibrium density profiles across the free interface we follow the procedure used in chapter 3 for the free interface profiles within Landau theory, i.e. we take the functional derivative of (5.3.1) which, using (5.2.2) and in the absence of an external field yields the Euler-Lagrange equation

$$\mu_i = \mu_{i,id}(\rho_i(z_1)) + \sum_{j=1}^2 \int d\mathbf{r}_2 \rho_j(z_2) v_{ij}(|\mathbf{r}_1 - \mathbf{r}_2|), \quad i = 1, 2. \quad (5.3.2)$$

$\mu_{i,id}$ is the chemical potential of species i in an ideal gas, $\beta\mu_{i,id}(\rho_i) = \ln(\Lambda_i^3 \rho_i)$ (Λ_i is the thermal de Broglie wavelength). Eliminating the chemical potentials in favor of the bulk coexisting densities ρ_i^b that were found from the calculation of the binodal we have:

$$\rho_i(z_1) = \rho_i^b \exp\left[\sum_{j=1}^2 \int d\mathbf{r}_2 (\rho_j^b - \rho_j(z_2)) v_{ij}(|\mathbf{r}_1 - \mathbf{r}_2|)\right], \quad i = 1, 2. \quad (5.3.3)$$

This coupled pair of equations can be solved self consistently for the density profiles of the two species. The results for a mixture of Gaussian particles representing a mixture of

polymers of length ratio 2:1 are shown in Fig. 5.6. The striking feature is the development of pronounced oscillations in the density profile of the larger species, $\rho_1(z)$ for states well removed from the critical point. Closer inspection shows that for states C,D,E and F *both* density profiles $\rho_1(z)$ and $\rho_2(z)$ exhibit non-monotonic decay into the bulk phase which is rich in species 1. On the other side of the interface, approaching the bulk phase rich in species 2, magnification shows that both $\rho_1(z)$ and $\rho_2(z)$ are non-monotonic for states D,E and F. For states A and B, closer to the critical point, there is no sign of oscillations on either side of the interface.

This is not the first time that damped oscillatory density profiles have been calculated for fluid-fluid interfaces treated by DFT. Evans *et al.* [49] found that the planar liquid-vapour density profiles for a one component square-well fluid treated by means of non-local weighted density approximation for repulsive forces exhibited oscillations on the liquid side of the interface provided the thermodynamic state lay sufficiently far from the bulk critical point. The oscillations we find for species 1 in the present calculations are considerably more pronounced than those found in Ref. [49] and resemble those found for the colloidal profile in a recent DFT study [50, 51] of a model colloid-(ideal) polymer mixture in which colloid-colloid and colloid-polymer interactions are hard-sphere like. The oscillations were found in both the colloid and polymer profiles but only on the colloid rich side of the interface. Here we find, for a range of thermodynamic states, oscillations on *both* sides of the interface. Moreover these oscillations arise for a system in which the interparticle potentials are very soft and are treated by means of the simplest mean field DFT.

In the original analysis of oscillatory one-body density profiles $\rho(z)$ at the liquid-vapour interface it was shown [49] that oscillations should occur when the bulk fluid, in that case a liquid, lies on the oscillatory side of the FW line. The latter divides the bulk phase diagram into regions where the longest range decay of $rh(r)$ is either pure exponential or (exponentially) damped oscillatory [2]. $h(r) = g(r) - 1$ is the total pairwise correlation function of the fluid. It was also argued that the wavelength and the decay length of the oscillations in $\rho(z)$ as $z \rightarrow \infty$ (deep into the bulk phase) should be identical to those characterizing the asymptotic decay ($r \rightarrow \infty$) of $rh(r)$ [49]. In order to understand the genesis of oscillations in $\rho_1(z)$ and $\rho_2(z)$ for our present model we calculated the FW line for the bulk mixture, now defined as the line in the phase diagram where the leading asymptotic decay of all three pairwise correlation functions $h_{ij}(r)$, $1 \leq i, j \leq 2$, crosses over from monotonic to oscillatory; these FW lines are shown in Figs. 5.1 – 5.5. Details of

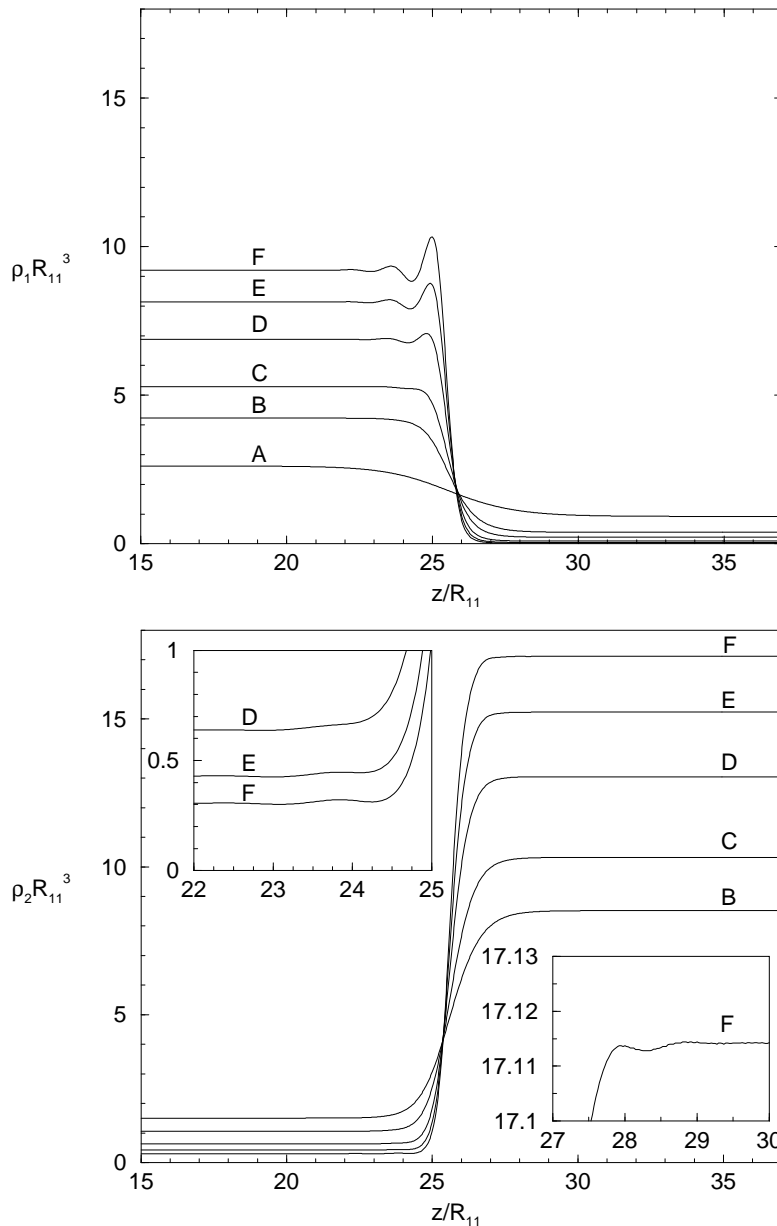


Figure 5.6: The equilibrium density profiles of species 1, the larger particles (top figure), and species 2 (lower figure), at the planar interface between coexisting fluid phases for states specified in Fig. 5.1, i.e. a mixture of two polymers with length ratio 2:1. For state A near the critical point, the interface is broad whereas far from the critical point, states E and F, the interface becomes much sharper. Oscillatory profiles are found for states C-F. The insets show magnifications of regions where the profiles exhibit oscillations. Note that the profiles of both species decay into a given bulk state with the same decay length and, when oscillatory, the same wavelength. The amplitude and the phase do depend on the species.

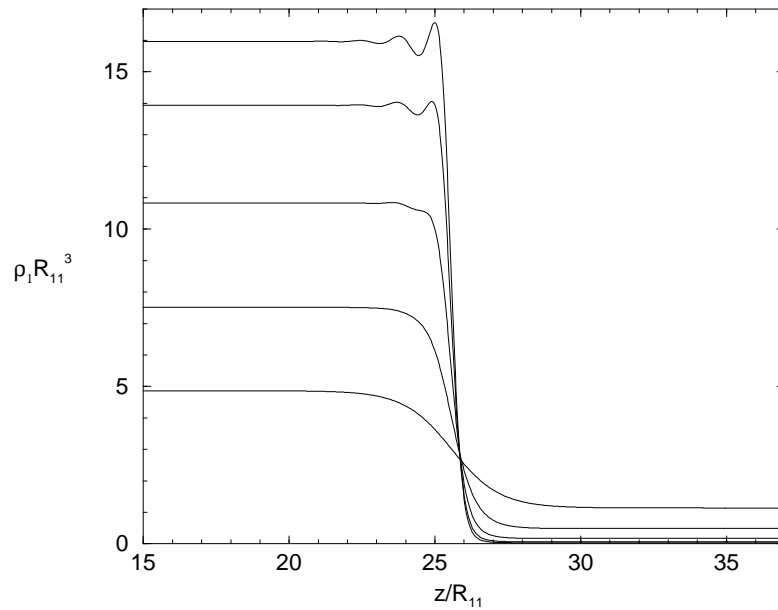


Figure 5.7: Equilibrium density profiles of species 1 for the symmetric mixture with $\epsilon_{12}/\epsilon_{11} = 1.035$ and $R_{22}/R_{11} = 1.0$ whose phase diagram is given in Fig. 5.5. The density profiles are calculated at total bulk densities $\rho R_{11}^3 = 6, 8, 11, 14$ and 16 (from bottom to top in the left hand phase). The density profiles of species 2 are merely reflections of these profiles in the line $z/R_{11} = 25.6$.

the calculations are described in Sec. 5.4. Here it suffices to say that we find oscillations on both sides of the interface when the tie lines intersect both sides of the binodal at points which lie above the two intersections of the FW line (this has two branches) with the binodal, i.e. states D,E and F in Fig. 5.1. A similar situation occurs for the more symmetrical case $\epsilon_{12}/\epsilon_{11} = 1.0$ and $R_{22}/R_{11} = 0.8$, shown in Fig. 5.4. However, for the more asymmetrical cases in Figs. 5.2 and 5.3 where the right hand branch of the FW line lies very close to the $x = 1$ axis and therefore intersects the binodal at very high densities, oscillations are observable at fairly low pressures on the side of the interface rich in species 1 (small x) whereas for the side rich in species 2, very high pressures are required before the oscillations arise.

For the perfectly symmetrical mixture $R_{22}/R_{11} = 1.0$, whose phase diagram is shown in Fig. 5.5, the binodal and the FW line are symmetric about $x = 0.5$ and the density profiles $\rho_1(z)$ and $\rho_2(z)$ are simply reflections of each other – see Fig. 5.7. Because of the symmetry, if oscillations occur in the profiles on one side of the interface they must occur

on the other side. As can be seen from Fig. 5.5, the intersection of the FW line with the binodal is at a total density not very far above the critical density and oscillatory profiles should occur for $\rho R_{11}^3 > 6.5$. However for states not too far above the intersection of the FW line and the binodal the amplitude of the oscillatory contribution to the profile is often small making it difficult to distinguish this contribution in the numerical results.

The general theory of the asymptotic decay of correlations in fluid mixtures with short ranged interparticle potentials predicts [52] that the longest range decay of the profiles should be

$$\rho_i(z) - \rho_i^b \sim \rho_i^b A_i \exp(-\alpha_0 z) \quad , z \rightarrow \infty \quad (5.3.4)$$

on the monotonic side of the FW line and

$$\rho_i(z) - \rho_i^b \sim \rho_i^b \tilde{A}_i \exp(-\tilde{\alpha}_0 z) \cos(\alpha_1 z - \theta_i) \quad , z \rightarrow \infty \quad (5.3.5)$$

on the oscillatory side. Equivalent relations apply for $z \rightarrow -\infty$, with the appropriate identification of the bulk densities ρ_i^b . The decay lengths α_0^{-1} and $\tilde{\alpha}_0^{-1}$ and the wavelength of oscillations $2\pi/\alpha_1$ are properties of the bulk fluid and are the same for both species (see Sec. 5.4). Only the amplitudes A_i and \tilde{A}_i and, for oscillatory profiles, the phase θ_i depend on the particular species. Our numerical results are consistent with these general predictions. Note that on the FW line $\alpha_0 = \tilde{\alpha}_0$ and that for states near this line both types of contribution must be taken into account.

5.3.2 Surface tension

Having calculated the equilibrium density profiles at the free interface, these can be used to obtain the surface tension of the interface. The latter is defined as the excess grand potential per unit area and can be written as

$$\gamma = \int_{-\infty}^{\infty} dz (P + \omega(z)) \quad (5.3.6)$$

where P is the bulk pressure at coexistence and $\omega(z)$ is the grand potential density obtained from Eqs. (5.2.2) and (5.3.1) with $V_i(z) = 0$. The reduced tension $\gamma^* = \beta\gamma R_{11}^2$ is plotted in Fig. 5.8 for the interfaces corresponding to Fig. 5.6, i.e. the phase diagram of Fig. 5.1. We have chosen to plot γ^* versus the order parameter $(\rho_1^{b,A} - \rho_1^{b,B})R_{11}^3$, where $\rho_1^{b,A}$ is the bulk density of species 1 in phase A, rich in species 1 and $\rho_1^{b,B}$ is the same quantity in phase B, poor in species 1 [53]. On approaching the critical point simple mean-field arguments

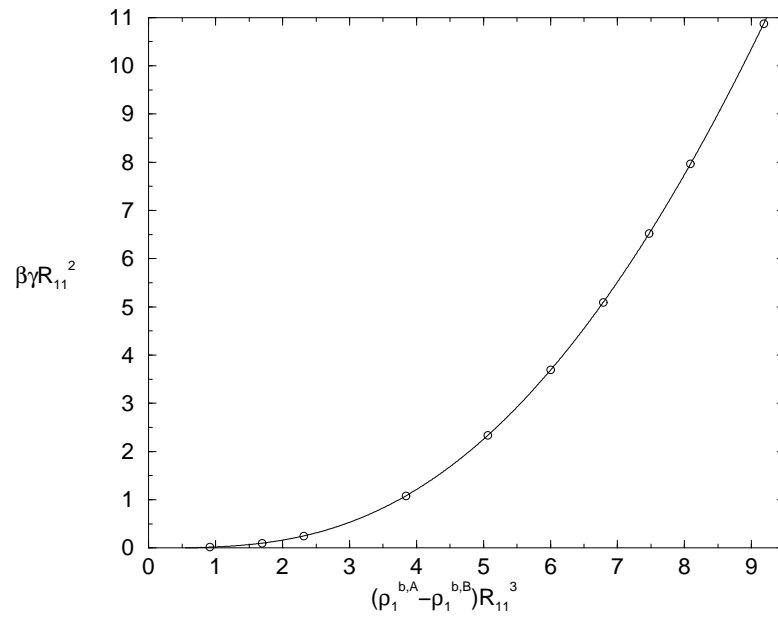


Figure 5.8: The reduced surface tension $\gamma^* = \beta\gamma R_{11}^2$ calculated for the planar interface between coexisting fluid phases in the system specified in Fig. 5.1, i.e. a mixture of two polymers with length ratio 2:1. $(\rho_1^{b,A} - \rho_1^{b,B})R_{11}^3$, the difference in density of species 1 between bulk phases A and B, and γ vanish at the critical point. The circles are the results of our calculations and the solid line joining these is a guide to the eye.

imply that γ^* should vanish as $(\rho_1^{b,A} - \rho_1^{b,B})^3$ and this is confirmed by our numerical results – see also Fig. 8.6 which displays results for a closely related fluid, namely a binary fluid composed of particles interacting via pair potentials which model the interaction between star polymers. A similar plot of γ^* for the perfectly symmetric mixture is displayed in Fig. 5.9. Note that for a given value of $(\rho_1^{b,A} - \rho_1^{b,B})R_{11}^3$, γ^* is significantly larger for the asymmetric mixture (Fig. 5.8).

We can obtain an estimate for the surface tension of a phase separated mixture of ‘polymers’ by choosing $\gamma^* = 5$, corresponding to a state well removed from the critical point, $T = 300K$ and $R_{11} = 20nm$. We find $\gamma = 52\mu N/m$, a value one order of magnitude greater than that calculated and measured for a colloid-polymer mixture [53], but two orders of magnitude smaller than the tensions of simple atomic fluids near their triple points.

Further insight into the factors which determine the surface tension in our binary mixtures can be obtained by working with linear combinations of the density profiles

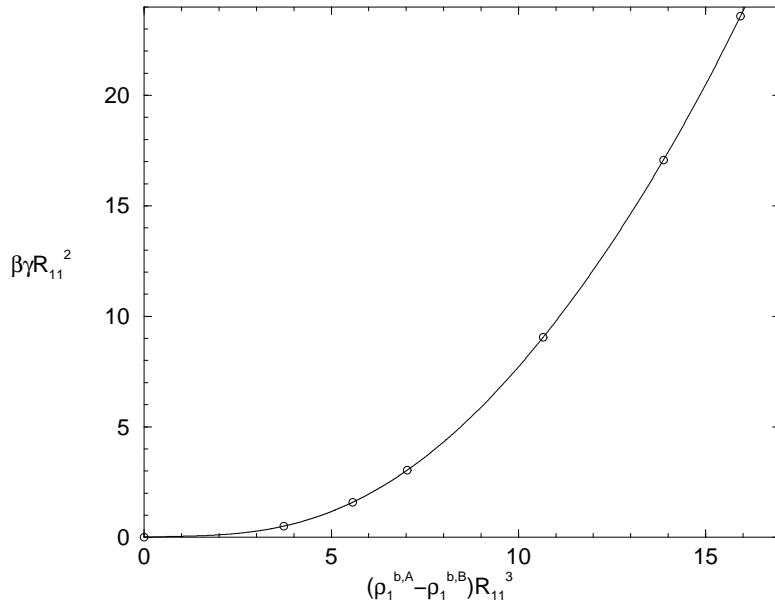


Figure 5.9: The reduced surface tension $\gamma^* = \beta\gamma R_{11}^2$ calculated for the planar interface between coexisting fluid phases in the perfectly symmetric system specified in Fig. 5.5. $(\rho_1^{b,A} - \rho_1^{b,B})R_{11}^3$, the difference in density of species 1 between bulk phases A and B, and γ vanish at the critical point. The circles are the results of our calculations and the solid line joining these is a guide to the eye.

$\rho_1(z)$ and $\rho_2(z)$. The total number density $N(z)$ and a local concentration variable $C(z)$, the surface segregation, may be defined for a fluid-fluid interface by

$$N(z) = \rho_1(z) + \rho_2(z) \quad (5.3.7)$$

$$C(z) = \frac{x\rho_1(z) - (1-x)\rho_2(z)}{x(1-x)} \quad (5.3.8)$$

where x is the concentration of species 2 in the bulk liquid phase. These variables are normally introduced for a liquid-gas interface. For the situation where the ‘gas’ phase has a non-zero density, the integral over $C(z)$ diverges. When the densities of both phases are comparable, $C(z)$ should be replaced by the symmetrized segregation [54]

$$\Delta(z) = \frac{a_2(\rho_1(z) - \rho_1^{b,A}) - a_1(\rho_2(z) - \rho_2^{b,A})}{a_1 a_2} \quad (5.3.9)$$

where the a_i are given by

$$a_i = \frac{\rho_i^{b,A} - \rho_i^{b,B}}{(\rho_1^{b,A} + \rho_2^{b,A}) - (\rho_1^{b,B} + \rho_2^{b,B})}, \quad i = 1, 2. \quad (5.3.10)$$

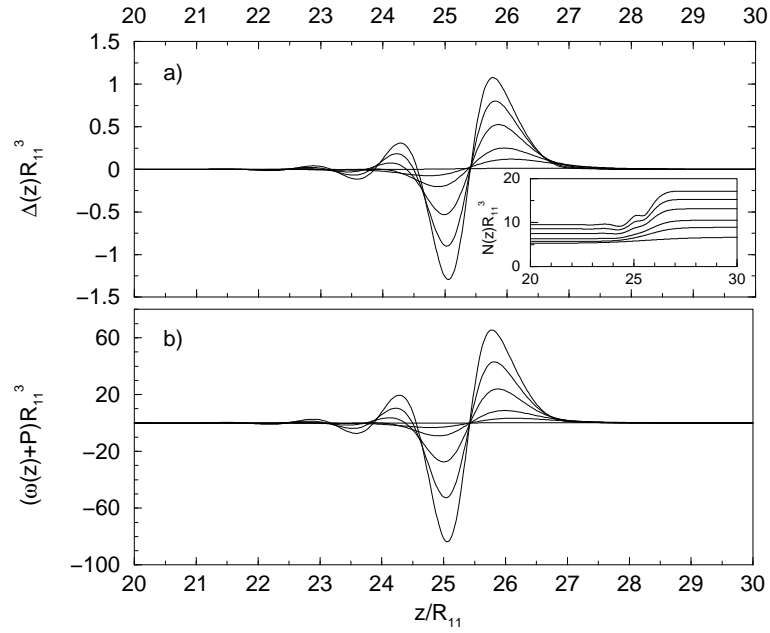


Figure 5.10: The top graph a) shows the function $\Delta(z)$ obtained from the density profiles shown in Fig. 5.6. $\Delta(z)$, defined by Eq. 5.3.9, measures the surface segregation at the interface. Below it in b) is plotted $(\omega(z) + P)$, the integral of which is the surface tension. Each set of curves correspond to state points A-F on the phase diagram (Fig. 5.1); the most oscillatory refers to state F. Apart from the scales on the y-axes the two sets of curves are almost identical, demonstrating that the surface tension arises primarily from concentration fluctuations. The total density $N(z) = \rho_1(z) + \rho_2(z)$, shown in the inset to a), has very different variation from the surface tension integrand.

with A and B referring to the two coexisting phases. Clearly $a_1 + a_2 = 1$. $\Delta(z)$ may also be expressed as

$$\Delta(z) = \frac{a_2(\rho_1(z) - \rho_1^{b,B}) - a_1(\rho_2(z) - \rho_2^{b,B})}{a_1 a_2} \quad (5.3.11)$$

The integral of $\Delta(z)$ yields the thermodynamic function $\Gamma_{2,1}$, i.e. the relative adsorption of species 2 with respect to species 1 [54]:

$$\Gamma_{2,1} = -a_2 \int_{-\infty}^{\infty} dz \Delta(z) \quad (5.3.12)$$

Thus $\Delta(z)$, which has the dimension of number density, measures the variation of local concentration through the interface. Fig. 5.10 shows a plot of $\Delta(z)$ calculated from the profiles in Fig. 5.6. Below it is displayed $(\omega(z) + P)$, the integrand of Eq. (5.3.6) which

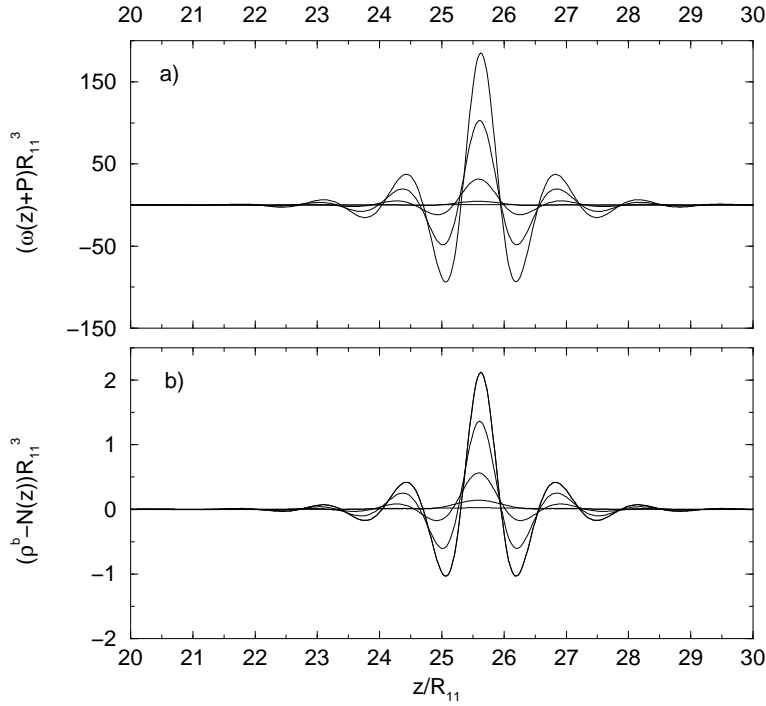


Figure 5.11: The top graph a) shows the function $(\omega(z) + P)$ for the symmetric mixture obtained from the density profiles shown in fig. 5.7, the integral of which is the surface tension. Below it in b) is plotted the total density fluctuation variable $\tilde{N}(z) \equiv \rho^b - N(z)$. Apart from the scales on the y-axes the two sets of curves are almost identical.

gives the surface tension. Both functions are only non-zero in the interfacial region. The similarity between the two sets of curves shows that the major contribution to the surface tension comes from concentration fluctuations at the interface rather than from fluctuations of the total density since $N(z)$ has a very different form – see the inset to part a) of the figure.

The situation is quite different for the perfectly symmetric mixture considered in Fig. 5.5. Because of the symmetry exhibited by the density profiles, $a_2\Delta(z) = \rho^b - N(z)$, where $\rho^b = \rho_1^{b,A} + \rho_2^{b,A}$ is the total density in both bulk phases. In Fig. 5.11 we compare plots of the surface tension integrand $(\omega(z) + P)$ and the function $\tilde{N}(z) \equiv \rho^b - N(z)$ corresponding to the density profiles of Fig. 5.7. It is clear that the two sets of curves are very similar.

5.4 Asymptotic decay of correlation functions and the Fisher-Widom line

In this section we describe the asymptotic decay, $r \rightarrow \infty$, of the total pairwise correlation functions $h_{ij}(r)$ in our model mixture and the determination of the FW line. The basic procedure follows that in [52]. In Fourier space the Ornstein-Zernike (OZ) equations for $h_{ij}(r)$ in terms of the pairwise direct correlation functions $c_{ij}(r)$ of a two component liquid are:

$$\hat{h}_{ij}(q) = \frac{N_{ij}(q)}{D(q)} \quad (5.4.1)$$

where $\hat{h}_{ij}(q)$ is the three-dimensional Fourier transform (FT) of $h_{ij}(r)$. The numerator is given by

$$\begin{aligned} N_{11}(q) &= \hat{c}_{11}(q) + \rho_2^b (\hat{c}_{12}^2(q) - \hat{c}_{11}(q)\hat{c}_{22}(q)) \\ N_{22}(q) &= \hat{c}_{22}(q) + \rho_1^b (\hat{c}_{12}^2(q) - \hat{c}_{11}(q)\hat{c}_{22}(q)) \\ N_{12}(q) &= \hat{c}_{12}(q) \end{aligned} \quad (5.4.2)$$

and

$$D(q) = [1 - \rho_1^b \hat{c}_{11}(q)][1 - \rho_2^b \hat{c}_{22}(q)] - \rho_1^b \rho_2^b \hat{c}_{12}^2(q) \quad (5.4.3)$$

Inverting the FT, and noting that $\hat{h}_{ij}(q)$ is even we can write:

$$\begin{aligned} r h_{ij}(r) &= \frac{1}{4\pi^2 i} \int_{-\infty}^{\infty} dq q e^{iqr} \hat{h}_{ij}(q) \\ &= \frac{1}{4\pi^2 i} \int_{-\infty}^{\infty} dq q e^{iqr} \frac{N_{ij}(q)}{D(q)} \end{aligned} \quad (5.4.4)$$

which can be evaluated by contour integration [52]. From Eq. (5.2.5) it follows that within our mean-field treatment of the GCM

$$\hat{c}_{ij}(q) = -\beta \hat{v}_{ij}(q) = -\beta \pi^{\frac{3}{2}} R_{ij}^3 \epsilon_{ij} \exp(-R_{ij}^2 q^2 / 4) \quad (5.4.5)$$

and the singularities of $\hat{h}_{ij}(q)$ are simple poles. Choosing an infinite radius semi-circle in the upper half of the complex plane, we obtain

$$r h_{ij}(r) = \frac{1}{2\pi} \sum_n R_n^{ij} e^{iq_n r} \quad (5.4.6)$$

where R_n^{ij} is the residue of $q N_{ij}(q)/D(q)$ for the n th pole at $q = q_n$. The q_n are solutions of $D(q_n) = 0$ and there is normally an infinite number of poles. If a pole lies on the imaginary

axis, $q_n = i\alpha_0$, it contributes a pure exponential term of the form $\exp(-\alpha_0 r)$ to the sum in Eq. (5.4.6). Poles lying off the imaginary axis occur in conjugate pairs $q_n = \pm\alpha_1 + i\tilde{\alpha}_0$ and such a pair contributes a damped oscillatory term of the form $\exp(-\tilde{\alpha}_0 r) \cos(\alpha_1 r - \theta)$ to the sum in Eq. (5.4.6). The longest range decay of $h_{ij}(r)$ is determined by the pole or the conjugate pair of poles with the smallest imaginary part. If $\alpha_0 < \tilde{\alpha}_0$ the longest range decay is monotonic (pure exponential), otherwise it is damped oscillatory. Since all three $\hat{h}_{ij}(q)$ have a common denominator $D(q)$ all three $h_{ij}(r)$ decay ultimately with the same decay length and wavelength; only the residues depend on the particular species and these determine only the amplitudes and phases of the leading order decay [52, 55]. Similar arguments [52] apply for the one-body density profiles in a binary mixture and give rise to Eqs. (5.3.4) and (5.3.5). The α_0 , $\tilde{\alpha}_0$ and α_1 appearing in these equations are determined by the poles of $\hat{h}_{ij}(q)$ – as described above.

The FW line alluded to earlier is the cross-over line in the phase diagram where $\alpha_0 = \tilde{\alpha}_0$. As the fluid-fluid spinodal corresponds to points in the phase diagram at which the pure imaginary pole vanishes, i.e. $\alpha_0 = 0$, cross-over from oscillatory to monotonic decay must occur before the spinodal is reached which implies that the FW line lies below the spinodal in the (ρ, x) plane. By calculating the zeros of $D(q)$, i.e. the first few poles, for a range of state points it is straightforward to map out the FW lines displayed in Figs. 5.1 – 5.5.

For the first three cases, Figs. 5.1 – 5.3, the dashed FW line has two separate branches terminating in a cusp at low total density ρ_{cu} . As the mixture is made more asymmetric, i.e. R_{22}/R_{11} decreases, the right hand branch lies closer to the axis $x = 1$. On the left hand branch the crossover (at fixed $\rho > \rho_{cu}$) is from longest range oscillatory decay with wavelength $2\pi/\alpha_1 \approx 2R_{11}$ to monotonic decay. Whereas on the right hand branch it is from monotonic to oscillatory with wavelength $\approx 2R_{22}$. For $\rho < \rho_{cu}$ there is a separate crossover line, denoted by the solid line in the bottom right corner of Figs. 5.1 – 5.3. On each side the long range decay is given by

$$r h_{ij}(r) \sim \tilde{A}_{ij} \exp(-\tilde{\alpha}_0 r) \cos(\alpha_1 - \theta_{ij}) + \tilde{\tilde{A}}_{ij} \exp(-\tilde{\tilde{\alpha}}_0 r) \cos(\alpha'_1 - \theta'_{ij}), \quad r \rightarrow \infty \quad (5.4.7)$$

where $\alpha_1 \approx \pi/R_{11}$ and $\alpha'_1 \approx \pi/R_{22}$. To the left of the line $\tilde{\alpha}_0 < \tilde{\tilde{\alpha}}_0$ while on the right, $\tilde{\alpha}_0 > \tilde{\tilde{\alpha}}_0$, i.e. there is crossover from oscillatory decay with one wavelength to oscillatory decay with another wavelength when $\tilde{\alpha}_0 = \tilde{\tilde{\alpha}}_0$. At the cusp, where the two branches of the FW line meet the new line, the pure imaginary (monotonic) pole $\alpha_0 = \tilde{\alpha}_0 = \tilde{\tilde{\alpha}}_0$.

Making the mixture more symmetric shifts the cusp to smaller x and for $R_{22}/R_{11} > 0.707$ there is no cusp in the FW line and the new crossover line, separating regions with different types of oscillatory decay, is absent – see Figs. 5.4 and 5.5. Further details of the pole structure which gives rise to the crossover lines are given in Appendix B.

To the best of our knowledge this is the first time that the FW line has been mapped out for a binary mixture exhibiting fluid-fluid phase separation of the type displayed here¹ and it is important to inquire how robust results based on the simple RPA (5.2.2) might be. For the pure GCM the comprehensive study of Louis *et al.* [39] showed that for $\epsilon^* = 2$ the radial distribution functions $g(r)$ obtained from the hyper-netted chain approximation (HNC) were virtually indistinguishable from Monte Carlo data at reduced densities $\rho R^3 = 0.1, 0.5$ and 2.0 . These authors also argued that the HNC should become exact in the high density limit and suggested that the HNC pair correlation function should provide an (‘exact’) reference against which other approximations might be gauged. In this spirit we compare, in Fig. 5.12, the RPA results for $g(r)$ with those obtained from our own HNC calculations at reduced densities $\rho R^3 = 2, 4$ and 6 (see also Fig. 4.2). As the density is increased the correlation hole is reduced and the degree of particle overlap increases leading to a $g(r)$ which is closer to that of the ideal gas [39]. For $\rho R^3 = 2$ the RPA result lies well below the HNC for $r/R \lesssim 0.4$, i.e. in the central overlap region. However, for $\rho R^3 = 6$ the two closures yield very similar results for all except the smallest separations r . What is more significant for our present purposes is that for all three densities the simple RPA result is very close to that of the HNC for *large* separations, i.e. $r/R \gtrsim 0.8$. In particular, the oscillations in $g(r)$ are very well captured by the RPA – see inset to Fig. 5.12. This implies that the RPA provides a rather accurate account of the asymptotic decay of $g(r)$ and therefore of the leading pole² in $\hat{h}(q)$, at least for reduced densities $\gtrsim 2$. But this is the range of (total) densities most relevant in determining the FW lines in the mixtures (see Figs. 5.1 – 5.5) so we are confident that our results for the latter should be qualitatively correct.

¹Previous studies have focused on models such as the RPM and the Yukawa-RPM, designed for ionic fluids – see Ref. [56] and references therein.

²L.R. Croft (private communication), made an accurate comparison between the HNC and RPA poles for the one component GCM. It was found that the dominant HNC pole is very similar in value to that obtained from the analytically tractable RPA. This study showed that retaining only the leading pole contribution yields an excellent fit to $g(r)$ for r down to the position of the first maximum. For the method used to calculate the leading pole from numerical solutions of the HNC see Ref. [57].

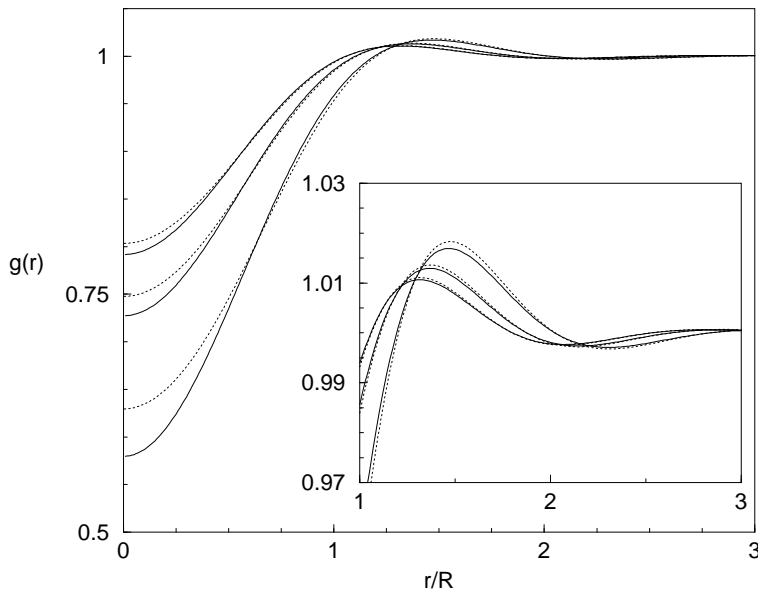


Figure 5.12: The radial distribution function $g(r)$ for a pure fluid of Gaussian particles with $\epsilon^* = 2$ and radius R , calculated at reduced densities $\rho R^3 = 2, 4, 6$ (from bottom to top). For each density the dotted line is from the HNC result and the solid line is that of the RPA closure. The inset shows a magnification of the oscillations.

Further evidence for the existence of the new oscillatory-oscillatory crossover line comes from considering the low density approximation

$$c_{ij}(r) = f_{ij}(r) \equiv \exp(-\beta v_{ij}(r)) - 1 \quad (5.4.8)$$

where $f_{ij}(r)$ denotes the Mayer function. We calculated the zeros of $D(q)$, Eq. (5.4.3), using this approximation and found a crossover line approaching $\rho = 0$, $x = 1$, similar to that shown in the bottom right corner of Figs. 5.1 and 5.2³. Finally we should remark that in Ch. 8.3 we describe in greater detail the accuracy of the RPA in comparison to the HNC for determining the fluid structure (pair correlation functions) and thermodynamic properties of a binary mixture of particles interacting via potentials mimicking the effective interaction between star-polymers in solution.

³Very recently an oscillatory-oscillatory crossover line was found for binary hard-sphere mixtures treated in the Percus-Yevick approximation and for a binary mixture of hard rods in one dimension treated exactly (R. Roth, private communication).

5.5 Discussion

In this chapter we have calculated the properties of the planar interface between two coexisting fluid phases in the binary GCM using the simplest mean-field free energy functional (5.2.2). We considered various choices of the size ratio R_{22}/R_{11} , employing the rule (5.2.14) for the range parameter R_{12} . It is the positive non-additivity embodied in (5.2.14) which drives the demixing in Figs. 5.2 – 5.4 since the corresponding energy parameters favour mixing, i.e. $\epsilon_{11}^* = \epsilon_{22}^* \geq \epsilon_{12}^*$. The surface tension in these systems is governed by the segregation $\Delta(z)$, which measures the local relative concentration in the interface, rather than by the local total density $N(z)$ – see Fig. 5.10. For comparison we also considered a symmetric system with $R_{22}/R_{11} = 1.0$ and $\epsilon_{12}^* > \epsilon_{11}^*$ where the demixing is driven by energy considerations. Symmetry then dictates that the phase diagram is symmetric about $x = 0.5$ (Fig. 5.5) and the surface tension is governed by $N(z)$ – see Fig. 5.11. However, in all the cases we considered, plots of the reduced surface tension γ^* versus the order parameter $(\rho_1^{b,A} - \rho_1^{b,B})R_{11}^3$ showed similar behaviour as those in Figs. 5.8 and 5.9 with γ^* vanishing at the critical point as $(\rho_1^{b,A} - \rho_1^{b,B})^3$. Beyond mean-field the exponent should be replaced by the ratio $2\nu/\beta$, where ν denotes the correlation length and β the coexistence curve (order parameter) critical exponent, respectively. As we expect the critical behaviour of this system to lie in the Ising Universality class, for which $2\nu/\beta \simeq 3.9$, the curves in Figs. 5.8 and 5.9 should, in reality, be flatter near the origin.

The most striking aspect of the results presented in this chapter (Figs. 5.6 and 5.7) is the presence of pronounced oscillations in the interfacial density profiles for certain thermodynamic states. We accounted for the occurrence of damped oscillations in terms of general arguments involving the asymptotic decay of the bulk pairwise correlation functions $h_{ij}(r)$, i.e. by means of an analysis of the leading poles of $\hat{h}_{ij}(q)$ and determination of the FW lines which parallels earlier DFT treatments of interfaces [49, 50, 51]. The oscillations arise from packing effects which are still present in these soft core systems. Although our present mean-field functional (5.2.2) should provide reliable estimates for $\tilde{\alpha}_0$ and α_1 and, hence, for the decay length and wavelength of the oscillations (see Eq. (5.3.5)), it is not clear that it will yield reliable amplitudes \tilde{A}_i . The latter depend on the strength and extent of the inhomogeneity rather than on properties of the bulk phase. Thus for states such as E and F in Fig. 5.1, which are very far from the critical point and deep in the oscillatory region of the phase diagram, the theory must treat density profiles

that decrease from $\rho_1 R_{11}^3 \simeq 9$ to extremely low values $\rho_1 R_{11}^3 \simeq 0.03$ over a distance of about $2R_{11}$ (see Fig. 5.6). One could expect the the functional (i.e. the RPA) to fail in the very low density region. The situation seems rather more favourable for species 2 (Fig. 5.6) where $\rho_2 R_{11}^3 \geq 0.3$ throughout the interface for all states. However, even for state F, the oscillations in $\rho_2(z)$ are extremely weak! The total density $N(z)$ is, of course, large throughout the interface and shows only mild variation for all states (see inset to Fig. 5.10). But the theory must be able to describe the individual profiles. These exhibit a degree of inhomogeneity which is higher than for the pure GCM near a hard-wall where the functional performs well [39]. We believe that a more refined DFT, which incorporates a more accurate treatment of low densities, might yield smaller amplitudes for the oscillations in $\rho_1(z)$ without altering significantly their decay length and wavelength⁴.

For the present system, the development of oscillatory density profiles for the free interface seems to be determined by the location of the FW line. However, this does not always seem to be the case. In Monte Carlo simulations of a liquid-metal described by a classical pair potential model [58, 59, 60], very pronounced oscillations on the liquid side of the planar liquid-gas interface were found, and the development of the oscillations seems unrelated to the location in the phase diagram of the FW line. This model was constructed in order to suppress the melting temperature T_m relative to the critical temperature T_c , i.e., $T_m/T_c \lesssim 0.2$, and in these circumstances the surface tension can be large. The high surface tension results in a rather ‘stiff’ interface, and this seems to be the origin of the strongly oscillatory density profiles near the interface. We can therefore distinguish two factors which need to be considered when analyzing oscillatory free interface density profiles: Firstly, one can envisage that if an interface is particularly ‘stiff’, then oscillatory profiles can arise near to the interface, in a way somewhat analogous to the profile of a fluid at a hard planar wall. These oscillations are determined by the stiff interface, rather than the location of the FW line. However, a second, slightly different consideration is the *asymptotic* decay of the density profiles, which is determined by the leading order pole in the structure factor, and in this case the location of the FW line determines whether the decay is oscillatory or monotonic, i.e. no matter how stiff the interface is, if one is on the monotonic side of the FW line, the ultimate asymptotic decay of the density profiles will

⁴A.J. Masters (private communication) has made such a modification and used this to investigate the interfacial profiles of a binary mixture of particles interacting via repulsive parabolic potentials. He finds the modification does reduce the amplitude of the oscillations.

be monotonic.

All approximate DFT treatments omit the effects of capillary-wave fluctuations of the interface [7]. Incorporating the latter usually requires some ad-hoc prescription. The standard procedure is to assume that DFT furnishes the ‘bare’ or ‘intrinsic’ profiles – which might be oscillatory, as in the present case, and that fluctuations can be unfrozen on these. At the simplest level one performs a Gaussian smearing of the profiles over the interfacial thermal roughness ξ_{\perp} . If the profile has an oscillatory tail with the form of Eq. (5.3.5) one finds the wavelength $2\pi/\alpha_1$ and decay length $\tilde{\alpha}_0^{-1}$ are unaltered but the amplitude is reduced by a factor $\exp[-(\alpha_1^2 - \tilde{\alpha}_0^2)\xi_{\perp}^2/2]$ [52, 61]. As we have seen, α_1 is an intrinsic property of the bulk fluid and is approximately π/R_{11} or π/R_{22} . The roughness ξ_{\perp} depends on the interfacial area L_x^2 and on the external potential, e.g. gravity, that might be present at a real planar interface. If we ignore the latter $\xi_{\perp}^2 = (2\pi\beta\gamma)^{-1} \ln(K_{max}/K_{min})$ where K_{max} and K_{min} are the upper and lower cut-off wavenumbers for the capillary wave fluctuations [7]. We may take $K_{min} = 2\pi/L_x$ and $K_{max} = 2\pi/\xi$ where $\xi \equiv \tilde{\alpha}_0^{-1}$ is the bulk correlation length. It follows that the amplitude of the oscillations in the density profile should be reduced by a factor $(L_x/\xi)^{-\omega[(\alpha_1/\tilde{\alpha}_0)^2-1]}$ where $\omega \equiv (4\pi\beta\gamma\xi^2)^{-1}$ (see Eq. (3.7.10)) is the standard dimensionless parameter which measures the strength of capillary wave fluctuations. Clearly the larger the value of ω , i.e. the smaller the surface tension γ , the more damped are the oscillations. What is significant about this formula is that the amplitude is predicted to have a power-law dependence on the interfacial area L_x^2 . This prediction has been examined by Toxvaerd and Stecki [62] (see also [59]) in molecular dynamics simulations of a liquid-liquid interface. Their model is an equi-molar binary mixture in which the 11 and 22 interatomic potentials are identical, both are (truncated) Lennard-Jones, whereas the 12 potential is purely repulsive. Thus their model mixture resembles the symmetric case in our present study. For small L_x the density profiles reported in [62] exhibit oscillations similar to those in Fig. 5.7. The oscillations appear to be insensitive to the length of the simulation box (perpendicular to the interface) but their amplitude depends on the area L_x^2 of the box. Increasing L_x reduces the amplitude in a manner that is consistent with power law decay [62] lending support to the picture of ‘Gaussian unfreezing’ of fluctuations on an intrinsic profile that is oscillatory.

It is important to consider the various length scales in the problem. For the mixture in Ref. [62] we expect $\xi \sim \sigma$, the Lennard-Jones diameter, and $\alpha_1 \sim 2\pi/\sigma$ for states well-removed from the critical point where pronounced oscillations are observed. σ would

be a few Å if we were modeling an atomic mixture. In our present GCM we have in mind polymers where the radius of gyration R_{11} is, of course, much longer. Nevertheless, it is evident that the absolute length scales cancel out in the combinations $(\alpha_1/\tilde{\alpha}_0)^2 - 1$ and ω . Thus one might expect similar power-laws for the damping of oscillations with interfacial area. Detailed estimates depend on the precise values of the reduced tension γ^* , $\tilde{\alpha}_0$ and α_1 . As an illustration we consider the symmetric case of the GCM with total bulk density $\rho R_{11}^3 = 14$ where the oscillations are fairly well pronounced – see Fig. 5.7. At coexistence we find $\alpha_1 R_{11} = 4.69$, $\tilde{\alpha}_0 R_{11} = 1.34$ and the reduced surface tension $\gamma^* = 17.1$ which implies $\omega = 8.37 \times 10^{-3}$ and $(\alpha_1/\tilde{\alpha}_0)^2 - 1 = 11.3$. Thus the exponent in the power-law is -0.1 , implying that the amplitude of the oscillations is only weakly damped by the capillary wave fluctuations. If we repeat the calculation for the interface simulated by Toxvaerd and Stecki [62], using their values $\tilde{\alpha}_0\sigma = 0.28$, $\alpha_1\sigma = 6.98$ and $\gamma^* \equiv \beta\gamma\sigma^2 = 2.7$ we find a much stronger damping: the exponent is -1.4 . For the liquid-vapour interface of a simple one-component fluid near its triple point the corresponding exponent is usually estimated to be about -3 . In other words our present binary GCM exhibits a particularly ‘stiff’ interface for those states where the the oscillations in the mean-field treatment are pronounced. Of course, these states are far from the critical point and correspond to very high total densities and very high surface tensions. One does not normally observe such a situation at the liquid-vapour interface of the one-component fluid since the triple point (solid phase) intervenes. (Note that the liquid-metal model mentioned earlier [58, 59, 60], is constructed so that the triple point is far removed from the critical point, allowing for high liquid-gas surface tensions). There should be no solid phases in the relevant high-density region of the phase diagram of the binary GCM. This suggests that computer simulations of the fluid-fluid interface might be very revealing⁵.

⁵We note that A.J. Masters and P.B. Warren (private communication) have performed dissipative particle dynamics (DPD) simulations of a model binary mixture of particles interacting via repulsive parabolic potentials. They find oscillatory density profiles. An earlier DPD simulation study, Ref. [63], describes the model and the technique and examines the validity of mean-field theory for the pure fluid and the mixture, see also Ref. [64].

Chapter 6

Wetting in the Binary Gaussian Core Model

Using a simple mean-field density functional approach we investigate the adsorption of a binary fluid mixture of repulsive Gaussian core particles at a repulsive planar wall. For certain choices of wall-fluid potential we find a first-order wetting transition, and the accompanying pre-wetting line, whereby the fluid phase rich in the larger species completely wets the interface between the wall and the fluid phase rich in the smaller species. We show that in the complete wetting regime the film thickness diverges as $l \sim -l_0 \ln(x - x_{coex.})$, where $(x - x_{coex.})$ is the deviation in concentration x of the smaller species from the bulk binodal, for all the (short ranged) wall potentials we have considered but the amplitude l_0 depends on the precise details of these potentials.

6.1 Introduction

This chapter is concerned with the adsorption at a purely repulsive planar wall of the binary mixture of Gaussian particles, treated within the same (RPA) density functional approximation that was used in Ch. 5 for the planar free interface. We shall build upon the ideas introduced in Ch. 3, in our (Landau theory) analysis of wetting transitions for simple one-component fluids. For one-component fluids we find that a suitable order parameter in the description of wetting transitions is the adsorbed film thickness l . For binary fluids, one could derive a Landau free energy of the form (3.1.2), where the order parameter $\phi(\mathbf{r})$ is in this case the concentration of one of the components in the binary

fluid. Thus we could expect the (Landau theory) analysis of Ch. 3 to apply also for the wetting behaviour of binary fluids. This is indeed what we find in the present DFT theory for wetting in the binary GCM, and we analyze our results in terms of effective interface potentials such as Eq. (3.6.5), generalised for the description of a binary fluid. We show that for certain choices of wall-fluid potentials, a first-order wetting transition occurs from partial to complete wetting of the interface between the wall and the fluid phase rich in species 2 by the fluid phase rich in species 1. The transition is induced by decreasing the total density ρ of the bulk mixture. Within the complete wetting regime the thickness of the wetting film diverges logarithmically with $[x - x_{coex.}]$ (which plays the role of $\delta\mu$ in Eq. (3.6.5)), where x denotes the concentration of species 2 and $x_{coex.}$ its value at bulk coexistence, for all the (short-ranged) wall-fluid potentials that we investigate. However, the length scale associated with the film growth depends sensitively on the details of these potentials. We also find a critical wetting transition when the decay-length of the wall-fluid potential is particularly short.

6.2 The model mixture and choice of wall-fluid potentials

Recall from Ch. 5 that the GCM binary mixture is specified by the pair potentials between particle species i and j . These are given by the Gaussian form

$$v_{ij}(r) = \epsilon_{ij} \exp(-r^2/R_{ij}^2) \quad (6.2.1)$$

where $\epsilon_{ij} > 0$ denotes the energy and R_{ij} , which is approximately the radius of gyration of the polymer, determines the range of the ij interaction; $1 \leq i, j \leq 2$. We employ a simple mean field form for the intrinsic Helmholtz free energy functional, $\mathcal{F}[\{\rho_i\}]$, of the inhomogeneous mixture, Eq. (5.2.2). As described in Ch. 5, the functional defined by Eq. (5.2.2) generates the random phase approximation for the pair direct correlation functions: $c_{ij}^{(2)}(\mathbf{r}_1, \mathbf{r}_2) = c_{ij}^{(2)}(|\mathbf{r}_1 - \mathbf{r}_2|) = -\beta v_{ij}(|\mathbf{r}_1 - \mathbf{r}_2|)$, for all inhomogeneities. In the present study we work with the grand potential functional

$$\Omega_V[\{\rho_i\}] = \mathcal{F}[\{\rho_i\}] - \sum_i \int d\mathbf{r} [\mu_i - V_i(\mathbf{r})] \rho_i(\mathbf{r}) \quad (6.2.2)$$

where $V_i(\mathbf{r})$, $i = 1, 2$, is the external potential acting on species i and μ_i is the chemical potential of that species. An obvious choice of wall-fluid potential is a Gaussian wall with

a form analogous to (6.2.1):

$$\beta V_i(z) = \begin{cases} \infty & z \leq 0 \\ A_i \exp[-(z/R_{ii})^2] & z > 0, \end{cases} \quad (6.2.3)$$

where z is the distance from the wall and $A_i > 0$ is an amplitude and we investigated the wetting behaviour of such a model system. Recall that complete wetting by a liquid in a typical one-component fluid may occur at an attractive wall when the bulk gas phase is close to coexistence. Then a film of the liquid phase is adsorbed at the wall whose thickness diverges on approaching coexistence [11]¹. For the GCM binary fluid we sought wetting at the wall by one of the demixed fluid phases. More specifically, the bulk fluid phase was chosen to be that rich in species 2, the smaller particle, (see Fig. 6.1) and we sought complete wetting by the fluid phase rich in species 1 by calculating the density profiles $\rho_i(z)$ and adsorption

$$\Gamma_i = \int_0^\infty dz(\rho_i(z) - \rho_i^b), \quad (6.2.4)$$

where $\rho_i^b = \rho_i(\infty)$ is the bulk density of species i , on paths corresponding to decreasing x towards x_{coex} . (the bulk binodal point) at fixed total density ρ . The profiles are obtained by minimizing the functional (6.2.2). With the wall potential given by (6.2.3) and amplitude ratios A_2/A_1 which are not far removed from unity one does not find a transition to complete wetting. However, if one chooses the wall potentials to be of the same Gaussian form, but now with the same decay length λ for both species:

$$\beta V_i(z) = \begin{cases} \infty & z \leq 0 \\ A_i \exp[-(z/\lambda)^2] & z > 0, \end{cases} \quad (6.2.5)$$

one does find a transition to complete wetting. By making the decay length of the wall-fluid potential the same for both species one has set the decay length measured on the scale of the smaller of the two species of particles to be longer ranged. The result is an effective attraction between the wall and the larger of the two species which ensures that the smaller species of particles is depleted more strongly from the wall than is the larger. This is in spite of the fact that all the intrinsic particle-particle and wall-particle potentials are repulsive. (Note that although the potentials of Eq. (6.2.3) also generate an

¹A first-order wetting transition and the accompanying pre-wetting were first obtained by J.W. Cahn [65] and by C. Ebner and W.F. Saam [66]

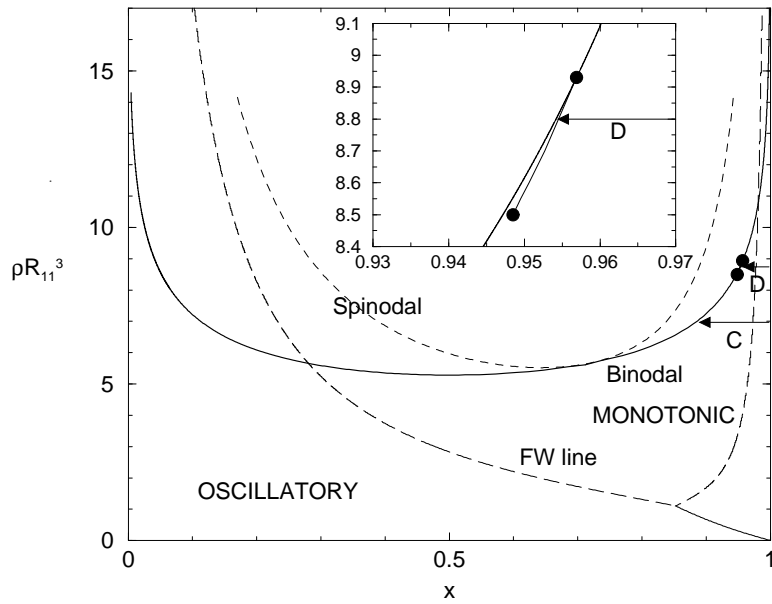


Figure 6.1: The phase diagram for a mixture of Gaussian particles, equivalent to a mixture of two polymers with length ratio 2:1 – i.e. the same as Fig. 5.1. ρ is the total density and x is the concentration of the smaller species 2. The inset shows a magnification of the pre-wetting line, meeting the binodal (solid line) tangentially at the wetting point, for a wall potential given by Eq. (6.2.7) with $\lambda/R_{11} = 1$. The lower point denotes the pre-wetting critical point. The path in the phase diagram marked C is at fixed $\rho R_{11}^3 = 7.0$ along which the density profiles in Fig. 6.3 are calculated. The path marked D is at fixed $\rho R_{11}^3 = 8.8$ along which the profiles in Fig. 6.2 are calculated. This path intersects the pre-wetting line.

effective attraction this appears to be insufficiently strong to drive the transition). As a consequence of this attraction one finds that if the bulk fluid is a phase poor in the larger species, but is near to phase separation, then a wetting film of the coexisting phase, rich in the larger particles, may grow on the wall provided ρ is sufficiently low. Complete wetting is not limited to this particular form of the wall potential. For example, an exponentially decaying wall potential of the form

$$\beta V_i(z) = \begin{cases} \infty & z \leq 0 \\ A_i \exp[-z/\lambda] & z > 0, \end{cases} \quad (6.2.6)$$

also yields complete wetting. The effective attraction has the same origin as for Eq. (6.2.5).

The studies of Louis *et al.* [19, 39] have considered a wall-fluid potential of the form $\beta V(z) = \exp(-z/R)/(z/R)$ for the one component Gaussian core fluid. This form was motivated by the effective wall potentials obtained from inverting Monte Carlo simulation density profiles of self avoiding walk polymers at a hard wall, i.e. the density profile of the Gaussian core fluid at a wall potential of the form $\beta V(z) = \exp(-z/R)/(z/R)$ mimics the polymer center of mass profile at a hard-wall. The obvious generalization to the two component fluid is to set $\beta V_i(z) = \exp(-z/R_{ii})/(z/R_{ii})$. With this choice of wall potential one does not observe complete wetting; the situation is the same as for the Gaussian wall potential of Eq. (6.2.3). Not surprisingly, if one chooses the wall potentials to be of the same form but with both having the same decay length λ :

$$\beta V_i(z) = \begin{cases} \infty & z \leq 0 \\ A_i \exp[-z/\lambda]/[z/\lambda] & z > 0 \end{cases} \quad (6.2.7)$$

with $A_i \propto R_{ii}$, then one observes complete wetting for sufficiently low ρ , approaching the bulk critical (consolute) point. For those models where complete wetting occurs, one finds that as one moves up the binodal, away from the critical point, there is a ‘wetting point’, above which partial wetting occurs; one finds a thin layer, at most two particle diameters thick, adsorbed at the wall. The location of the wetting point on the binodal is dependent on the details of the wall potential. As the transition is (usually) first-order there is a pre-wetting line descending to lower ρ from the wetting point. This line is a tangent to the binodal at the wetting point, and ends in a critical point away from the binodal, see the inset to Fig. 6.1. The pre-wetting line is a line of a first order surface phase transitions [11]. For a path in the phase diagram intersecting the pre-wetting line, the film thickness grows very slowly until the pre-wetting transition where there is a jump in the film thickness. Inside the pre-wetting line the wetting film thickness increases and finally diverges at the binodal. For a path which lies below the pre-wetting critical point, the film thickness increases continuously; there is no jump.

6.3 Results of calculations

6.3.1 First-order wetting transition

We illustrate the wetting characteristics for a particular choice of the parameters specifying the binary GCM and for a given choice of the parameters specifying the wall potential

(6.2.7). We chose the pair potential parameters $\epsilon_{11} = \epsilon_{22} = 2k_B T$, $\epsilon_{12}/\epsilon_{11} = 0.944$, $R_{22}/R_{11} = 0.665$ and $R_{12}/R_{11} = 0.849$, which is equivalent to a mixture of two polymers with length ratio 2:1 – i.e. corresponding to the phase diagram in Fig. 5.1, some of which is reproduced in Fig. 6.1. This binary mixture demixes at sufficiently high total densities, $\rho = \rho_1 + \rho_2$, with a lower critical point at $(x_c, \rho_c R_{11}^3) = (0.70, 5.6)$ (see Fig. 6.1), where x is the concentration of species 2, the smaller particles. Fig. 6.1 is a typical binary GCM phase diagram. We have marked on it the wetting point and the pre-wetting line calculated for the wall potential given by Eq. (6.2.7), with $\lambda/R_{11} = 1$, and amplitudes $A_1 = 1$ and $A_2 = R_{22}/R_{11} = 0.665$. The wetting point is at $(x, \rho R_{11}^3) = (0.957, 8.93)$. Descending from the wetting point is the pre-wetting line ending in a critical point at $(x, \rho R_{11}^3) = (0.949, 8.50)$. This line is very short (in ρ) and lies very close to the binodal. The wetting point and the pre-wetting line are determined by analysing the density profiles and the adsorption Γ_1 ; the latter exhibits a discontinuous jump at the pre-wetting transition.

Fig. 6.2 displays some typical density profiles for states approaching the binodal, along path D in Fig. 6.1, at a constant bulk density $\rho R_{11}^3 = 8.8$ intersecting the pre-wetting line and Fig. 6.3 displays some typical density profiles for states along path C in Fig. 6.1, at a constant bulk density $\rho R_{11}^3 = 7.0$. Since this lower density lies below that of the pre-wetting critical point, the wetting film grows continuously as x is decreased towards $x_{coex.}$. In Fig. 6.4A Γ_1 , the adsorption of species 1, corresponding to the density profiles in Fig. 6.3, is plotted against the logarithm of the deviation $|x - x_{coex.}|$, from coexistence. In the limit $x \rightarrow x_{coex.}^+$, Γ_1 as defined by Eq. (6.2.4), is proportional to the thickness l of the wetting film, i.e. $\Gamma_1 \sim l(\rho_1^{b,A} - \rho_1^{b,B})$, where $\rho_1^{b,A}$ is the bulk coexisting density of species 1 in phase A, rich in species 1 and $\rho_1^{b,B}$ is the same quantity in phase B, poor in species 1. Γ_1 , and therefore l , increase linearly with $-\ln(x - x_{coex.})$.

In Fig. 6.4B Γ_1 is plotted along the constant density path $\rho R_{11}^3 = 8.8$ (path D in Fig. 6.1), corresponding to the density profiles in Fig. 6.2, which intersects the pre-wetting line. The jump in Γ_1 occurs at the intersection with the pre-wetting line. As $x \rightarrow x_{coex.}^+$, Γ_1 and l diverge logarithmically.

These results, along with those for several other choices of potential parameters, point to a classic first-order wetting scenario equivalent to that described in Ch. 3, see Fig. 3.4. Reducing ρ corresponds to increasing T and $(x - x_{coex.})$ plays the role of $\delta\mu$. The general trend is: the larger the range λ in Eq. (6.2.7), the further is the wetting point from the consolute point. Reducing λ shifts the wetting point towards the consolute point

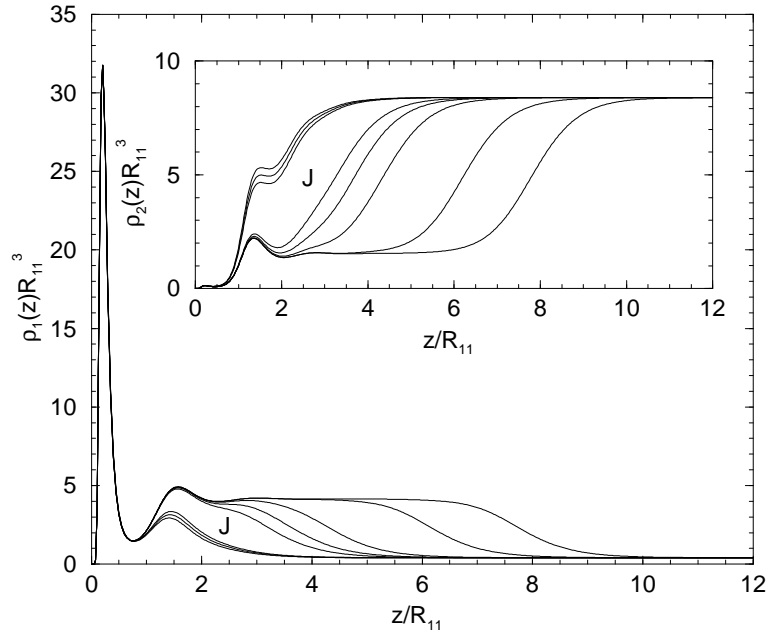


Figure 6.2: The density profiles of species 1, the larger particles, adsorbed at a wall with external potential given by Eq. (6.2.7) with $\lambda/R_{11} = 1$, calculated along a path of constant total density, $\rho R_{11}^3 = 8.8$, i.e. path D in Fig. 6.1 (from left to right the profiles refer to $x = 0.955, 0.9547, 0.9546, 0.9545, 0.9544, 0.9543, 0.9542$ and 0.95419 , where x is the concentration of species 2. $x_{coex.} = 0.95418431$). The thickness of the adsorbed film increases slowly as x decreases until the pre-wetting transition, when there is a jump between $x = 0.9546$ and 0.9545 , (marked J) in the profile, and then the thickness of the adsorbed film increases continuously as $x \rightarrow x_{coex.}^+$, indicating complete wetting. The inset shows the density profiles of species 2 for the same values of x .

and for sufficiently small values there can be a crossover to a critical wetting transition. For example, when $\lambda/R_{11} = 0.125$, and amplitudes $A_1 = 1$ and $A_2 = R_{22}/R_{11} = 0.665$, the wetting point moves well below that for $\lambda/R_{11} = 1.0$, to $(x, \rho R_{11}^3) = (0.88, 6.9)$ and there is no indication of a pre-wetting transition. The adsorption Γ_1 appears to diverge continuously (as $-\ln(\rho - \rho_w)$, where ρ_w is the value of the total density at the wetting transition) as we reduce ρ along the binodal. Further work is required to determine how crossover to critical wetting depends on λ and whether other choices of wall-fluid potential will also lead to critical wetting. Note that crossover to critical wetting with decreasing (exponential) wall decay length was observed in a generalization of the Sullivan [67, 68]

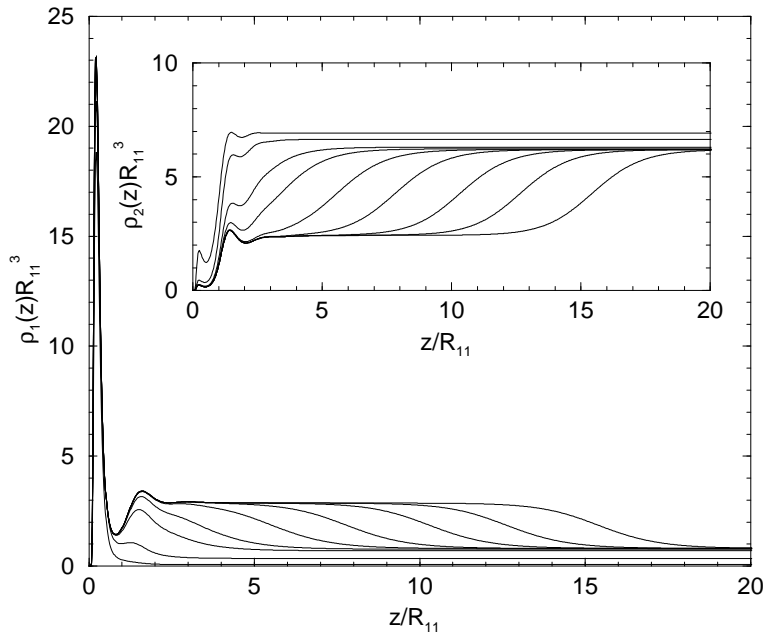


Figure 6.3: The density profiles of species 1, the larger particles, adsorbed at a wall with external potential given by Eq. (6.2.7) with $\lambda/R_{11} = 1$, calculated along a path of constant total density, $\rho R_{11}^3 = 7.0$, i.e. path C in Fig. 6.1 (from left to right the profiles refer to $x = 0.99, 0.95, 0.9, 0.89, 0.886, 0.8855, 0.885446, 0.885442$ and 0.8854416 , where x is the concentration of species 2. $x_{coex.} = 0.885441572$). The thickness of the adsorbed film increases continuously as $x \rightarrow x_{coex.}^+$, indicating complete wetting. The inset shows the density profiles of species 2 for the same values of x . Note that species 2 is depleted from the region adjoining the wall.

model for a one-component fluid with Yukawa fluid-fluid attraction [69, 15].

6.3.2 Thickness of the wetting film

In this subsection we focus on the details of how the thickness l of the wetting film diverges for different choices of wall-fluid potentials. Recall from Ch. 3 that in the mean-field description, as is used in the present study, of wetting for a typical one-component fluid whose interparticle potential is short-ranged (potential with finite support, Yukawa, exponential or faster decay) l diverges as $-l_0 \ln \delta\mu$, where $\delta\mu = (\mu_{coex.} - \mu)$ is the difference in chemical potential from bulk coexistence, provided the wall-fluid potential is also short ranged [11]. The prefactor l_0 , i.e. the length scale determining the logarithmic growth, depends in a

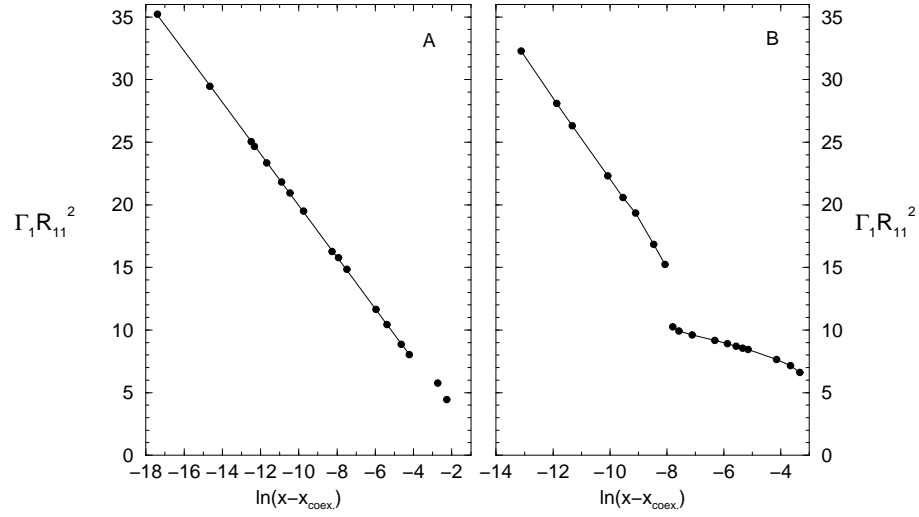


Figure 6.4: Plots of the adsorption of species 1, Γ_1 , at a wall with external potential given by Eq. (6.2.7) with $\lambda/R_{11} = 1$, along two paths of constant total density as a function of the logarithm of the deviation from bulk coexistence, $\ln(x - x_{coex.})$. Fig. A refers to the path $\rho R_{11}^3 = 7.0$, labeled C in Fig. 6.1, corresponding to the density profiles in Fig. 6.3, which lies below the pre-wetting critical point. Fig. B refers to the path $\rho R_{11}^3 = 8.8$, labeled D in Fig. 6.1, corresponding to the density profiles in Fig. 6.2, which intersects the pre-wetting line. The jump in Γ_1 occurs at the intersection. On approaching the binodal Γ_1 increases linearly with $-\ln(x - x_{coex.})$ in both A and B.

subtle way on the relative ranges of the wall-fluid and fluid-fluid interparticle potentials. If the former decays exponentially with distance from the wall one must compare the decay length with ξ_w , the bulk correlation length of the (liquid) phase which is wetting [11, 15]. The amplitude l_0 will be determined by which length is longer. On the other hand, for Gaussian wall-fluid attraction or for a wall-fluid potential with finite support, one expects the only relevant length scale to be ξ_w . How does this phenomenology carry over to the present situation of the binary GCM near a wall?

We begin by noting that for all models where we find complete wetting the calculated adsorption Γ_1 and film thickness l diverge as $-\ln(x - x_{coex.})$. For the case of Gaussian wall-fluid potentials, Eq. (6.2.5), we find that regardless of the wall decay length λ , $l \sim -\xi_w \ln(x - x_{coex.})$, i.e. the amplitude is ξ_w , the bulk correlation length in phase A, rich in species 1, which is wetting the wall-phase B interface. It is important to define the bulk correlation length ξ of a binary mixture. This is the exponential decay length describing

the (common) asymptotic decay of the three partial pairwise total correlation functions $h_{ij}(r)$. ξ can be obtained from the poles of the Fourier transform of $h_{ij}(r)$ [52] (see the description of the calculation of poles in the GCM in Ch. 5.4). All three $\hat{h}_{ij}(q)$ have the same set of poles: $q_n = \pm\alpha_1 + i\alpha_0$. It is the pole with the smallest imaginary part α_0 that dominates the decay of $h_{ij}(r)$ as $r \rightarrow \infty$ and it is this pole that determines the bulk correlation length: $\xi = 1/\alpha_0$. For the path labeled C in Fig. 6.1, the coexisting (wetting) phase A is at $(x, \rho R_{11}^3) = (0.458, 5.30)$ for which $\xi_w/R_{11} = 0.905$.

A different scenario occurs for a wall potential of the form given by Eq. (6.2.6). Now we find that the wetting film thickness still grows logarithmically as a function of $(x - x_{coex.})$, but the amplitude l_0 is no longer necessarily the bulk correlation length of the wetting phase, ξ_w . Rather we find that $l \sim -l_0 \ln(x - x_{coex.})$ where l_0 depends on λ , the wall potential decay length. When $\lambda < \xi_w$, $l_0 = \xi_w$, but when $\lambda > \xi_w$, $l_0 = \lambda$. The variation of l_0 with λ for both types of wall is shown in Fig. 6.5.

These results can be accounted for by considering the following expression for the surface excess grand potential per unit area (or effective interface potential) of a GCM subject to a wall potential whose decay is exponential, Eq. (6.2.6):

$$\omega_{ex}(l; x) = l[\omega^{b,A} - \omega^{b,B}] + \gamma_{w,A} + \gamma_{A,B} + ae^{-l/\xi_w} + be^{-l/\lambda} + \mathcal{O}(e^{-2l/\xi_w}, e^{-2l/\lambda}), \quad (6.3.1)$$

which is Eq. (3.6.5) suitably generalised for a binary fluid. $\gamma_{w,A}$ is the surface tensions of the wall-phase A interface, $\gamma_{A,B}$ that of the free A-B interface and a and b are coefficients that depend on ρ [11, 15]. Eq. (6.3.1) is valid for a complete wetting situation; minimisation of ω_{ex} with respect to l yields the equilibrium film thickness l for a given undersaturation $(x - x_{coex.})$ ². $\omega^{b,B}$ is the grand potential per unit volume in bulk phase B at given chemical potentials μ_1 and μ_2 , while $\omega^{b,A}$ is the corresponding quantity in phase A at the same chemical potentials. To lowest order in the chemical potential deviations:

$$[\omega^{b,A} - \omega^{b,B}] \simeq (\rho_1^{b,A} - \rho_1^{b,B})\delta\mu_1 + (\rho_2^{b,A} - \rho_2^{b,B})\delta\mu_2 \quad (6.3.2)$$

where, as previously, $\rho_i^{b,A}$ denotes the bulk coexisting density of species i in phase A etc. Since $\delta\mu_i \equiv (\mu_i - \mu_{i,coex.}) \propto (x - x_{coex.})$, to lowest order, it follows that the first term on

²Note that Eq. (6.3.1) is appropriate for fluid states where the wetting phase (A) at bulk coexistence lies on the monotonic side of the FW line. This is the case for path C in Fig. 6.1. If the wetting phase lies on the oscillatory side of the FW line the term in $\exp(-l/\xi_w)$ should be multiplied by a factor of $\cos(\alpha_1 l + \phi)$, where α_1 is the real part of the dominating pole and ϕ is a phase factor – see Ref. [70]

the right hand side of Eq. (6.3.1) is proportional to $(x - x_{coex.})$. If $\lambda < \xi_w$, the term in $\exp(-l/\xi_w)$ dominates and minimisation yields $l \sim -\xi_w \ln(x - x_{coex.})$ whereas if $\lambda > \xi_w$, the other exponential dominates and $l \sim -\lambda \ln(x - x_{coex.})$. When the wall potential is a Gaussian, Eq. (6.2.5), the term in $\exp(-l/\lambda)$ is absent from ω_{ex} and minimisation yields $l \sim -\xi_w \ln(x - x_{coex.})$ for all λ .

Eq. (6.3.1) is not appropriate to the wall potential given by Eq. (6.2.7), i.e. the damped exponential. Although l diverges logarithmically for all choices of λ and $l_0 = \xi_w$ for $\lambda < \xi_w$ ³, when $\lambda > \xi_w$, l_0 is equal to neither ξ_w nor λ , but is a monotonically increasing function of λ , see Fig. 6.5. For $\lambda/R_{11} \gtrsim 5$, l_0 increases linearly with λ but with the slope < 1 . This implies that the relevant term in Eq. (6.3.1) is not of the form $b \exp(-l/\lambda)$. Rather it should be $b' \exp(-l/\lambda')$, where the length $\lambda' \simeq 0.7\lambda$. Whether such a form for $\omega_{ex}(l; x)$ can be derived by the methods of Ref. [15] starting from the full binary mixture density functional, Eq. (5.2.2), remains to be seen.

6.4 Concluding remarks

We have shown that the binary GCM subject to purely repulsive, short-ranged, wall-fluid potentials can exhibit a first order wetting transition, with the accompanying pre-wetting, similar to that found in systems where the fluid-fluid and wall-fluid potentials are explicitly attractive. Our results illustrate the ubiquity of wetting transitions and related interfacial phenomena. The wetting transition in the present case is driven by an effective attraction between the wall and the larger species of Gaussian core particle, which arises from the fact that the wall potential is longer ranged on the scale of the smaller particles than on the scale of the larger, leading to strong depletion at the wall of the smaller species. Generating sufficient effective attraction between the wall and one of the particle species for a wetting transition to be observed is not only achieved by setting the wall decay length to be the same in both wall potentials. One could achieve sufficient effective attraction between the wall and species 1 by setting the amplitude, A_2 (see Eqs. (6.2.5) – (6.2.7)), of the potential acting on the smaller species 2 to be much larger than A_1 . We also showed that the precise form of the decay of the wall potential determines the amplitude l_0 of the thickness, l , of a wetting film. For an exponentially decaying wall-fluid potential with decay length λ , Eq. (6.2.6), l_0 is determined by the larger of ξ_w , the bulk correlation length

³We do not include very small values of λ where the wetting point might lie below $\rho R_{11}^3 = 7.0$.

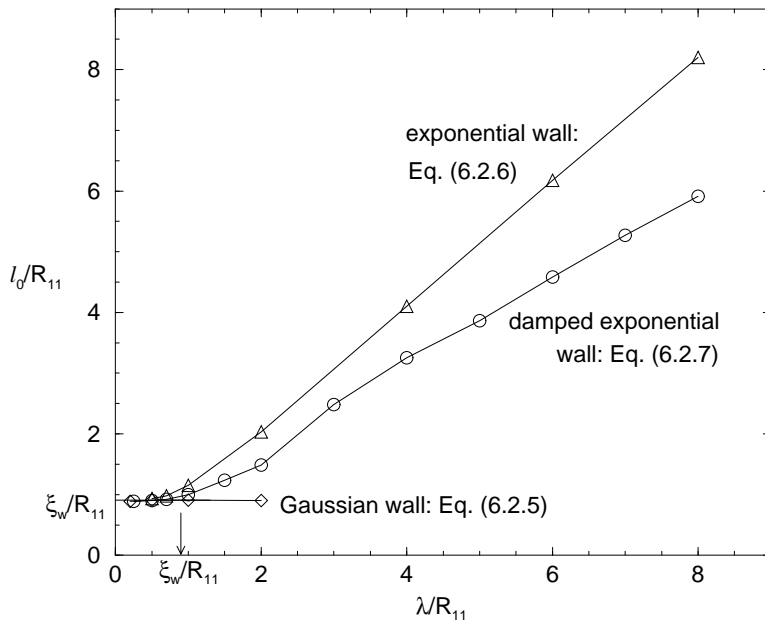


Figure 6.5: The pre-factor l_0 of the wetting film thickness ($l \sim -l_0 \ln(x - x_{coex.})$) versus the wall potential decay length λ . In all cases the density profiles were calculated along the constant density path $\rho R_{11}^3 = 7.0$ (path C in Fig. 6.1). For the Gaussian wall (\diamond) $l_0 = \xi_w$, the bulk correlation length of the wetting phase, independent of λ . For the exponential wall (Δ) $l_0 = \xi_w$ for $\lambda < \xi_w$ and $l_0 = \lambda$ for $\lambda > \xi_w$. For the wall potential $\beta V_i(z) = A_i \exp(-z/\lambda)/(z/\lambda)$, $z > 0$, (\circ) $l_0 = \xi_w$ for $\lambda < \xi_w$ but has a complex variation for $\lambda > \xi_w$. The results for the three choices of potential do not appear to depend on the amplitudes A_i .

in the wetting phase, and λ , i.e. the effective interface potential Eq. (6.3.1) provides an accurate description of the relevant length scales. However, for a wall potential of the form (6.2.7), a new length scale may enter which is neither ξ_w nor λ .

Our results are based upon what is arguably the simplest density functional theory, namely the mean-field functional (5.2.2), that one might contemplate for any binary fluid mixture. That such a simple theory should predict such rich wetting behaviour is pleasing, but we should inquire how our results might be changed by utilizing more sophisticated functionals. The study of Louis *et al.* [39] indicated that for a one-component GCM near a repulsive wall of the type (6.2.7), the mean-field functional yields density profiles close to those from a functional which generates the HNC closure of the wall-particle Ornstein-Zernike equation. (Recall that for the bulk structure of the one-component GCM, the

HNC closure gives results almost indistinguishable from simulation data [39]). For the binary GCM there are, as yet, no simulation or theoretical results against which we can test those of the present functional. However, for high total density situations we expect the random phase approximation and the functional (5.2.2) to be reliable for this soft core fluid. We speculate that the location of the wetting point might depend sensitively on the details of the free energy functional but that the gross features of the interfacial phase behaviour should be captured by the simplest treatment.

The theory we have presented is strictly mean-field; capillary-wave fluctuations are omitted in this as well as in other, more refined, density functional approaches to wetting. There is a rich phenomenology associated with these, in particular for systems with short-ranged forces [11, 15, 18]. It would be of some interest to examine fluctuation effects in the present model of a binary mixture, especially for those choices of parameters where a critical wetting transition occurs ⁴.

Finally we note that in recent studies of a model colloid-polymer mixture at a hard wall, Brader *et al.* [50, 51, 71] found layering transitions at points on the binodal, above the wetting transition point. Although the binary GCM exhibits oscillatory density profiles at the free fluid-fluid interface (see Ch. 5), similar to those found in Refs. [50, 51, 71], we do not find any layering transitions in the present model, i.e. the transition from partial to complete wetting is not accompanied by the pre-cursor layering. Layering transitions are associated with many body terms in the effective one-component Hamiltonian for the colloids [50, 51, 71]. Analogous terms are not expected in the present case.

⁴As we noted in Ch. 3.7, in treatments based on an effective interface potential, it is the dimensionless parameter $\omega = (4\pi\beta\gamma_{A,B}\xi_w^2)^{-1}$, where $\gamma_{A,B}$ is the surface tension, which determines the strength of fluctuation effects. For critical wetting transitions even the exponents depend on ω [11, 18]. For the present model it might be possible to vary ω over a large range by tuning the parameters of the potentials.

Chapter 7

Solvent Mediated Interactions and Solvation Close to Fluid-Fluid Phase Separation

We apply a general density functional approach for calculating the force between two big particles immersed in a solvent of smaller ones to calculate the solvent mediated (SM) potential between two big Gaussian core particles in a binary mixture of smaller Gaussian particles, a simple model of polymers in solution. Within a simple mean field free energy functional, which generates the random phase approximation (RPA) for the bulk pair direct correlation functions, the binary solvent exhibits fluid-fluid phase separation and we show that the theory for calculating the SM potential captures effects of thick adsorbed films surrounding the big solute particles. For a single big particle there is a first order thin-thick adsorbed film transition and in the thick film regime, i.e. for solvent state points lying close to the binodal, on the side where the solvent is poor in the species which is favoured by the big particles, we find extremely attractive, long ranged SM potentials between the big particles whose range is determined by the film thickness. For state points away from the binodal in the thin film regime or above the ‘wetting point’ the SM potentials are short ranged and less attractive. We show that the effects of the thick adsorbed films around the big particles are not included when the SM potential is obtained from the big-big radial distribution function $g_{bb}(r)$, calculated using the RPA closure to the Ornstein-Zernike equations. In the region of the solvent critical point we also find extremely attractive SM potentials whose range is now set by the bulk correlation length in the binary solvent and

which increases and eventually diverges for state points approaching the critical point. We calculate the excess chemical potential of the big solute particle in the binary solvent as a function of the concentration of one of the smaller species and show that this quantity also reflects the formation of thick adsorbed films. The form of the excess chemical potential and, hence, the solvation for the soft Gaussian core fluid is contrasted with that expected for a hard core solute.

7.1 Introduction

Effective interactions between big particles immersed in a solvent of other (smaller) particles play a key role in liquid state physics. For multicomponent fluids of different sized particles it is often useful to describe the fluid by an effective Hamiltonian, often a sum of effective pair potentials between the big particles, having integrated out the degrees of freedom of the small particles [72]. This approach is particularly useful in the case of colloidal systems, where the colloidal component is usually dilute and its size is very much larger than that of the particles constituting the solvent. The DLVO potential for charge stabilized systems [73], the hard-sphere potential for sterically stabilized systems [22] and the depletion potential for mixtures of colloids and non-adsorbing polymers [74] and for asymmetric binary mixtures of hard spheres [3] are well-known examples of effective potentials. In general the form of the effective solvent mediated (SM) potential between two big particles will depend on the nature of the solvent and the details of the solvent-particle interaction. However the range of the SM potential should be determined by the range of correlations in the solvent of small particles. If the solvent is composed of (small) particles interacting via short-ranged forces (potentials that are of finite range or that decay exponentially, or faster, with interparticle separation) bulk pairwise correlations decay exponentially with a correlation length that is of order the size of the solvent particle, provided the solvent is not in a near critical state. Thus, for any thermodynamic state that is well removed from solvent fluid-fluid phase coexistence we expect to find short-ranged SM potentials.

In this chapter we examine the situation which arises when two big particles are immersed in a solvent that is close to fluid-fluid (liquid-gas or liquid-liquid) phase separation. Here we expect correlations in the solvent to take on a different character which should be reflected in the form of the SM potential. There are two distinct mechanisms to be

considered. First, critical fluctuations of the solvent, associated with a diverging correlation length, will give rise to long-ranged forces between plates or big particles [75, 76]. Such ‘critical Casimir forces’ are expected to induce flocculation of colloidal particles suspended in near-critical solvents. For a mesoscopic, field-theoretic description of these critical Casimir forces see Refs. [77, 78, 79, 80, 81]. The second mechanism for generating long ranged SM potentials is that associated with the growth of thick adsorbed ‘wetting’ films around sufficiently big particles. If one of the solvent phases (species) is preferentially adsorbed on the surface of the big particles, then on approaching the binodal from the phase which is not preferentially adsorbed, a thick adsorbed layer can grow around the big particles. At a planar surface, where complete wetting can occur, the thickness of the wetting film can eventually diverge (become macroscopic) as the bulk binodal is approached and we have seen examples of this in the last chapter. In the case of big particles, thick adsorbed films will develop but, because of the finite radius of curvature, the adsorbed films will remain of finite thickness even at bulk coexistence [11]. The presence of such ‘wetting’ films should induce long-ranged attractive forces between the big particles which could also be relevant for flocculation in colloidal systems. Indeed aggregation of colloids in a binary mixture of 2,6-lutidine and water has been observed experimentally by Beysens and co-workers, reviewed in [82] (see also [83, 84, 85, 86]), and by Maher and co-workers [87, 88, 89], for state points of the solvent which are near to phase separation. Although there is still much debate about the interpretation of these experiments and the precise roles played by ‘wetting’ films, critical fluctuations and by screening effects in the case of charged colloidal particles [90, 91], it is accepted that adsorbed films have an important influence on the behaviour of these systems. In charged systems the adsorbed layer is supposed to be responsible for screening the surface charge on the colloids [90, 91].

There have been several attempts to develop theories of ‘wetting’ induced SM interactions. Much of this work is motivated by the experimental studies of flocculation phenomena and is summarised in Ref. [92]. A Ginzburg-Landau description [93], an interface potential approach [94, 95] and an interface displacement approach based on a sharp-kink description of the solvent density distribution [92] have been employed. The latter two approaches suggest that ‘wetting’ films adsorbed around the big particles can result in bridging transitions of the adsorbed phase between the two big particles, a phenomenon closely related to capillary condensation, and this could result in the flocculation of the big particles. Note that bridging is observed in computer simulations of a two di-

mensional, microscopic model of lipid-protein interactions [96] and the effective attraction between the big particles resulting from such bridging has been discussed in some detail [97, 98]. Although well-suited to very big particles where very thick films can develop, and to systems where dispersion forces dominate, the approach of Ref. [92], which inputs an idealized density distribution for the solvent particles, is less well-suited to situations where the size of the solute particles is not vastly bigger than those of the solvent particles, so that the adsorbed films are thinner, and where dispersion forces do not dominate.

There are, of course, many microscopic theories based upon integral equation approaches for calculating SM potentials. For general asymmetric solute-solvent mixtures Amokrane and co-workers [99] have investigated various closure approximations, including those which input bridge functions from density functional theory. The SM potential $W_{bb}(r)$ is obtained from the relation $g_{bb}(r) = \exp[-\beta(v_{bb}(r) + W_{bb}(r))]$, where $g_{bb}(r)$ is the big-big radial distribution function in the limit of infinite dilution of the big particles. $v_{bb}(r)$ is the direct (bare) potential between the pair of (big) solute particles and $\beta = (k_B T)^{-1}$. Integral equation approaches are successful for solvent thermodynamic states well away from phase separation, but as we shall argue later, theories based upon the Ornstein-Zernike (OZ) equations do not usually include the effects of thick adsorbed films and therefore cannot describe properly the SM potential for states near bulk coexistence.

Our present approach is based on a general microscopic method, using density functional theory (DFT). It implements the procedure for including correlation effects in the solvent developed in the calculation of depletion potentials for hard-sphere mixtures [4, 48, 3]. The theory makes no assumption about the form of the density distributions so, in principle, it should apply for all (fluid) states, including those close to the critical point where a sharp-kink approximation is inappropriate. The procedure is as follows: We first fix one big particle at the origin and then calculate the equilibrium density profile(s) of the solvent particles in the external potential due to the big one, i.e. we incorporate the presence of the ‘wetting’ film if we are near coexistence (or the long range decay of the density profile(s) if we are near the critical point). We then obtain the SM potential by inserting a second big particle using the potential distribution theorem [3, 100, 101, 102]. This second step requires a density functional that can describe *reliably* a mixture of the solvent and big particles in the limit of vanishing density of big particles [3]. It is not easy to construct suitable functionals but there has been progress. For example, the Rosenfeld

functional [103] for additive hard sphere mixtures was used successfully to calculate depletion potentials for both additive [3] and non-additive [48] cases, over a wide range of size ratios. However, in additive hard-sphere mixtures fluid-fluid demixing does not occur [23].

Here we investigate SM potentials using the simple RPA functional, that has been used throughout this thesis for a mixture of soft core repulsive Gaussian particles, which we believe is also capable of treating mixtures with large size asymmetries. The RPA is surprisingly accurate for the GCM when the fluid density is sufficiently high. We introduced the one-component Gaussian core model (GCM) in Ch. 4. Since the GCM pair potential is purely repulsive the one component fluid does not separate into two fluid phases. However, a binary mixture of two different sized GCM particles, treated using the mean-field DFT which generates the RPA for the mixture, does separate into two fluid phases (see Ch. 5) and exhibits wetting transitions (see Ch. 6) for certain, purely repulsive, planar walls. Our strategy is to treat, by DFT, a ternary GCM mixture in which the density of the biggest (repulsive) Gaussian particles $\rho_b^0 \rightarrow 0$. This allows us to study the effects of solvent critical fluctuations and of thick adsorbed films on the SM potentials between two of the biggest particles in terms of a particularly simple model.

This chapter is arranged as follows: In Sec. 7.2 we describe the DFT procedure used to calculate the effective solvent mediated potentials and the RPA functional. Sec. 7.3 describes numerical results and some approximate analytical results for the density profile and SM potential between two big Gaussian particles immersed in a single component fluid of smaller GCM particles. We also investigate solvation by calculating μ_b^{ex} , the excess chemical potential of a single big particle in this solvent by two different routes, thereby testing the consistency of the functional. In Sec. 7.4 we present the results for the SM potential between two big GCM particles immersed in a binary fluid of smaller GCM particles. We perform the calculations at state points approaching the binodal, in order to determine the effect of thick adsorbed films on the SM potential. The SM potential becomes long ranged, the length scale being set by the thickness of the adsorbed film rather than the sizes of the solvent particles, and strongly attractive. This is in spite of all the direct particle interactions being repulsive. For certain state points we observe thin-thick transitions of the adsorbed film and these result in discontinuities (jumps) in the SM potential and in the derivative of μ_b^{ex} as a function of the concentration of the smaller species. Thick adsorbed films have a significant effect on the nature of the solvation. In

Sec. 7.4.5 we calculate the SM potential along a thermodynamic path which approaches the critical point. Here we find long ranged attractive SM potentials associated with the long correlation length in the solvent. Sec. 7.5 discusses the pros and cons of the test particle and OZ routes to the calculation of $g_{bb}(r)$ and, hence, of the SM potential. We show that the former route is equivalent to the DFT procedure we employ in earlier sections and that the OZ route, which uses the RPA direct pair correlation functions $c_{ij}^{(2)}(r) = -\beta v_{ij}(r)$, where $v_{ij}(r)$ is the pair potential between species i and j , does not incorporate the effects of thick adsorbed films and yields, therefore, much less attractive SM potentials. We also discuss the overall consistency of the test particle route by considering the radial distribution functions $g_{ij}(r)$ in a ternary mixture. Finally in Sec. 7.6 we make some concluding remarks and discuss the consequences of our results.

7.2 Theory of the solvent mediated potential

7.2.1 General formalism

We follow the presentation in Ref. [3] and consider a multicomponent fluid mixture in the grand ensemble, where i labels the different species, each with chemical potential μ_i . The potential distribution theorem [100, 101, 102] relates the partition function $\Xi(\mathbf{r}_b; \{\mu_i\}; T)$ after a particle of species b has been inserted into the fluid at \mathbf{r}_b , to the partition function $\tilde{\Xi}(\{\mu_i\}; T)$, the external potential $V_b(\mathbf{r})$ and the one body density profile $\rho_b(\mathbf{r})$ of species b before insertion:

$$\Xi(\mathbf{r}_b; \{\mu_i\}; T) = \exp[\beta V_b(\mathbf{r}_b) - \beta \mu_b] \Lambda_b^3 \rho_b(\mathbf{r}_b) \tilde{\Xi}(\{\mu_i\}; T), \quad (7.2.1)$$

where Λ_b is the thermal de Broglie wavelength of species b and $\beta = (k_B T)^{-1}$. We are particularly interested in the case where subscript b labels the big particle species (although Eq. (7.2.1) applies for all species) and where the external potential $V_b(\mathbf{r})$ is that due to another big particle, species a , i.e. the case where $V_b(\mathbf{r}) = v_{ab}(\mathbf{r})$, the a - b pair potential. Then $\rho_b(\mathbf{r})$ is the density profile of species b due to a particle of species a treated as an external potential. However, $V_b(\mathbf{r})$ could be the external potential arising from any fixed object, such as a wall [3]. Combining Eq. (7.2.1) with a well known result from DFT [7, 3]

$$\Lambda_b^3 \rho_b(\mathbf{r}) = \exp[\beta \mu_b - \beta V_b(\mathbf{r}) + c_b^{(1)}(\mathbf{r}; \{\mu_i\})], \quad (7.2.2)$$

which is the multi-component generalization of Eq. (2.3.13), we can express the one-body direct correlation function $c_b^{(1)}(\mathbf{r}; \{\mu_i\})$ of species b as

$$\begin{aligned} c_b^{(1)}(\mathbf{r}; \{\mu_i\}) &= \ln \left(\frac{\Xi(\mathbf{r}_b; \{\mu_i\}; T)}{\tilde{\Xi}(\{\mu_i\}; T)} \right) \\ &= \beta\tilde{\Omega}(\{\mu_i\}; T) - \beta\Omega(\mathbf{r}_b; \{\mu_i\}; T). \end{aligned} \quad (7.2.3)$$

i.e. $-\beta c_b^{(1)}(\mathbf{r}; \{\mu_i\})$ is the change in grand potential Ω due to inserting a particle of species b into the fluid at \mathbf{r}_b , subject to an external potential $V_b(\mathbf{r}) = v_{ab}(\mathbf{r})$ exerted by a particle of species a . From this result we can determine the quantity $\tilde{W}_{ab}(\mathbf{r}_b)$ (without loss of generality we set $\mathbf{r}_a = 0$), which is the difference in the grand potential of the fluid between the situation where the test particle (species b) is near the fixed particle (species a) and when it is deep in the bulk, $\mathbf{r}_b \rightarrow \infty$:

$$\begin{aligned} \beta\tilde{W}_{ab}(\mathbf{r}_b) &= \beta\Omega(\mathbf{r}_b; \{\mu_i\}; T) - \beta\Omega(\mathbf{r}_b \rightarrow \infty; \{\mu_i\}; T) \\ &= c_b^{(1)}(\mathbf{r}_b \rightarrow \infty; \{\mu_i\}) - c_b^{(1)}(\mathbf{r}_b; \{\mu_i\}). \end{aligned} \quad (7.2.4)$$

If we evaluate $\tilde{W}_{ab}(\mathbf{r}_b)$ in the low density limit of species b , $\rho_b^0 \rightarrow 0$ (i.e. $\mu_b \rightarrow -\infty$), where we have only a single particle of species b , then $\tilde{W}_{ab}(\mathbf{r}_b)$ is the SM potential $W_{ab}(\mathbf{r}_b)$ between the particle b and the fixed object (particle) a [3, 23]:

$$\begin{aligned} \beta W_{ab}(\mathbf{r}) &= \lim_{\mu_b \rightarrow -\infty} \tilde{W}_{ab}(\mathbf{r}) \\ &= c_b^{(1)}(\mathbf{r} \rightarrow \infty; \{\mu_{i \neq b}\}; \mu_b \rightarrow -\infty) - c_b^{(1)}(\mathbf{r}; \{\mu_{i \neq b}\}; \mu_b \rightarrow -\infty). \end{aligned} \quad (7.2.5)$$

As emphasized in Ref. [3], only the density profiles of the species $i \neq b$ around the fixed particle a enter into (7.2.5). This simplifies greatly the calculation of the SM potential since the density profiles $\{\rho_{i \neq b}(\mathbf{r})\}$ have the symmetry of the potentials arising from the fixed particle a . If the latter are spherically symmetrical, i.e. $v_{ai}(\mathbf{r}) \equiv v_{ai}(r)$, $i \neq b$, then so are the the density profiles $\rho_i(r)$ which enter into the calculation of $c_b^{(1)}(\mathbf{r})$.

7.2.2 Application of the RPA functional

In order to calculate the SM potential from (7.2.5) we use DFT methods to obtain $c_b^{(1)}(\mathbf{r})$ [3]. Here we employ a particularly simple, approximate mean field Helmholtz free energy functional, which is surprisingly accurate for the GCM. The functional is the RPA functional which we used in chapters 5 and 6 to calculate inhomogeneous density profiles for

planar interfaces in a binary GCM fluid:

$$\mathcal{F}[\{\rho_i\}] = \mathcal{F}_{id}[\{\rho_i\}] + \frac{1}{2} \sum_{ij} \int d\mathbf{r} \int d\mathbf{r}' \rho_i(\mathbf{r}) \rho_j(\mathbf{r}') v_{ij}(|\mathbf{r} - \mathbf{r}'|), \quad (7.2.6)$$

where $\rho_i(\mathbf{r})$ is the one body density profile of species i and $v_{ij}(\mathbf{r})$ is the pair potential between particles of species i and j (both i and j run over all the species). The ideal gas part of the free energy functional is

$$\mathcal{F}_{id}[\{\rho_i\}] = \frac{1}{\beta} \sum_i \int d\mathbf{r} \rho_i(\mathbf{r}) [\ln(\Lambda_i^3 \rho_i(\mathbf{r})) - 1], \quad (7.2.7)$$

where Λ_i is the thermal de Broglie wavelength of species i . In density functional theory the one body direct correlation function is given by the generalization of Eq. (2.3.14):

$$c_b^{(1)}(\mathbf{r}) = -\beta \frac{\delta(\mathcal{F}[\{\rho_i\}] - \mathcal{F}_{id}[\{\rho_i\}])}{\delta \rho_b(\mathbf{r})} \quad (7.2.8)$$

which for the functional (7.2.6) gives:

$$c_b^{(1)}(\mathbf{r}) = - \sum_i \int d\mathbf{r}' \rho_i(\mathbf{r}') \beta v_{bi}(|\mathbf{r} - \mathbf{r}'|). \quad (7.2.9)$$

Taking the limit $\rho_b^0 \rightarrow 0$ in (7.2.9) and substituting into (7.2.5) gives the following result for the SM potential:

$$\beta W_{ab}(\mathbf{r}) = \sum_{\nu} \int d\mathbf{r}' (\rho_{\nu}(\mathbf{r}') - \rho_{\nu}^0) \beta v_{b\nu}(|\mathbf{r} - \mathbf{r}'|). \quad (7.2.10)$$

Here ρ_{ν}^0 refers to the bulk density of species ν , where ν denotes all the small species, $\nu \neq b$. The density profiles $\rho_{\nu}(\mathbf{r})$ entering into (7.2.10) are those calculated around a single particle of species a , fixed at the origin and exerting an external potential on species ν . We calculate these density profiles for the external potentials $V_{\nu}(\mathbf{r}) = v_{a\nu}(r)$ by minimizing the grand potential functional

$$\Omega_V[\{\rho_{\nu}\}] = \mathcal{F}[\{\rho_{\nu}\}] - \sum_{\nu} \int d\mathbf{r} \rho_{\nu}(\mathbf{r}) [\mu_{\nu} - V_{\nu}(\mathbf{r})], \quad (7.2.11)$$

using (7.2.6) for the Helmholtz free energy functional. The effective potential between two *identical* big particles is then the sum of the bare interaction $v_{bb}(r)$ and the SM potential:

$$v_{bb}^{eff}(r) = v_{bb}(r) + W_{bb}(r). \quad (7.2.12)$$

Recall that the Helmholtz free energy functional (7.2.6) is that which generates the RPA for the pair direct correlation functions since

$$\begin{aligned} c_{ij}^{(2)}(\mathbf{r}, \mathbf{r}') &= -\beta \frac{\delta^2(\mathcal{F}[\{\rho_i\}] - \mathcal{F}_{id}[\{\rho_i\}])}{\delta\rho_i(\mathbf{r})\delta\rho_j(\mathbf{r}')} \\ &= c_{ij}^{(2)}(|\mathbf{r} - \mathbf{r}'|) = -\beta v_{ij}(|\mathbf{r} - \mathbf{r}'|). \end{aligned} \quad (7.2.13)$$

The RPA accounts well for bulk pair correlations at high densities.

7.3 Results for a one-component solvent

In this section we determine the SM potential $W_{bb}(r)$ between a pair of big particles (b), immersed in a single component solvent of small particles ($\nu = s$). This involves calculating first $\rho_s(\mathbf{r})$, the density profile of the small particles around a single big particle, i.e. we minimize the functional (7.2.11) which, using (7.2.6), yields the Euler-Lagrange equation

$$\mu_s = V_s(\mathbf{r}) + \beta^{-1} \ln \Lambda_s^3 \rho_s(\mathbf{r}) + \int d\mathbf{r}' \rho_s(\mathbf{r}') v_{ss}(|\mathbf{r} - \mathbf{r}'|), \quad (7.3.1)$$

where $V_s(\mathbf{r}) = v_{bs}(r)$. Substituting for the chemical potential μ_s in terms of ρ_s^0 , the bulk density of species s , we obtain

$$0 = -\beta V_s(\mathbf{r}) - \ln \left(\frac{\rho(\mathbf{r})}{\rho_s^0} \right) + \int d\mathbf{r}' (\rho_s^0 - \rho_s(\mathbf{r}')) \beta v_{ss}(|\mathbf{r} - \mathbf{r}'|) \quad (7.3.2)$$

for the equilibrium inhomogeneous density profile. We discuss solutions of this equation before describing results for $W_{bb}(r)$, obtained by substituting $\rho_s(\mathbf{r})$ into Eq. (7.2.10).

7.3.1 Solvent radial distribution function by test-particle route

In this subsection we consider the situation where the external potential is that due to a small particle s identical to the small particles in the fluid around it, i.e. $V_s(\mathbf{r}) = v_{ss}(\mathbf{r}) = v_{ss}(r)$. In this situation the solution to Eq. (7.3.2) is $\rho_s(r) = \rho_s^0 g(r)$ where $g(r)$ is the bulk radial distribution function of the pure fluid of species s . Introducing the total correlation function $h(r) = g(r) - 1$, Eq. (7.3.2) can be expressed as:

$$h(r) = -\beta v_{ss}(r) + h(r) - \ln(1 + h(r)) - \rho_s^0 \int d\mathbf{r}' h(\mathbf{r}') \beta v_{ss}(|\mathbf{r} - \mathbf{r}'|). \quad (7.3.3)$$

We compare this to the bulk Ornstein-Zernike (OZ) equation, Eq. (2.2.1):

$$h(r) = c^{(2)}(r) + \rho_s^0 \int d\mathbf{r}' h(\mathbf{r}') c^{(2)}(|\mathbf{r} - \mathbf{r}'|), \quad (7.3.4)$$

and note that omitting the second and third terms on the right hand side, Eq. (7.3.3) reduces to the OZ equation with the RPA (7.2.13) for the pair direct correlation function. Recall also that the HNC closure, Eq. (2.2.3), is given by [1]:

$$c_{\text{HNC}}^{(2)}(r) = -\beta v_{ss}(r) + h(r) - \ln(1 + h(r)), \quad (7.3.5)$$

and it follows that Eq. (7.3.3) has the form of the OZ equation (7.3.4) with the HNC closure for the pair direct correlation function outside the integral and the RPA closure inside the integral. When Eq. (7.3.3) is solved self-consistently then the resulting $h(r)$ will be neither that resulting from the HNC closure nor that from the RPA. As noted in Ch. 4, Lang *et al.* [37] and Louis *et al.* [19] have shown that the HNC approximation is quasi-exact for a GCM fluid, where the particles interact with a pair potential given by

$$v_{ss}(r) = \epsilon_{ss} \exp(-r^2/R_{ss}^2). \quad (7.3.6)$$

Since we are interested in the regime where Eq. (7.3.6) models the interaction between the centers of mass of polymer chains, we set $\epsilon_{ss} = 2k_B T$ and the length scale R_{ss} equal to the radius of gyration. In this case the HNC closure to the OZ equation for $h(r)$ reproduces the Monte-Carlo results very accurately [19, 37]. Furthermore, the RPA, $c_{\text{RPA}}^{(2)}(r) = -\beta v_{ss}(r)$, becomes increasingly accurate at sufficiently high densities, $\rho_s^0 R_{ss}^3 \gtrsim 5$ – see Fig. 4.2. On solving Eq. (7.3.3) at these densities we find that the resulting $h(r)$ resembles closely that from the HNC closure (7.3.5). Motivated by this observation, we expect solutions to Eq. (7.3.2) with a larger sized Gaussian particle as the test particle to be rather accurate.

7.3.2 Density profile of small GCM particles around a single big GCM particle

We now set the external potential $V_s(\mathbf{r})$ in Eq. (7.3.2) to be that due to a big GCM particle, located at the origin, exerting an external potential:

$$V_s(r) = v_{bs}(r) = \epsilon_{bs} \exp(-r^2/R_{bs}^2) \quad (7.3.7)$$

and we use the following mixing rule for the particle sizes:

$$R_{bs}^2 = \frac{1}{2}(R_{ss}^2 + R_{bb}^2). \quad (7.3.8)$$

This non-additive mixing rule was discussed in Ch. 5 and is what drives the fluid-fluid phase separation in binary mixtures; as remarked earlier, it is based partly on experience

from computer simulation studies of effective pair potentials in dilute solutions of polymers [30]. The quantity $\beta\epsilon_{bs} \equiv \epsilon_{bs}^* > 0$ sets the energy scale. $\epsilon_{bs} \simeq 2k_B T$ for polymers of similar size, but decreases from this value as the size asymmetry between the polymers increases, reflecting the fact that there is a lower energy penalty for a small polymer coil to sit inside the coils of a larger polymer.

Having specified the external potential we can solve Eq. (7.3.2) numerically to determine the equilibrium density profile of the small GCM particles in the presence of a single big GCM particle. This is plotted in Fig. 7.1 for the set of parameters: $R_{bb}/R_{11} = 7.0$, $R_{ss}/R_{11} = 0.665$, $\epsilon_{bs}^* = 0.8$, $\epsilon_{ss}^* = 2.0$, $\epsilon_{bb}^* = 2.0$ (the value of ϵ_{bb}^* is not actually used in the calculation of the SM potential), and $\rho_s^0 R_{11}^3 = 7.0$, which using (7.3.8), gives $R_{bs}/R_{11} = 4.97$. (R_{11} can be thought of as the length scale in the problem. It is actually the size of a different species of small particles that will be introduced in Sec. 7.4). Before commenting on the form of the density profile, we describe an approximate analytical solution to Eq. (7.3.2) for a sufficiently big test particle.

A first approximation to the inhomogeneous density profile, ignoring the interaction term in Eq. (7.3.2), is:

$$\rho_s(r) \simeq \rho_s^0 \exp[-\beta v_{bs}(r)] \simeq \rho_s^0 [1 - \beta v_{bs}(r)], \quad (7.3.9)$$

where we assumed the term in the exponential is small. This is, of course, not necessarily the case but it motivates the following ansatz for the small particle density profile:

$$\rho_s(r) = \rho_s^0 - \rho^* \exp(-r^2/R_{bs}^2), \quad (7.3.10)$$

where ρ^* is to be determined. If we assume the density profile is of this form and then substitute it back into Eq. (7.3.2) and perform the Gaussian integrals we find:

$$\rho_s(r) = \rho_s^0 \exp \left[-\epsilon_{bs}^* \exp(-r^2/R_{bs}^2) + \pi^{3/2} \epsilon_{ss}^* R_{ss}^3 \rho^* \exp \left(\frac{-r^2}{R_{bs}^2 + R_{ss}^2} \right) \right] \quad (7.3.11)$$

where

$$\frac{1}{R^2} = \frac{1}{R_{ss}^2} + \frac{1}{R_{bs}^2}. \quad (7.3.12)$$

When $R_{bb} \sim R_{bs} \gg R_{ss}$ then $R \simeq R_{ss}$, and expanding in Eq. (7.3.11) to $\mathcal{O}(R_{ss}/R_{bs})^2$, we obtain:

$$\rho_s(r) \simeq \rho_s^0 \exp \left[-(\epsilon_{bs}^* - \pi^{3/2} \epsilon_{ss}^* R_{ss}^3 \rho^*) \exp(-r^2/R_{bs}^2) \right]. \quad (7.3.13)$$

Provided $(\epsilon_{bs}^* - \pi^{3/2}\epsilon_{ss}^*R_{ss}^3\rho^*)$ is small then

$$\rho_s(r) \simeq \rho_s^0 \left[1 - (\epsilon_{bs}^* - \pi^{3/2}\epsilon_{ss}^*R_{ss}^3\rho^*) \exp(-r^2/R_{bs}^2) \right], \quad (7.3.14)$$

which is of the same form as Eq. (7.3.10), with $\rho^* = (\epsilon_{bs}^* - \pi^{3/2}\epsilon_{ss}^*R_{ss}^3\rho^*)\rho_s^0$. This result can be rewritten as

$$\rho^* = \frac{\rho_s^0 \epsilon_{bs}^*}{1 + \beta \hat{v}_{ss}^0 \rho_s^0} \quad (7.3.15)$$

where

$$\hat{v}_{ij}^0 = \hat{v}_{ij}(0) = \int d\mathbf{r} v_{ij}(r) = \pi^{3/2} \epsilon_{ij} R_{ij}^3, \quad (7.3.16)$$

is the zeroth Fourier coefficient of the pair potential. Inputting the same pair potential parameters and bulk density $\rho_s^0 R_{11}^3 = 7.0$ as used earlier, Eq. (7.3.15) gives $\rho^* R_{11}^3 = 0.234$. The approximate density profile, Eq. (7.3.10), with this value for ρ^* is plotted (dashed line) alongside the full solution to Eq. (7.3.2) (solid line) in Fig. 7.1. The value for ρ^* calculated from Eq. (7.3.15) is much smaller than the non interacting (ideal gas) result $\rho_s^0 \epsilon_{bs}^*$ that would result if Eq. (7.3.9) were the correct solution, i.e. correlations in the fluid have a significant effect. Note that Eq. (7.3.10) is an approximate solution, but it is correct up to terms of order $\mathcal{O}(R_{ss}/R_{bs})^2$, and provided the fixed particle is sufficiently big, Eq. (7.3.10) is a good approximation to the full solution, becoming increasingly accurate as $R_{ss}/R_{bs} \rightarrow 0$. Strikingly, for intermediate values of R_{ss}/R_{bs} it is a very good approximation, as can be seen in Fig. 7.1.

However, this simple ansatz, Eq. (7.3.10), for the density profile does not describe the correct asymptotic decay behaviour $r \rightarrow \infty$, of the small particle density profile. We know that within the RPA for the one-component GCM, the ultimate asymptotic decay into bulk of the radial distribution function, $g_{ss}(r)$ is always exponentially damped oscillatory for a pure fluid of GCM particles – see Sec. 5.4. It follows from general considerations that the density profile $\rho_s(r)$ around the big fixed particle should also be exponentially damped oscillatory as $r \rightarrow \infty$ [49, 52]. Thus we expect

$$(\rho_s(r) - \rho_s^0) \sim \frac{A}{r} \exp(-\alpha_0 r) \cos(\alpha_1 r - \theta), \quad r \rightarrow \infty \quad (7.3.17)$$

where the decay length α_0^{-1} and the wavelength $2\pi/\alpha_1$ are the same as those characterizing the decay of $g_{ss}(r)$, while A is an amplitude and θ is a phase factor which depend on $v_{bs}(r)$. It turns out that because the external potential due to the big test particle is slowly varying on the scale of the small particles, the amplitude, A , of the damped oscillatory

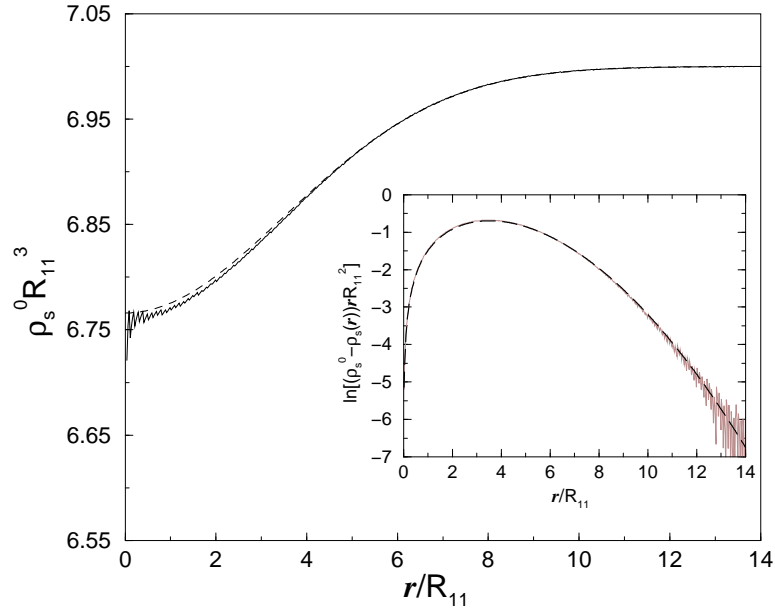


Figure 7.1: The density profile of small GCM particles, radius $R_{ss}/R_{11} = 0.665$, around a single big GCM particle located at the origin with radius $R_{bb}/R_{11} = 7.0$ ($R_{bs}/R_{11} = 4.97$, $\epsilon_{bs}^* = 0.8$ and $\epsilon_{ss}^* = \epsilon_{bb}^* = 2.0$) for a bulk density $\rho_s^0 R_{11}^3 = 7.0$. The solid line is the full numerical solution to Eq. (7.3.2) and the dashed line is the approximate analytical solution, Eq. (7.3.10). In the inset we plot the same data but now $\ln([\rho_s^0 - \rho_s(r)]rR_{11}^2)$ is plotted versus r/R_{11} so that any oscillations in the density profile would show clearly. None can be seen; numerical noise sets in for $r/R_{11} \geq 12$. Moreover there is no straight line tail, which would be indicative of an exponentially decaying tail in the density profile. Rather the decay is effectively Gaussian because the amplitude of the exponentially damped oscillatory decay term is extremely small – see text.

contribution is very small. Indeed it is impossible to detect the contribution (7.3.17) in numerical results and Eq. (7.3.10) remains a good approximation to the density profile even at large separations r .

Although there is no general theory for obtaining A and θ via the test particle route we can estimate the amplitude A using the OZ equation. (A more detailed account of these methods can be found in Ch. 5 and Refs. [49, 52]). The Fourier transformed (FT) OZ equation for the total pair correlation function $h_{bs}(r) = g_{bs}(r) - 1 = (\rho_s(r) - \rho_s^0)/\rho_s^0$,

in a binary fluid of big and small GCM particles is (see Eqs. (5.4.1) – (5.4.3))

$$\hat{h}_{bs}(q) = \frac{\hat{c}_{bs}(q)}{D(q)}, \quad (7.3.18)$$

where the denominator is given by

$$D(q) = [1 - \rho_b^0 \hat{c}_{bb}(q)][1 - \rho_s^0 \hat{c}_{ss}(q)] - \rho_b^0 \rho_s^0 \hat{c}_{sb}^2(q). \quad (7.3.19)$$

$\hat{c}_{ij}(q)$ is the FT of $c_{ij}^{(2)}(r)$, the pair direct correlation function. In the limit of infinite dilution of the big ones, $\rho_b^0 \rightarrow 0$, $D(q) = [1 - \rho_s^0 \hat{c}_{ss}(q)]$. Inverting the FT in (7.3.18) we obtain

$$\begin{aligned} rh_{bs}(r) &= \frac{1}{4\pi^2 i} \int_{-\infty}^{\infty} dq q \exp(iqr) \hat{h}_{bs}(q) \\ &= \frac{1}{4\pi^2 i} \int_{-\infty}^{\infty} dq q \exp(iqr) \frac{\hat{c}_{bs}(q)}{[1 - \rho_s^0 \hat{c}_{ss}(q)]} \end{aligned} \quad (7.3.20)$$

which can be evaluated by contour integration; the singularities of $\hat{h}_{bs}(q)$ are simple poles. As in Eq. (5.4.6), choosing an infinite radius semi-circle in the upper half of the complex plane, we obtain

$$rh_{bs}(r) = \frac{1}{2\pi} \sum_n R_n^{bs} \exp(iq_n r) \quad (7.3.21)$$

where R_n^{bs} is the residue of $q\hat{c}_{bs}(q)/D(q)$ for the n th pole at $q = q_n$. The q_n are solutions of $D(q_n) = 0$ and there are normally an infinite number of poles – see Ch. 5. For the one component GCM fluid there are no purely imaginary poles within the RPA, so the asymptotic decay is always damped oscillatory.

Calculating the residue of $q\hat{c}_{bs}(q)/[1 - \rho_s^0 \hat{c}_{ss}(q)]$ within the RPA, we find for the n^{th} pole

$$\begin{aligned} R_n^{bs} &= \frac{q_n \hat{c}_{bs}(q_n)}{-\rho_s^0 (-q_n R_{ss}^2/2) \hat{c}_{ss}(q_n)} \\ &= \frac{2\hat{v}_{bs}^0}{\rho_s^0 R_{ss}^2 \hat{v}_{ss}^0} \exp(-q_n^2 (R_{bs}^2 - R_{ss}^2)/4), \end{aligned} \quad (7.3.22)$$

where we have used the RPA result for the pair direct correlation function:

$$\hat{c}_{ij}(q) = -\beta \hat{v}_{ij}^0 \exp(-q^2 R_{ij}^2/4). \quad (7.3.23)$$

The pole with the smallest value of α_0 is the one that gives the leading asymptotic decay of $h_{bs}(r)$. This pole has $\alpha_1 \simeq \pi/R_{ss}$, and $|\alpha_1| > |\alpha_0|$, so $q_n^2 = \alpha_1^2 - \alpha_0^2 + 2i\alpha_1\alpha_0 \simeq \alpha_1^2 + 2i\alpha_1\alpha_0$. When $R_{bs} \gg R_{ss}$, the real part of the exponential factor in (7.3.22) is \simeq

$\exp(-(\pi R_{bs}/2R_{ss})^2)$. Inserting the ratio $R_{bs}/R_{ss} = 7.47$, the value used in the calculation of the density profile in Fig. 7.1, gives a factor $\simeq \exp(-140)$ in the residue and thus in the amplitude of the exponentially damped oscillatory decay term in $h_{bs}(r)$. This implies that the amplitude of the oscillations in $h_{bs}(r)$, obtained from the OZ route, are so small as to be undetectable. The results for the density profile $\rho_s(r)$, obtained from Eq. (7.3.2), are consistent with this observation, as illustrated in the inset to Fig. 7.1, where $\ln([\rho_s^0 - \rho_s(r)]rR_{11}^2)$ is plotted against r . Any oscillations, with a reasonable amplitude, should be readily visible in such a plot but there is no sign of these before numerical noise sets in at very large separations. We conclude that the decay of the density profile of small GCM particles around a single big one is effectively Gaussian and that the approximate density profile, Eq. (7.3.10), captures much of the physics.

7.3.3 The SM potential

Having determined the density profile of the small particles we can now calculate the SM potential between two big particles by inserting this profile into Eq. (7.2.10), with $\nu = s$, denoting the single component solvent of small particles. The SM potential plotted in Fig. 7.2, corresponds to the density profile displayed in Fig. 7.1, i.e. bulk density $\rho_s^0 R_{11}^3 = 7.0$. We can also employ our approximate, analytical density profile, Eq. (7.3.10). On substituting this into Eq. (7.2.10) and performing the Gaussian integrals, we find a simple formula:

$$\beta W_{bb}^{pure}(r) = -(\pi/2)^{3/2} \epsilon_{bs}^* \rho^* R_{bs}^3 \exp(-r^2/2R_{bs}^2), \quad (7.3.24)$$

for the SM potential in a one component solvent of GCM particles. This result is also plotted in Fig. 7.2. Since the approximate density profile, Eq. (7.3.10), captures all of the features of the true density profile (solution to Eq. (7.3.2)) we expect Eq. (7.3.24) to describe accurately the true SM potential. Indeed, as can be seen from Fig. 7.2, Eq. (7.3.24) (dashed line) accounts for the numerically calculated SM potential (solid line) very well for all separations r . The SM potential is strongly attractive ($W_{bb}(r=0) \simeq -45k_B T$ for $\rho_s^0 R_{11}^3 = 7.0$). This large amplitude is associated with the factor $\rho^* R_{bs}^3$ in Eq. (7.3.24); this is roughly the number of small particles expelled from the volume of the big one. In high density states this factor is large and it is this number multiplied by the individual big-small interaction energy, ϵ_{bs} , that determines the overall energy scale of the SM potential. When the small particle bulk density ρ_s^0 is large, ρ^* is only weakly dependent on ρ_s^0 ,

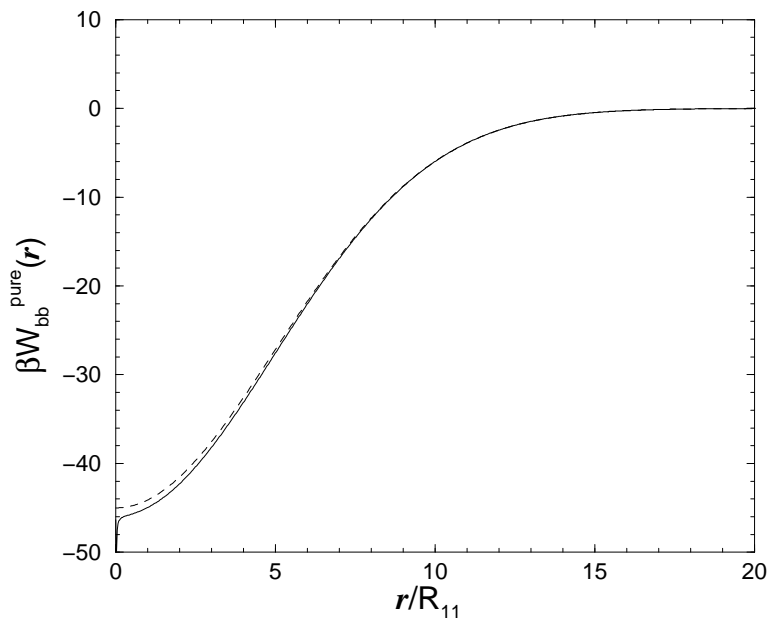


Figure 7.2: The SM potential between two big GCM particles with radius $R_{bb}/R_{11} = 7.0$ in a pure solvent of small GCM particles of radius $R_{ss}/R_{11} = 0.665$ ($R_{bs}/R_{11} = 4.97$, $\epsilon_{bs}^* = 0.8$ and $\epsilon_{ss}^* = \epsilon_{bb}^* = 2.0$) for a bulk density $\rho_s^0 R_{11}^3 = 7.0$. The solid line is the numerical result, Eq. (7.2.10), and the dashed line is the approximate analytical solution, Eq. (7.3.24). Note the vertical scale; the SM potential is strongly attractive – see text.

i.e. $\rho^* \simeq \epsilon_{bs}/\hat{v}_{ss}^0$ (see Eq. (7.3.15)). The strength of the (attractive) SM potential is an indication that the big GCM particles will not be very soluble in the fluid of small GCM particles. We shall return to this issue in Sec. 7.6.

We can also calculate the SM potential between two different sized big Gaussian particles (a and b) immersed in a pure solvent of smaller ones. The resulting SM potential should be symmetric under a - b interchange $W_{ab}^{pure}(r) = W_{ba}^{pure}(r)$. If we employ the approximate analytical result (7.3.10) for the profile the symmetry is respected. We rewrite Eq. (7.3.10), using Eq. (7.3.15), for the case where the fixed big particle is species a :

$$\rho_s(r) - \rho_s^0 = -\frac{\rho^*}{\epsilon_{as}} v_{as}(r) = -\frac{\rho_s^0}{1 + \beta \hat{v}_{ss}^0 \rho_s^0} \beta v_{as}(r). \quad (7.3.25)$$

Substituting in Eq. (7.2.10) it follows that

$$\begin{aligned} \beta W_{ab}^{pure}(r_1) &= \int d\mathbf{r}_2 (\rho_s(\mathbf{r}_2) - \rho_s^0) \beta v_{bs}(|\mathbf{r}_1 - \mathbf{r}_2|) \\ &= \left(-\frac{\rho_s^0}{1 + \beta \hat{v}_{ss}^0 \rho_s^0} \right) \beta \int d\mathbf{r}_2 v_{as}(\mathbf{r}_2) \beta v_{bs}(|\mathbf{r}_1 - \mathbf{r}_2|) \end{aligned} \quad (7.3.26)$$

which is easily shown to be identical to $\beta W_{ba}^{pure}(r_1)$, obtained by calculating the profile around a fixed particle of species b . This symmetry between $W_{ab}(r)$ and $W_{ba}(r)$ also *appears* to be present in a numerical calculation, using the route outlined in Sec. 7.2.2, of the SM potential in a pure solvent. However, when the calculation is extended to that of a binary solvent (i.e. adding a fourth species, of small particles, to the two large species a , b and the small (solvent) species s already present) we find that when the binary solvent is near fluid-fluid phase separation, the symmetry $W_{ab}(r) = W_{ba}(r)$ is *not* respected. This asymmetry becomes evident when there is a significant difference between the sizes of particles a and b and when the solvent phase is very close to the fluid-fluid phase boundary. Moreover we believe that the symmetry is not perfect in other situations, including that where there is a pure solvent, i.e. $W_{ab}^{pure}(r) \neq W_{ba}^{pure}(r)$ although any differences are extremely small. This point is discussed further in Sec. 7.5.

7.3.4 The excess chemical potential of the big particle

A key quantity in the physical chemistry of solutions is the excess chemical potential of the solute. Within DFT there are different routes to this quantity. The consistency test for our approximate Helmholtz free energy functional, Eq. (7.2.6), concerns the excess chemical potential of a single big particle. The potential distribution theorem states that $-\beta^{-1}c_b^{(1)}(\mathbf{r})$ is the excess grand potential for inserting a particle of species b at \mathbf{r} in the inhomogeneous fluid [3, 100]. It follows that $-\beta^{-1}c_b^{(1)}(\infty) = \mu_b^{ex}$, the $\rho_b^0 \rightarrow 0$ limit of the excess chemical potential of the big particles in a homogeneous mixture of big and small particles¹. In this limit, $\rho_b^0 \rightarrow 0$, we set $\rho_s(\mathbf{r}) = \rho_s^0$ (a constant bulk density) in Eq. (7.2.9) and we obtain the simple result:

$$\mu_b^{ex} = -\beta^{-1}c_b^{(1)}(\infty) = \rho_s^0 \int d\mathbf{r} v_{sb}(\mathbf{r}) = \rho_s^0 \hat{v}_{sb}^0. \quad (7.3.27)$$

Of course, the same result is obtained from the free energy of the bulk mixture. The free energy density of the bulk mixture, see Eq. (7.2.6), is

$$f(\{\rho_i^0\}) = f_{id}(\{\rho_i^0\}) + \frac{1}{2} \sum_{ij} \rho_i^0 \rho_j^0 \hat{v}_{ij}^0, \quad (7.3.28)$$

¹Note that $\exp(-\beta\mu_b^{ex}) = \lim_{\rho_b^0 \rightarrow 0} (\rho_b^0/z_b) = h(z_s)$, Henry's law constant, with z_b , the activity of the big particles given by $z_b = \Lambda_b^{-3} \exp(\beta\mu_b)$. $h(z_s)$ provides a measure of the average big-small interaction. See e.g. Ref. [104]

and in the limit $\rho_b^0 \rightarrow 0$, one finds $\mu_b^{ex} = \partial(f - f_{id})/\partial\rho_b^0 = \rho_s^0 \hat{v}_{sb}^0$. We can shed further light on the status of Eq. (7.3.27) by considering the following, formally exact, Kirkwood-Hill formula for μ_b^{ex} in the $\rho_b^0 \rightarrow 0$ limit [100, 104, 105, 106]:

$$\mu_b^{ex} = \int_0^1 d\lambda \int_0^\infty dr 4\pi r^2 \rho_s^0 g_{bs}(r; \lambda) v_{bs}(r), \quad (7.3.29)$$

where λ is a parameter which ‘turns on’ the big-small external potential $v_{bs}(r)$ and $g_{bs}(r; \lambda)$ is the big-small radial distribution function corresponding to the potential $\lambda v_{bs}(r)$, with $0 \leq \lambda \leq 1$, and density ρ_s^0 for the small particles. For hard-core particles (7.3.29) is limited in its usefulness, however for the present soft core GCM, it is illuminating. We see that if we make the simplest approximation: $g_{bs}(r; \lambda) \equiv 1$, for all λ , then the integrand of Eq. (7.3.29) is independent of λ and using Eq. (7.3.16) and Eq. (7.3.29) we find the same result as Eq. (7.3.27). This treatment demonstrates the mean-field nature of the approximation for the bulk free energy of the mixture which is used in deriving Eq. (7.3.27).

The excess chemical potential, μ_b^{ex} , can be calculated by a very different route, thereby testing the functional’s internal consistency. Now we treat the single big GCM particle, centered at the origin, as an external potential acting on the small GCM particles and calculate μ_b^{ex} directly as an excess grand potential:

$$\mu_b^{ex} = \int_0^\infty dr 4\pi r^2 (\omega(r) - \omega(\infty)) \quad (7.3.30)$$

where $\omega(r)$ is the grand potential density and $\omega(\infty) = -P$, the bulk pressure. From Eq. (7.2.11), $\omega(r)$ is given by

$$\omega(r) = f(r) - \rho_s(r)[\mu_s - v_{bs}(r)] \quad (7.3.31)$$

where $\rho_s(r)$ is the density profile of the small GCM particles around the big GCM particle, given by solving Eq. (7.3.2). $f(r)$ is the intrinsic Helmholtz free energy density, which from Eq. (7.2.6) is

$$f(r) = \frac{1}{\beta} \rho_s(r) [\ln(\Lambda_s^3 \rho_s(r)) - 1] + \frac{1}{2} \rho_s(r) \int_0^\infty dr' \rho_s(r') \tilde{v}_{ss}(r, r') \quad (7.3.32)$$

where

$$\begin{aligned} \tilde{v}_{ss}(r, r') &= \frac{2\pi r'}{r} \int_{r-r'}^{r+r'} d\tau \tau v_{ss}(\tau) \\ &= \frac{-\pi \epsilon_{ss} R_{ss}^2 r'}{r} [\exp(-(r+r')^2/R_{ss}^2) - \exp(-(r-r')^2/R_{ss}^2)]. \end{aligned} \quad (7.3.33)$$

The equilibrium density profile $\rho_s(r)$ satisfies Eq. (7.3.2), which can be re-expressed as

$$\mu_s = \frac{1}{\beta} \ln(\Lambda_s^3 \rho_s(r)) + \int_0^\infty dr' \rho_s(r') \tilde{v}_{ss}(r, r') + v_{bs}(r). \quad (7.3.34)$$

Using Eqs. (7.3.32) and (7.3.34) we can write the grand potential density in Eq. (7.3.31) as:

$$\omega(r) = -\frac{1}{\beta} \rho_s(r) - \frac{1}{2} \rho_s(r) \int_0^\infty dr' \rho_s(r') \tilde{v}_{ss}(r, r'). \quad (7.3.35)$$

In the limit of a uniform (bulk) fluid this reduces to

$$\omega(\infty) = -\frac{1}{\beta} \rho_s^0 - \frac{1}{2} (\rho_s^0)^2 \hat{v}_{ss}^0 = -P \quad (7.3.36)$$

where ρ_s^0 is the bulk density. In order to calculate μ_b^{ex} from Eq. (7.3.30), we could insert the density profile $\rho_s(r)$ calculated from the Euler-Lagrange equation (7.3.34) into (7.3.35) and then numerically integrate to obtain μ_b^{ex} . However we can also calculate μ_b^{ex} analytically using the approximate density profile Eq. (7.3.10). We showed that this approximation is correct up to terms of $\mathcal{O}(R_{ss}/R_{bs})^2$. On inserting Eq. (7.3.10) into Eq. (7.3.30), performing the Gaussian integrals and then expanding in powers of (R_{ss}/R_{bs}) we find (see Appendix C):

$$\mu_b^{ex} = \rho_s^0 \hat{v}_{bs}^0 - \frac{\sqrt{2} \hat{v}_{ss}^0 \hat{v}_{bs}^0}{8\epsilon_{bs}} (\rho_s^*)^2 + \mathcal{O}\left(\frac{R_{ss}}{R_{bs}}\right)^2. \quad (7.3.37)$$

The first term in Eq. (7.3.37) is that given by Eq. (7.3.27), the first route to μ_b^{ex} . When $R_{bs} \gg R_{ss}$, the correction terms are very small. Indeed, if one includes the second term in Eq. (7.3.37), then one obtains almost exactly the same result as that from the numerical calculation of μ_b^{ex} , i.e. inputting the density profile calculated numerically from the Euler-Lagrange equation (7.3.2). For example, using the pair potential parameters given in text between Eqs. (7.3.8) and (7.3.9) and a bulk density $\rho_s^0 R_{11}^3 = 7.0$ yields $\beta \rho_s^0 \hat{v}_{bs}^0 = 3833$, whilst the first two terms in Eq. (7.3.37) give $\beta \mu_b^{ex} = 3833 - 22 = 3811$, which should be compared to $\beta \mu_b^{ex} = 3806$ from the full numerical calculation. It is clear that there is a high level of consistency within our functional for the calculation of μ_b^{ex} , provided the bulk density is sufficiently high, $\rho_s^0 R_{ss}^3 \gtrsim 5.0$ and the ratio R_{bb}/R_{ss} is sufficiently large.

We can again use the Kirkwood-Hill formula for μ_b^{ex} , Eq. (7.3.29), to examine the status of Eq. (7.3.37). Inserting $g_{bs}(r; \lambda) = 1 + h_{bs}(r, \lambda)$, where $h_{bs}(r, \lambda)$ is the big-small total pair correlation function, into Eq. (7.3.29) we find

$$\mu_b^{ex} = \rho_s^0 \hat{v}_{sb}^0 + \int_0^1 d\lambda \int_0^\infty dr 4\pi r^2 \rho_s^0 h_{bs}(r; \lambda) v_{bs}(r). \quad (7.3.38)$$

In the $\rho_b \rightarrow 0$ limit, the OZ equation for $h(r; \lambda)$ in Fourier space is (see Eqs. (7.3.18) and (7.3.19)):

$$\hat{h}_{bs}(q; \lambda) = \frac{\hat{c}_{bs}(q; \lambda)}{1 - \rho_s^0 \hat{c}_{ss}(q)}, \quad (7.3.39)$$

where $\hat{c}_{ss}(q)$ refers to the direct correlation function of the pure fluid of species s . Within the RPA closure, $\hat{c}_{bs}(q; \lambda) = -\lambda\beta\hat{v}_{bs}(q)$ and

$$h_{bs}(r; \lambda) = \lambda h_{bs}(r; \lambda = 1). \quad (7.3.40)$$

We can use Eq. (7.3.40) with Eq. (7.3.10) for the density profile corresponding to the external potential (7.3.7), to obtain an approximate form for $h_{bs}(r; \lambda)$, i.e.

$$h_{bs}(r; \lambda) = -\frac{\lambda\rho^*}{\rho_s^0} \exp(-r^2/R_{bs}^2). \quad (7.3.41)$$

When Eq. (7.3.41) is inserted into Eq. (7.3.38) we find, on performing the Gaussian integral,

$$\mu_b^{ex} = \rho_s^0 \hat{v}_{bs}^0 - \frac{\sqrt{2}}{8} \hat{v}_{bs}^0 \rho^*. \quad (7.3.42)$$

From Eq. (7.3.15) we note that when ρ_s^0 is large, then $\rho^* \simeq \epsilon_{bs}/\hat{v}_{ss}^0$. Using this further approximation we find that the second terms on the right hand side of both Eq. (7.3.37) and Eq. (7.3.42) are equal. Indeed, for the bulk density $\rho_s^0 R_{11}^3 = 7.0$ we find that there is only a very small difference between the results of Eq. (7.3.37) and Eq. (7.3.42). The present derivation shows explicitly that the second term in Eq. (7.3.37) is a manifestation of correlation effects in the small particle fluid.

Finally, we note that the form of the excess chemical potential of the solute particle, μ_b^{ex} , in the present soft core system is completely different from that which one finds for hard core particles. For particles with hard core repulsion one must create a cavity of radius R_b in the solvent in order to insert a single big hard sphere of radius R_b and μ_b^{ex} takes the form [100, 107]:

$$\mu_b^{ex} = \frac{4}{3}\pi R_b^3 P + 4\pi R_b^2 \gamma(R_b), \quad (7.3.43)$$

where the first term represents the work done against the pressure of the solvent to create spherical cavity of radius R_b . The second term is the free energy of the particle (spherical wall)-interface; it is proportional to the surface area of the cavity. $\gamma(R_b)$ is the surface tension of the spherical wall-fluid interface and for large R_b it is usually assumed this quantity can be expanded as follows:

$$\gamma(R_b) = \gamma(\infty) \left(1 - \frac{2\delta}{R_b} + \dots \right) \quad (7.3.44)$$

where δ is the analogue of the Tolman length [100, 107]. $\gamma(\infty)$ is the surface tension of the fluid at the corresponding planar wall. Comparing Eq. (7.3.43) with the result for a big GCM particle, Eq. (7.3.37), we see that there is a significant difference between the two. For a hard core system, μ_b^{ex} is determined primarily by surface effects, i.e. how the solvent behaves at the interface with the big particle. However, for the soft core system it is determined by the solvent behaviour *inside* the big solute particle. We return to the role of the interfacial tension in determining μ_b^{ex} when we consider thick adsorbed films in the next section.

7.4 Results for the binary mixture solvent

Here we consider the SM potential for the situation where two big GCM particles are immersed in a binary solvent of small GCM particles. We follow the route described in the previous section, using the notation where the subscript ν is either 1 or 2, referring to the two different sized smaller particles. All species interact via a pair potential: $v_{ij}(r) = \epsilon_{ij} \exp(-r^2/R_{ij}^2)$ with the non-additive mixing rule $R_{ij}^2 = \frac{1}{2}(R_{ii}^2 + R_{jj}^2)$, where $i, j = 1, 2, b$, i.e. we employ the three component generalizations of Eqs. (7.3.6), (7.3.7) and (7.3.8).

7.4.1 Phase diagram of the binary solvent

For the solvent we consider a binary mixture which exhibits fluid-fluid phase separation and choose pair potential parameters corresponding to a binary solution of polymers of length ratio 2:1; this is the system that we considered in chapters 5 and 6. The pair potential parameters are as follows: $R_{22}/R_{11} = 0.665$, $\epsilon_{11}^* = \epsilon_{22}^* = 2.0$ and $\epsilon_{12}/\epsilon_{11} = 0.944$ and the phase diagram of the binary solvent is plotted in the total density, $\rho^0 = \rho_1^0 + \rho_2^0$, concentration, $x = \rho_2^0/\rho^0$, plane in Fig. 7.3 (see also Fig. 5.1). For low total density the binary solvent is in a mixed state, but for higher values the fluid separates into two fluid phases. The critical point is at $x = 0.71$ and $\rho^0 R_{11}^3 = 5.6$. Also plotted in Fig. 7.3 are the spinodal and the Fisher-Widom line where the asymptotic decay, $r \rightarrow \infty$, of the bulk total pair correlation functions $h_{ij}(r)$ crosses over from monotonic to exponentially damped oscillatory. These cross over lines are calculated by analysing the zeros of $D(q)$ in Eq. (7.3.19) – see Ch. 5.4.

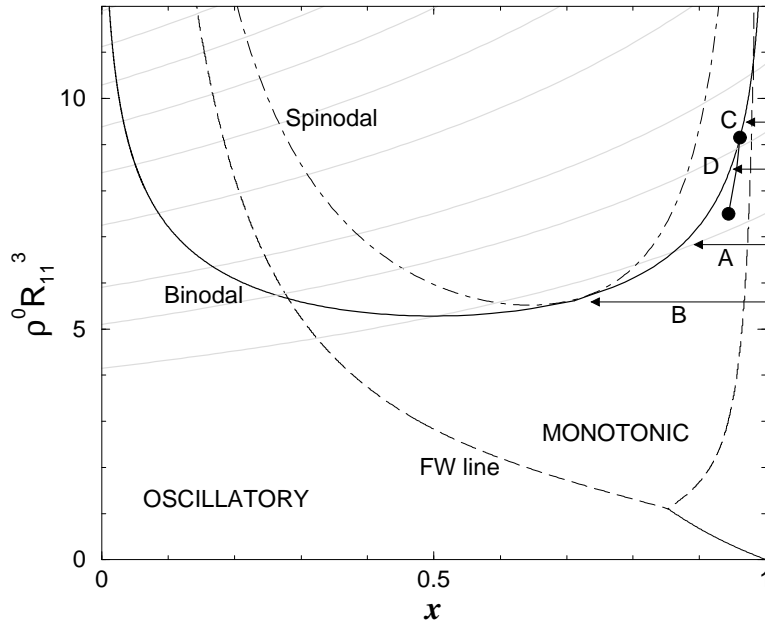


Figure 7.3: The bulk phase diagram for a binary mixture of GCM particles with $\epsilon_{12}/\epsilon_{11} = 0.944$ and $R_{22}/R_{11} = 0.665$, equivalent to a mixture of two polymers with length ratio 2:1. ρ^0 is the total density and x is the concentration of the smaller species 2. The gray lines are lines of constant pressure; the lowest is at reduced pressure $P\beta R_{11}^3 = 100$, the next at $P\beta R_{11}^3 = 150$, then 200 and the subsequent ones increase in increments of 100. The dashed line denotes the Fisher-Widom (FW) line where the asymptotic decay of the bulk pairwise correlation functions crosses over from exponentially damped oscillatory to monotonic. The solid line in the bottom right corner denotes a line of crossover from asymptotic oscillatory decay with a certain wavelength to a similar oscillatory decay but with a different wavelength – see Ch. 5.4. The arrow labeled *A* indicates the path along which the density profiles in Fig. 7.4 are calculated, and that labeled *B* approaching the critical point is the path for the density profiles in Fig. 7.10. *C* is the path for the density profiles in Fig. 7.5 and *D* is the path for the density profiles in Fig. 7.6. Path *D* intersects what we term the thin-thick transition line (solid line whose ends are denoted by filled circles). This line refers to the thin-thick film transition of the binary fluid adsorbed around a big GCM particle with pair potential parameters $\epsilon_{b1}^* = 1.0$, $\epsilon_{b2}^* = 0.8$, $\epsilon_{bb}^* = 2.0$ and $R_{bb}/R_{11} = 7.0$. It meets the binodal at the ‘wetting point’ (upper circle) with $x = 0.96$ and $\rho^0 R_{11}^3 = 9.15$ and terminates at a critical point (lower circle) with $x = 0.94$ and $\rho^0 R_{11}^3 = 7.5$.

7.4.2 Density profiles of the binary mixture around a single big GCM particle

For the big particle we choose the pair potential parameters $\epsilon_{b1}^* = 1.0$, $\epsilon_{b2}^* = 0.8$, $\epsilon_{bb}^* = 2.0$ and $R_{bb}/R_{11} = 7.0$, and the mixing rules give $R_{b1}/R_{11} = 5.00$ and $R_{b2}/R_{11} = 4.97$. These parameters are such that the big-species 2 parameters are the same as the big-small pair potential parameters of the previous section. We calculate the density profiles $\rho_\nu(r)$ of the two small GCM species, $\nu = 1, 2$, around a single big GCM particle by minimizing the grand potential functional given by Eqs. (7.2.11) and (7.2.6). The external potentials in (7.2.11) are $V_\nu(\mathbf{r}) = v_{b\nu}(r) = \epsilon_{b\nu} \exp(-r^2/R_{b\nu}^2)$, $\nu = 1, 2$ and the Euler-Lagrange equations are straightforward generalisations of Eq. (7.3.1). In Fig. 7.4 we display the density profiles $\rho_\nu(r)$ for a constant total density path $\rho^0 R_{11}^3 = 6.9$, approaching the binodal (this is path *A* in Fig. 7.3). The Gaussian form for $\rho_2(r)$, the density profile of species 2, (see Eq. (7.3.10)) that was found for the one component solvent (previous section), remains accurate for low concentrations of species 1 (i.e. for $x > 0.98$). However, even at these low concentrations the density profile of species 1, $\rho_1(r)$, cannot be described by a Gaussian of the form $\rho_1(r) = \rho_1^0 + \rho_1^* \exp(-r^2/R_{b1}^2)$. Note the plus sign in the right hand side of this equation; the density $\rho_1(r = 0) > \rho_1^0$, the bulk value, even for low concentrations of species 1. We often find clustering of species 1 in the volume enclosed by the big test particle when species 1 is the minority solvent component. This was also observed in calculations of $h_{ij}(r)$ using the HNC closure to the OZ equations for less asymmetric size ratios in the binary GCM [47]. Decreasing x further, i.e. increasing the concentration of species 1, $\rho_2(r)$ loses the Gaussian form given by Eq. (7.3.10). As x is decreased, keeping the total bulk density, ρ^0 , constant, we approach the bulk binodal and the density profiles begin to show the development of films of the coexisting phase. In particular a ‘knee’ develops in the density profile of both species which is different from the smooth Gaussian-like form – see Fig. 7.4. The knee has a similar shape to that one would find in the profiles of a ‘wetting’ film around a very big hard core spherical particle. Note that the thickness of the adsorbed film around the spherical GCM particle does not diverge at bulk coexistence, as it does in the planar wetting geometry, but tends to a finite thickness which is limited by the finite curvature of the fixed particle or spherical wall [11]. This is clear from the plot of the adsorption of species 1 around the big particle,

$$\Gamma_1 = \int_0^\infty dr 4\pi r^2 (\rho_1(r) - \rho_1^0), \quad (7.4.1)$$

shown in the inset to Fig. 7.4. Γ_1 is plotted versus the logarithm of the deviation from bulk coexistence, $\ln(x - x_{coex})$, for two reasons. First, in order to display the region close to coexistence, and second because Γ_1 diverges logarithmically at a planar wall for systems which exhibit short-ranged wall-fluid and fluid-fluid potentials – see chapters 3 and 6. We do see a linear portion in the inset to Fig. 7.4, indicative of some logarithmic film thickening. However, near to coexistence, Γ_1 saturates at its curvature limited value. For x away from the binodal, in a regime where there is no adsorbed film, the adsorption increases slowly as x decreases, and the gradient of Γ_1 as a function of $\ln(x - x_{coex})$ has a much smaller magnitude than it does when there is a thick adsorbed film. Profiles very similar to those in Fig. 7.4 are obtained for the slightly higher total density $\rho^0 R_{11}^3 = 7.0$ – see Fig. 2 of Ref. [108].

If one calculates the density profiles around the big GCM particle at higher total densities, one finds very different behaviour. For example, in Fig. 7.5 we show some typical density profiles calculated at constant total bulk density, $\rho^0 R_{11}^3 = 9.5$, approaching the binodal on path C in Fig. 7.3. In this case no thick adsorbed films develop for any concentration x . For paths at fixed total density in the range $9.15 \gtrsim \rho^0 R_{11}^3 \gtrsim 7.5$ we find a thin-thick film transition as x is decreased towards x_{coex} . In Fig. 7.6 we display some typical density profiles, calculated on path D in Fig. 7.3 at constant total bulk density, $\rho^0 R_{11}^3 = 8.5$. For large values of x ($\gtrsim 0.957$) there is no adsorbed film, and the density profiles resemble those of Fig. 7.5. However for concentrations $x \lesssim 0.956$ there is a thick adsorbed film which develops in a similar fashion to that in Fig. 7.4 as $x \rightarrow x_{coex}$ (Note, however, that the profiles in Fig. 7.6, are much steeper than those of Fig. 7.4, since these state points are much further from the bulk critical point than the state points where the profiles of Fig. 7.4 were calculated). There is a discontinuity in the film thickness between $x = 0.957$ and 0.956 which leads to a discontinuity in the adsorption of each species. Γ_1 is plotted in the inset to Fig. 7.6 and the jump signals the thin-thick transition. Within the present mean-field treatment this is a first order phase transition; the derivative with respect to x of the excess grand potential of the fluid exhibits a discontinuity at the transition point. Beyond mean-field, finite-size effects will round the transition since a *finite* amount of adsorbed fluid is involved if the fixed big particle has a finite radius. We shall return to the rounding of the transition in Sec. 7.6.

By performing calculations of density profiles and adsorption as a function of x for a series of bulk densities $\rho^0 R_{11}^3$ one can map out a line of thin-thick transitions in the (ρ^0, x)

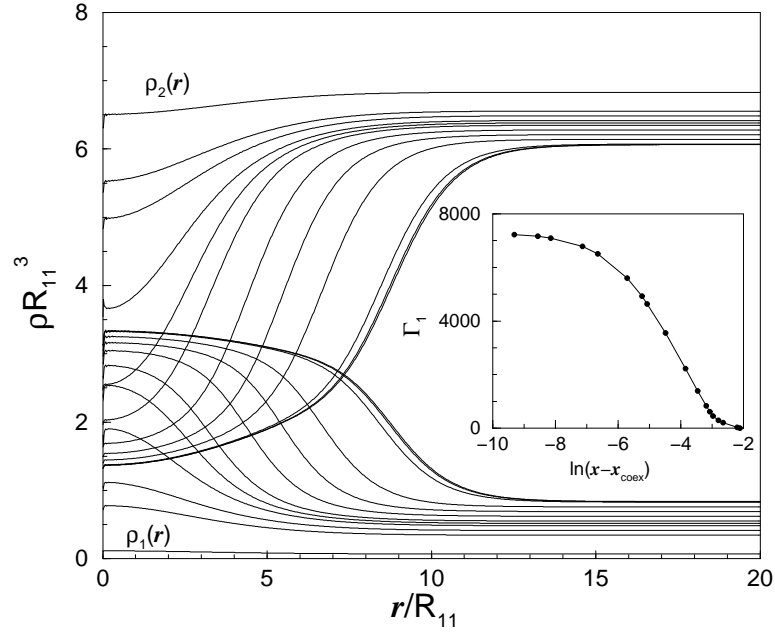


Figure 7.4: The density profiles of a binary solvent of small GCM particles, radii R_{11} and R_{22} with $R_{22}/R_{11} = 0.665$, around a big GCM test particle with $R_{bb}/R_{11} = 7.0$ ($R_{b1}/R_{11} = 5.0$, $R_{b2}/R_{11} = 4.97$, $\epsilon_{b1}^* = 1.0$, $\epsilon_{b2}^* = 0.8$ and $\epsilon_{11}^* = \epsilon_{22}^* = 2.0$), calculated at constant total bulk density $\rho^0 R_{11}^3 = 6.9$ approaching the binodal (path A in Fig. 7.3). The profiles refer to concentration $x = \rho_2^0/\rho^0 = 0.99, 0.95, 0.94, 0.93, 0.925, 0.92, 0.91, 0.9, 0.89, 0.88, 0.879$, and 0.8788 ($x_{coex.} = 0.87871$). The top set of profiles are those of the smaller of the two species, species 2. The very top one is the profile for $x = 0.99$ and the one below is for 0.95 etc. The set of profiles at the bottom correspond to species 1; the very lowest profile is at $x = 0.99$, the one above it is for 0.95 etc. There is a pronounced change in shape of the density profiles, from roughly Gaussian away from coexistence, to a non-Gaussian shape with a flat portion near the origin and a free interface-like ‘knee’ characterizing a thick adsorbed film of the coexisting phase, rich in species 1, growing around the big GCM particle close to coexistence. The inset shows Γ_1 , the adsorption of species 1, plotted versus $\ln(x - x_{coex})$. Note that the film thickness and Γ_1 saturate as $x \rightarrow x_{coex}$.

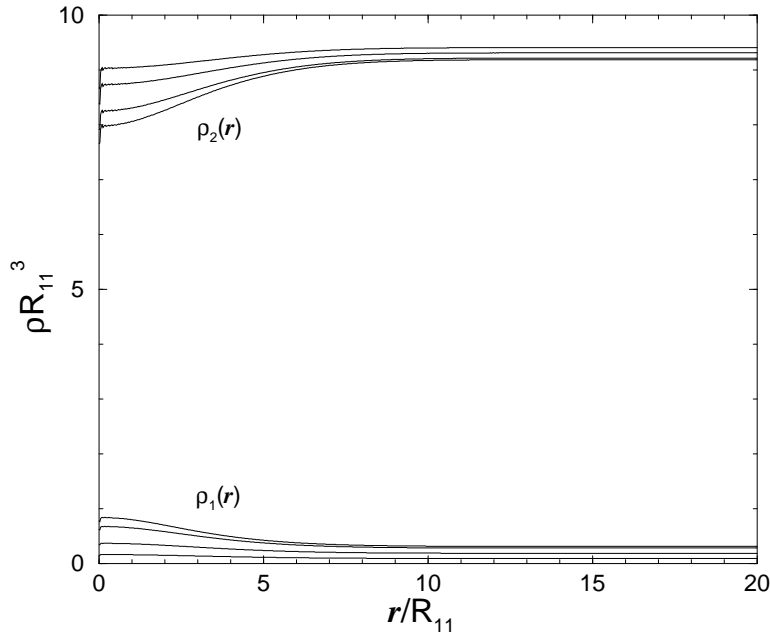


Figure 7.5: As in Fig. 7.4 but now profiles are calculated at constant total bulk density, $\rho^0 R_{11}^3 = 9.5$ approaching the binodal (path C in Fig. 7.3). Results refer to $x = 0.99, 0.98, 0.97$ and $x = x_{coex} = 0.96682$. This path is above the ‘wetting point’; there are no thick adsorbed films.

plane. This line is shown in the phase diagram of Fig. 7.3 for a big particle with radius $R_{bb}/R_{11} = 7.0$. It terminates at low ρ^0 in a critical point near $x = 0.94$ and $\rho^0 R_{11}^3 = 7.5$; below this total density there is no discontinuity in the adsorption as x is reduced and the film thickens continuously c.f. Fig. 7.4. The thin-thick transition line meets the bulk coexistence curve at the point $x = 0.96$ and $\rho^0 R_{11}^3 = 9.15$. We confirmed that on following the binodal, starting from high values of $\rho^0 R_{11}^3$, no thick adsorbed films were present (the profiles were similar to those of Fig. 7.5) until we reached the point when the adsorption jumped discontinuously.

This scenario is, of course, similar to that which occurs for a first order wetting transition at a planar substrate – see Chs. 3 and 6. There the adsorption measured along the bulk coexistence curve jumps discontinuously from a finite value in the partial wetting regime above the wetting point to an infinite value and below this point there is a pre-wetting line of first order thin-thick film transitions out of bulk coexistence, see Fig. 6.1. The pre-wetting line meets the bulk coexistence curve tangentially – a consequence of the

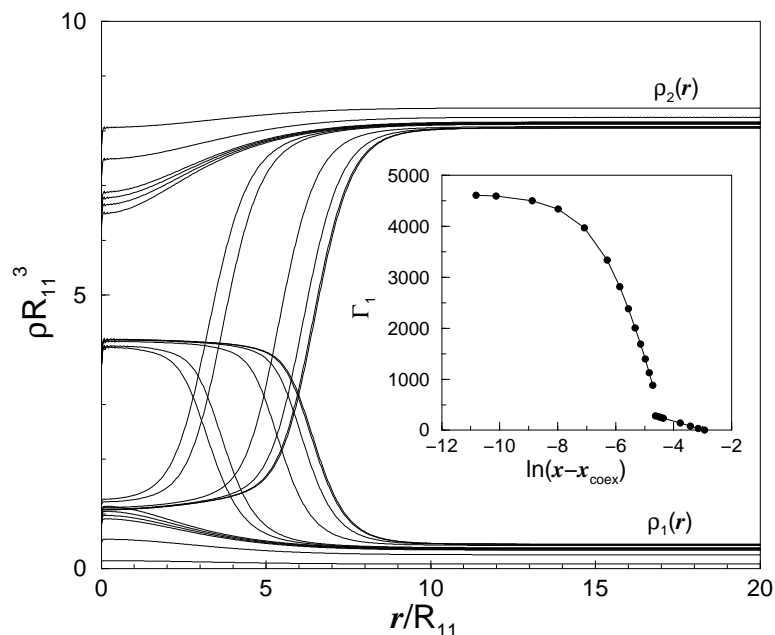


Figure 7.6: As in Fig. 7.4 but now profiles are calculated at constant total bulk density, $\rho^0 R_{11}^3 = 8.5$ approaching the binodal (path D in Fig. 7.3). Results refer to $x = 0.99, 0.97, 0.96, 0.959, 0.958, 0.957, 0.956, 0.955, 0.95, 0.948, 0.9473$ and 0.9472 ($x_{coex} = 0.94716$). Note the jump in the profiles between 0.957 and 0.956 , signaling the thin-thick film transition. The latter can also be identified from the jump in the adsorption Γ_1 , see inset.

Gibbs adsorption diverging at coexistence [11]. In the present case we have adsorbed films of finite thickness and the thin-thick transition line meets the bulk coexistence curve at a non-zero angle. We continue to refer to the point where the two lines meet as the ‘wetting point’ because of the similarity to the case of a true first-order wetting transition. However, we must bear in mind that there are significant differences between the two cases. Our present results are reminiscent of what is found in studies of the wetting transition and pre-wetting for fluids adsorbed on spherical or cylindrical substrates [109, 110, 111]. In such studies the radius of curvature is usually very large and the authors inquire how the wetting behaviour at a planar interface is affected by curvature. Here we find a *substantial* thin-thick transition line (see Fig. 7.3) for adsorption on a GCM particle which has a radius only seven times that of the (larger) adsorbed species. We shall discuss these analogies further in Sec. 7.6.

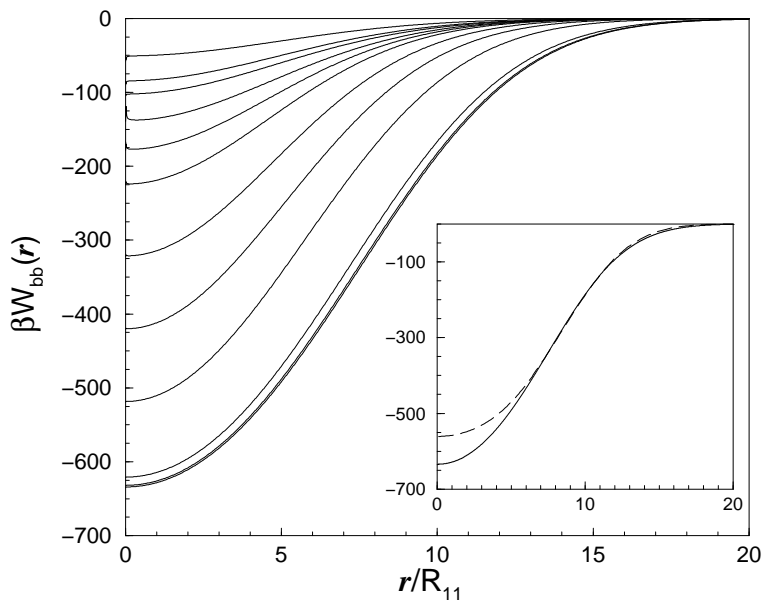


Figure 7.7: The SM potential between two big GCM particles, with radius $R_{bb}/R_{11} = 7.0$, in a binary solvent of small GCM particles of radius R_{11} and R_{22} , where $R_{22}/R_{11} = 0.665$ ($R_{b1}/R_{11} = 5.0$, $R_{b2}/R_{11} = 4.97$, $\epsilon_{b1}^* = 1.0$, $\epsilon_{b2}^* = 0.8$ and $\epsilon_{11}^* = \epsilon_{22}^* = 2.0$). These are calculated from the density profiles in Fig. 7.4, at total bulk density $\rho^0 R_{11}^3 = 6.9$ and at concentration $x = 0.99, 0.95, 0.94, 0.93, 0.925, 0.92, 0.91, 0.9, 0.89, 0.88, 0.879$, and 0.8788 , going from top to bottom ($x_{coex.} = 0.87871$). Note how the SM potential increases in depth and range as the binodal is approached. In the inset we re-plot the SM potential calculated at $x = 0.8788$ (solid line) along with our analytic approximation, Eq. (7.4.3) (dashed line), with $l/R_{11} = 9.6$.

7.4.3 SM potentials for the binary mixture solvent

We now employ Eq. (7.2.10), with $\nu = 1, 2$ and $a = b$, and the density profiles displayed in Figs. 7.4 and 7.6, to calculate the SM potential between two big Gaussian particles in a binary solvent of smaller Gaussian particles. The potentials are displayed in Figs. 7.7 and 7.8. For the results of Fig. 7.7 we follow path *A* in Fig. 7.3 which lies below the thin-thick critical point, adding more of species 1 to the solvent. We find that as the binodal is approached the SM potential, obtained by inserting the profiles of Fig. 7.4 into Eq. (7.2.10), becomes longer ranged and deeper. For example, when $x = \rho_2^0/\rho^0 = 0.8788$ then $W_{bb}(r = 2R_{bb}) \simeq -40k_B T$ and $W_{bb}(r = 0) \simeq -635k_B T$. Note that the underlying (bare) repulsive big-big potential $v_{bb}(r)$ will be negligible (usually $\epsilon_{bb}^* \sim 2.0$) in comparison

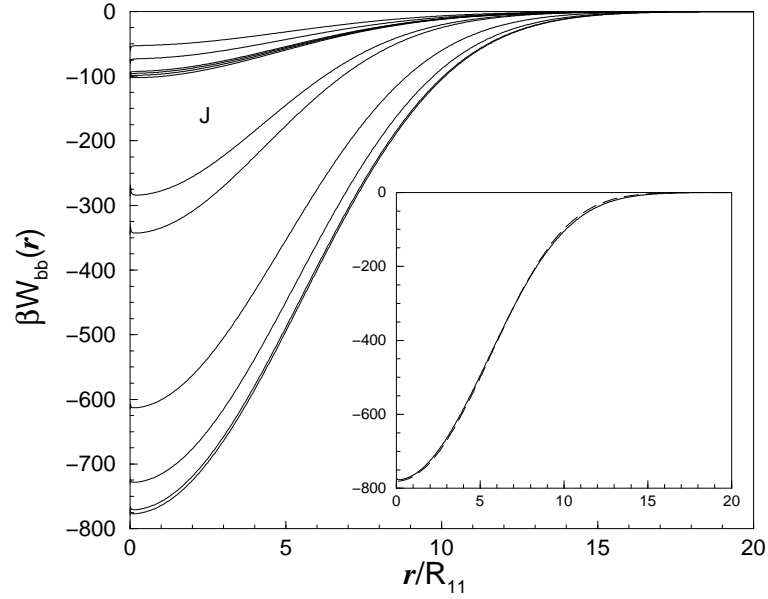


Figure 7.8: As in Fig. 7.7 but now the SM potentials are calculated from the density profiles in Fig. 7.6, at total bulk density $\rho^0 R_{11}^3 = 8.5$ and at concentration $x = 0.99, 0.97, 0.96, 0.959, 0.958, 0.957, 0.956, 0.955, 0.95, 0.948, 0.9473$ and 0.9472 , going from top to bottom ($x_{coex.} = 0.94716$). The jump (marked J) in the SM potential between $x = 0.957$ and 0.956 is associated with the thin-thick film transition – see text. In the inset we re-plot the SM potential calculated at $x = 0.9472$ (solid line) along with our analytic approximation, Eq. (7.4.3) (dashed line), with $l/R_{11} = 6.9$.

with such strongly attractive SM potentials so that the effective pair potential $v_{bb}^{eff}(r)$, given by Eq. (7.2.12), is also strongly attractive for all separations r .

The results in Fig. 7.8 refer to path D in Fig. 7.3 and correspond to the density profiles of Fig. 7.6. Since this path intersects the thin-thick transition line we expect to find a jump in the SM potential, associated with the jump in film thickness. The jump is indeed observed (marked J in Fig. 7.8); the depth of $W_{bb}(r)$ changes discontinuously with concentration x . Similar jumps occur for all paths which intersect the thin-thick transition line. Note that for x close to $x_{coex.}$, where thick films are present, the SM potentials in Fig. 7.8 are very similar in shape to the corresponding results in Fig. 7.7.

It is important to understand why the presence of thick adsorbed films induces such deep SM potentials. We can obtain some insight using the so-called sharp-kink (sk) ap-

proximation [11] for the density profiles of the solvent, i.e.

$$\rho_\nu(r) = \begin{cases} \rho_\nu^{coex} & r \leq l \\ \rho_\nu^0 & r > l \end{cases} \quad (7.4.2)$$

where $\{\rho_\nu^{coex}\}$ with $\nu = 1, 2$, are the densities of the coexisting bulk fluid rich in species 1 and l is the thickness of the adsorbed film. On substituting Eq. (7.4.2) for $\rho_\nu(r)$ into Eq. (7.2.10) we find that

$$\beta W_{bb}^{sk}(r) = \frac{\pi}{2} \sum_{\nu=1}^2 \Delta\rho_\nu \epsilon_{b\nu}^* R_{b\nu}^3 \left[\sqrt{\pi} [\operatorname{erf}(r_-) + \operatorname{erf}(r_+)] - \frac{R_{b\nu}}{r} (e^{-r_-^2} - e^{-r_+^2}) \right], \quad (7.4.3)$$

where $\Delta\rho_\nu = (\rho_\nu^{coex} - \rho_\nu^0)$ is the difference in coexisting density for species ν , $\operatorname{erf}(x) = (2/\sqrt{\pi}) \int_0^x dt \exp(-t^2)$ is the error function and $r_\pm = (l \pm r)/R_{b\nu}$. The energy scale appearing in Eq. (7.4.3) is determined by

$$\Delta\mu_b^{ex} \equiv \mu_b^{ex}(\{\rho_\nu^0\}) - \mu_b^{ex}(\{\rho_\nu^{coex}\}), \quad (7.4.4)$$

which, using the two component generalization of Eq. (7.3.27)

$$\mu_b^{ex} = \sum_{\nu=1}^2 \rho_\nu^0 \hat{v}_{b\nu}^0 = \sum_{\nu=1}^2 \rho_\nu^0 \pi^{3/2} \epsilon_{b\nu} R_{b\nu}^3, \quad (7.4.5)$$

yields

$$\beta \Delta\mu_b^{ex} = - \sum_{\nu=1}^2 \Delta\rho_\nu \pi^{3/2} \epsilon_{b\nu}^* R_{b\nu}^3 > 0. \quad (7.4.6)$$

This is our first estimate of the difference in the grand potential between inserting a single big GCM particle in the bulk fluid near the phase boundary (bulk densities ρ_ν^0) and inserting the same particle in the bulk coexisting phase (the phase adsorbing on the big particle, densities ρ_ν^{coex}). Provided the adsorbed film is thick enough, there will be a region inside the film where we can insert the second big particle sufficiently far away from both the fluid-fluid interface and from the central big particle at the origin, that the grand potential for inserting the big particle is approximately that of inserting it into the bulk of the coexisting phase. Eq. (7.4.4) gives the same value for the depth of the SM potential as that obtained from Eq. (7.4.3) when $l \rightarrow \infty$. For the point on the binodal at $\rho^0 R_{11}^3 = 6.9$ (the intersection with path *A*, Fig. 7.3), with coexisting densities $\rho_1^{coex} R_{11}^3 = 2.79$ and $\rho_2^{coex} R_{11}^3 = 2.50$, we find $\Delta\mu_b^{ex} = 592k_B T$, the large value arising mainly from the high values of $(R_{b\nu}/R_{11})^3$ in Eq. (7.4.6). The well depth obtained from the full numerical

calculation is $634k_B T$. The inset to Fig. 7.7 shows the comparison between the results of the sharp kink approximation and the full calculation, taking a film thickness $l/R_{11} = 9.6$. This value for l was chosen to give the best agreement between the analytic form, Eq. (7.4.3), and the full numerical SM potential, i.e. l is treated as the fitting parameter. Eq. (7.4.3) clearly captures the gross features of the SM potential calculated numerically for x very close to x_{coex} . For states further from the bulk critical point, such as those where the SM potentials in Fig. 7.8 are calculated and where the interfacial profiles are much steeper, our sharp-kink approximation (7.4.3) fares even better – see the inset to Fig. 7.8 where we plot the SM potential calculated very close to coexistence along with our analytic approximation, taking $l/R_{11} = 6.9$. The two results are almost indistinguishable on the scale of the figure.

However, the approximate form for the SM potential, Eq. (7.4.3), does not have the correct value for $W_{bb}(r = 0)$, as we did not include the effect that the big GCM particle has on the small particle densities near the origin; this alters the densities from their coexisting values $\{\rho_\nu^{coex}\}$. The sharp kink approximation also fails to capture the correct asymptotic decay of the SM potential since it does not input the correct asymptotic decay of the density profiles $\rho_\nu(r)$ far from the fixed big particle. The profiles of both species, $\nu = 1, 2$, should decay monotonically into bulk with a common decay length equal to the bulk correlation length, ξ , of the bulk binary mixture – see Ch. 5.4 and Ref. [52]. The sharp-kink approximation does not contain this information, and $W_{bb}^{sk}(r)$, Eq. (7.4.3), decays faster than the true $W_{bb}(r)$ as $r \rightarrow \infty$. (We shall comment further on the asymptotic decay of $W_{bb}(r)$ in Sec. 7.5). The main virtue of Eq. (7.4.3) is that it gives the correct scaling for the depth of the SM potential: $W_{bb}(r = 0) \sim -\Delta\mu_b^{ex}$, when there is a thick adsorbed film. The quantity $\Delta\mu_b^{ex}$, defined by Eq. (7.4.4), should also set the energy scale for $W_{bb}(r = 0)$ in other types of fluids that are close to bulk coexistence. However, the particular form of μ_b^{ex} will depend on the particular fluid under consideration – we will return to this in the next subsection.

7.4.4 The excess chemical potential of the big particle immersed in the binary mixture

Solvation of a single big particle in the binary solvent should reflect the proximity of the thermodynamic state to the bulk coexistence curve. In this subsection we extend the analysis of Sec. 7.3.4 to the binary solvent. Eq. (7.4.5), the two component generalisation

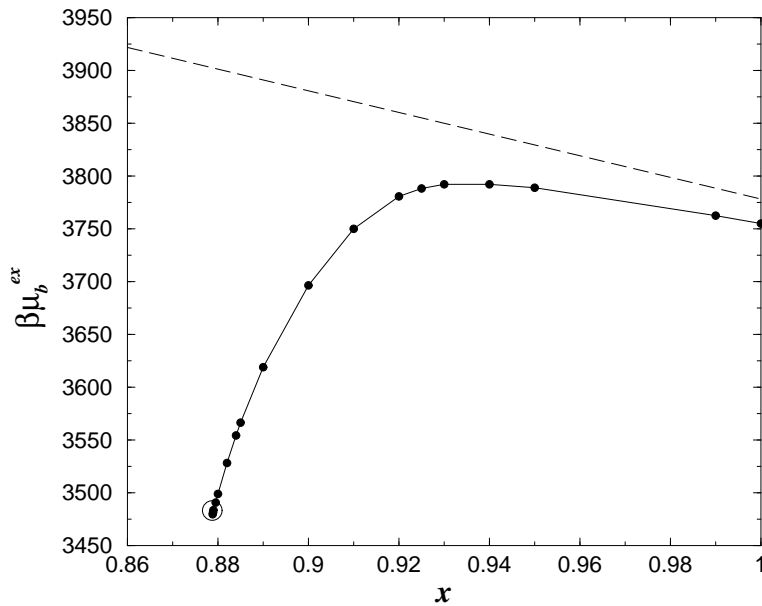


Figure 7.9: μ_b^{ex} , the excess chemical potential of a big GCM particle, radius $R_{bb}/R_{11} = 7.0$, in a binary solvent of small GCM particles of radius R_{11} and R_{22} , where $R_{22}/R_{11} = 0.665$ ($R_{b1}/R_{11} = 5.0$, $R_{b2}/R_{11} = 4.97$, $\epsilon_{b1}^* = 1.0$, $\epsilon_{b2}^* = 0.8$ and $\epsilon_{11}^* = \epsilon_{22}^* = 2.0$) calculated along a path of constant total bulk density $\rho^0 R_{11}^3 = 6.9$ (path *A* in Fig. 7.3) at concentrations x between $x_{coex} = 0.87871$ and $x = 1.0$. The straight (dashed) line denotes the results of the simplest approximation, Eq. (7.4.5), and the lower (solid) line those obtained by the second route, Eq. (7.3.30), which inputs the density profiles of Fig. 7.4. The open circle at $x = x_{coex}$ shows the value of μ_b^{ex} from the approximation Eq. (7.4.7).

of Eq. (7.3.27), is the simplest estimate for the excess chemical potential, μ_b^{ex} , of the big GCM particle in a binary mixture of smaller particles. As demonstrated by Eq. (7.3.37) for the one-component solvent, this result is only the leading order approximation to μ_b^{ex} . Away from the phase boundary, the corrections to Eq. (7.4.5) turn out to be very small. Along any path of constant total bulk density $\rho^0 R_{11}^3$ Eq. (7.4.5) is a linear function of x ($x = \rho_2^0/\rho^0$) – see Fig. 7.9 for the case of path *A* in Fig. 7.3. This route to μ_b^{ex} does not include information about thick adsorbed films around the big particle. We can incorporate this information by adopting the second route that we introduced in Sec. 7.3.4, i.e. we now input into the grand potential density $\omega(r)$ in Eq. (7.3.30) density profiles which incorporate a thick adsorbed film (see Fig. 7.4). μ_b^{ex} calculated this way should include a surface tension contribution, associated with the (spherical) fluid-fluid interface, for those

state points where a thick film is present. The results from this second route, are also plotted in Fig. 7.9. We see that for states with $x \gtrsim 0.93$, where there is no thick film, both Eq. (7.4.5) and the numerical results from Eq. (7.3.30), give a similar value for μ_b^{ex} (the small difference is well-accounted for by the second term in Eq. (7.3.37) in the case of the pure fluid, $x = 1.0$). However, at smaller x , as the thick film develops, the results for μ_b^{ex} versus x from the two different routes diverge – see Fig. 7.9. The results from Eq. (7.3.30), which includes the effects of a film, show μ_b^{ex} decreasing as x decreases and the film thickens. This seems surprising at first sight since one expects the addition of a (positive) fluid-fluid surface tension contribution to increase the excess grand potential. However, this term is more than offset by the fact that the big particle at the origin is now surrounded by a thick film of the coexisting phase rich in species 1, in which it has a lower excess grand potential. To some extent the two competing contributions cancel each other out, so that Eq. (7.4.5) remains a reasonable first approximation for μ_b^{ex} (note the vertical scale in Fig. 7.9), even near x_{coex} when there are thick films present.

Can we find a better approximation for μ_b^{ex} for the case when there is a thick adsorbed film around the big GCM particle? In the spirit of Eq. (7.3.43), we might suppose that

$$\mu_b^{ex} \simeq \sum_{\nu=1}^2 \rho_{\nu}^{coex} \hat{v}_{b\nu}^0 + 4\pi l^2 \gamma(l). \quad (7.4.7)$$

The first term is the excess chemical potential, from Eq. (7.4.5), of inserting the big GCM particle into the *coexisting* bulk phase – i.e. the phase constituting the adsorbed film; Eq. (7.4.5) should be accurate for this quantity. The second term is the free energy associated with the fluid-fluid interface which is located near $r = l$, the film thickness. $\gamma(l)$ is the fluid-fluid surface tension, which we approximate by $\gamma(\infty)$, the planar tension, defined at bulk coexistence and calculated in Ch. 5. As an example, consider the point on the binodal at total density $\rho^0 R_{11}^3 = 6.9$. We find, using $l/R_{11} = 9.6$, that Eq. (7.4.7) gives a value $\beta\mu_b^{ex} = 3483$. This result is plotted in Fig. 7.9 as the open circle. It agrees very well with the numerical result for $x = x_{coex}$.

We can also use Eq. (7.4.7) to shed some light on why there is a ‘wetting point’. In the case where there is no thick adsorbed film at bulk coexistence Eq. (7.4.5) provides a good estimate for μ_b^{ex} , the excess grand potential for inserting the big particle into the binary solvent. However, when thick adsorbed films are present Eq. (7.4.7) is a more reliable approximation. At high values of $\rho^0 R_{11}^3$, Eq. (7.4.5) yields a lower excess chemical potential than Eq. (7.4.7). The situation is reversed as $\rho^0 R_{11}^3$ is decreased towards the

critical point value along the binodal and the ‘wetting point’ occurs when the two different expressions for μ_b^{ex} , corresponding to with and without the thick film, are equal. This argument implies that the thick film forms for states near the bulk critical point because the free energy of inserting the big GCM particle into the coexisting phase plus the free energy penalty of forming the interface between the two fluid phases is lower than inserting the particle into the bulk phase, with no thick adsorbed film. Far from the critical point, where the fluid-fluid surface tension is much greater, there is no longer a free energy gain from forming the thick film. In order to implement Eq. (7.4.7) one must insert a value for the film thickness l at bulk coexistence. Consequently the estimate of the ‘wetting point’ is necessarily crude. The actual ‘wetting point’ occurs when the numerical results for the excess grand potentials of the two configurations (with and without thick adsorbed films), calculated along the binodal, are equal. Note that for a path such as D in Fig. 7.3 that intersects the thin-thick transition line the derivative with respect to concentration of the excess grand potential and, hence, of μ_b^{ex} is discontinuous at the transition within the present mean-field treatment.

7.4.5 The SM potential in the vicinity of the binary mixture critical point

When a pair of big GCM particles is immersed in a binary mixture of small GCM particles which is at a state point near the bulk critical point, a long ranged SM potential should arise between the big particles, due to the long ranged (critical) correlations in the host fluid. This is a very different phenomenon from that we encountered earlier where, approaching the binodal, the development of thick adsorbed films gives rise to strongly attractive and long-ranged SM potentials. Near the critical point, the asymptotic decay of the bulk pairwise correlation functions $h_{\nu\mu}(r)$ is monotonic, with a common decay length ξ , the bulk correlation length of the mixture – see Ch. 5.4. ξ diverges on approaching the critical point. Whilst the present approach is mean field-like and therefore does not capture correctly the behaviour of the fluid in the region of the critical point, i.e. quantities such as ξ diverge with the (incorrect) mean field exponent, we still expect the theory to describe qualitatively the behaviour of the SM potential in a near critical solvent.

We employ the same strategy as in earlier sections, i.e. we calculate the small particle density profiles around the big GCM particle and insert these into Eq. (7.2.10), with $a = b$. Each profile consists of a Gaussian-like perturbation at the origin plus an exponentially

decaying tail so that:

$$\rho_\nu(r) \sim \rho_\nu^0 - \frac{A_\nu}{r} \exp(-r/\xi), \quad r \rightarrow \infty \quad (7.4.8)$$

for $\nu = 1, 2$ A_ν is the species dependent amplitude and ξ is the common bulk correlation length. Fig. 7.10 a) displays the density profiles of small particle species 1 and species 2 (the pair potential parameters are those used in the calculations of the previous subsection), around a single big particle with radius $R_{bb}/R_{11} = 7.0$, calculated along a path of constant density, $\rho^0 = \rho_{crit}^0$, the critical point density, with concentration decreasing from $x = 1.0$ to x slightly larger than x_{crit} . In Fig. 7.10 b) we show that the decay of the density profiles is indeed of the form given in Eq. (7.4.8). By plotting $\ln([\rho_2^0 - \rho_2(r)]rR_{11}^2)$ versus r , the exponentially decaying tail is manifest as a straight line, and the magnitude of the gradient $= 1/\xi$, where ξ is the bulk correlation length. This figure should be compared with the inset to Fig. 7.1 where there is no straight line portion and only the effective Gaussian decay can be ascertained. Note that the bulk correlation length ξ can also be calculated from the poles of $\hat{h}_{\nu\mu}(q)$, see Ch. 5.4, which corresponds to calculating the zeros of $D(q)$ in Eq. (7.3.19) but with s, b replaced by ν, μ – the indices now representing the two small species. Near the critical point the lowest lying pole is pure imaginary and $\alpha_0^{-1} = \xi$. This route gives results which agree with those obtained from the gradients.

Near the critical point we find that the depth of the SM potential between two large GCM particles immersed in a binary solvent of smaller ones is roughly constant, but the range diverges as the bulk correlation length ξ in the solvent diverges. The SM potentials calculated from the density profiles of Fig. 7.10 are plotted in Fig. 7.11. We see that in the vicinity of the critical point the depth of the SM potential is approximately constant, $W_{bb}(r = 0) \simeq -300k_B T$, but the range is strongly dependent on the value of the bulk correlation length ξ . Note the length scale in Fig. 7.11; the longest ranged SM potentials are still substantial for $r > 30R_{11}$. At this range the (reduced) direct potential between the big particles is $\sim \exp(-(30/7)^2) \simeq 10^{-8}$.

At this stage it is instructive to recall that the effective potential between two big particles is

$$v_{bb}^{eff}(r) \equiv v_{bb}(r) + W_{bb}(r) = -k_B T \ln g_{bb}(r) \quad (7.4.9)$$

where the radial distribution function $g_{bb}(r) \equiv 1 + h_{bb}(r)$ is evaluated at infinite dilution, $\mu_b \rightarrow -\infty$. Thus $\beta W_{bb}(r)$ decays in the same fashion as $-h_{bb}(r)$, $r \rightarrow \infty$. For fluids in which the interparticle potentials are short ranged, we expect *all* the pair correlation

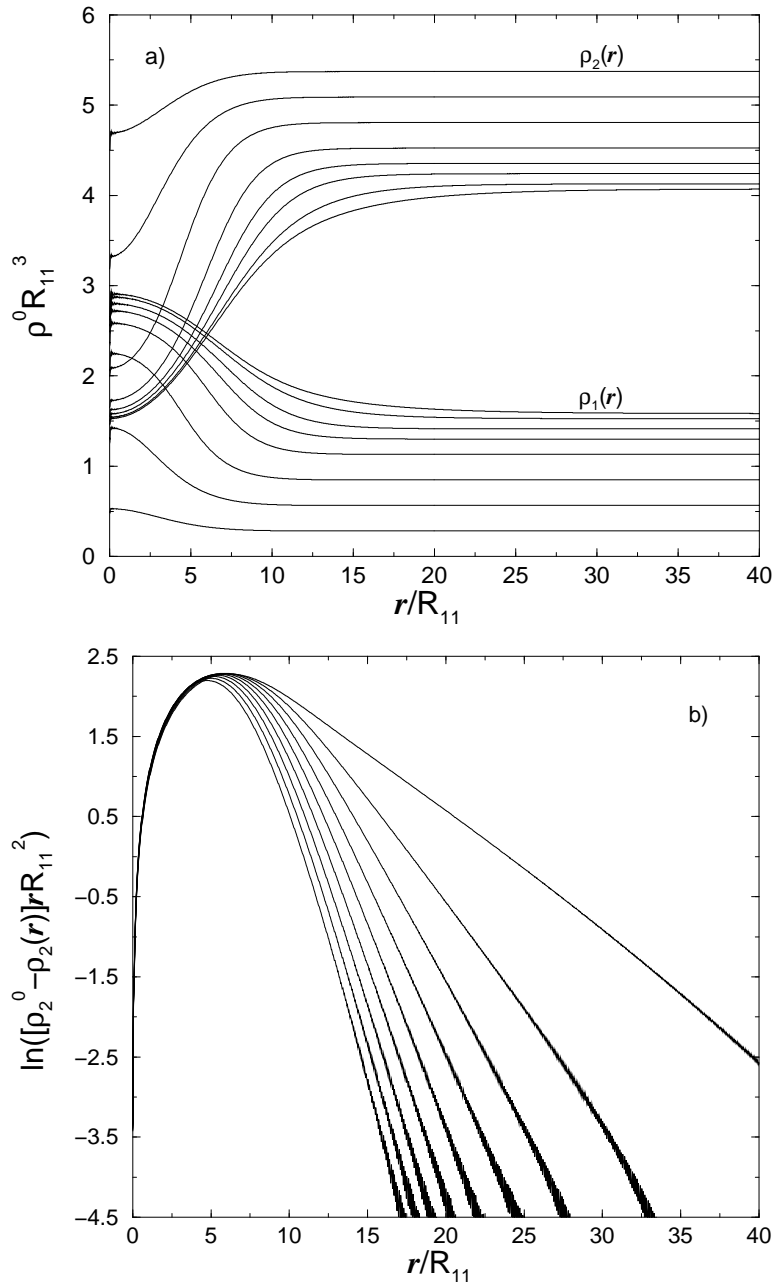


Figure 7.10: a) shows the density profiles of a binary mixture of small GCM particles with $R_{22}/R_{11} = 0.665$, around a big GCM test particle with $R_{bb}/R_{11} = 7.0$, calculated along path *B* in Fig. 7.3 at constant total bulk density $\rho^0 R_{11}^3 = \rho_{crit} R_{11}^3 = 5.6$, the critical point density, and concentration $x = \rho_2^0/\rho^0 = 0.95, 0.9, 0.85, 0.8, 0.77, 0.75, 0.73$ and 0.72 ($x_{crit} = 0.71$). The upper profiles are those of species 2. The very top one is the profile at $x = 0.95$ and the one below is at $x = 0.9$ etc. The lower profiles are those of species 1. The very bottom one is the profile at $x = 0.95$ and the one above is at $x = 0.9$ etc. Note the slow decay for states approaching the critical point. In b) $\ln([\rho_2^0 - \rho_2(r)]rR_{11}^2)$ is plotted versus r/R_{11} . The gradient of the straight line portion yields the inverse correlation length ξ^{-1} – see Eq. (7.4.8).

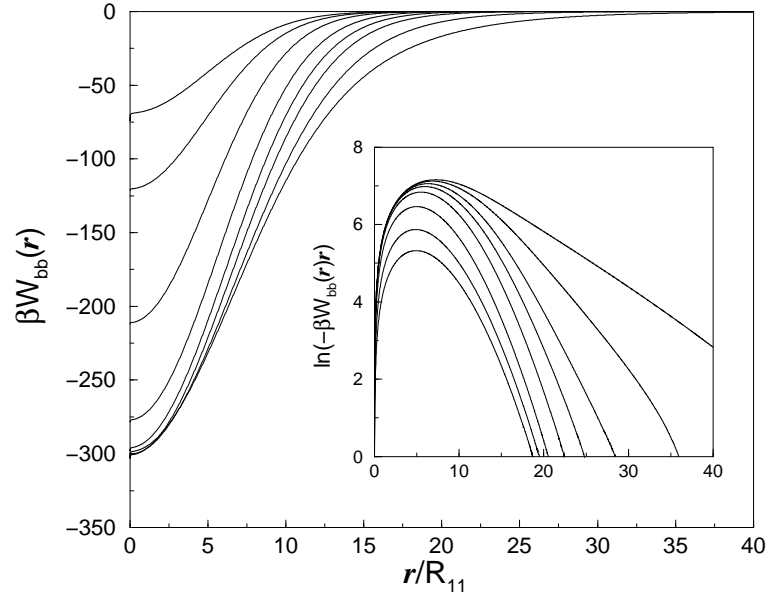


Figure 7.11: The SM potential, obtained from the density profiles displayed in Fig. 7.10, calculated at $\rho^0 R_{11}^3 = \rho_{crit} R_{11}^3 = 5.6$ and concentration $x = 0.95, 0.9, 0.85, 0.8, 0.77, 0.75, 0.73$ and 0.72 ($x_{crit} = 0.71$). Near the critical point the potentials have roughly the same depth but the range increases as the critical point is approached. The inset plots $\ln(-\beta r W_{bb}(r))$ versus r/R_{11} ; this should be compared with Fig. 7.10 b).

functions $h_{ij}(r)$ in the mixture to decay with the same asymptotic form – see Ch. 5.4 and Ref. [52]. It follows that near the critical point, inside the monotonic regime in Fig. 7.3, $W_{bb}(r)$ should decay in the same fashion as the density profiles $\rho_\nu(r)$ in Eq. (7.4.8), i.e. with the same exponential decay length ξ . (The amplitude will, of course, be different). This expectation is borne out by plotting $\ln(-\beta r W_{bb}(r))$ versus r . In the vicinity of the critical point we find straight line portions with gradient $-1/\xi$.

Note that for the state point nearest to the critical point in Figs. 7.10 and 7.11, namely $x = 0.72$, $\xi/R_{11} \simeq 7.1$, i.e. we are not particularly close to bulk criticality and that is why we still observe exponential decay of the density profiles and of $W_{bb}(r)$. Were we to perform calculations much closer to the critical point, so that ξ is very much larger than R_{bb} , we should observe interesting cross over to power law decay. This takes us into the regime investigated in studies of the effect of curvature on the critical Casimir effect – see Ref. [81] and references therein. We have not attempted to investigate this regime in our present study.

7.5 Test particle versus OZ route to the SM potential

As we recalled in the last section (see Eq. (7.4.9)), one way to determine the SM potential is to calculate $g_{bb}(r)$, the radial distribution function of the big particles in the limit $\mu_b \rightarrow -\infty$. It is important to recognize that this procedure is formally equivalent to that described in Sec. 7.2.1. In order to understand this we use Eqs. (7.2.2) and (7.2.5) to obtain the expression

$$\beta W_{bb}(r) = - \lim_{\mu_b \rightarrow -\infty} \ln \left(\frac{\rho_b(r)}{\rho_b(\infty)} \right) + \beta(V_b(\infty) - V_b(r)), \quad (7.5.1)$$

where $\rho_b(r)$ is the density profile of the big particles (b) around another big particle fixed at the origin exerting the potential $V_b(r) = v_{bb}(r)$ on species b and $\rho_b(\infty) \equiv \rho_b^0$ is the bulk density. Since $\rho_b(r)/\rho_b^0 = g_{bb}(r)$ (this is the Percus test particle identity), Eq. (7.4.9) then follows directly. Thus, in an exact treatment it would not matter whether one calculates $g_{bb}(r)$ and uses (7.4.9) or whether one follows the procedure of Sec. 7.2.1, evaluating $c_b^{(1)}(\mathbf{r})$ etc; they must give the same result.

What is the situation within an *approximate* DFT, such as the one we use here? The procedure we followed in the calculations of the earlier sections, i.e. calculating $c_b^{(1)}(\mathbf{r}; \mu_b \rightarrow -\infty)$, should correspond to the test particle route to $g_{bb}(r)$, in the limit $\mu_b \rightarrow -\infty$. We confirmed this assertion by calculating $g_{bb}(r)$ via the test particle route, minimizing the 3-component functional (Eq. (7.2.6) with $i, j = 1, 2$ and b) for the ternary mixture of GCM particles. The density profiles of the three components around the fixed big particle were calculated for smaller and smaller values of ρ_b^0 (corresponding to the limit $\mu_b \rightarrow -\infty$), until $g_{bb}(r)$ remained unchanged, then this limiting value was used in Eq. (7.4.9) to obtain $W_{bb}(r)$. As expected, this test particle route gave exactly the same SM potential as that obtained in the preceding sections where we had to calculate only the small particle density profiles around the big particle, rather than those of the full ternary mixture. That we reproduce exactly the SM potentials in Fig. 7.7 attests to the accuracy of the numerics; see also the discussion of depletion potentials in Ref. [3].

There is, of course, an alternative route to the calculation of $g_{bb}(r)$, namely via $c_{ij}^{(2)}(r)$ and the OZ equations for the bulk mixture, i.e. the generalization of Eqs. (7.3.18) and (7.3.19) to the ternary case. Since the pair direct correlation functions, obtained from second derivatives of $\mathcal{F}[\{\rho_i\}]$, correspond to the RPA, Eq. (7.2.13), it is very easy to obtain all the partial radial distribution functions $g_{ij}(r)$ via this route. We investigated the standard mixture, with $R_{22}/R_{11} = 0.665$, $R_{bb}/R_{11} = 7.0$, $\epsilon_{b1}^* = 1.0$, $\epsilon_{b2}^* = 0.8$, $\epsilon_{12}^* = 1.888$

and $\epsilon_{11}^* = \epsilon_{22}^* = \epsilon_{bb}^* = 2.0$, along the same path A in Fig. 7.3 as for the results of Figs. 7.4 and 7.7. The functions $g_{b1}(r)$ and $g_{b2}(r)$, calculated in the limit $\rho_b^0 \rightarrow 0$, do not exhibit the feature of a thick adsorbed film which is apparent in the density profiles $\rho_1(r)$ and $\rho_2(r)$ in Fig. 7.4 for states close to bulk coexistence. When we calculate $g_{bb}(r)$ in the same limit and insert this into Eq. (7.4.9) for $W_{bb}(r)$ we obtain results, see Fig. 7.12, that are totally different from those obtained in our earlier calculations, i.e. from the test particle route (Fig. 7.7). The present results yield SM potentials that are almost two orders of magnitude weaker, for states near bulk coexistence, than the earlier results. Clearly the difference is due to the omission of the effects of thick adsorbed films. Significantly, even far from bulk coexistence, at concentration $x = 0.99$, the test particle route (Fig. 7.7) yields a value for $W_{bb}(r = 0)$ that is a factor of 9 times that from the OZ route. Thus, it is evident that for large asymmetries in the sizes of the particles the two different routes to $W_{bb}(r)$ are vastly different. Only within an exact treatment could we expect the two routes to yield the same results. We speculate that the test particle results of Fig. 7.7 will be much more reliable than those from OZ. The former route fixes the big particle and then determines an (accurate) response of the small species to the external potential; this is not a particularly demanding requirement for a DFT. By contrast, the OZ route makes no distinction between big and small; it attempts to treat all types of correlations equally accurately and this is a tall order! Note that the OZ route predicts the same *type* of asymptotic decay ($r \rightarrow \infty$) for $g_{bb}(r)$ as does the test particle route. In both cases the decay is determined by the zero of the denominator in the Fourier transform of the OZ equations, i.e. by the requirement that

$$[1 - \rho_1^0 \hat{c}_{11}(q)][1 - \rho_2^0 \hat{c}_{22}(q)] - \rho_1^0 \rho_2^0 \hat{c}_{12}^2(q) = 0, \quad (7.5.2)$$

which is analogous to the treatment in Sec. 7.3.2 (see also Ref. [3]). The ultimate decay may be monotonic or exponentially damped oscillatory, depending on the location of the state point relative to the Fisher-Widom line – see Fig. 7.3. However, the amplitude (and any phase factor) will not be the same when calculated by the two different routes. The test particle route predicts a much larger amplitude for the decay of $g_{bb}(r) - 1$ and, hence, of $W_{bb}(r)$.

We conclude this subsection by returning to the issue raised in Sec. 7.3.3 of the symmetry, under interchange of species i, j , of the SM potential $W_{ij}(r)$. In general, we find that for two different sized big GCM particles, a and b , immersed in a binary solvent of

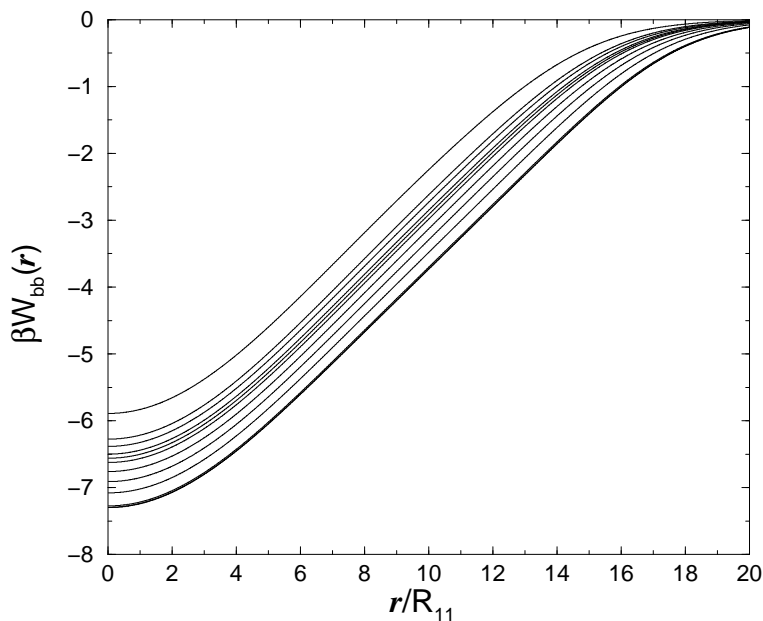


Figure 7.12: SM potentials calculated using Eq. (7.4.9) with $g_{bb}(r)$ obtained from the RPA closure to the OZ equations. These results should be compared with those calculated via the test particle route in Fig. 7.7. They are calculated for the same pair potential parameters and at the same points in the phase diagram. From top to bottom they refer to $x = 0.99, 0.95, 0.94, 0.93, 0.925, 0.92, 0.91, 0.9, 0.89, 0.88, 0.879$ and 0.8788 (note that the last three curves lie almost on top of one another). These potentials are markedly less attractive (note the vertical scale) from those of Fig. 7.7.

smaller particles $W_{ab}(r) \neq W_{ba}(r)$ when the calculations are performed using the test particle route, whereas the OZ route (for the 4 component mixture) automatically respects the symmetry, since $g_{ab}(r) = g_{ba}(r)$ is a direct consequence of the OZ equations. However, as we have argued above, there are good reasons to suppose that the test particle route should be more reliable so we examine some of its consequences.

We focus on the radial distribution functions $g_{ij}(r)$ in a ternary mixture with $i, j = 1, 2, 3$, where ρ_3^0 , the number density of the biggest species, is chosen to be small. We find that for state points far from the fluid-fluid phase boundary $g_{ij}(r) \simeq g_{ji}(r)$, i.e. for a given set of bulk densities one can fix species i at the origin, and calculate $\rho_j(r)$ around it giving $g_{ij}(r) = \rho_j(r)/\rho_j^0$, or one can fix a particle of species j at the origin and calculate $\rho_i(r)$ around this particle giving $g_{ji}(r) = \rho_i(r)/\rho_i^0$, which will be almost the same as $g_{ij}(r)$. Some examples of pair correlation functions are plotted in Fig. 7.13, for a ternary mixture

of particles with $R_{22}/R_{11} = 0.665$ and $R_{33}/R_{11} = 1.5$. The energy parameters are $\epsilon_{ii}^* = 2$ ($i = 1, 2, 3$), $\epsilon_{12}^* = \epsilon_{13}^* = 1.888$ and $\epsilon_{23}^* = 1.6$ and the bulk densities are $\rho_1^0 R_{11}^3 = 0.07$, $\rho_2^0 R_{11}^3 = 6.93$ and $\rho_3^0 R_{11}^3 = 0.01$, which corresponds to adding a small concentration of species 3 to a binary mixture of 1 and 2 with total density $(\rho_1^0 + \rho_2^0) R_{11}^3 = 7.0$ and $x = 0.99$. As can be seen from Fig. 7.13, it makes almost no difference which particle is fixed at the origin, the curves $g_{ij}(r)$ and $g_{ji}(r)$ ($i \neq j$) lie extremely close to one another. We find a similar degree of consistency for states well away from the phase boundaries in the more asymmetric ternary mixture that we investigated in the previous sections. However, near the phase boundary the symmetry is broken severely. The reason is as follows: if one fixes a big particle (b) at the origin and calculates the density profiles around it then near the phase boundary there will be an adsorbed film of the smaller particles – see for example the plots in Fig. 7.4. In this case $g_{b\nu}(r) = \rho_\nu(r)/\rho_\nu^0$ will incorporate the film. On the other hand, if one fixes one of the small particles, species ν , at the origin and calculates the density profile of the fluid around it, there will not be a thick adsorbed film on this small particle since the curvature is too great. Thus, $g_{\nu b}(r) = \rho_b(r)/\rho_b^0$ will not be the same as $g_{b\nu}(r)$. To summarize: within the present mean-field DFT, the test particle route to the radial distribution functions usually respects the symmetry $g_{ij}(r) = g_{ji}(r)$ to a high level of accuracy, even when there are large size asymmetries between the particles. However, close to the binodal and when there are big particles present, so that thick adsorbed films can develop, the symmetry requirement breaks down. In these circumstances one supposes that it is preferable to treat the largest of the particle species as the external potential, in order to best include the effects of the adsorbed film.

7.6 Concluding remarks

In this chapter we have calculated the SM potential between a pair of big GCM particles immersed in a binary solvent of small GCM particles, using a general DFT method [3]. Within our simple mean-field treatment, we are able to include some of the effects of thick adsorbed films of the solvent fluid around the big solute particles, as well as effects associated with a thin-thick transition in these adsorbed films. Thick films result in long ranged SM potentials, the range being determined by the adsorbed film thickness. Furthermore, the DFT method was able to incorporate, albeit within mean-field, the long ranged decay of the solvent density profiles around the big solute particle which occurs

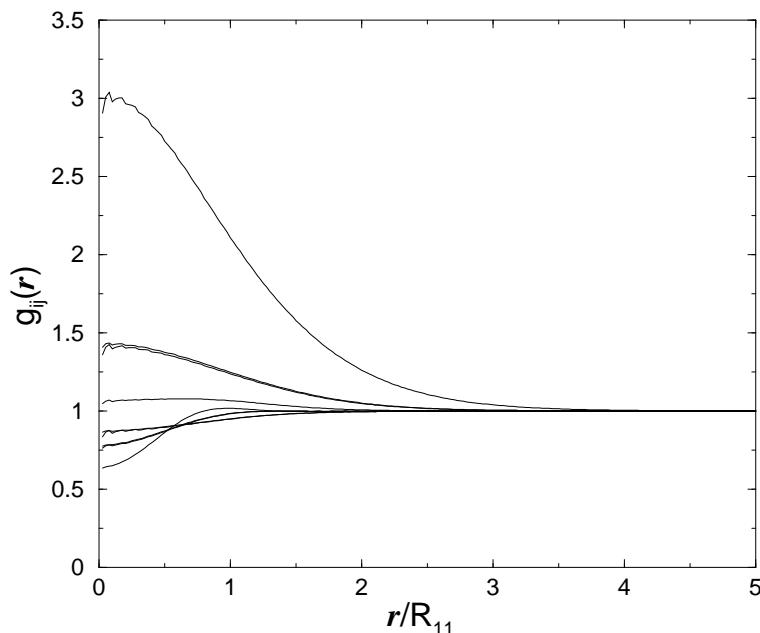


Figure 7.13: The pair correlation functions calculated by the test particle route for a ternary mixture of GCM particles. The sizes are $R_{22}/R_{11} = 0.665$ and $R_{33}/R_{11} = 1.5$ and the energy parameters are $\epsilon_{ii}^* = 2$ ($i = 1, 2, 3$), $\epsilon_{12}^* = \epsilon_{13}^* = 1.888$ and $\epsilon_{23}^* = 1.6$. The bulk densities are $\rho_1^0 R_{11}^3 = 0.07$, $\rho_2^0 R_{11}^3 = 6.93$ and $\rho_3^0 R_{11}^3 = 0.01$. From top to bottom the curves corresponds to $g_{33}(r)$, $g_{13}(r)$ ($g_{31}(r)$), $g_{11}(r)$, $g_{23}(r)$ ($g_{32}(r)$), $g_{12}(r)$ ($g_{21}(r)$) and $g_{22}(r)$. One observes that $g_{13}(r)$ is almost identical to $g_{31}(r)$, $g_{23}(r)$ to $g_{32}(r)$ and $g_{12}(r)$ to $g_{21}(r)$ for this state point. Note the strong 3-3 clustering even at these small size asymmetries.

when the solvent is in a state near the bulk critical point. This effect also results in long ranged SM potentials. Since the RPA Helmholtz free energy functional that we use, Eq. (7.2.6), is probably the most simple one can devise, we expect that using the same general DFT approach but with more sophisticated functionals for the present system and for other model fluids that exhibit fluid-fluid phase separation should also be able to describe similar effects.

Given that our approach does incorporate thick adsorbed films around the solute particles, an important question is: have we incorporated all aspects of the films into the SM potentials? Since we do not have any simulations with which to compare directly, we can only conjecture as to what is omitted. A feature of several studies of hard core

particles surrounded by thick adsorbed films is a bridging ‘transition’ occurring when the big particles are sufficiently close that the two adsorbed films join [92, 94, 95, 96, 97, 98]. We see no signature of this phenomenon, which is closely related to capillary condensation. There are three possible reasons for this. The first is that in the present soft core system there is no bridging transition, and that bridging is associated only with solute particles that have a hard core. The second possibility is that a bridging transition occurs only for big particles which are very much larger than we consider here. The third, and most likely explanation for not observing bridging transitions in the present model, is that we are using a very crude mean field Helmholtz free energy functional, Eq. (7.2.6). This simple RPA functional, used in the context of the present theory, probably does not incorporate these effects. We can obtain further insight by examining the (formally exact) inhomogeneous Kirkwood-Hill equation for the one-body direct correlation function of a (big) particle b immersed in solvent of (small) particles, labeled ν [100]:

$$-\beta^{-1}c_b^{(1)}(\mathbf{r}) = \sum_{\nu} \int_0^1 d\lambda \int d\mathbf{r}' \rho_{\nu}(\mathbf{r}') g_{b\nu}(\mathbf{r}, \mathbf{r}'; \lambda) v_{b\nu}(|\mathbf{r} - \mathbf{r}'|), \quad (7.6.1)$$

where, as in Eq. (7.3.29), λ is a parameter which ‘turns on’ the big-small external potential $v_{b\nu}(r)$ and $g_{b\nu}(\mathbf{r}, \mathbf{r}'; \lambda)$ is the big-small (inhomogeneous) pair distribution function corresponding to the potential $\lambda v_{b\nu}(r)$, with $0 \leq \lambda \leq 1$. By making the approximation $g_{b\nu}(\mathbf{r}, \mathbf{r}'; \lambda) \equiv 1$ in Eq. (7.6.1), we recover Eq. (7.2.9), obtained earlier by taking one functional derivative of our mean-field Helmholtz free energy functional, Eq. (7.2.6), and the limit $\rho_b^0 \rightarrow 0$. Combining Eqs. (7.6.1), (7.3.29) and (7.2.5), we arrive at a formally exact result for the SM potential:

$$\beta W_{ab}(\mathbf{r}) = \sum_{\nu} \int_0^1 d\lambda \int d\mathbf{r}' [\rho_{\nu}(\mathbf{r}') g_{b\nu}(\mathbf{r}, \mathbf{r}'; \lambda) - \rho_{\nu}^0 g_{b\nu}(|\mathbf{r} - \mathbf{r}'|; \lambda)] \beta v_{b\nu}(|\mathbf{r} - \mathbf{r}'|). \quad (7.6.2)$$

Setting $g_{b\nu}(\mathbf{r}, \mathbf{r}'; \lambda) \equiv 1$ in Eq. (7.6.2) provides an alternative way to derive Eq. (7.2.10), our mean-field approximation for the SM potential. Clearly we omit two-body correlations in the fluid, and it is these which would give rise to any bridging transition. However, to ascertain fully what correlation effects are omitted by our approach, it is necessary to compare our results with simulation studies.

Another, related, aspect of correlation effects concerns our observation in Sec. 7.5 that the radial distribution functions $g_{b\nu}(r)$ calculated by the test particle route do not maintain the symmetry $g_{b\nu}(r) = g_{\nu b}(r)$. This is particularly clear near phase separation when there are thick adsorbed films of the small particles around the big particles: if

one calculates $g_{b\nu}(r)$ by fixing the big particle, then one finds the signature of a thick adsorbed film, since $g_{b\nu}(r) = \rho_\nu(r)/\rho_\nu^0$ and $\rho_\nu(r)$, the density profile of the small particles around the big particle, describes the thick adsorbed film. If, instead, one fixes a small particle and calculates $g_{\nu b}(r) = \rho_b(r)/\rho_b^0$, there is no signature, within the present mean-field treatment, of the thick adsorbed film around the big particles and $g_{b\nu}(r) \neq g_{\nu b}(r)$. It would be instructive to examine this issue of symmetry, within the test particle route, for other approximate DFT's since we believe that a theory which maintains $g_{b\nu}(r) = g_{\nu b}(r)$ symmetry and includes correlation effects in the presence of thick adsorbed films would be very difficult to construct. Within *any* approximate DFT approach, fixing the biggest particle as the external potential and then calculating the response of the remaining particles to this external potential should be the most reliable way of including the effects of thick adsorbed films. One can then take these density profiles and insert the second (smaller) particle in order to calculate the SM potential between these two particles. In this way we ensure some effects due to thick adsorbed films are incorporated into the calculation and these lead to predictions of very strongly attractive and long-ranged SM potentials. Very different behaviour (much less attractive potentials) is manifest in the alternative OZ route to the radial distribution functions. Comparing the results of Figs. 7.7 and 7.12 shows that the RPA closure to the OZ equations yields much weaker SM potentials than those from the test particle route. More generally, we expect the OZ route, which does have the advantage of enforcing the $g_{ij}(r) = g_{ji}(r)$ symmetry, to be less reliable than test particle when employed within the context of approximate DFT's. Whether integral equation closure approximations, of the type discussed in Ref. [99], will fare any better for states close to phase separation remains to be examined in detail. However, incorporating effects of thick adsorbed films into a closure approximation is non-trivial. Once again it would be advantageous to have simulation results so that careful comparisons could be made.

The mean-field nature of our Helmholtz free energy functional introduces other limitations to the present approach. First, our calculation of the SM potential in the vicinity of the solvent critical point does not capture the effects of true (bulk) criticality. In our treatment, the bulk correlation length ξ , which determines the range of the SM potential in this region of the phase diagram, diverges with the mean field exponent $\nu = 1/2$, rather than the true (Ising) exponent $\nu = 0.63$. However, we believe that our present approach captures correctly the qualitative behaviour of the SM potential that one would find in

the vicinity of the critical point. As emphasized in Sec. 7.4.5, we have deliberately avoided the regime where ξ is of the same size or larger than the biggest radius in the system. The field theoretic approaches described in Refs. [77, 78, 79, 80, 81] are better suited to such investigations. The advantage of the present (microscopic) approach is that it provides a qualitative description of the SM potential in different regions of the solvent phase diagram; it is not restricted to particular state points nor to situations where the solute particles are very much bigger than the solvent particles.

Second we must inquire about the limitations in our treatment of the thin-thick transition. As remarked in Sec. 7.4.2, the sharp transition that we find should be rounded by finite-size effects in a treatment going beyond mean-field. Since there is only a finite number of particles adsorbed around the (big) solute particle fluctuation effects will round the transition. Although the thin-thick transition in the adsorbed film that we find is related to the pre-wetting transition that one can find for fluids adsorbed on the surface of a hard-core spherical substrate [109, 110, 111], there are important differences due to the soft core nature of the GCM. In particular, a significant portion of the adsorbed film lies *inside* the big particle. The origin of the adsorbed film is due to the fact that the big particle favours the larger of the two small species (species 1) and this is caused by the interplay between the length scales associated with the sizes of the different particles, and the non-additive mixing rule, Eq. (7.3.8), which governs the interaction between un-like species. Moreover, for some states near the phase boundary there is a free energy gain if the big GCM particle is surrounded by the coexisting phase rich in species 1, which can more than outweigh the free energy penalty of forming the interface between the two fluid phases. It is this balance which determines the final configuration of the fluid surrounding the big particle: either a thin or a thick adsorbed film. The transition occurs when the penalty for forming the spherical fluid-fluid interface is equal to the free energy gain for the big particle to be surrounded by the coexisting phase. Of course, these general considerations apply to other fluid systems, including hard-core fluids, however the significant difference between the soft GCM and hard-core big particles immersed in a wetting solvent appears to be the size ratio between the solute particles and the solvent particles which is required to obtain thick films. For the present GCM we observe rather thick films for a size ratio $R_{bb}/R_{ss} \simeq 10$, whereas for hard core systems a size ratio of at least 100, and often much larger, is required. For example, we calculated the density profiles of the binary solvent of small GCM particles considered in the phase diagram of Fig. 7.3 subject to a spherical

potential of the form:

$$\beta V_\nu(r) = \begin{cases} \infty & r \leq R_b \\ A_\nu \exp(-r/R_{11})/(r/R_{11}) & r > R_b \end{cases} \quad (7.6.3)$$

with amplitude $A_1 = 1$ and $A_2 = R_{22}/R_{11} = 0.665$. In the planar limit ($R_b \rightarrow \infty$) this wall potential exhibits a first order wetting transition with the associated pre-wetting line – see Ch. 6. However, when $R_b/R_{11} = 30$ the typical adsorbed film thickness at bulk coexistence is $\simeq 5R_{11}$ and the pre-wetting line is about one third the length of that in the planar limit – see Appendix D. Strikingly, it is 13 times shorter than the length of the thin-thick transition line found in the present study (Fig. 7.3) for a big GCM particle with $R_{bb}/R_{11} = 7.0$. Thus, there are pronounced differences between the mechanism generating the thin-thick transition around a *soft* core particle and that for the pre-wetting transition occurring in adsorbed films on the surface of a hard spherical substrate. Nevertheless, the thickness of the adsorbed film around the soft GCM particle must be limited, in the usual way, by curvature. For a spherical substrate, the usual approach [11, 109, 110] is to perturb about the planar limit noting that the curvature of the substrate acts (exactly) as a bulk field, i.e. a displacement from coexistence. This idea should also be valid for the present GCM. However, it is not clear how best to construct the planar limit, given the need to impose the mixing rules, for this soft core system. Therefore we have not carried out a systematic investigation of how the thin-thick transition line depends on the radius R_{bb} of the big solute particles. What we can say is that increasing R_{bb} shifts the ‘wetting point’ to higher values of the total density ρ^0 and lengthens the thin-thick transition line. Such behaviour is in keeping with that found for pre-wetting on spherical substrates where decreasing the radius shifts the wetting transition closer to the bulk critical point [109]. It follows that the nature of the rounding of our thin-thick transition should be similar to that discussed for prewetting on spheres [109, 110]. There finite-size fluctuation effects lead to a broadening over a temperature interval δT around the prewetting line which is proportional to R_b^{-2} and we would expect a similar dependence for the present case. In Ref. [109] estimates are made for the case where $R_b = 100$ solvent atomic diameters and the rounding $|\delta T|/T \sim 10^{-4}$. For our much smaller particle radii we must expect much more pronounced broadening. However, we have not attempted a detailed calculation for the present system where the interparticle forces are short ranged rather than power-law, as in Ref. [109].

What are the consequences for experiment of our predictions of long-ranged attractive SM potentials resulting from thick adsorbed films? Our predictions should not be specific to the present GCM system but should hold for any solvent exhibiting fluid-fluid phase separation. There are implications for atomic force microscope (AFM) measurements since when the microscope tip is immersed in a fluid that is close to phase separation both the tip and the substrate may be covered in a thick film of the adsorbed phase, resulting in much longer ranged forces than the intrinsic (bare) forces arising between the tip and the surface or those which are exerted when the solvent is far from phase separation. This is indeed what has been found in a Monte Carlo study of the force between a large sphere (modeling the AFM tip) and a planar wall [112]. Our DFT approach is well-suited to this situation since one can easily input the density profile(s) of the solvent, $\rho_s(z)$, at the planar wall, which will exhibit a thick adsorbed film, and then insert the spherical test particle. Indeed this procedure should be rather accurate, and capture all of the physics, when the size of the test particle is such that the adsorbed film on the particle is not very thick.

Alternatively, were one to perform a direct measurement of the force between two large colloidal particles in a binary solvent near to fluid-fluid phase separation, using optical tweezers [113], one should find a long ranged force due to the presence of thick adsorbed films surrounding the big colloid particles. Light scattering measurements, see e.g. Ref. [114], of the second virial coefficient B_2 for big colloidal particles suspended in a near phase-separating solvent could also be most revealing. Long ranged attraction should give rise to very large negative values of

$$B_2 = 2\pi \int_0^\infty dr r^2 (1 - \exp[-\beta v_{bb}^{eff}(r)]). \quad (7.6.4)$$

Moreover there should be very pronounced variation of B_2 as the solvent binodal is approached and any thin-thick or bridging transition should lead to a jump in this coefficient. We are not aware of systematic studies of B_2 in an appropriate solvent although there are experiments [115] on B_2 for a globular protein in a solution of non-adsorbing polymer which show that B_2 depends on the proximity of the polymer solution to its spinodal line. However, this study corresponds to the ‘protein limit’ since the radius of gyration of the polymer is larger than the radius of the protein for which other physical considerations are relevant. Of course any measurements of B_2 require the concentration of the big particles to be small but non-zero and strongly attractive SM forces promote clustering of the

colloidal particles causing the big particles to be very weakly soluble.

We can estimate the solubility of big GCM particles in the fluid of smaller GCM particles by calculating the spinodal for the binary mixture of these big and small species. This is obtained analytically (see Eq. (5.2.11)), from the mixture free energy, Eq. (7.3.28). For the binary fluid considered in Sec. 7.3 with $R_{bb}/R_{11} = 7.0$, $R_{ss}/R_{11} = 0.665$, $\epsilon_{bb}^* = \epsilon_{ss}^* = 2.0$, $\epsilon_{bs}^* = 0.8$ and density of the small GCM particles $\rho_s^0 R_{11}^3 = 7.0$, then the density at the spinodal of the big particles is $\rho_b^0 R_{11}^3 = 1.2 \times 10^{-5}$, i.e. they phase separate when there is about one big GCM particle per 10^6 of the small particles. This should be compared with the binodal calculated for the binary mixture of species 1 and 2 with $R_{22}/R_{11} = 0.665$ given in Fig. 7.3. Such considerations are important when seeking to determine the mechanism for the flocculation of the big colloidal particles observed [82, 83, 84, 85, 86, 87, 88, 89] in a binary solvent; one cannot necessarily assume that the non-zero concentration of colloid particles does not change the solvent phase diagram, i.e. the flocculation may be linked to phase separation in the ternary mixture [116, 117, 82, 118]. In the experiments of Beysens and co-workers [82, 83, 84, 85, 86] and of Maher and co-workers [87, 88, 89] it is possible that two factors play a role: a) the presence of thick adsorbed films could lead to strongly attractive SM forces between big particles which result in pronounced clustering and b) the concentration of the big particles could be sufficient to alter the solvent phase diagram. However, developing a theory which treats the relevant ternary mixture accurately is not straightforward.

A well trodden path in colloidal systems is to tackle the problem by calculating the SM potential between two big colloidal particles in the sea of small ones and use this to model the colloids as an effective one-component system, from which one could obtain the phase diagram by theory or simulation [22]. Such an approach proved very powerful for asymmetric binary hard sphere mixtures [23] and for certain models of colloid-polymer mixtures [22]. It is tempting to follow the same path for the present GCM system but one finds quickly that there are significant differences. As we have seen, the SM potential between two big particles, $W_{bb}(r)$, is attractive for all separations r . Depending on ϵ_{bb}^* , the strength of the repulsive bare big-big potential $v_{bb}(r)$, this implies that the effective pair potential $v_{bb}^{eff}(r) = v_{bb}(r) + W_{bb}(r)$ can also be negative for all r . Indeed for most situations pertaining to polymer mixtures, where $\epsilon_{bb}^* \sim 2.0$, $v_{bb}^{eff}(r)$ will be very strongly negative (many $k_B T$). This implies, in turn, that the effective one component fluid of big particles described *solely* in terms of the pairwise potential $v_{bb}^{eff}(r)$ would be thermody-

namically unstable; it would collapse². However, in addition to the two-body term the effective Hamiltonian contains a zero-body term $-PV$, where P is the pressure of the reservoir of solvent and V is the volume, a one-body term $N_b\mu_b^{ex}$, where N_b is the number of big particles *and* many body contributions [23]. The stability of the system depends on the total compressibility of the mixture which contains contributions from the structure independent terms as well as the structural, osmotic compressibility [120]. By contrast the phase behaviour of the mixture is not influenced by the structure independent terms [23]. Whether one can make useful progress in tackling the properties of a multi-component soft core fluid by constructing effective one component Hamiltonians requires further investigation. If, as seems likely, one is forced to retain the many body contributions [119] this will limit the usefulness of the one component description for *soft core* models.

Whilst we have focused in the main on $W_{bb}(r)$, the two-body SM potential between two big solute particles immersed in the small particle solvent, we should emphasize that our results for a one-body quantity, the excess chemical potential of a single big particle, μ_b^{ex} , contains much rich information about solvation. Moreover our DFT approach should calculate μ_b^{ex} very reliably – the subtleties and possible failings of the test particle procedure in mixtures are not germane to the one body quantity. μ_b^{ex} exhibits an interesting variation with concentration as the binary solvent approaches phase separation (Fig. 7.9), reflecting the formation of a thick adsorbed film surrounding the big particle. Understanding how the presence of an adsorbed phase influences the solvation of a big particle is of general interest in physical chemistry. It is thought to be relevant in the theory of hydrophobic solvation. Lum *et al.* [121] studied the formation of a low density (drying) film of water vapour around a spherical hydrophobic (hard-sphere) solute particle immersed in a model of liquid water that was very close to bulk coexistence. Their theory for the density profile and for μ_b^{ex} was based upon the effective reference fluid approach of Weeks and co-workers [122, 123] but similar results emerge from a recent DFT treatment [124]. The presence of the adsorbed vapour film gives rise to a liquid-vapour surface tension contribution to μ_b^{ex} when the hard-sphere radius is sufficiently large. This contribution is the direct analogue of the fluid-fluid tension we find in the present study – see Sec. 7.4.4. However, we find that the overall form of μ_b^{ex} in the GCM fluid is very different from that which one would expect for a typical hard-core fluid [107, 125]; compare the results for μ_b^{ex} in the GCM,

²Parola *et al.* [119] make the same point on the basis of an alternative, linear response, calculation of $W_{bb}(r)$.

Eqs. (7.3.37) or (7.4.7), with Eq. (7.3.43), the formula for μ_b^{ex} when the solute particle has a hard core. The leading terms have a very different origin: in the soft-core Gaussian system this is essentially the volume occupied by the big particle multiplied by the number density of small particles and by the energy cost, ϵ_{bs} , for these particles to overlap, whereas in a hard core system the leading term is the work done in creating the cavity for the big particle, i.e. the volume of the big particle multiplied by the pressure of the solvent. Comparing the excess chemical potential, calculated as a function of the size of the big particle and of the distance of the state point from the fluid-fluid phase boundary, for soft core and hard-core fluids could shed some interesting light on solvation.

Chapter 8

Binary star-polymer solutions: bulk and interfacial properties

Using an effective logarithmic-Gaussian pair potential that models the interaction between star-polymers, we compare the hypernetted chain (HNC) and random phase approximations (RPA) for calculating the bulk structure (including the Fisher-Widom and Lifshitz lines), thermodynamic functions and phase diagram of a phase separating binary fluid of star-polymers, of two-arm length ratio 2:1. Thereby, the stars considered here are equivalent to linear chains in the mid-point representation of their effective interaction. We find that at densities where the star coronas overlap the quasi-exact HNC and RPA give very similar results. Using a density functional approach, with a functional which generates the RPA, we calculate properties of the inhomogeneous binary fluid. We determine the surface tension and one-body density profiles at the free fluid-fluid interface. For states well-removed from the critical point the profiles exhibit pronounced oscillations. For a purely repulsive planar wall potential that models the effective potential between a star-polymer and a hard wall, we find a first order wetting transition with the associated pre-wetting line.

8.1 Introduction

In chapter 4 we introduced the idea of effective interactions: When considering the problem of polymers in solution one is faced with a huge task if one starts the theoretical description from the monomeric degrees of freedom. The problem is greatly simplified if one can

calculate an effective potential between the polymers, using a single position coordinate for each polymer, typically the center of mass or the mid chain monomer [22, 21]; in Ch. 4 we outlined some of the strategies used to calculate effective potentials. The effective potential between the polymer chains is in general a many body potential, and is density dependent. However one finds that a density independent pair potential approximation for the interaction between the individual polymer chains is sufficient to give a reasonable description of the bulk structure and thermodynamics [22, 20, 34]. With this perspective, one is then able to bring to bear on the problem the machinery developed for simple fluids, e.g. using integral equation theories for bulk fluid structure and thermodynamics [1]. A natural tool for calculating the properties of inhomogeneous fluids is density functional theory (DFT) [7]. In this chapter we study a binary fluid of demixing star-polymers. Star-polymers are made up of a number of polymer chains (referred to as arms) covalently bonded to one common central core [126]. The arm number f , also called *functionality*, is the physical property that allows one to interpolate between linear chains ($f = 1, 2$) and the colloidal limit $f \gg 1$ in which the stars resemble hard spheres [22, 127, 128, 129].

We choose a binary mixture of star polymers with $f = 2$ arms (i.e., polymers) with polymerisation ratio $N_1 : N_2 = 2 : 1$, in order to compare our results with those obtained for the binary Gaussian core model (GCM) in chapters 5 and 6. Recall that the GCM is a model for polymers in solution, modeling the effective potential between the centers of mass of the polymers by a repulsive Gaussian potential, $v(r) = \epsilon \exp(-r^2/R^2)$, where for polymers at room temperature in an athermal solvent $\epsilon \simeq 2k_B T$ and $R \simeq R_g$, the polymer radius of gyration. Note that the GCM potential remains finite for all separations r , representing the fact that in the underlying polymer system the centers of mass can completely overlap, even if the individual monomers cannot. In this chapter we use an alternative representation for the chains: we choose their *central monomers* as generalised coordinates for a coarse-grained description and employ accordingly the effective interactions between central monomers in treating the polymers as ultrasoft colloids. In contrast to the center-of-mass potential, the central-monomer effective potential does have a divergence as $r \rightarrow 0$, albeit a very weak, logarithmic one. This property, derived in the pioneering work of Witten and Pincus [130], stems from the scaling properties of the partition function of self-avoiding random walks and can be generalized to stars with an arbitrary number of arms [130]. Thus, the divergence is caused by the self-avoidance that restricts the number of available configurations of infinitely thin polymer threads

and not by the direct monomer-monomer interaction. We choose to focus on $f = 2$ arm star-polymers in order to compare with the GCM because there is no difference between a $f = 2$ arm star-polymer and a simple polymer, hence we are simply calculating the properties of a binary polymer solution. In this case the star polymer potential is an effective polymer pair potential between the central monomers on each of the two polymers. Since it is the same underlying system that these two effective potentials represent, these two different effective potentials should result in the same thermodynamic properties and phase behaviour. Indeed many of the results in this chapter are similar to those obtained in chapters 5 and 6.

The present chapter is laid out as follows: in Sec. 8.2, we describe the model binary star-polymer mixture. Then in Sec. 8.3, by comparing with the more accurate HNC, we show that at sufficiently high densities the bulk structure and thermodynamics of the binary fluid can be approximated well by the simple RPA. The HNC is essentially exact for soft core particles, giving results almost indistinguishable from simulation for sufficiently high densities of GCM particles [22, 37] and of star polymers with as many as 32 arms [131]. We calculate both the HNC and the RPA fluid-fluid coexistence curves in the total density-composition plane, and we find that at high densities, there is very little difference between the two. In the same section we also calculate the Fisher-Widom line, i.e., the line in the bulk phase diagram at which the asymptotic decay of the radial distribution functions $g_{ij}(r)$ cross over from monotonic to damped oscillatory, see Ch. 5.4, and the Lifshitz lines, which separate regions where the partial structure factors $S_{ij}(k)$ have a maximum at $k = 0$ from those where there is a minimum at $k = 0$. In Secs. 8.4 and 8.5 we use a Helmholtz free energy functional which generates the RPA for bulk correlation functions to calculate the density profiles of the inhomogeneous binary fluid. We calculate the density profiles, along with the surface tension, for the planar interface between the demixed fluid phases in Sec. 8.4, and then in Sec. 8.5 we calculate the density profiles of the binary fluid at a planar wall with a purely repulsive wall-fluid potential chosen to model the effective interaction between a star polymer and a hard wall. We find that there is a first order wetting transition, with the associated pre-wetting line, whereby the fluid phase rich in the larger species completely wets the interface between the wall and the fluid phase rich in the smaller species. Finally in Sec. 8.6 we summarize and conclude.

8.2 The model mixture

In Refs. [132, 133], Jusufi *et al.* proposed a repulsive logarithmic-Gaussian form for the effective potential between the centers of a pair (arm number $f < 10$) of star polymers in athermal solvents. This potential features a weak, $-\ln(r)$ divergence for small separations r , reflecting the fact that polymers are ultrasoft ‘colloids’. The Gaussian decay pertains for large r and is identical in its functional form with the effective interaction between the centers of mass (the GCM) [20, 30, 19, 39]. Note that for arm numbers $f > 10$, the Gaussian decay of the pair potential is replaced by a Yukawa decay [127]. The multi-component generalization of the logarithmic-Gaussian potential reads as

$$\beta v_{ij}(r) = \frac{5}{18} f^{3/2} \begin{cases} -\ln\left(\frac{r}{\sigma_{ij}}\right) + \frac{1}{2\tau_{ij}^2 \sigma_{ij}^2} & \text{for } r \leq \sigma_{ij}; \\ \frac{1}{2\tau_{ij}^2 \sigma_{ij}^2} \exp\left[-\tau_{ij}^2 (r^2 - \sigma_{ij}^2)\right] & \text{for } r > \sigma_{ij}, \end{cases} \quad (8.2.1)$$

where σ_{ij} is the corona diameter and τ_{ij} is a parameter of order $1/R_{ij}$ where R_{ij} is the radius of gyration [132] and $\beta = 1/k_B T$. In the present work we choose to set the arm number $f = 2$, so that the star polymer pair potential (8.2.1) is equivalent to the effective potential between the central monomers on a polymer chain, and we can therefore compare the the present ‘central-monomer’ representation with the ‘center of mass’ effective potential used in chapters 5 and 6. The arm number f only appears in the prefactor of the pair potential (8.2.1), so we expect that all results presented will be qualitatively correct for $f < 10$. For the interaction parameters between unlike species in a binary mixture, $i, j = 1, 2$, we choose the mixing rules:

$$\sigma_{12} = \frac{1}{2}(\sigma_{11} + \sigma_{22}) \quad (8.2.2)$$

and

$$\frac{1}{\tau_{12}^2} = \frac{1}{2} \left(\frac{1}{\tau_{11}^2} + \frac{1}{\tau_{22}^2} \right). \quad (8.2.3)$$

The additive rule, Eq. (8.2.2), is roughly what we expect for the effective cross interaction corona diameter σ_{12} . The precise value chosen for σ_{12} does not have much of an effect on the overall phase behaviour of the system; it simply sets the critical point total bulk density, ρ_c of the binary phase separating mixture. It thereby plays a role similar to ϵ_{12} for the GCM in locating the critical point – see Sec. 5.2. The rule described by Eq. (8.2.3), plays a more significant role in determining the behaviour of the binary fluid. Since $\tau_{ij} \simeq 1/R_{ij}$, we use Eq. (8.2.3) to determine τ_{12} , because this relation has been found in

simulations when considering the effective interaction between the centers of mass of the polymers [30, 39] – this procedure is equivalent to the mixing rule (5.2.14).

In order to make a comparison with our earlier work in chapters 5 and 6, we choose $\sigma_{22}/\sigma_{11} = 0.665$ which is equivalent to a binary mixture of polymers of polymerisation ratio $N_1 : N_2 = 2 : 1$.¹ In Ref. [132], it was found that $\tau_{ii} = 1.03/\sigma_{ii}$ gives excellent agreement with simulation results and, in addition, it brings about the best agreement for the second virial coefficient of polymer solutions. Using these ratios along with Eqs. (8.2.2) and (8.2.3), the model mixture parameters are completely determined.

8.3 Bulk structure and phase diagram

We consider a system consisting of M_1 long and M_2 short chains enclosed in the volume V . Accordingly, we define the partial densities $\rho_i = M_i/V$, $i = 1, 2$ of the components, as well as the total density $\rho = \rho_1 + \rho_2$ and the concentration of the small component, $x = \rho_2/\rho$. Due to the athermal character of the solvent the effective interactions are purely entropic, i.e., they scale linearly with $k_B T$ and the thermal energy is the only energy scale of the problem, as is clear from Eq. (8.2.1). Thereby, the temperature drops out of the problem as an irrelevant variable and the thermodynamic space of the system is spanned by the partial densities or equivalently the pair (x, ρ) .

In order to determine the bulk structure of the binary fluid we use the hypernetted chain (HNC) closure for direct pair correlation function, $c_{ij}(r)$, in terms of the pair correlation function $h_{ij}(r) = g_{ij}(r) - 1$ in the Ornstein-Zernike equations (the two component generalisation of Eq. (2.2.1) [1]), which for a multi-component fluid is (c.f. Eq. (2.2.3)):

$$c_{ij}(r) = -\beta v_{ij}(r) + h_{ij}(r) - \ln[1 + h_{ij}(r)]. \quad (8.3.1)$$

We expect the HNC to be almost exact for describing the bulk structure of these soft core particles at densities where the cores of the particles start to overlap ($\rho\sigma^3 \gtrsim 1.0$). This expectation is corroborated on the one hand from the known fact that for the one component GCM the HNC results are indistinguishable from the simulation results at these densities – see Ch. 4 and Refs. [22, 37, 38, 39] and on the other hand by the finding that the HNC at high densities exhibits excellent agreement with simulation for a pure

¹Recall that this arises from the scaling law $R \sim N^\nu$ connecting the spatial extent R of a self avoiding polymer with its degree of polymerisation N , using the value $\nu = 3/5$ for the Flory exponent.

star-polymer fluid with functionality $f = 32$ [131].²

We define the partial structure factors $S_{ij}(k)$, $i, j = 1, 2$ of the mixture as

$$\begin{aligned} S_{11}(k) &= 1 + \rho_1 \hat{h}_{11}(k); \\ S_{22}(k) &= 1 + \rho_2 \hat{h}_{22}(k); \\ S_{12}(k) &= \sqrt{\rho_1 \rho_2} \hat{h}_{12}(k), \end{aligned} \quad (8.3.2)$$

where $\hat{h}_{ij}(k)$ denotes the Fourier transform of $h_{ij}(r)$. In addition, we consider later the concentration-concentration structure factor $S_{cc}(k)$, given by [134, 135]

$$S_{cc}(k) = (1 - x)^2 S_{11}(k) + x^2 S_{22}(k) - 2x(1 - x) S_{12}(k). \quad (8.3.3)$$

In Fig. 8.1 we show the HNC partial structure factors for the binary fluid, comparing also with the much simpler random phase approximation (RPA), which is given by $c_{ij}(r) = -\beta v_{ij}(r)$. The RPA closure to the Ornstein-Zernike equations becomes more accurate as the density is increased and is very reliable for interaction potentials that diverge slowly at the origin or are bounded there [38, 136]. Indeed, the RPA is in principle a good candidate for examining the structure of uniform *and* nonuniform fluids, when the condition $\int d^3r v_{ij}(r) < \infty$ is fulfilled [136, 129] – as is the case for the GCM one- and two-component systems. For non-bounded but slowly diverging interactions, the RPA is a good approximation at least for the thermodynamics, but it can also hold for the structure when the prefactor of the weakly diverging potential is small [136]. For the case at hand, the prefactor of the logarithmically diverging potentials is indeed small, $(5/18)f^{3/2} = 0.786$ for $f = 2$, and thus the RPA should be valid at sufficiently high densities; a hypothesis we confirm.

The comparison in Fig. 8.1 reveals that the HNC and the RPA yield very similar structure factors. The discrepancies between the two occur mostly for small k -values and are most pronounced in the neighbourhood of the critical point. The existence of a spinodal (and thus of phase separation) in the mixture is witnessed in both the HNC and the RPA by the increase (and eventual divergence) of the structure factors at $k = 0$. As we move along a path of fixed concentration x increasing the total density ρ , the RPA-structure factors are seen to diverge earlier than the HNC-ones, a feature pointing to the fact that the

²Due to the $f^{3/2}$ -prefactor of the star-star potential, the $f = 32$ -effective interaction is much steeper than the $f = 2$ -one. The success of the HNC for this steeper interaction, then, guarantees its validity for the much softer interaction considered here.

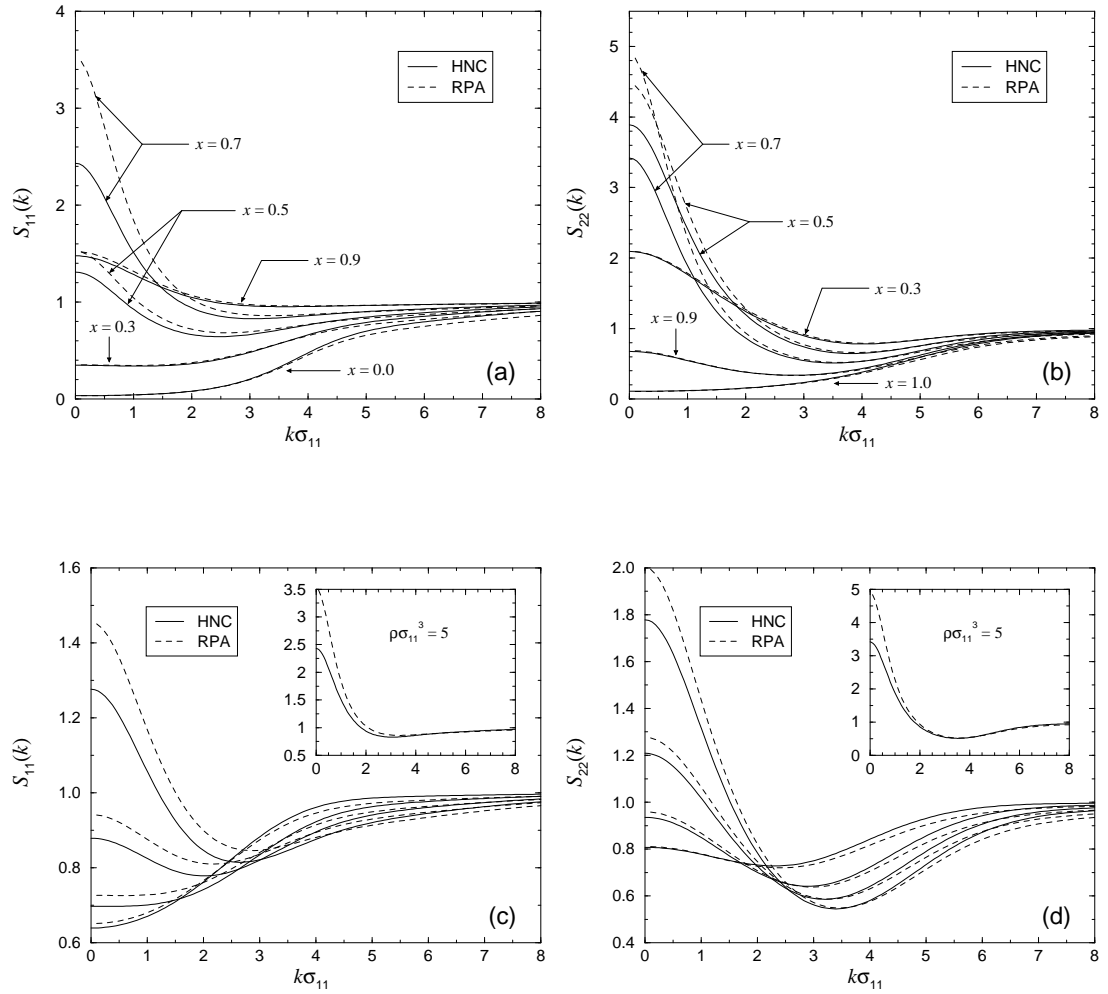


Figure 8.1: The partial structure factors, calculated along two different thermodynamic paths in the (x, ρ) -plane of the star polymer mixture obtained from the HNC (solid lines) and RPA (broken lines). (a) $S_{11}(k)$ for fixed total density $\rho\sigma_{11}^3 = 5$ and for different concentrations x of species 2, as indicated on the plot. (b) Results for $S_{22}(k)$ along the same path. (c) $S_{11}(k)$ at fixed concentration $x = 0.7$ and for increasing total densities, from bottom to top $\rho\sigma_{11}^3 = 1, 2, 3$ and 4. The inset shows the result for $\rho\sigma_{11}^3 = 5$, a point lying close to the RPA-critical (consolute) point $(x_c, \rho_c\sigma_{11}^3) = (0.7095, 5.71628)$, see also Fig. 8.3. The inset axes have the same labels as those of the main plot. (d) Same as in (c) but for the partial structure factor $S_{22}(k)$. Note that in all plots the $k \rightarrow 0$ -limits predicted by the RPA are larger than those from the HNC and the discrepancies become more pronounced in the neighbourhood of the RPA-critical point. At the critical point $S_{11}(k=0)$ and $S_{22}(k=0) \rightarrow +\infty$ whereas $S_{12}(k=0) \rightarrow -\infty$.

RPA-coexistence region will be broader than the one predicted by the HNC. In addition, the fluid structure factors are quite similar to the equivalent GCM partial structure factors $S_{ij}(k)$. The reason for this is that in calculating $S_{ij}(k)$ one Fourier transforms the pair potentials, $v_{ij}(r)$, which involves integrals of the form $\int dr r \sin(kr) v_{ij}(r)$. Therefore, the weak divergence of the pair potential $v_{ij}(r)$ at small r has little effect because it is suppressed by the multiplication with $r \sin(kr)$. It is rather the fashion in which $v_{ij}(r)$ decays as $r \rightarrow \infty$ that has greater influence on the structure and the thermodynamics of the mixture [20, 137]: as we show later, the quantity $\hat{v}_{ij}(0) \propto \int dr r^2 v_{ij}(r)$ enters into the RPA equation of state and is thus decisive in determining the phase boundaries.

We now turn our attention to the partial radial distribution functions (rdf's) $g_{ij}(r)$, $i, j = 1, 2$, in particular at high densities and close to the borderlines $x = 0$ and $x = 1$. In these cases, the HNC and the RPA yield practically identical results, so we examine the HNC results here. As shown in Fig. 8.2, we find a signature of ‘clustering’ in the rdf's $g_{ij}(r)$ of the minority phase, i.e., the development of a pronounced maximum. This feature was also found for the GCM, e.g. see Fig. 7.13 and Ref. [47], but there the maxima are at $r = 0$. In the present model $g_{ij}(r)$ does not have a maximum at $r = 0$, because our potentials have the logarithmic divergence at $r = 0$. Rather, the minority phase rdf's $g_{ii}(r)$, have a peak in the range $\sigma_{ii}/2 \lesssim r \lesssim \sigma_{ii}$. Since σ_{ii} is the diameter of the i -species and r denotes distances between the central monomers, this corresponds, roughly, to the centers of mass accumulating in one region and the polymers in the minority phase building clusters. There is therefore good agreement between the center-of-mass and the central monomer representation. Moreover, this clustering effect, which is more pronounced for the large polymers, is an additional signature of phase separation.

Next we consider the overall phase behaviour of the mixture and make a comparison between the binodal obtained from the HNC equation of state and that obtained from the particularly simple RPA equation of state. The simplest (RPA) mean-field Helmholtz free energy functional for the mixture reads as

$$\mathcal{F}[\{\rho_i\}] = \mathcal{F}_{id}[\{\rho_i\}] + \frac{1}{2} \sum_{ij} \int d^3 r_1 \int d^3 r_2 \rho_i(\mathbf{r}_1) \rho_j(\mathbf{r}_2) v_{ij}(|\mathbf{r}_1 - \mathbf{r}_2|) \quad (8.3.4)$$

where \mathcal{F}_{id} is the ideal gas part – recall from Ch. 5 that this functional generates the RPA direct pair correlation functions

$$c_{ij}^{(2)}(\mathbf{r}_1, \mathbf{r}_2) = c_{ij}^{(2)}(|\mathbf{r}_1 - \mathbf{r}_2|) = -\beta v_{ij}(|\mathbf{r}_1 - \mathbf{r}_2|). \quad (8.3.5)$$

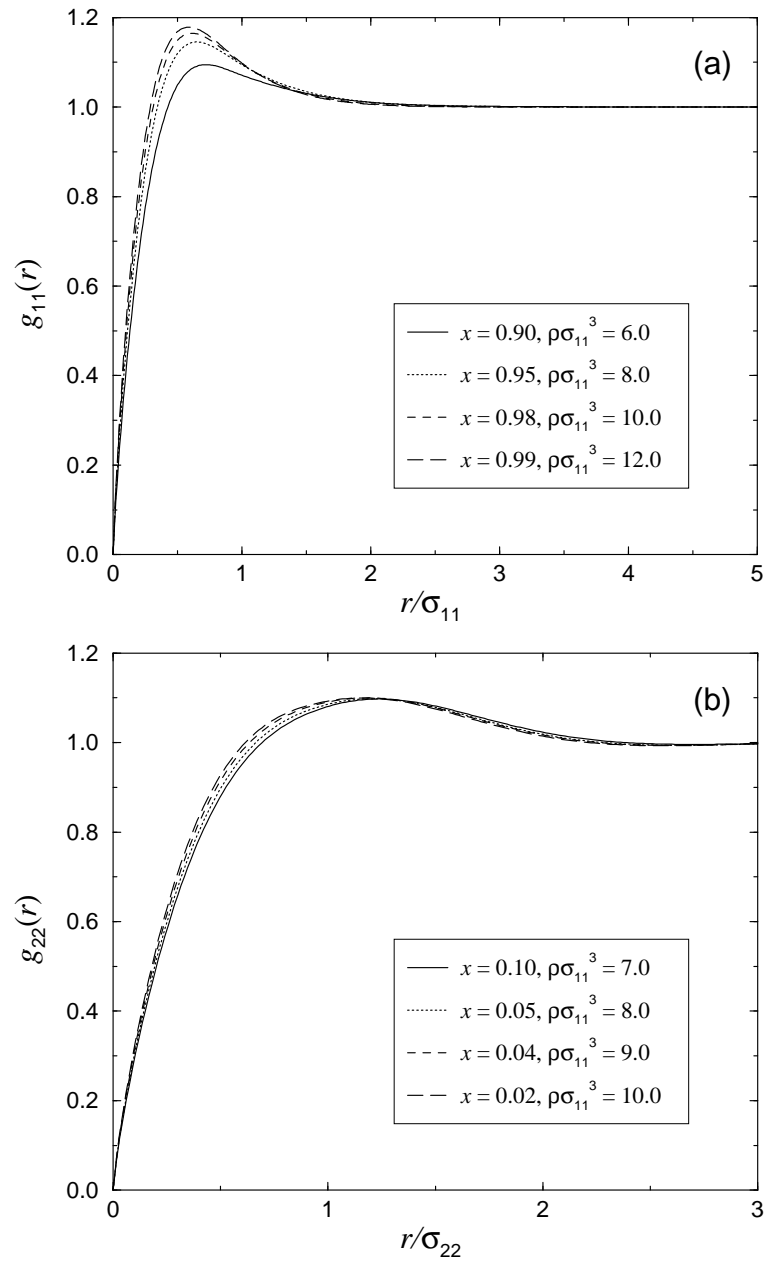


Figure 8.2: The HNC radial distribution functions $g_{ii}(r)$ of the minority phases at high total densities. (a) Large particles, $g_{11}(r)$ and (b) small particles, $g_{22}(r)$.

This functional (8.3.4) replaces all excess free energy contributions with the mean-field interaction terms that are bilinear in the density profiles $\rho_i(\mathbf{r})$ of the components. Such an approximation is expected to be accurate for the system at hand, which is deprived of hard cores and of significant short-range, excluded-volume correlations, in particular at high densities when the particles interact with a very large number of ‘neighbours’. In the bulk mixture the densities are constants, $\rho_i(\mathbf{r}) = \rho_i$. Expressing these in terms of the total density ρ and the composition variable x , we can write the bulk Helmholtz free energy per particle \tilde{f} , as

$$\tilde{f}(\rho, x) = \tilde{f}_{id}(\rho, x) + \frac{1}{2}\rho[(1-x)^2 \hat{v}_{11}(0) + 2x(1-x) \hat{v}_{12}(0) + x^2 \hat{v}_{22}(0)], \quad (8.3.6)$$

which is equivalent to Eqs. (5.2.6) and (5.2.7). The ideal contribution, $\tilde{f}_{id}(\rho, x)$, contains the ideal free energy of mixing, $\beta^{-1}\{x \ln(x) + (1-x) \ln(1-x)\}$ as well as an irrelevant term with linear- ρ dependence. $\hat{v}_{ij}(0)$ is the $q = 0$ limit of the Fourier transform (FT) of the pair potential:

$$\hat{v}_{ij}(0) = \int d^3r v_{ij}(r). \quad (8.3.7)$$

Note that Eq. (8.3.6) is equivalent to calculating \tilde{f} from the compressibility route. We Legendre transform to obtain the Gibbs free energy per particle $g = \tilde{f} + Pv$; where $v = 1/\rho$ is the volume per particle, and the pressure is given as $P = -(\partial \tilde{f} / \partial v)_x$. The common tangent construction on g yields the binodal (see also Ch. 5 Sec. 5.2) which is plotted along with the spinodal in Fig. 8.3. We find that the binodal has a very similar shape to that found for the GCM in Ch. 5, since they both have the same form for the bulk Helmholtz free energy (8.3.6), but they differ in where they locate the critical point. For the present star polymer model we find the critical point at $\rho_c \sigma_{11}^3 = 5.7$ where the star corona diameter $\sigma_{11} \simeq 1.32 R_{11}^g$, with R_{11}^g the radius of gyration [132, 138]. On the other hand, for the GCM studied in Ch. 5 we found $\rho_c R_{11}^3 = 5.6$ with radius $R_{11} \simeq R_{11}^g$.

We also determined the HNC-phase diagram. The HNC closure breaks down before a spinodal is reached, as is well-known from previous studies [139, 140]. However, this poses no difficulties in calculating the HNC binodals.³ For all points in the region where the HNC converges, we calculate the pressure P and partial chemical potentials μ_1, μ_2 on a grid. For the HNC, this calculation is local, i.e., one needs no thermodynamic integration

³We found, in fact, that the locus of points on which the HNC fails to converge is a curve that runs close to the RPA-spinodal and in the U-shaped region in the high-density part of this curve the HNC has no solutions.

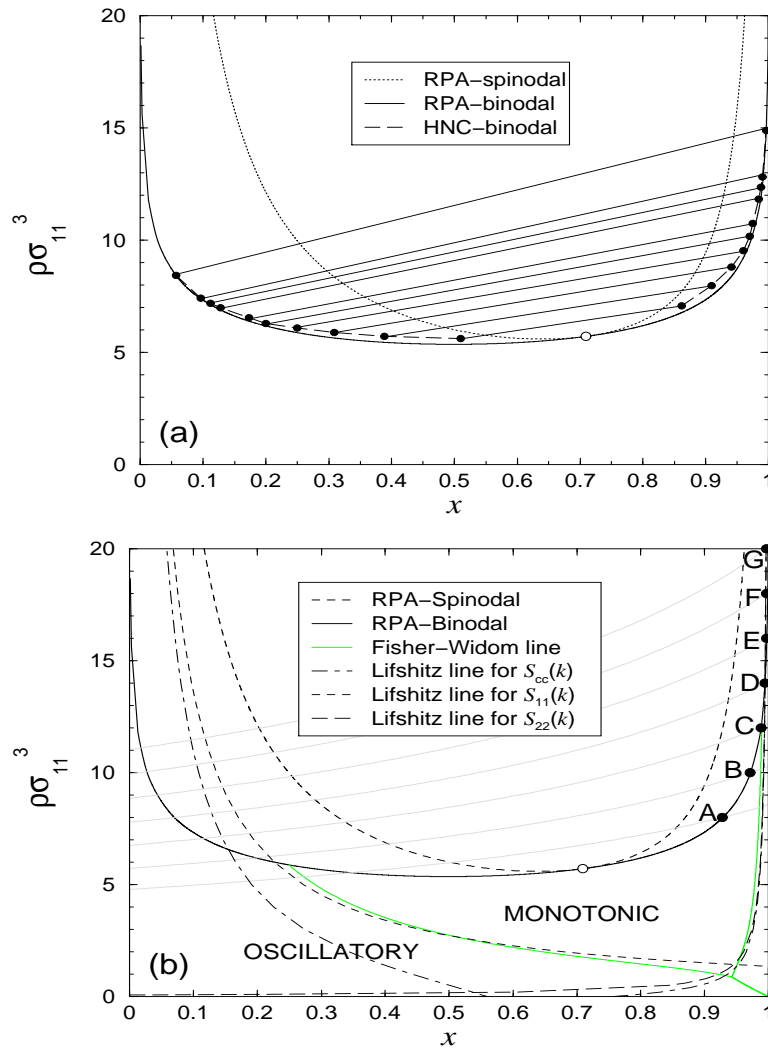


Figure 8.3: (a) The RPA-spinodal and binodal lines for the star-polymer mixture (dotted and solid lines) along with the HNC-binodal (dashed line). x is the concentration of species 2, the smaller component. The straight segments denote HNC-tielines between coexisting fluid phases whose coordinates are given by the closed circles at their ends. (b) The RPA-phase diagram along with the Fisher-Widom line (light solid line) and the Lifshitz lines of the various structure factors. The left hand branch of the FW line lies close to the Lifshitz line for $S_{11}(k)$ (short dashed line) while the right hand branch lies close to the Lifshitz line for $S_{22}(k)$ (long dashed line). The dash-dotted line is the Lifshitz line for $S_{cc}(k)$. The points A-G on the right-hand branch of the binodal are located at total densities $\rho\sigma_{11}^3 = 8, 10, 12, 14, 16, 18$ and 20 , at which the free interface density profiles will be calculated in Section 8.4. The gray lines are RPA-isobars through the points A-G and their intersections with the left-hand branch of the binodal yield the state points coexisting with A-G. The open circle denotes the RPA-critical point.

to obtain μ_1 and μ_2 [47, 141], since within the HNC

$$\beta\mu_i = \ln(\Lambda_i^3 \rho_i) + \sum_j \left[\frac{\rho_j}{2} \int d\mathbf{r} h_{ij}(r)[h_{ij}(r) - c_{ij}(r)] - \rho_j \hat{c}_{ij}(0) \right] \quad (8.3.8)$$

where $h_{ij}(r)$ and $c_{ij}(r)$ are the HNC total and direct pair correlation functions. From μ_1 and μ_2 , the Gibbs free energy per particle $g = (1-x)\mu_1 + x\mu_2$ is readily obtainable. We perform a 2d-interpolation of the pressure results to obtain $P(x, \rho)$ as a function of two variables for any x and ρ , and on this surface we determine the isobar curves $P = \text{constant}$. We then draw the Gibbs free energy along the isobars to obtain $g_P(x)$, where the subscript now denotes that P is fixed. For those pressures for which $g_P(x)$ is a convex function of x , the system is in a single (mixed) state. For those for which it is not, the common tangent construction determines the coexistence concentrations and densities. The region in which the HNC has no solutions presents no difficulties. For the isobars that intersect the borderline of this region, we simply have $g_P(x)$ with two ‘branches’ on either side of the prohibited domain and we perform the common tangent construction on those.

The HNC binodal is plotted in Fig. 8.3 along with the RPA one. It can be seen that there is very good agreement between the two. The RPA-binodal is slightly broader but the discrepancies become quickly suppressed in moving away from the critical point. If one interprets the total density as an ‘inverse temperature’ and the concentration as a ‘density’ of a hypothetical one-component system, then the phase diagram can be regarded as that corresponding to ‘liquid-gas’ coexistence. The RPA is then equivalent to the mean-field approximation, which usually delivers critical temperatures *higher* than the true result. That the RPA critical density is *lower* than the HNC-one can be explained by means of this analogy. The largest discrepancies between HNC and RPA occur close to the critical point but these are less than 10% for the location of the binodal on the density axis. Otherwise, the remarkable accuracy of the RPA can be understood by the fact that the phase separation for our binary fluid occurs at a sufficiently high density that the differences between the RPA and HNC routes to the bulk structure and thermodynamics are indeed very small. We demonstrate this in Fig. 8.4, where we show representative results for the chemical potentials and the pressure obtained by the two approaches. We note that Finken *et al.* [47] have also made comparisons between the RPA and HNC results for the binodal in the case of a binary mixture of repulsive GCM particles. They report larger differences between the two theories than we find here. At present it is not

clear why the differences should be larger for GCM particles than for the (very similar) logarithmic-Gauss potentials we consider in the present study.

More detailed information about the nature of the interparticle correlations in the mixture can be obtained by investigating the Fisher-Widom (FW) line [2]. The FW line is determined by the asymptotic decay, $r \rightarrow \infty$, of the total pairwise correlation functions $h_{ij}(r)$. It is the locus of points in the phase diagram, at which the ultimate decay of the pair correlation functions crosses over from monotonic (Ornstein-Zernike like) to damped oscillatory. The method for determining the FW line in mixtures is described in Ch. 5 Sec. 5.4, see also Ref. [52]. Using the RPA approximation for the direct pair correlation function, $\hat{c}_{ij}(q) = -\beta\hat{v}_{ij}(q)$, greatly facilitates the calculation of the FW-line (as it did for the GCM), since the Fourier transforms $\hat{v}_{ij}(q)$ are analytic (see Appendix E). The FW line for the present mixture is displayed in Fig. 8.3. We find that FW line is almost exactly the same in shape and location in the phase diagram as that found, also using the RPA, for the binary GCM corresponding to a 2:1 length ratio mixture of polymers – see Fig. 5.1. We also find the same cusp in the FW line (bottom right hand corner, Fig. 8.3(b)) and the new line found for the GCM in Ch. 5. The latter denotes the crossover from oscillatory decay with one wavelength, corresponding to the length-scale associated with one of the particle species, to oscillatory decay with another wavelength, determined by the size of the other species of particles. Because the RPA binodal and FW lines are so similar in the present model to those found for the binary GCM in Ch. 5, we expect the trends found as particle size asymmetry was varied in the GCM, to carry over to the present model, i.e., as the size asymmetry is increased, the location of the critical point should move towards the side of the phase diagram rich in the smaller species and the cusp in the FW line should move to this side also. Note also that the pole determining the asymptotic decay of $g_{ij}(r)$ also sets the common bulk correlation length: $\xi = 1/\alpha_0$ [52]. It is possible to calculate the leading pole from numerical solutions of the HNC [57], however we expect the asymptotic decay to be very well captured by the RPA, and the dominant HNC pole to be very similar in value to that obtained from the analytically tractable RPA, as was the case for the one-component GCM,⁴ – see Fig. 5.12.

The Lifshitz line [142, 143]⁵ separates the region in the phase diagram in which $S_{ij}(k)$

⁴L.R. Croft, private communication.

⁵We note that for microemulsions both the Lifshitz- and the FW-line are used to signify the crossover from the ‘sponge phase’ to the ‘random phase’ (there is no sharp thermodynamic transition between

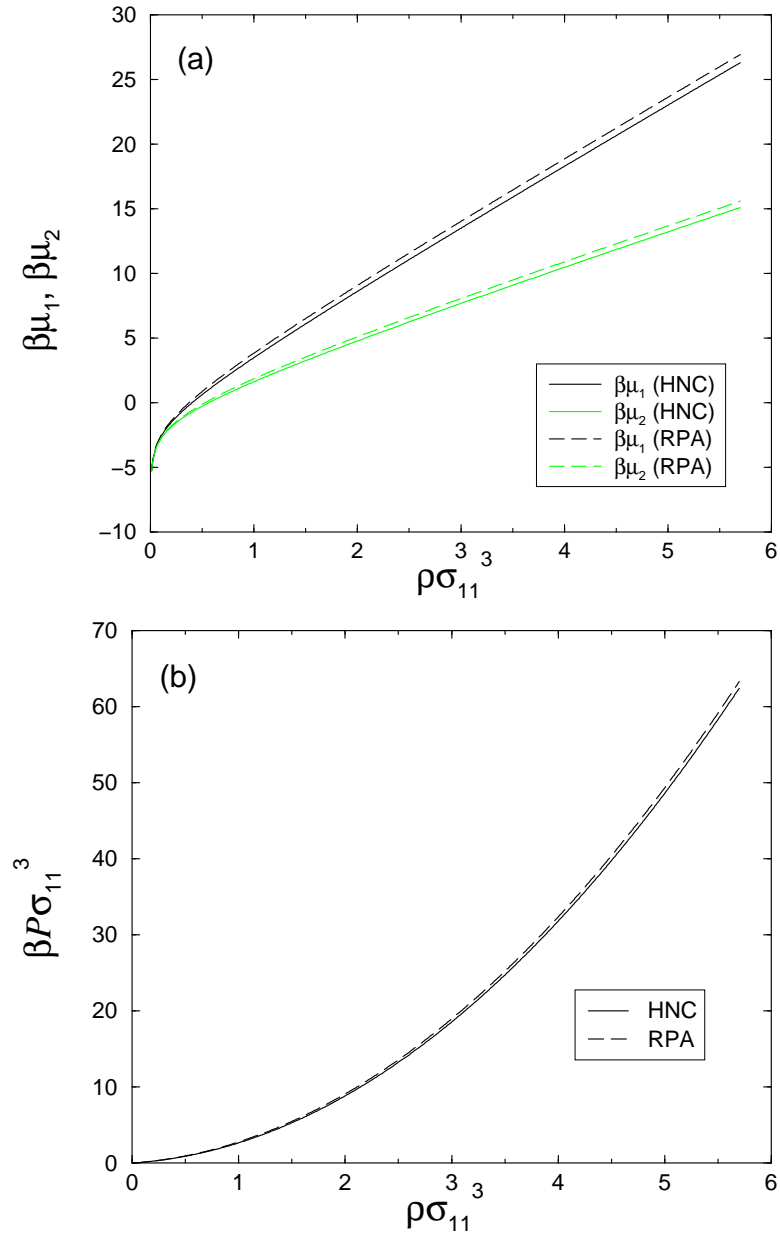


Figure 8.4: Comparison of the HNC- and RPA-results for the partial chemical potentials (a) and the total pressure (b), at fixed concentration $x = 0.5$ and increasing total density ρ .

has a local maximum at $k = 0$ (as occurs near a critical point or spinodal) from that in which it has a local minimum at $k = 0$. Making a small k expansion of the partial structure factors

$$S_{ij}(k) = a(\rho, x) + b(\rho, x)k^2 + O(k^4), \quad (8.3.9)$$

and examining the sign of the term $b(\rho, x)$, one sees that the Lifshitz line is the locus of points $b(\rho, x) = 0$. The Lifshitz lines for two of the partial structure factors are displayed in Fig. 8.3 and their shapes are similar to branches of the FW-line. This is because their locations are driven by the proximity of the spinodal, which forces $S_{11}(k)$ and $S_{22}(k)$ to have maxima at $k = 0$. These maxima survive as long as the pure imaginary pole (away from the spinodal) is the dominant one. Close to the crossover to damped oscillatory decay in $h_{ij}(r)$, at the FW line, the maximum turns into a minimum. Hence the Lifshitz and the FW-lines are closely related to one another but they are not identical. Since phase separation in liquid mixtures is driven by concentration fluctuations it is natural to examine the Lifshitz line for the concentration-concentration structure factor $S_{cc}(k)$ defined in Eq. (8.3.3). As can be seen in Fig. 8.3, the domain enclosed by the Lifshitz line, in which $S_{cc}(k = 0)$ is a maximum, is broader than the domain in which both $S_{11}(k = 0)$ and $S_{22}(k = 0)$ are local maxima. This is the effect of the term $-2x(1-x)S_{12}(k)$. In fact, the Lifshitz line for $S_{cc}(k = 0)$ does not close: even at very low densities, there survives a domain, in this case $0.55 \lesssim x \lesssim 0.77$, in which $S_{cc}(k)$ has a small maximum at $k = 0$. The Lifshitz line for $S_{12}(k)$ runs similarly to the one for $S_{11}(k)$, but the regions it separates are inverted with respect to the ones for $S_{11}(k)$ and $S_{22}(k)$: above the Lifshitz line for $S_{12}(k)$, the latter has a local minimum at $k = 0$ and below it a local maximum,⁶ whereas the situation is inverted for the other two.

8.4 The free fluid-fluid interface

In this section we calculate the inhomogeneous one-body density profiles of the fluid at the planar interface between two coexisting phase-separated liquid phases and the corre-

the two, hence one resorts to structural criteria) [142, 143]. The locations of the two lines in the phase diagram are related, as in the present fluid. We note also that in the microemulsion literature the FW-line is referred to as the disorder line [142], the latter terminology being the common one for Ising models [144, 145, 146, 49].

⁶Note that at the spinodal $S_{12}(k = 0)$ diverges to minus infinity, not to plus infinity as do $S_{11}(k = 0)$ and $S_{22}(k = 0)$.

sponding surface tension γ , using the same DFT (8.3.4) which generates the RPA. Once again we work with the grand potential functional

$$\Omega_V[\{\rho_i\}] = \mathcal{F}[\{\rho_i\}] - \sum_i \int d^3r (\mu_i - V_i(\mathbf{r})) \rho_i(\mathbf{r}), \quad (8.4.1)$$

where μ_i is the chemical potential of species $i = 1, 2$, and determine the free interface density profiles by setting the external potentials $V_i(\mathbf{r}) = V_i(z) = 0$. Recall from Ch. 5.3 that within the present mean field approach the resulting profiles $\rho_i(z)$, with z normal to the interface, are non trivial, i.e., the interface has a finite width. Minimising (8.4.1) and using (8.3.4) for $\mathcal{F}[\{\rho_i\}]$ yields a pair of coupled Euler-Lagrange equations for the profiles. Due to the planar symmetry these can be reduced to a pair of 1-dimensional equations:

$$\mu_i - V_i(z) = \mu_{i,id}(\rho_i(z)) + \sum_j \int dz' \rho_j(z') \tilde{v}_{ij}(|z - z'|), \quad \text{for } i, j = 1, 2 \quad (8.4.2)$$

where the ideal gas chemical potential $\mu_{i,id}(\rho_i) = \beta^{-1} \ln(\Lambda_i^3 \rho_i)$ (Λ_i is the thermal de-Broglie wave-length) and

$$\tilde{v}_{ij}(|z - z'|) = \int_{-\infty}^{\infty} dx \int_{-\infty}^{\infty} dy v_{ij}(|\mathbf{r} - \mathbf{r}'|). \quad (8.4.3)$$

Eqs. (8.4.2) can be solved self consistently for the density profiles of the two species. We find results very similar to those for the binary GCM in Ch. 5; again, the weak divergence of the pair potential $v_{ij}(r)$ has little effect. When (8.2.1) is substituted into (8.4.3) we find that $\tilde{v}_{ij}(z)$ is finite for all z : on integrating over the $x - y$ plane the $-\ln(r)$ divergence in $v_{ij}(r)$ yields a term $\sim z^2 \ln(z)$, which is finite as $z \rightarrow 0$. In fact $\tilde{v}_{ij}(z)$ resulting from Eqs. (8.2.1) and (8.4.3) has a very similar shape to that resulting from substituting $v_{ij}(r) = \epsilon_{ij} \exp(-r^2/R_{ij}^2)$ (GCM) into (8.4.3). The resulting density profiles for the coexisting states marked in Fig. 8.3(b) are displayed in Fig. 8.5. We find pronounced oscillations in the density profile of the larger species, $\rho_1(z)$, for states well removed from the critical point, similar to those we found for the GCM in Ch. 5. For states B-G (see the phase diagram Fig. 8.3) both density profiles $\rho_1(z)$ and $\rho_2(z)$ exhibit non-monotonic decay into the bulk phase which is rich in species 1. On the other side of the interface, approaching the bulk phase rich in species 2, magnification shows that both $\rho_1(z)$ and $\rho_2(z)$ are non-monotonic for states E-G. For state A, closer to the critical point, there is no sign of oscillations on either side of the interface.

As with the GCM, it seems to be the location of the FW line that determines the crossover from monotonic to damped oscillatory decay in the free interface density profiles.

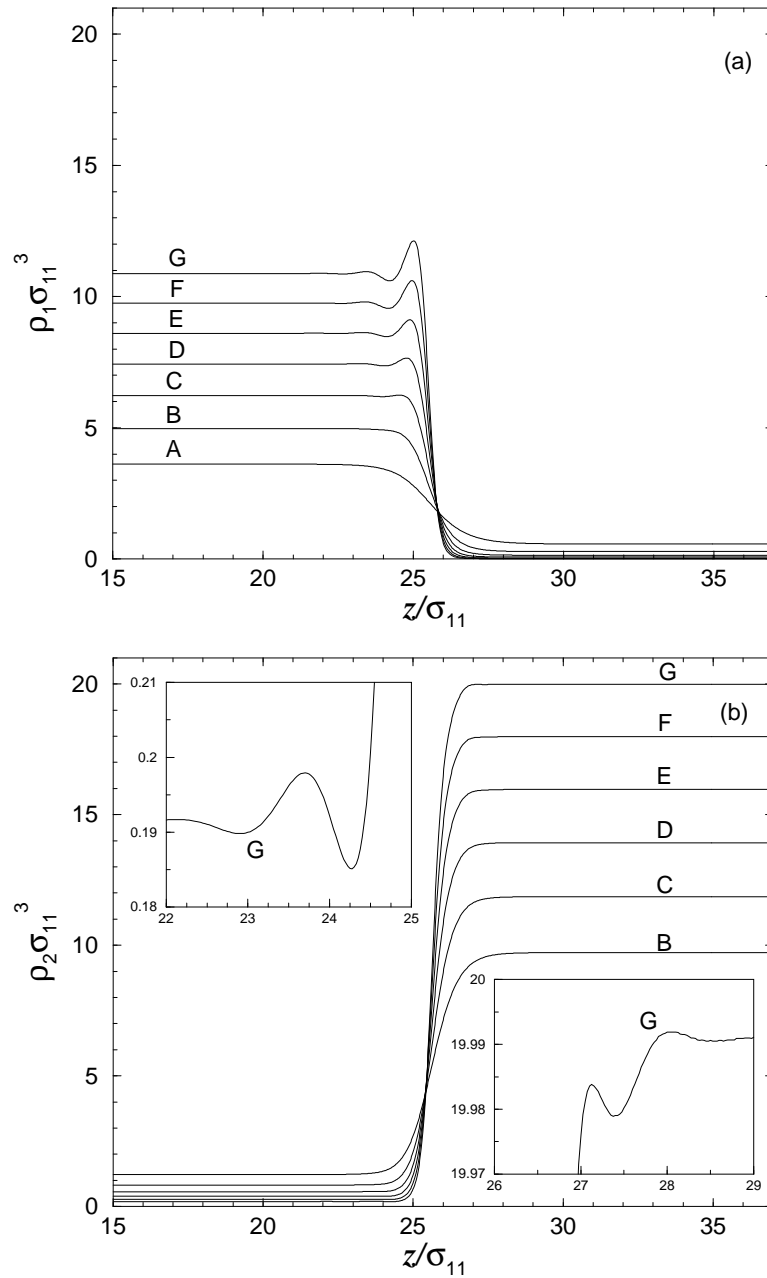


Figure 8.5: The fluid-fluid interface density profiles, calculated at states A-G in the phase diagram [see Fig. 8.3(b)]. State A lies near the critical point and state G, for which the interface is much sharper, far away from the critical point. These states correspond to total bulk densities $\rho \sigma_{11}^3 = 8, 10, 12, 14, 16, 18$ and 20 in the phase rich in species 2. (a) Density profiles of species 1, the larger species. (b) Density profiles of species 2. The insets show magnified regions for state G. Note the oscillations on both sides of the interface.

On moving along the binodal away from the critical point, and crossing the intersection with the FW line, there are bulk states (on the binodal) at which the pair correlation functions, $h_{ij}(r)$, decay in a damped oscillatory fashion. Since it is the same pole in the structure factors that determines the asymptotic decay of the one-body density profiles, $\rho_i(r)$, for these states on the oscillatory side of the FW line one should expect damped oscillatory decay of $\rho_i(r)$ into the bulk phase. For the present model the FW line intersects the binodal on both sides so that when both bulk coexisting states are on the oscillatory side of the FW line, then the asymptotic decay of the density profiles will be damped oscillatory on both sides of the interface – as we found in Ch. 5 for the binary GCM.

Having calculated the equilibrium free interface density profiles we can determine the surface tension, which is defined as the excess grand potential per unit area and can be written as

$$\gamma = \int_{-\infty}^{\infty} dz (P + \omega(z)), \quad (8.4.4)$$

where P is the bulk pressure at coexistence and $\omega(z)$ is the grand potential density obtained from Eqs. (8.3.4) and (8.4.1) with $V_i(z) = 0$. The reduced tension $\gamma^* = \beta\gamma\sigma_{11}^2$ is plotted in Fig. 8.6 for the interfaces corresponding to Fig. 8.5. We have chosen to plot γ^* versus the order parameter $(\rho_1^A - \rho_1^B)\sigma_{11}^3$, where ρ_1^A is the bulk density of species 1 in phase A , rich in species 1, and ρ_1^B is the same quantity in phase B , poor in species 1 – as we did for the binary GCM in Ch. 5. Mean-field arguments imply that γ^* should vanish as $(\rho_1^A - \rho_1^B)^3$ on approaching the critical point and this is confirmed by our numerical results (see inset to Fig. 8.6).

We can obtain an estimate for the surface tension of a phase separated mixture of ‘real’ star-polymers by choosing $\gamma^* = 5$, corresponding to a state well removed from the critical point, and setting $T = 300$ K and $\sigma_{11} = 20$ nm. We find $\gamma = 52 \mu\text{N/m}$, the same as for the GCM.

The numerical values of γ^* determine whether we can expect to observe oscillatory density profiles in a more accurate treatment of the free interface. As the present mean field functional does not include the effects of capillary wave fluctuations one needs to make an estimate of these fluctuation effects on oscillatory structure [7]. In Ch. 5 on the GCM free interface we addressed the issue of whether capillary-wave fluctuations would destroy the layering structures we found in the DFT treatment of the interface. The situation for the present model is the same as for the GCM; i.e., we assume that DFT describes the ‘bare’ or ‘intrinsic’ profiles – which might be oscillatory, as in the

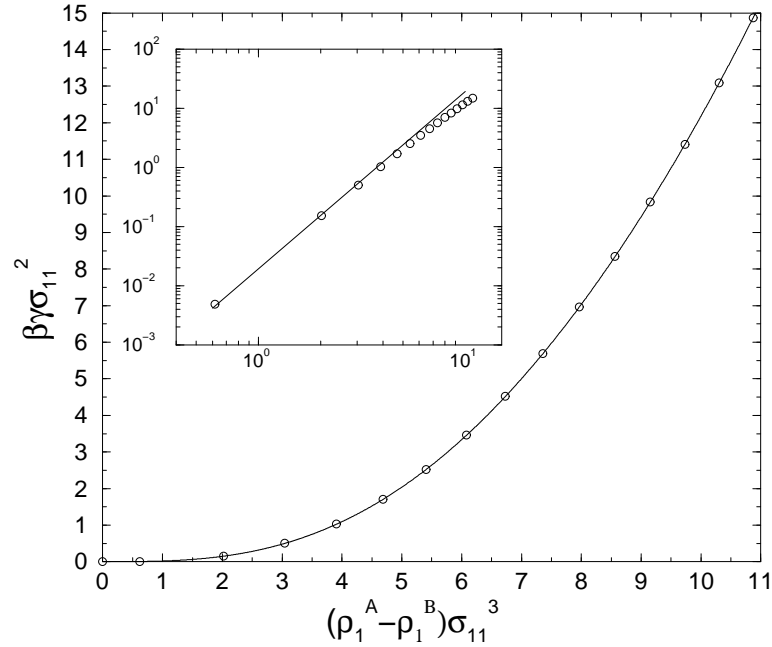


Figure 8.6: The reduced surface tension, $\gamma^* = \beta\gamma\sigma_{11}^2$, at the planar free interface, plotted against the order parameter $(\rho_1^A - \rho_1^B)\sigma_{11}^3$, the density difference in species 1 between the two phases, which vanishes at the critical point. The line joining the data points is a guide to the eye. Inset: double-logarithmic plot of the same quantities, demonstrating the power-law dependence of γ^* ; the straight line has gradient 3.

present case – and that fluctuations can be unfrozen on these. If one performs a Gaussian smearing of the profiles over the interfacial thermal roughness ξ_\perp for a density profile with decaying oscillations of wavelength $2\pi/\alpha_1$ and decay length $\tilde{\alpha}_0^{-1}$, these quantities are unaltered but the amplitude is reduced by a factor $\exp[-(\alpha_1^2 - \tilde{\alpha}_0^2)\xi_\perp^2/2]$ [52, 61]. The roughness ξ_\perp depends on the interfacial area L_x^2 and on the external potential, e.g. gravity. Ignoring the latter one finds that the amplitude of the oscillations in the density profile should be reduced by a factor $(L_x/\xi)^{-\omega[(\alpha_1/\tilde{\alpha}_0)^2-1]}$ where $\omega \equiv (4\pi\beta\gamma\xi^2)^{-1}$ is, as usual, the dimensionless parameter which measures the strength of capillary wave fluctuations and $\xi \equiv (\tilde{\alpha}_0)^{-1}$. The larger the value of $\omega \propto 1/\gamma^*$, the more damped are the oscillations. As mentioned in Ch. 5.5 the power law dependence on the interfacial area L_x^2 that this unfreezing procedure predicts is supported by the simulations of Toxvaerd and Stecki [62] and those of Chacón *et al.* [58, 59, 60]. For the present model at states where the oscillations in the DFT profiles are very pronounced, as with the GCM, the calculated

exponent in the power law is small, typically -0.1 , which implies that the the amplitude of the oscillations at these particularly ‘stiff’ interfaces should only be weakly damped by the capillary-wave fluctuations. As emphasized in Ch. 5 the reduced surface tension γ^* far from the critical point is very large in these liquid mixtures since the coexisting phases correspond to a very high pressure and there are very large density differences, for the individual species, between the phases – see Fig. 8.3. Such large values of γ^* do not normally arise at the liquid-vapour interface of simple, one-component fluids where the solid phase intervenes at low temperatures. However the model considered by Chacón *et al.* [58, 59, 60] ensures that the ratio of the melting temperature T_m to the critical temperature T_c is small, i.e., $T_m/T_c \lesssim 0.2$, and in these circumstances γ^* can be large and then damping of the oscillations is weak.

8.5 Star-polymers at a hard wall: wetting behaviour

By integrating the normal component of the osmotic pressure in the interior of the star polymer along the area of contact between the star and the wall, Jusufi *et al.* [132] were able to calculate the force, $F(z)$, and therefore the potential acting between a star-polymer and a hard wall, with z denoting the distance from the star center to the planar wall surface. The force scales as $F(z) \sim 1/z$ as $z \rightarrow 0$, and for $z \rightarrow \infty$ the form $F(z) \sim (\partial/\partial z)\text{erf}(\kappa_i z)$ pertains, where $\text{erf}(x) = (2/\sqrt{\pi}) \int_0^x dt \exp(-t^2)$ is the error function and κ_i^{-1} is a length scale of order the radius of gyration of the polymer. For a star polymer with $f = 2$, the value $\kappa_i = 1.16/\sigma_{ii}$ was found to give the best fit to simulations [132]. By matching these two forms at $z = \sigma_{ii}/2$ and then integrating to get the potential, Jusufi *et al.* [132] proposed the following form for the effective potential $V_i(z)$ between a star polymer and a hard, planar wall:

$$\beta V_i(z) = \Lambda f^{3/2} \begin{cases} -\ln\left(\frac{2z}{\sigma_{ii}}\right) - \left(\frac{4z^2}{\sigma_{ii}^2} - 1\right) \left(\psi_i - \frac{1}{2}\right) + \zeta_i & \text{for } z \leq \sigma_{ii}/2; \\ \zeta_i \text{erfc}(\kappa_i z) / \text{erfc}(\kappa_i \sigma_{ii}/2) & \text{for } z > \sigma_{ii}/2 \end{cases} \quad (8.5.1)$$

where $\text{erfc}(x) = 1 - \text{erf}(x)$ is the complementary error function, $\psi_i = (1 + \kappa_i^2 \sigma_{ii}^2/2)^{-1}$ is a parameter chosen to guarantee the continuity of the local osmotic pressure in the interior of the star polymer and

$$\zeta_i = \frac{2\sqrt{\pi}\psi_i}{\kappa_i\sigma_{ii}} \text{erfc}\left(\frac{\kappa_i\sigma_{ii}}{2}\right) \exp\left(\frac{\kappa_i^2\sigma_{ii}^2}{4}\right). \quad (8.5.2)$$

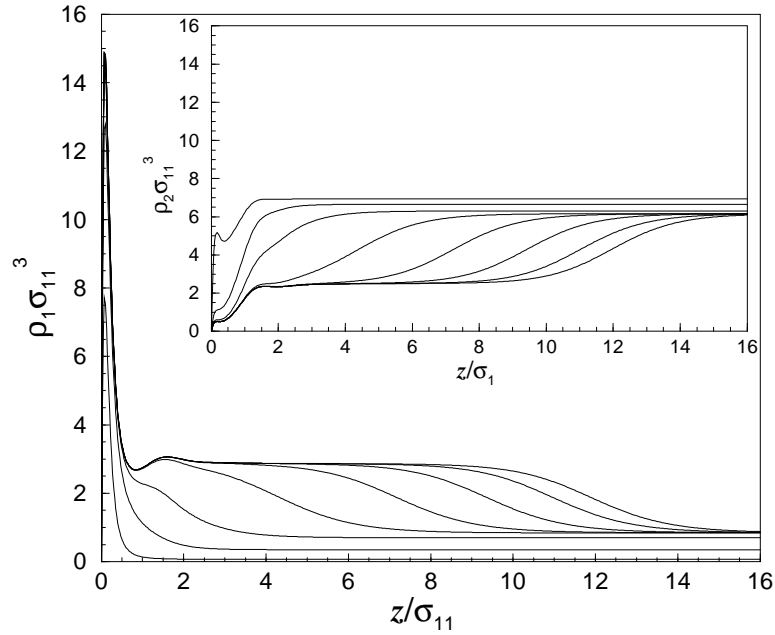


Figure 8.7: The density profiles of species 1, the larger particles, adsorbed at a wall described by the potential (8.5.1), calculated along a path of constant total density, $\rho\sigma_{11}^3 = 7.0$, i.e., path A in Fig. 8.8. From left to right the profiles refer to $x = 0.99, 0.95, 0.9, 0.88, 0.879, 0.878955, 0.878951$ and 0.8789505 , where x is the concentration of species 2 and $x_{\text{coex}} = 0.87895019$. The thickness of the adsorbed film increases continuously as $x \rightarrow x_{\text{coex}}^+$, indicating complete wetting. The inset shows the density profiles of species 2 for the same values of x . Note that species 2 is depleted from the region adjoining the wall.

The final parameter Λ , which has a weak f dependence, is also chosen to match the simulation results, giving $\Lambda = 0.46$ when $f = 2$ [132].

By using Eq. (8.5.1) for the external potential in Eq. (8.4.1) we are modeling the binary star polymer fluid at a hard wall. We found that for certain states approaching the binodal on the side poor in species 1, the larger particles, a thick wetting layer of the coexisting phase rich in species 1 was adsorbed at the wall, the thickness of which diverged at the binodal. Typical wetting density profiles are displayed in Fig. 8.7. These were calculated along a constant density path $\rho\sigma_{11}^3 = 7.0$, approaching the binodal (path A in Fig. 8.8). Upon investigating higher total densities we found there is a first order wetting transition, above which the wall no longer wets completely. The point on the binodal at which the

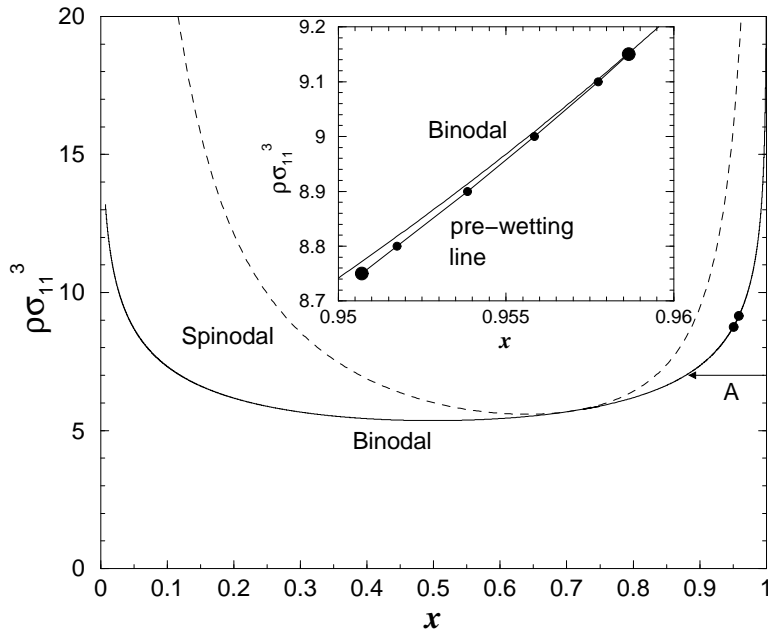


Figure 8.8: The phase diagram obtained from the RPA (as in Fig. 8.3). The two filled circles show the location of the pre-wetting line. The upper point on the binodal is the wetting point where the pre-wetting line meets the binodal tangentially and the lower point is the critical point at the end of the pre-wetting line. The inset shows the pre-wetting line at greater magnification. The horizontal path labeled A is that along which the density profiles in Fig. 8.7 are calculated.

wetting transition occurs, the wetting point, is at $(x, \rho\sigma_{11}^3) = (0.959, 9.15)$. Descending from the wetting point is a short pre-wetting line, ending in a pre-wetting critical point at $(x, \rho\sigma_{11}^3) = (0.951, 8.75)$. The pre-wetting line is displayed in Fig. 8.8. This wetting scenario is very similar to that which we found in Ch. 6 for the binary GCM fluid at a planar wall with a repulsive Yukawa potential mimicking the effective potential between the Gaussian particles and a hard wall.

The wetting point and the pre-wetting line were determined by analysing the density profiles and the adsorption of species 1, Γ_1 , defined by

$$\Gamma_1 = \int_0^\infty dz (\rho_1(z) - \rho_1), \quad (8.5.3)$$

where $\rho_1 = \rho_1(\infty)$, the density of species 1 in the bulk, i.e., far away from the wall. At the pre-wetting line, the adsorption exhibits a discontinuous jump. In Fig. 8.9, the adsorption calculated along constant total density paths ($\rho\sigma_{11}^3 = 9.0, 8.9, 8.8$ and 8.7) approaching

the binodal is plotted. Figs. 8.9(a)-(c) correspond to paths that intersect the pre-wetting line, whereas the path of Fig. 8.9(d) passes just below the pre-wetting line critical point. We determine the location of the pre-wetting line by monitoring the jump in Γ_1 and, in the region of the pre-wetting critical point, the erosion of two branches in the free energy. On solving numerically for the density profiles, one moves first along one branch, and then jumps to the other before converging to the equilibrium solution. Note also that the interfacial compressibility, $\chi_{12} = \partial\Gamma_1/\partial\mu_2 \propto (\partial\Gamma_1/\partial x)_\rho$ still has a pronounced peak below the critical point – see Fig. 8.9(d). The jump in the adsorption decreases for intersecting paths approaching the pre-wetting critical point. These results should be compared with those of Fig. 8.10, where Γ_1 is plotted along the $\rho\sigma_{11}^3 = 7.0$ path (path A in Fig. 8.8), along which the density profiles in Fig. 8.7 are calculated. This path is far away from the wetting transition, and the film thickness increases smoothly with no jumps as the binodal is approached; the thickness eventually diverging at the binodal.

We find that in the limit $x \rightarrow x_{\text{coex}}^+$, below the wetting point Γ_1 increases linearly with $-\ln \Delta x$, where $\Delta x = (x - x_{\text{coex}})$ is the deviation from coexistence. This linear increase with $-\ln \Delta x$ is illustrated in Fig. 8.10. For $\Delta x \rightarrow 0^+$, Γ_1 , as defined by (8.5.3), scales proportionally to the film thickness l , i.e., $\Gamma_1 \sim l(\rho_1^A - \rho_1^B)$, where ρ_1^A is the bulk coexisting density of species 1 in phase A , rich in species 1 and wetting the wall, and ρ_1^B is the bulk density in phase B , poor in species 1. Equivalent behaviour was found for the GCM in Ch. 6 where we were able to describe the results by considering an effective interface potential, Eq. (6.3.1), of the form

$$\omega_{ex}(l; x) = l(\omega^A - \omega^B) + \gamma_{w,A} + \gamma_{A,B} + ae^{-l/\xi_w} + \mathcal{O}(e^{-2l/\xi_w}), \quad (8.5.4)$$

where $\gamma_{w,A}$ is the surface tension of the wall-phase A interface, $\gamma_{A,B}$ that of the free A - B interface, a is a coefficient dependent on ρ and ξ_w is the bulk correlation length in the phase wetting the wall [11, 69, 15]. Eq. (8.5.4) is valid for a complete wetting situation; minimisation of ω_{ex} with respect to l yields the equilibrium film thickness l for a given undersaturation Δx . ω^B is the grand potential per unit volume in bulk phase B at given chemical potentials μ_1 and μ_2 , while ω^A is the corresponding quantity in phase A at the same chemical potentials. To lowest order in the chemical potential deviations:

$$\omega^A - \omega^B \simeq (\rho_1^A - \rho_1^B)\Delta\mu_1 + (\rho_2^A - \rho_2^B)\Delta\mu_2. \quad (8.5.5)$$

Since $\Delta\mu_i \equiv (\mu_i - \mu_{i,\text{coex}}) \propto \Delta x$ to lowest order, it follows that the first term on the right hand side of Eq. (8.5.4) is proportional to $l\Delta x$. Minimisation of Eq. (8.5.4) then yields

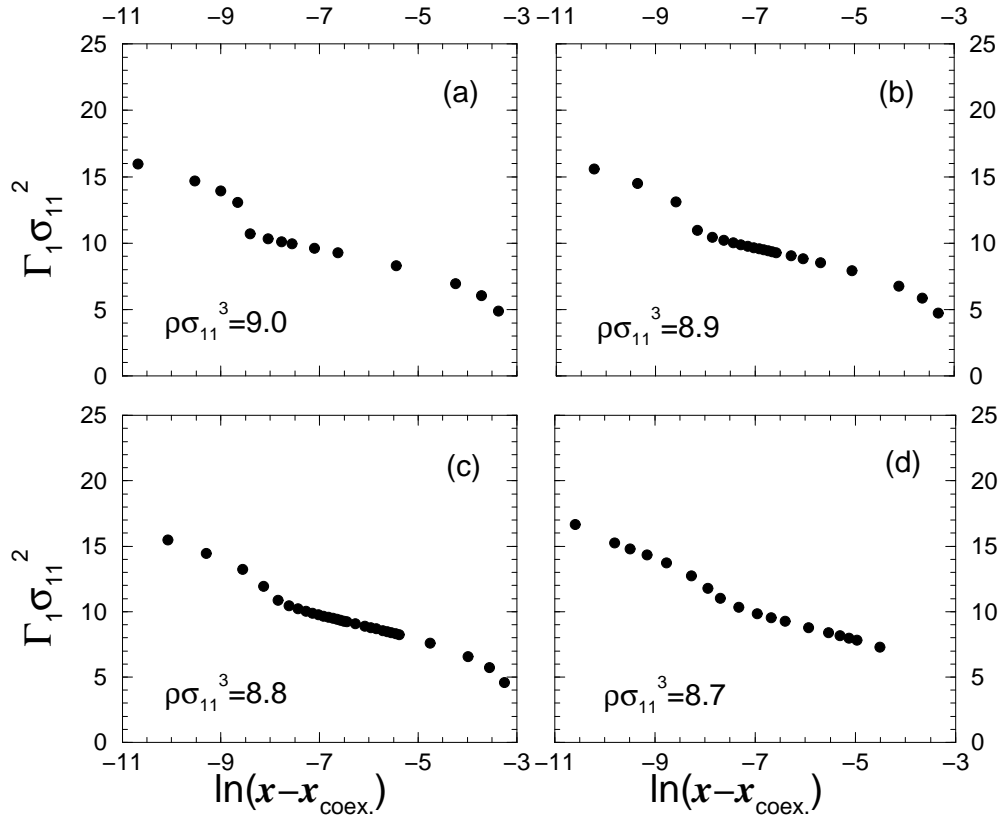


Figure 8.9: Plots of the adsorption of species 1, Γ_1 , versus the logarithm of the deviation from bulk coexistence $\ln(x - x_{\text{coex.}})$, at constant total density ρ , for paths intersecting [(a)-(c)] and passing just below (supercritical) (d) the pre-wetting line. The jumps in (a)-(c) indicate the first-order pre-wetting transition.

$l \sim -\xi_w \ln \Delta x$. We were able to confirm that the pre-factor to the logarithm is indeed $\xi_w = 1/\alpha_0$, where α_0 is the imaginary part of the pole with the smallest imaginary part (see Sec. 8.3), in the structure factors, for the bulk wetting phase A .

The wall potential (8.5.1) that we employ decays as $\text{erfc}(\kappa_i z) \sim \exp(-\kappa_i^2 z^2)/\sqrt{\pi}\kappa_i z$ as $z \rightarrow \infty$. If the wall potential we had chosen had a slower decay, then the effective interface potential (8.5.4) might have additional wall contributions – see chapters 3 and 6, in particular Sec. 6.3.2.

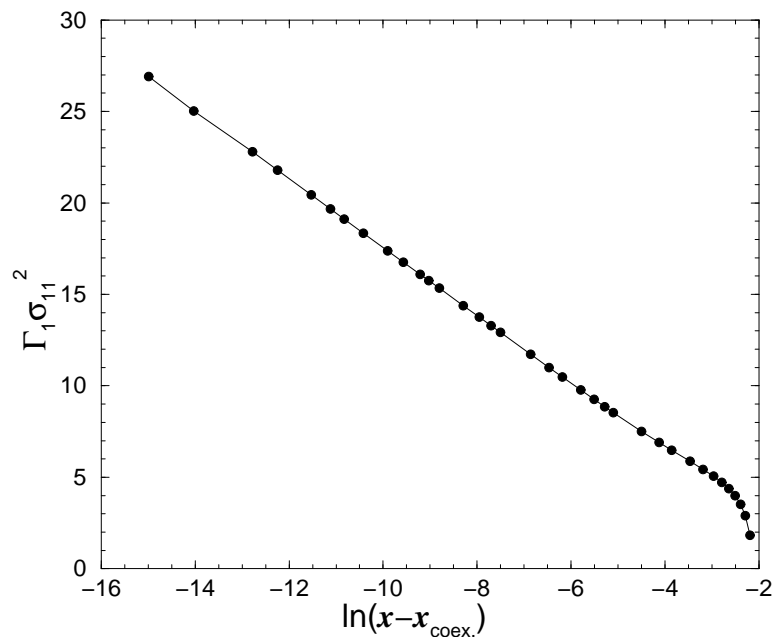


Figure 8.10: The adsorption of species 1, Γ_1 , along path A in Fig. 8.8 with constant total density, $\rho\sigma_{11}^3 = 7$, as a function of the logarithm of the deviation from bulk coexistence, $\ln(x - x_{\text{coex.}})$. The adsorption corresponds to the density profiles in Fig. 8.7. On approaching the binodal, Γ_1 increases linearly with $-\ln(x - x_{\text{coex.}})$.

8.6 Summary and concluding remarks

We have shown that a binary fluid of star-polymers, where the interactions between the star-polymers are modeled by purely repulsive effective pair potentials, can phase separate into two fluid phases. When the binodal lies at sufficiently high densities ($\rho\sigma_{11}^3 \gtrsim 5$), the quasi-exact HNC closure to the Ornstein-Zernike equations gives results for the bulk structure and thermodynamics (including the binodal) which are very similar to those from the much simpler RPA. We chose pair potential parameters to correspond to a binary fluid of $f = 2$ arm star-polymers with length ratio 2:1 in order to compare with our results for the binary GCM in Ch. 6. The GCM is an effective pair potential between the centers of mass of polymer chains, so by choosing $f = 2$ the star-polymer pair potential should also be that between the central monomers on a pair of polymers. We are therefore comparing two perspectives: ‘central monomer’ versus ‘center of mass’ as the coordinate for the effective pair potential between the polymers. Since it is the same underlying polymer system that both are describing, the thermodynamics and, therefore, phase diagrams should be

similar, and this is indeed what is found. Since the structure of the fluid is dependent on the particular ‘perspective’ one takes for describing the fluid, one should expect somewhat different structure factors and pair correlation functions. However, the two approaches give a surprisingly similar picture in terms of the location of the FW line relative to the binodal and the values for the bulk correlation length ξ . At this level it appears to matter little that one approach employs an effective pair potential that is finite at $r = 0$ (the GCM) whereas the other has a weakly diverging pair potential (the star-polymer). We also found the same line denoting the crossover in the asymptotic decay of the pair correlation functions $h_{ij}(r)$ from damped oscillatory decay with one wavelength to damped oscillatory with another wavelength, joining the cusp in the FW line, that was found for the GCM in Ch. 5.4. By calculating the Lifshitz lines we showed that the location of these is closely related to that of the FW line.

Having shown that the RPA closure is a very good approximation for bulk pair correlation functions, we used the simple Helmholtz free energy functional (8.3.4) which generates the RPA to calculate one-body density profiles for the inhomogeneous fluid mixture. In the case of the free fluid-fluid interface the density profiles of both species showed oscillations on both sides of the interface for certain states. The onset of the oscillations was accounted for by the location of the FW line. We also calculated the density profiles of the fluid at a repulsive wall potential equivalent to the effective potential between a star-polymer and a hard wall, and showed that there was a first order wetting transition, with the associated pre-wetting line. The picture that emerged from these studies of the inhomogeneous fluid is very similar to that for the binary GCM.

Chapter 9

Final Remarks

To conclude we return to possible applications of the binary GCM and the log-Gauss potentials used in Ch. 8 to describe mixtures of polymers. As mentioned in chapter 4, the effective interaction between two identical isolated nonintersecting polymer chains, averaged over the internal conformations, is well represented by a Gaussian whose width R is of the same order as the radius of gyration and whose height is a few $k_B T$. The simulation study of Louis *et al.* [19, 20] showed that the Gaussian shape remains a good approximation to the effective potential in dilute and semi-dilute solutions of self-avoiding random walk (SAW) polymers and that the parameters ϵ and R do not vary strongly with the concentration of the polymer: $\epsilon \simeq 2k_B T$. The same authors showed that the Gaussian effective potential reproduces the structure and thermodynamic properties of SAW polymer solutions over a wide concentration range. Such a procedure has great appeal as the monomer degrees of freedom no longer appear; one treats the chains as ‘soft colloids’ [19, 20]. Much less is established for mixtures of polymers; it is not known how well the phase separation found for the GCM (using the RPA and the HNC [47]) accounts for that which is observed at high concentration in mixtures of polymers with different chain lengths¹. Our results predict demixing phase separation in the semi-dilute regime, in agreement with the results of Refs. [147, 148]. Phase separation is, of course, also observed in polymer blends (melts). Given the predictions of rich interfacial behaviour that have emerged from the present study of the GCM it would be worthwhile to pursue further possible connections between demixing in polymer systems and in the GCM.

¹In order to introduce phase separation it may be necessary to introduce explicit monomer-monomer repulsion in the underlying polymer system (A.A. Louis, private communication).

One could improve upon the state-independent pair potential approximation used here which is most reliable for modeling polymers in dilute solutions ($\rho R^3 < 1$), and is only approximately correct in the semi-dilute regime [34, 20]. In the semi-dilute regime we could expect the GCM (and log-Gauss) pair potentials to acquire some additional density-dependence in their parameters, mimicking the effects of many-body forces. Since we have ignored any such dependence in this work, we expect our results to be only semi-quantitatively correct for modeling polymer mixtures in the semi-dilute regime.

The rich bulk and interfacial phenomena displayed by the simple model presented in this thesis show that the ‘colloidal approach’ of deriving effective pair potentials between complex polymeric molecules can be very fruitful. Moreover, the remarkable success of the simple and analytically tractable RPA in accounting for bulk correlation functions and thermodynamic properties of the present log-Gauss and Gaussian model opens new perspectives for the study of the properties of inhomogeneous mixtures of such ultrasoft-particle fluids. Given the variety of ways that exist in colloidal science to externally manipulate the conformations of chain-like molecules, we expect the RPA-approach to be a tool whose applicability will be much wider than simply the system of chains in athermal solvents presented here.

Although the (binary) GCM provides a simple, zeroth order model for polymers in solution, we believe the most appealing aspect of the model is that the simple RPA Helmholtz free energy functional Eq. (5.2.2), seems to provide quite an accurate description of the GCM fluid. It is the simplicity of the RPA that is useful: The GCM can be treated as a ‘test-bed’ for new theories in any of a variety of different aspects of liquid-state physics. We are referring particularly to the results in Ch. 7, where we were able to use this simple model to test whether the effects of thick adsorbed wetting films are incorporated in a general DFT method for calculating the solvent mediated potential between two large particles dissolved in a solvent near to fluid-fluid coexistence. Thanks to the simplicity of the model we were able to resolve which correlation effects were included in the theory, and which were neglected, and, for example, to determine what factors determined the depth of the SM potential. Had we used a more sophisticated functional, then we doubt whether such a detailed analysis of the influence of thick adsorbed wetting films on the SM potentials would have been possible.

Another use to which the GCM has been put, was to test the dynamical DFT proposed by Marconi and Tarazona [149, 150]. Dzubiella and Likos [151] used the one-component

GCM to test whether the dynamical DFT was able to describe a fluid confined in an external potential that was suddenly changed (for example, the situation one might envisage if there were a number of colloids confined in an optical tweezer). These authors compared the results of dynamical DFT with those of Brownian Dynamics simulations. The significance of the results of Dzubiella and Likos [151] was not in the specific properties of the dynamics of the *Gaussian* particles, rather it was the ability to test the basic formalism of the dynamical DFT using a simple model. We plan to use the binary GCM in a similar way, in order to develop theories for the dynamics of binary fluids, for example, the dynamics of phase separation for a fluid confined in an external potential. The (binary) GCM can therefore be viewed as a useful ‘test-bed’ for testing new theories.

As a final remark we note that the binary Gaussian Core Model is very different from the binary Gaussian Model introduced by Helfand and Stillinger [152] – see also Ref. [153]. In the latter $v_{11}(r) = v_{22}(r) = 0$ while the Mayer- f -function $f_{12}(r) \equiv \exp(-\beta v_{12}(r)) - 1$ is a Gaussian. This model also exhibits fluid-fluid phase separation at high densities [152, 153].

Appendix A

DFT and the Einstein Model

In this Appendix we begin by reminding the reader of the Classical Einstein model of a solid. We subsequently attempt to treat the Einstein model within a DFT framework, and show why this approach breaks down. Finally we make some, rather speculative, conclusions about DFT theories for solids in general.

The Einstein model is perhaps the simplest model of a solid. In the Einstein model we consider a set of N particles each labeled i with position \mathbf{r}_i , momentum \mathbf{p}_i and mass m . Each particle is bound by a harmonic potential

$$v_i(\mathbf{r}_i) = \alpha(\mathbf{r}_i - \mathbf{R}_i)^2, \quad (\text{A.0.1})$$

where α is the binding strength parameter, which determines how tightly the particle is bound to the lattice site for this particle at \mathbf{R}_i . The Hamiltonian for the Einstein model is

$$\mathcal{H} = \sum_{i=1}^N \left[\frac{\mathbf{p}_i^2}{2m} + v_i(\mathbf{r}_i) \right]. \quad (\text{A.0.2})$$

Since this is just the Hamiltonian for a set of N independent harmonic oscillators, the partition function for the system $Q_N = Q_1^N$, where Q_1 is the partition function for a single oscillator. The partition function is

$$Q_N = h^{-3N} \int d\mathbf{r}^N \int d\mathbf{p}^N \exp(-\beta\mathcal{H}). \quad (\text{A.0.3})$$

Note that this does not have a $1/N!$ indistinguishability factor – each particle is bound to a different lattice site, and so the particles are distinguishable. The integrals in (A.0.3) are all Gaussian, and so we obtain:

$$Q_N = \Lambda^{-3N} \left(\frac{\beta\alpha}{\pi} \right)^{-3N/2}, \quad (\text{A.0.4})$$

where

$$\Lambda = \sqrt{\frac{2\pi\beta\hbar^2}{m}} \quad (\text{A.0.5})$$

is the thermal de Broglie wavelength. The Helmholtz free energy is therefore

$$F^{Ein} = -k_B T \ln Q_N = \frac{3}{2} N k_B T \ln \left(\frac{\Lambda^2 \beta \alpha}{\pi} \right). \quad (\text{A.0.6})$$

Note that this free energy does not reduce to the ideal gas Helmholtz free energy in the limit $\alpha \rightarrow 0$. This is a manifestation of the fact that by considering each particle bound to a particular lattice site from the outset, the particles are distinguishable, which is not the case for the ideal gas, or any other fluid. The internal energy is simply $3Nk_B T$, which we can obtain via the equipartition theorem, and the pressure $P = -(\partial F / \partial V)_T = 0$ for the Einstein model, since the free energy (A.0.6) is independent of the volume V .

The (time averaged) density profile for a single particle in an external potential is simply proportional to the Boltzmann factor of that potential, which in the present case of a harmonic potential, gives us a Gaussian density profile. The total density distribution profile for the particles in the Einstein solid is therefore a sum of Gaussian peaks, each centered around the set of lattice sites $\{\mathbf{R}_i\}$:

$$\rho(\mathbf{r}) = \sum_{i=1}^N \rho_i(\mathbf{r}) = \sum_{i=1}^N \left(\frac{\beta\alpha}{\pi} \right)^{3/2} e^{-\beta\alpha(\mathbf{r}-\mathbf{R}_i)^2}, \quad (\text{A.0.7})$$

where $\rho_i(\mathbf{r})$ is the density contribution from the i^{th} particle which has a Gaussian density distribution centered around \mathbf{R}_i and the prefactor to the Gaussian is determined from the normalization condition of one particle per lattice site. As a consistency check we can use the density profiles (A.0.7) to calculate the contribution to the Helmholtz free energy, from the external potentials (A.0.1):

$$\begin{aligned} \langle V \rangle &= \sum_{i=1}^N \int d\mathbf{r} \rho_i(\mathbf{r}) v_i(\mathbf{r}) \\ &= \alpha \left(\frac{\beta\alpha}{\pi} \right)^{3/2} \sum_{i=1}^N \int d\mathbf{r} (\mathbf{r} - \mathbf{R}_i)^2 e^{-\beta\alpha(\mathbf{r}-\mathbf{R}_i)^2} \\ &= \frac{3}{2} N k_B T, \end{aligned} \quad (\text{A.0.8})$$

which is, of course, simply the result one would obtain by applying the equipartition theorem for the potential energy degrees of freedom.

Having recalled the Einstein solid, we shall now consider the results from DFT for the same system. The basic idea behind most attempts to construct a classical DFT for solids,

is that one can treat the solid as a (highly) inhomogeneous fluid and that one can apply a DFT constructed for the fluid phase to treat the solid phase. In DFT's for the solid phase one often assumes the one-body density profile is of the form in Eq. (A.0.7) with α , an inverse width parameter for the Gaussian peaks, treated as a variational parameter to minimize the free energy. In classical DFT one considers the following Helmholtz free energy functional:

$$F[\rho] = \mathcal{F}[\rho] + \int d\mathbf{r} \rho(\mathbf{r}) V(\mathbf{r}), \quad (\text{A.0.9})$$

where $\mathcal{F}[\rho]$ is the intrinsic Helmholtz free energy functional and $V(\mathbf{r})$ is the external potential on the fluid. For the present Einstein system we cannot express the external potential contribution to the Helmholtz free energy in this way because the external potential is different for each particle – see Eq. (A.0.1) – in the Einstein model the i^{th} particle sees the i^{th} potential well. This should alert us to the possibility that the present DFT approach may fail. However, for the present, we shall assume that the external potential contribution to the Helmholtz free energy is $\langle V \rangle = \frac{3}{2} N k_B T$, i.e. that given by Eq. (A.0.8).

Returning to Eq. (A.0.9), the intrinsic Helmholtz free energy functional $\mathcal{F}[\rho]$ is normally split up as follows

$$\mathcal{F}[\rho] = \mathcal{F}_{id}[\rho] + \mathcal{F}_{ex}[\rho], \quad (\text{A.0.10})$$

where $\mathcal{F}_{id}[\rho]$ is the ideal gas contribution and $\mathcal{F}_{ex}[\rho]$ is the excess part, which includes the effects of any interactions that there are between the particles. The ideal gas contribution to the intrinsic Helmholtz free energy functional is

$$\mathcal{F}_{id}[\rho] = k_B T \int d\mathbf{r} \rho(\mathbf{r}) [\ln \Lambda^3 \rho(\mathbf{r}) - 1]. \quad (\text{A.0.11})$$

We consider an ideal gas (i.e. $\mathcal{F}_{ex}[\rho] = 0$), with the external potential on the i^{th} particle given by Eq. (A.0.1) – i.e. corresponding to the Hamiltonian for the Einstein model, Eq. (A.0.2). It appears reasonable to substitute Eq. (A.0.7) into Eq. (A.0.11), in order to obtain the kinetic energy contribution to the Helmholtz free energy. If the parameter α in the external potential is large, then the Gaussian peaks in the density profile, Eq. (A.0.7), will be extremely narrow, and if we assume that the contribution from overlap between Gaussian density peaks on neighbouring lattice sites in the integral obtained from inserting Eq. (A.0.7) into (A.0.11) will be negligible, then one obtains:

$$F_{id}^{solid} = \frac{3}{2} N k_B T \ln \left(\frac{\Lambda^2 \beta \alpha}{\pi} \right) - \frac{5}{2} N k_B T. \quad (\text{A.0.12})$$

This is simply N times the contribution one would obtain from Eq. (A.0.11) on inserting a single Gaussian density peak, $\rho(\mathbf{r}) = \rho_i(\mathbf{r})$. Note that the second term consists of $-\frac{3}{2}Nk_B T$ from the $\rho(\mathbf{r}) \ln \rho(\mathbf{r})$ term and a further $-Nk_B T$ from the $-\rho(\mathbf{r})$ term. On the other hand one can define the kinetic energy contribution to the Helmholtz free energy for the Einstein model as (see Eqs. (A.0.6) and (A.0.8)):

$$\begin{aligned} F_{ni}^{Ein} &\equiv F^{Ein} - \langle V \rangle \\ &= \frac{3}{2}Nk_B T \ln \left(\frac{\Lambda^2 \beta \alpha}{\pi} \right) - \frac{3}{2}Nk_B T. \end{aligned} \quad (\text{A.0.13})$$

Clearly (A.0.13) differs from Eq. (A.0.12) by a term $Nk_B T$. In order to recover the correct Helmholtz free energy within a DFT approach, for the Einstein solid with $\mathcal{F}_{ex}[\rho] = 0$ and when α is large, we propose empirically a different functional for the non interacting solid, namely

$$\mathcal{F}[\rho] = \mathcal{F}_{ni}^*[\rho] = k_B T \int d\mathbf{r} \rho(\mathbf{r}) \ln \Lambda^3 \rho(\mathbf{r}), \quad (\text{A.0.14})$$

which simply omits the $-\rho(\mathbf{r})$ term in Eq. (A.0.11). Inserting Gaussian density profiles into (A.0.14) will, of course, increase (A.0.12) by $+Nk_B T$, thereby recovering (A.0.13).

We now briefly consider a solid composed of interacting particles. In this case, the particles can be confined to a lattice site by the interactions with the neighbouring particles, rather than by an external potential such as (A.0.1). For example, for particles interacting via a Gaussian pair potential, $\phi(r) = \epsilon \exp(-r^2)$, the following expression:

$$F_{solid}^{GCM} = \mathcal{F}_{ni}^*[\rho] + \frac{1}{2} \int d\mathbf{r} \int d\mathbf{r}' \rho^{(2)}(\mathbf{r}, \mathbf{r}') \phi(|\mathbf{r} - \mathbf{r}'|), \quad (\text{A.0.15})$$

with $\mathcal{F}_{ni}^*[\rho]$ given by Eq. (A.0.14), gives a good approximation for the Helmholtz free energy of the solid phases of the Gaussian core model, when one assumes that the one-body density $\rho(\mathbf{r})$ is of the same form as the density profile in the Einstein model, Eq. (A.0.7), and that the two-body density, $\rho^{(2)}(\mathbf{r}, \mathbf{r}')$, is also that of the reference Einstein model – i.e. products of Gaussian peaks centered on the lattice sites [22, 37]. In this theory α is treated as a variational parameter to minimize the free energy. This approach, based on Eq. (A.0.15), is equivalent to the approximation for the Helmholtz free energy obtained via the Gibbs-Bogoliubov inequality with the Einstein model as the reference system, that was used for the Gaussian core model in Ref. [37] (also described in chapter 4). In chapter 4 we also proposed an alternative DFT theory for the solid phases of the Gaussian core model, based on Eq. (A.0.11), which differs from that based on the Gibbs-Bogoliubov inequality by a term $-Nk_B T$ in the Helmholtz free energy. This leads to the

question, which is the better approximation for the Helmholtz free energy for the solid phase? The first comment to make is that the free energy from the Gibbs-Bogoliubov inequality provides an upper bound for the true free energy of the solid, however, the DFT is constructed empirically, as is the case for many DFTs, on the basis that it gives reasonable results for the phase behaviour of the GCM solid.

It is interesting to note that the extra $-Nk_B T$ term in the Helmholtz free energy of the solid does not change the value obtained for the pressure, P , of the solid. We demonstrate this as follows: The Helmholtz free energy per particle, $f = F/N = f_{ni} + f_{ex}$, where f_{ex} is the excess contribution for interacting particles and $f_{ni} = F_{ni}^{Ein}/N$ is the non-interacting part, can be written as (see Eq. (A.0.13)):

$$f_{ni} = \frac{3}{2}k_B T \ln \alpha + (\alpha \text{ independent terms}). \quad (\text{A.0.16})$$

The pressure is thus

$$\begin{aligned} \frac{\beta P}{\rho} &= \beta \rho \frac{\partial f}{\partial \rho} = \beta \rho \frac{\partial f_{ni}}{\partial \rho} + \beta \rho \frac{\partial f_{ex}}{\partial \rho} \\ &= \frac{3\rho}{2\alpha} \left(\frac{\partial \alpha}{\partial \rho} \right) + \beta \rho f'_{ex}. \end{aligned} \quad (\text{A.0.17})$$

For a given (ρ, T) , f is minimized with respect to α : $\partial f / \partial \alpha|_{\alpha=\alpha_{min}} = 0$. Since the term $Nk_B T$, which is the difference in the Helmholtz free energy obtained from the two theories, is independent of α , this means that α_{min} is the same within both theories and therefore $(\partial \alpha_{min} / \partial \rho)$ and the pressure P are the same within both theories. However, although this term in the Helmholtz free energy does not change the pressure, it should affect the values obtained for the chemical potential, and therefore any calculation of the liquid-solid coexisting densities, as well as many other thermodynamic quantities for the solid phase; for example, the extra term results in a difference of k_B per particle (a significant amount) in the value of the entropy calculated from the two theories for the Helmholtz free energy of the solid phase. However, we do not believe these differences will significantly change the phase diagram obtained for the GCM from these two theories.

Thinking beyond the GCM solid, we speculate, for certain model fluids, that it may be profitable, when attempting to construct a DFT theory for the solid phase, to use Eq. (A.0.14) as the non-interacting starting point for the theory, rather than Eq. (A.0.11). To the expression in Eq. (A.0.14) one would then add an ‘excess’ functional $\mathcal{F}_{ex}^*[\rho]$, incorporating the contribution to the Helmholtz free energy arising from the interactions between the particles.

We take the opportunity here to make a general point concerning the value obtained for the entropy of the solid phase, when calculated within the DFT framework. We note that DFT theories seem to systematically predict too low a value for the Lindemann ratio [46], or equivalently, too large a value for the width parameter, α , for the Gaussian density peaks – see Eq. (A.0.7). This can be seen in Baus’ review [45], where the Lindemann parameters for some of the early theories of hard-sphere freezing are tabulated. It is also a feature of the most recent theories for hard-sphere freezing, see for example Refs. [154, 46]. The entropy of the solid depends quite sensitively on the value of α . The entropy change per particle, $\Delta s = \Delta S/N$, on freezing has been calculated in several DFT theories of freezing (see Ref. [45] and references therein), and there seems to be a discrepancy in the value obtained for Δs , when compared to simulations, that can be accounted for by considering the discrepancy between the value obtained for α from DFT and from simulations: We write the Helmholtz free energy as

$$f = \frac{3}{2}k_B T \ln \alpha + \Sigma(T, \alpha), \quad (\text{A.0.18})$$

where we have separated the α dependent part from the non-interacting part of the Helmholtz free energy and we denote the remaining part by $\Sigma(T, \alpha)$. $\Sigma(T, \alpha)$ contains both the (excess) contribution to the Helmholtz free energy, i.e. that due to the particle interactions, as well as the α -independent terms in f_{id} , the ideal-gas contribution to the free energy. From Eq. (A.0.18) we can calculate the entropy per particle:

$$s = - \left(\frac{\partial f}{\partial T} \right)_\rho = -\frac{3}{2}k_B \ln \alpha - \frac{3}{2} \frac{k_B T}{\alpha} \left(\frac{\partial \alpha}{\partial T} \right)_\rho - \left(\frac{\partial \Sigma(T, \alpha)}{\partial T} \right)_\rho. \quad (\text{A.0.19})$$

The entropy is therefore, of course, dependent on the parameter α , the inverse width parameter for the Gaussian density peaks. We shall now turn to one of the more successful applications of DFT to the problem of hard-sphere freezing, the theory of Curtin and Ashcroft [155, 156]. In table A.1 we reproduce some of table I in Ref. [156] (see also Ref. [45]), comparing liquid-solid coexistence data for the hard-sphere solid, from the DFT theory and from simulations. ρ_s and ρ_l are the coexisting solid and liquid densities. The Lindemann parameter L is related to the parameter α by $L = (3/\beta\alpha a^2)^{1/2}$ and $a = (4/\rho_s)^{1/3}$ for the fcc lattice. Using these values we can determine the value of the Gaussian width parameter α . From the simulation results, $\beta\alpha_{SIM}\sigma^2 = 77$ and from the DFT theory, $\beta\alpha_{DFT}\sigma^2 = 112$, where σ is the hard-sphere diameter. Using these two values we can calculate the difference in the non-interacting (ideal gas) part of the entropy

	ρ_s	ρ_l	$\Delta s/k_B$	L
Simulation	1.04	0.94	1.16	0.126
Theory	1.025	0.905	1.31	0.104

Table A.1: Liquid-solid coexistence data for the hard-sphere solid, reproduced from Ref. [156]. ρ_s and ρ_l are the coexisting solid and liquid densities, L is the Lindemann parameter and Δs is the entropy change per particle on freezing.

in Eq. (A.0.19), $\frac{3}{2}k_B \ln(\alpha_{DFT}/\alpha_{SIM})$, from using these two different values for α (for hard-spheres $(\partial\alpha/\partial T)_\rho = 0$, and therefore the second term in Eq. (A.0.19) is zero). This difference is $\frac{3}{2}k_B \ln(112/77) = 0.56k_B$, which is clearly very substantial. Of course, in calculating Δs we must also consider the additional effect on the entropy of changing α in the term $\Sigma(T, \alpha)$ in the Helmholtz free energy. Nevertheless, the difference, $0.56k_B$, from the difference in α in the non-interacting part of the Helmholtz free energy does seem to be important in accounting for the discrepancy in the entropy change on freezing. This seems to suggest that to improve a DFT theory for freezing one should focus on generating the correct value for α in the theory.

Appendix B

Details of the binary GCM Pole Structure

In this Appendix we show some details of the pole structure for the binary GCM, which gives rise to the new crossover line (analogous to the Fisher-Widom line) marking the crossover in the asymptotic decay of $h(r)$ from damped oscillatory with a particular wavelength, to damped oscillatory with a different wavelength. Such crossover occurs when there is a large enough asymmetry in the sizes of the of the two different species of particles. In Figs. B.1 and B.2, we show the imaginary and real parts of the poles respectively, plotted versus x , the relative concentration of species 2, for a binary fluid of GCM particles with total density $\rho R_{11}^3 = 2.0$ and $\epsilon_{12} = \epsilon_{11} = \epsilon_{22} = 2k_B T$. In both figures, plots a) – f) show the trend as we change the size asymmetry, $q = R_{22}/R_{11}$, between the two species in the binary fluid. In Fig. B.1, we see that the pole with the smallest α_0 is one with $\alpha_1 \neq 0$ for $x \simeq 0$, but as x is increased $\rightarrow 1$, the curve for this pole intersects the curve for a purely imaginary pole (dashed line) twice – these two intersections give rise to the two branches of the Fisher-Widom line. For plots a) – d), in Fig. B.1, there is no crossover between poles with different real parts, α_1 . However, for plots e) – f), the two (solid) curves corresponding to the poles with the lowest values for α_0 , each with different values of $\alpha_1 \neq 0$, cross over. For $x \lesssim 0.7$, it is the branch of α_1 which is smallest in magnitude in Fig. B.2, which corresponds to the pole with the smallest value of α_0 in Fig. B.1. For plots e) – f), there is a crossover at $x \simeq 0.7$ from the pole with the smallest value of α_0 and α_1 , to a different pole, for which α_0 is the lowest in magnitude, but for which α_1 has the second lowest magnitude – i.e. for $x \gtrsim 0.7$ there is a pole with a lower value for α_1 ,

but a larger value for α_0 , than the pole which determines the asymptotic decay of $h(r)$ and which has the lowest value for α_0 . For this density the cross-over between the two poles occurs in the region of the phase diagram where the purely imaginary pole dominates the asymptotic decay of $h(r)$, but at lower densities ρ , these poles have α_0 with a value lower than that for the purely imaginary pole, and therefore the asymptotic decay of $h(r)$ crosses over from damped oscillatory, to damped oscillatory with a different wavelength – the locus of the cross over points in the phase diagram gives us the lines in the bottom right hand corner of Figs. 5.1, 5.2 and 5.3.

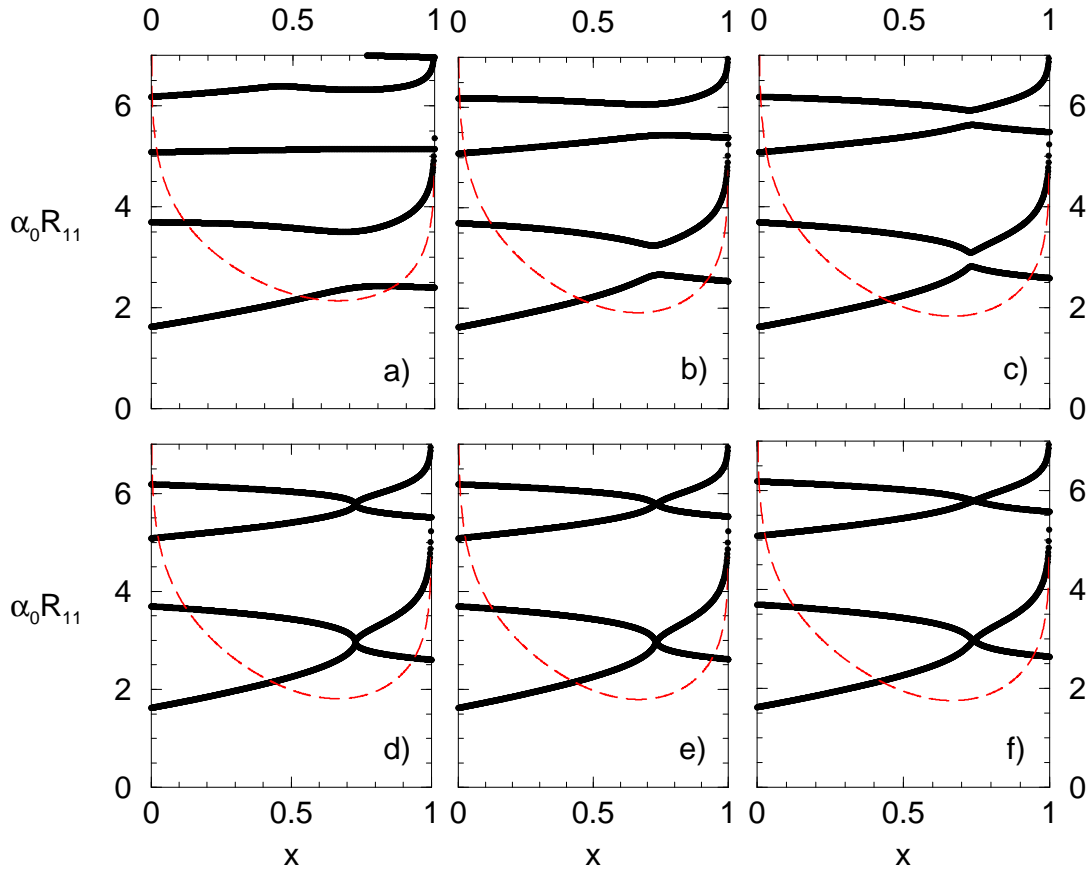


Figure B.1: Imaginary part of the poles, α_0 , plotted versus x , the relative concentration of species 2, for a binary fluid of GCM particles with fixed total density $\rho R_{11}^3 = 2.0$ and $\epsilon_{12} = \epsilon_{11} = \epsilon_{22} = 2k_B T$. The solid lines correspond to poles with a non-zero real part, and the dashed line, to the purely imaginary pole. Plots a) – f) correspond to different size asymmetries, $q = R_{22}/R_{11}$. In a), $q = 0.75$; in b) $q = 0.72$, in c) $q = 0.71$, in d) $q = 0.707$, in e) $q = 0.705$ and in f) $q = 0.7$.

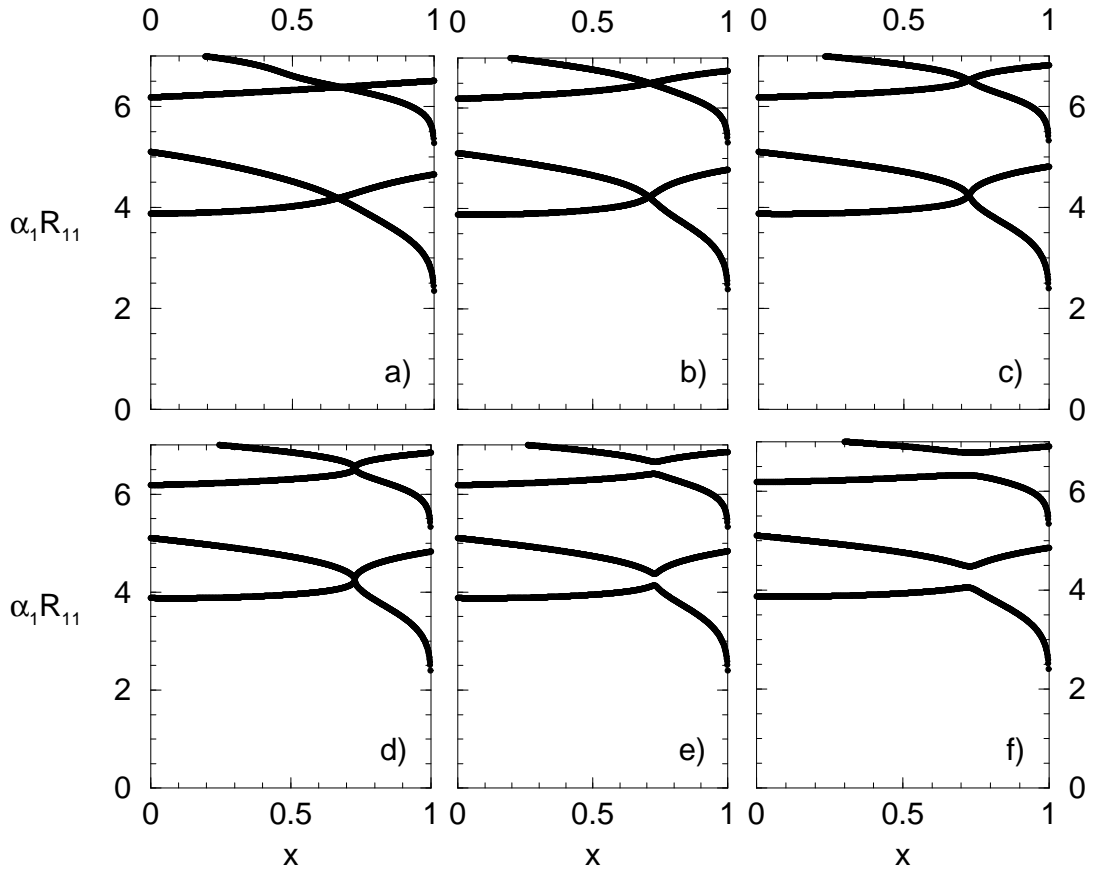


Figure B.2: Real part of the poles, α_1 , plotted versus x , the relative concentration of species 2, for a binary fluid of GCM particles with total density $\rho R_{11}^3 = 2.0$ and $\epsilon_{12} = \epsilon_{11} = \epsilon_{22} = 2k_B T$. Plots a) – f) correspond to different size asymmetries, $q = R_{22}/R_{11}$. In a), $q = 0.75$; in b) $q = 0.72$, in c) $q = 0.71$, in d) $q = 0.707$, in e) $q = 0.705$ and in f) $q = 0.7$.

Appendix C

Derivation of Eq. (7.3.37) for the excess chemical potential

Inserting Eq. (7.3.10) into Eq. (7.3.35) we obtain:

$$\omega(r) = -\frac{1}{\beta} \left(\rho_s^0 - \rho^* e^{-r^2/R_{bs}^2} \right) - \frac{1}{2} \left(\rho_s^0 - \rho^* e^{-r^2/R_{bs}^2} \right) \left(\rho_s^0 \hat{v}_{ss}^0 - \rho^* \pi^{3/2} \epsilon_{ss} R^3 e^{-\frac{r^2}{R_{ss}^2}} \left(1 - \frac{R^2}{R_{ss}^2} \right) \right) \quad (\text{C.0.1})$$

where R is given by Eq. (7.3.12). Subtracting Eq. (7.3.36) gives:

$$\begin{aligned} \omega(r) - \omega(\infty) &= \frac{1}{\beta} \rho^* e^{-r^2/R_{bs}^2} + \frac{1}{2} \rho_s^0 \rho^* \hat{v}_{ss}^0 e^{-r^2/R_{bs}^2} + \frac{1}{2} \rho_s^0 \rho^* \pi^{3/2} \epsilon_{ss} R^3 e^{-\frac{r^2}{R_{ss}^2}} \left(1 - \frac{R^2}{R_{ss}^2} \right) \\ &\quad - \frac{1}{2} (\rho^*)^2 \pi^{3/2} \epsilon_{ss} R^3 e^{-r^2 \left(\frac{1}{R_{bs}^2} + \frac{1}{R_{ss}^2} \right) \left(1 - \frac{R^2}{R_{ss}^2} \right)} \end{aligned} \quad (\text{C.0.2})$$

and after inserting Eq. (C.0.2) into Eq. (7.3.30) and performing the Gaussian integrals we find

$$\begin{aligned} \frac{\mu_b^{ex}}{\pi^{3/2}} &= \frac{1}{\beta} \rho^* R_{bs}^3 + \frac{1}{2} \rho_s^0 \rho^* \hat{v}_{ss}^0 R_{bs}^3 + \frac{1}{2} \rho_s^0 \rho^* \pi^{3/2} \epsilon_{ss} R^3 \left(\frac{1}{R_{ss}^2} \left(1 - \frac{R^2}{R_{ss}^2} \right) \right)^{-3/2} \\ &\quad - \frac{1}{2} (\rho^*)^2 \pi^{3/2} \epsilon_{ss} R^3 \left(\frac{1}{R_{bs}^2} + \frac{1}{R_{ss}^2} \left(1 - \frac{R^2}{R_{ss}^2} \right) \right)^{-3/2}. \end{aligned} \quad (\text{C.0.3})$$

We now expand R in powers of R_{ss}/R_{bs} , so that to $\mathcal{O}(R_{ss}/R_{bs})^2$, $R^3 = R_{ss}^3$. Thus Eq. (C.0.3) can be written as:

$$\frac{\mu_b^{ex}}{\pi^{3/2}} = \frac{1}{\beta} \rho^* R_{bs}^3 + \frac{1}{2} \rho_s^0 \rho^* \hat{v}_{ss}^0 R_{bs}^3 + \frac{1}{2} \rho_s^0 \rho^* \hat{v}_{ss}^0 R_{bs}^3 - \frac{1}{2} (\rho^*)^2 \hat{v}_{ss}^0 \frac{\sqrt{2}}{4} R_{bs}^3 + \mathcal{O} \left(\frac{R_{ss}}{R_{bs}} \right)^2. \quad (\text{C.0.4})$$

If we substitute for ρ^* using Eq. (7.3.15) then we find

$$\frac{\mu_b^{ex}}{\pi^{3/2}\epsilon_{bs}R_{bs}^3} = \frac{\mu_b^{ex}}{\hat{v}_{bs}^0} = \rho_s^0 - \frac{\sqrt{2}\hat{v}_{ss}^0}{8\epsilon_{bs}}(\rho^*)^2 + \mathcal{O}\left(\frac{R_{ss}}{R_{bs}}\right)^2, \quad (\text{C.0.5})$$

which is Eq. (7.3.37).

Appendix D

Wetting on Curved Substrates and the Pre-Wetting line

In this Appendix we demonstrate the effect that a curved substrate has on the wetting film thickness and pre-wetting line, for a fluid adsorbed on this substrate, rather than on a planar wall (obtained taking limit $R_b \rightarrow \infty$ for the curved substrate). The effect of curvature is to add an additional term to the surface excess grand potential (binding potential), Eq. (6.3.1). For example, for a spherical substrate, one must add a term $\Delta\omega_{ex}(l) \simeq 2l\gamma_{AB}/R_b$ to Eq. (6.3.1) [11]. This means that there are now two terms in (6.3.1) which are linear in l : this curvature term and the term $\propto l\Delta x$, which incorporates the effect of being off-coexistence. The equilibrium adsorbed film thickness is determined by minimising (6.3.1) with respect to l , so since both these terms are linear in l , they have a similar effect in determining the equilibrium adsorbed film thickness: curvature has (exactly for large R_b) the same effect when determining the adsorbed fluid film thickness as does being off-coexistence, when determining the wetting film thickness at a planar wall [157]. We can see this in Fig. D.1, where we plot the density profiles for a binary fluid of GCM particles (the phase diagram and pair-potential parameters are in Fig. 5.1), adsorbed on the surface of a spherical substrate, with the external potential given by (7.6.3), with $R_b = 30R_{11}$, $\lambda = R_{11}$ and $A_i = R_{ii}/R_{11}$. The bulk fluid has a total density $\rho R_{11}^3 = 7.0$ and is at coexistence: $x = x_{coex} \simeq 0.8854$. For this system, at a planar wall, with the external potential given by Eq. (7.6.3), with $R_b \rightarrow \infty$, the adsorbed film thickness, $l = \infty$, i.e. the substrate is completely wet. However, on the present curved substrate, the adsorbed film thickness is finite – due to the curvature. Curvature also reduces the length of the

pre-wetting line, and shifts the ‘wetting point’ to lower fluid total densities, i.e. closer to the bulk critical point – see Fig. D.2.

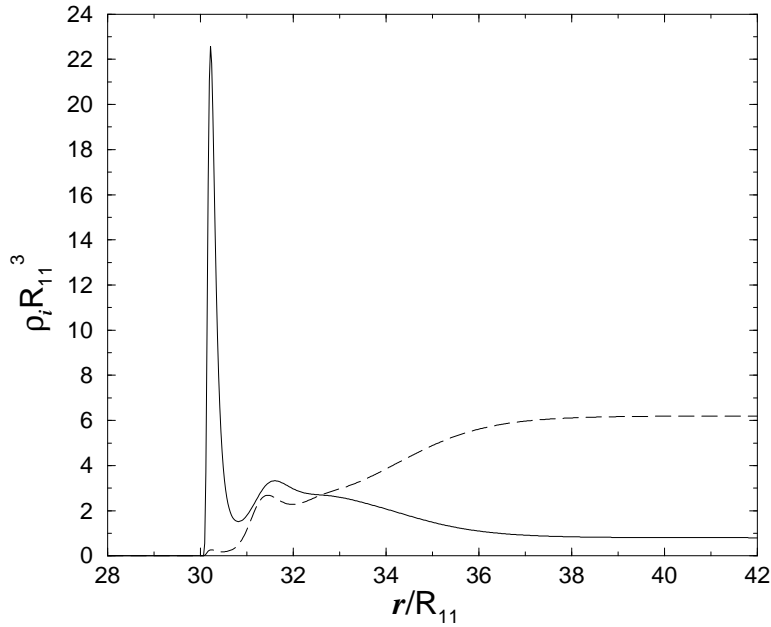


Figure D.1: Density profiles for the binary GCM on a curved substrate, with the external potential given by Eq. (7.6.3), with $R_b = 30R_{11}$, $\lambda = R_{11}$ and $A_i = R_{ii}/R_{11}$. The bulk fluid has a total density $\rho R_{11}^3 = 7.0$ and is at coexistence: $x = x_{coex} \simeq 0.8854$. The solid line corresponds to the profile for species 1 and the dashed line to species 2. Note that the adsorbed film thickness is finite, even at coexistence, due to the curvature of the substrate.

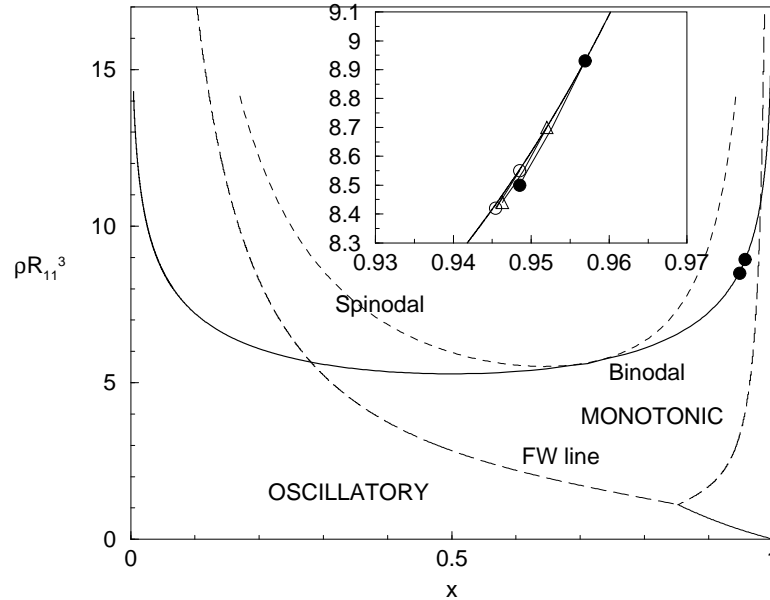


Figure D.2: Phase diagram for a mixture of Gaussian particles, equivalent to a mixture of two polymers with length ratio 2:1 – i.e. the same as Fig. 6.1. ρ is the total density and x is the concentration of the smaller species 2. The inset shows (as does Fig. 6.1) a magnification of the pre-wetting line, meeting the binodal at the wetting point (top solid circle), for a wall potential given by Eq. (6.2.7) with $\lambda/R_{11} = 1$. The lower solid circle denotes the pre-wetting critical point. The two additional lines in the inset, correspond to the pre-wetting line for a curved substrate, with external potentials given by (7.6.3), with $\lambda = R_{11}$ and $A_i = R_{ii}/R_{11}$. The pre-wetting line with ends marked by triangles corresponds to a substrate with $R_b = 50R_{11}$, and that with unfilled circles, $R_b = 30R_{11}$.

Appendix E

Fourier Transform of the Star Polymer Pair Potential

The Fourier transforms of the three pair potentials $v_{ij}(r)$ given in Eq. (8.2.1) can be calculated analytically. The pair potentials have the form

$$v_{ij}(r) = \frac{5}{18} k_B T f^{3/2} F(r/\sigma_{ij}; \tau_{ij} \sigma_{ij}), \quad (\text{E.0.1})$$

with a common function $F(x; y)$ for all combinations $i, j = 1, 2$. Let $Q \equiv k\sigma_{ij}$ and $\bar{\tau}_{ij} \equiv \tau_{ij}\sigma_{ij}$. Eq. (E.0.1) above implies that the FT $\hat{v}_{ij}(k)$ of the potentials satisfy the relation

$$\hat{v}_{ij}(k) = \frac{5}{18} k_B T f^{3/2} \sigma_{ij}^3 \tilde{F}(Q; \bar{\tau}_{ij}). \quad (\text{E.0.2})$$

Using the specific form of the function $F(x, y)$ given in Eq. (8.2.1) we obtain the function $\tilde{F}(Q; \bar{\tau}_{ij})$ as:

$$\begin{aligned} \tilde{F}(Q; \bar{\tau}_{ij}) &= \frac{2\pi}{\bar{\tau}_{ij}^2} \left(\frac{\sin Q - Q \cos Q}{Q^3} \right) - 4\pi \left(\frac{\sin Q - \text{Si}(Q)}{Q^3} \right) + \frac{\pi}{\bar{\tau}_{ij}^4} \frac{\sin Q}{Q} \\ &+ \frac{1}{2\bar{\tau}_{ij}^2} \left(\frac{\pi}{\bar{\tau}_{ij}^2} \right)^{3/2} \exp[\bar{\tau}_{ij}^2 - Q^2/(4\bar{\tau}_{ij})] \\ &\times \left\{ 1 - \frac{1}{2} \left[\text{erf} \left(\bar{\tau}_{ij} + \frac{iQ}{2\bar{\tau}_{ij}} \right) + \text{erf} \left(\bar{\tau}_{ij} - \frac{iQ}{2\bar{\tau}_{ij}} \right) \right] \right\}, \end{aligned} \quad (\text{E.0.3})$$

with the sine integral

$$\text{Si}(z) = \int_0^z \frac{\sin t}{t} dt \quad (\text{E.0.4})$$

and the complex error function $\text{erf}(z)$. Note that although the arguments of the error functions in Eq. (E.0.3) are complex, the FT is real due to the property $\text{erf}(z^*) = \text{erf}^*(z)$, with the asterisk denoting the complex conjugate [158].

Bibliography

- [1] J-P. Hansen and I.R. McDonald, *Theory of Simple Liquids*, 2 ed. (Academic, London, 1986).
- [2] M.E. Fisher and B. Widom, *J. Chem. Phys.* **50**, 3756 (1969).
- [3] R. Roth, R. Evans, and S. Dietrich, *Phys. Rev. E* **62**, 5360 (2000).
- [4] B. Götzelmann, R. Roth, S. Dietrich, M. Dijkstra, and R. Evans, *Europhys. Lett.* **47**, 398 (1999).
- [5] J.C. Crocker, J.A. Matteo, A.D. Dinsmore, and A.G. Yodh, *Phys. Rev. Lett.* **82**, 4352 (1999).
- [6] R. Evans, *Adv. Phys.* **28**, 143 (1979).
- [7] R. Evans, in *Fundamentals of Inhomogeneous Fluids*, edited by D. Henderson (Dekker, New York, 1992), Chap. 3.
- [8] N.D. Mermin, *Phys. Rev.* **137**, A1441 (1965).
- [9] P.M. Chaikin and T.C. Lubensky, *Principles of condensed matter physics*, 2 ed. (Cambridge University Press, Cambridge, 1995).
- [10] M. Schick, in *Liquids at Interfaces*, edited by J. Charvolin, J.F. Joanny, and J. Zinn-Justin (North-Holland, Amsterdam, 1990), Chap. 9.
- [11] S. Dietrich, in *Phase Transitions and Critical Phenomena*, edited by C. Domb and J.L. Lebowitz (Academic, London, 1988), Vol. 12, p. 1.
- [12] R. Evans, in *Liquids at Interfaces*, edited by J. Charvolin, J.F. Joanny, and J. Zinn-Justin (North-Holland, Amsterdam, 1990), Chap. 1.

- [13] J.R. Henderson, in *Fundamentals of Inhomogeneous Fluids*, edited by D. Henderson (Dekker, New York, 1992), Chap. 2.
- [14] T. Aukrust and E.H. Hauge, *Phys. Rev. Lett.* **54**, 1814 (1985).
- [15] T. Aukrust and E.H. Hauge, *Physica* **141A**, 427 (1987).
- [16] A.O. Parry and R. Evans, *Molec. Phys.* **78**, 1527 (1993).
- [17] R. Evans and P. Tarazona, *Phys. Rev. Lett.* **53**, 400 (1984).
- [18] A.O. Parry, *J. Phys.: Condens. Matter* **8**, 10761 (1996).
- [19] A.A. Louis, P.G. Bolhuis, J-P. Hansen, and E.J. Meijer, *Phys. Rev. Lett.* **85**, 2522 (2000).
- [20] P.G. Bolhuis, A.A. Louis, J-P. Hansen, and E.J. Meijer, *J. Chem. Phys.* **114**, 4296 (2001).
- [21] A.A. Louis, P.G. Bolhuis, R. Finken, V. Krakoviack, E.J. Meijer, and J-P. Hansen, *Physica A* **306**, 251 (2002).
- [22] C.N. Likos, *Phys. Reports* **348**, 267 (2001).
- [23] M. Dijkstra, R. van Roij, and R. Evans, *Phys. Rev. E* **59**, 5744 (1999).
- [24] P.G. Bolhuis, A.A. Louis, and J-P. Hansen, *Phys. Rev. E* **64**, 021801 (2001).
- [25] V. Krakoviack, J-P. Hansen, and A.A. Louis, *Phys. Rev. E* **67**, 041801 (2003).
- [26] P.J. Flory and W. Krigbaum, *J. Chem. Phys.* **18**, 1086 (1950).
- [27] O.F. Olaj, W. Lantschbauer, and K.H. Pelinka, *Macromolecules* **13**, 299 (1980).
- [28] B. Krüger, L. Schäfer, and A. Baumgärtner, *J. Phys. (Paris)* **50**, 3191 (1989).
- [29] L. Schäfer and A. Baumgärtner, *J. Phys. (Paris)* **47**, 1431 (1986).
- [30] J. Dautenhahn and C.K. Hall, *Macromolecules* **27**, 5399 (1994).
- [31] H.M. Harreis, C.N. Likos, and M. Ballauff, *J. Chem. Phys.* **118**, 1979 (2003).
- [32] C.N. Likos, M. Schmidt, H. Löwen, M. Ballauff, D. Pötschke, and P. Linder, *Macromolecules* **34**, 2914 (2001).

- [33] C. N. Likos, S. Rosenfeldt, N. Dingenouts, M. Ballauff, P. Lindner, N. Werner, and F. Vögtle, *J. Chem. Phys.* **117**, 1869 (2002).
- [34] P.G. Bolhuis and A.A. Louis, *Macromolecules* **35**, 1860 (2002).
- [35] F.H. Stillinger, *J. Chem. Phys.* **65**, 3968 (1976).
- [36] F.H. Stillinger and D.K. Stillinger, *Physica A* **244**, 358 (1997).
- [37] A. Lang, C.N. Likos, M. Watzlawek, and H. Löwen, *J. Phys.: Condens. Matter* **12**, 5087 (2000).
- [38] C.N. Likos, A. Lang, M. Watzlawek, and H. Löwen, *Phys. Rev. E* **63**, 031206 (2001).
- [39] A.A. Louis, P.G. Bolhuis, and J-P. Hansen, *Phys. Rev. E* **62**, 7961 (2000).
- [40] F.H. Stillinger and T.A. Weber, *J. Chem. Phys.* **68**, 3837 (1977).
- [41] F.H. Stillinger, *Phys. Rev. B* **20**, 299 (1979).
- [42] F.H. Stillinger and T.A. Weber, *J. Chem. Phys.* **70**, 4879 (1979).
- [43] F.H. Stillinger and T.A. Weber, *Phys. Rev. B* **22**, 3790 (1980).
- [44] C.F. Tejero, A. Daanoun, H.N.W. Lekkerkerker, and M. Baus, *Phys. Rev. E* **51**, 559 (1995).
- [45] M. Baus, *J. Phys.: Condens. Matter* **2**, 2111 (1990).
- [46] P. Tarazona, *Phys. Rev. Lett.* **84**, 694 (2000).
- [47] R. Finken, A.A. Louis, and J-P. Hansen, *J. Stat. Phys.* **110**, 1015 (2003).
- [48] R. Roth, R. Evans, and A.A. Louis, *Phys. Rev. E* **64**, 051202 (2001).
- [49] R. Evans, J.R. Henderson, D.C. Hoyle, A.O. Parry, and Z.A. Sabeur, *Molec. Phys.* **80**, 755 (1993).
- [50] J.M. Brader, PhD Thesis, University of Bristol (2001).
- [51] J.M. Brader, R. Evans, M. Schmidt, and H. Löwen, *J Phys.:Condens. Matter* **14**, L1 (2002).

- [52] R. Evans, R.J.F. Leote de Carvalho, J.R. Henderson, and D.C. Hoyle, *J. Chem. Phys.* **100**, 591 (1994).
- [53] J.M. Brader and R. Evans, *Europhys. Lett.* **49**, 678 (2000).
- [54] M.M. Telo da Gama and R. Evans, *Mol. Phys.* **48**, 229 (1983).
- [55] G.A. Martynov, *Fundamental Theory of Liquids: Methods of Distribution Functions* (A. Hilger, Bristol, 1992).
- [56] R.J.F. Leote de Carvalho and R. Evans, *Mol. Phys.* **92**, 211 (1997).
- [57] R.J.F. Leote de Carvalho, R. Evans, and Y. Rosenfeld, *Phys. Rev. E* **59**, 1435 (1999).
- [58] E. Chacón, M. Reinaldo-Falagán, E. Velasco, and P. Tarazona, *Phys. Rev. Lett.* **87**, 166101 (2001).
- [59] P. Tarazona, E. Chacón, M. Reinaldo-Falagán, and E. Velasco, *J. Chem. Phys.* **117**, 3941 (2002).
- [60] E. Velasco, P. Tarazona, , M. Reinaldo-Falagán, and E. Chacón, *J. Chem. Phys.* **117**, 10777 (2002).
- [61] L.V. Mikheev and A.A. Chernov, *Sov. Phys. JETP* **65**, 971 (1987).
- [62] S. Toxvaerd and J. Stecki, *J. Chem. Phys.* **102**, 7163 (1995).
- [63] R.D. Groot and P.B. Warren, *J. Chem. Phys.* **107**, 4423 (1997).
- [64] C.M. Wijmans, B. Smit, and R.D. Groot, *J. Chem. Phys.* **114**, 7644 (2001).
- [65] J.W. Cahn, *J. Chem. Phys.* **66**, 3667 (1977).
- [66] C. Ebner and W.F. Saam, *Phys. Rev. Lett.* **38**, 1486 (1977).
- [67] D.E. Sullivan, *Phys. Rev. B* **20**, 3991 (1979).
- [68] D.E. Sullivan, *J. Chem. Phys.* **74**, 2604 (1981).
- [69] T. Aukrust, PhD Thesis, Institutt for teoretisk fysikk Norges Tekniske Hogskole (1987).
- [70] J.R. Henderson, *Phys. Rev. E* **50**, 4836 (1994).

- [71] R. Evans, J.M. Brader, R. Roth, M. Dijkstra, M. Schmidt, and H. Löwen, *Phil. Trans. Roy. Soc. Lond. A* **359**, 961 (2001).
- [72] W.G. McMillan and J.E. Mayer, *J. Chem. Phys.* **13**, 276 (1945).
- [73] J-P. Hansen and H. Löwen, *Annu. Rev. Phys. Chem.* **51**, 209 (2000).
- [74] S. Asakura and F. Oosawa, *J. Chem. Phys.* **22**, 1255 (1954).
- [75] M.E. Fisher and P.G. de Gennes, *C.R. Acad. Sc. Paris B* **287**, 207 (1978).
- [76] P.G. de Gennes, *C.R. Acad. Sc. Ser. II* **292**, 701 (1981).
- [77] T.W. Burkhardt and E. Eisenreigler, *Phys. Rev. Lett.* **74**, 3189 (1995).
- [78] T.W. Burkhardt and E. Eisenreigler, *Phys. Rev. Lett.* **78**, 2867 (1997).
- [79] R. Netz, *Phys. Rev. Lett.* **76**, 3646 (1996).
- [80] A. Hanke, F. Schlesener, E. Eisenreigler, and S. Dietrich, *Phys. Rev. Lett.* **81**, 1885 (1998).
- [81] F. Schlesener, A. Hanke, and S. Dietrich, *J. Stat. Phys.* **110**, 981 (2003).
- [82] D. Beysens and T. Narayanan, *J. Stat. Phys.* **95**, 997 (1999).
- [83] D. Beysens and D. Estève, *Phys. Rev. Lett.* **54**, 2123 (1985).
- [84] V. Gurfein, D. Beysens, and F. Perrot, *Phys. Rev. A* **40**, 2543 (1989).
- [85] J.S. van Duijneveldt and D. Beysens, *J. Chem. Phys.* **94**, 5222 (1991).
- [86] T. Narayanan, A. Kumar, E.S.R. Gopal, D. Beysens, P. Guenoun, and G. Zalczer, *Phys. Rev. E* **48**, 1989 (1993).
- [87] P.D. Gallagher and J.V. Maher, *Phys. Rev. A* **46**, 2012 (1992).
- [88] P.D. Gallagher, M.L. Kurnaz, and J.V. Maher, *Phys. Rev. A* **46**, 7750 (1992).
- [89] M.L. Kurnaz and J.V. Maher, *Phys. Rev. E* **51**, 5916 (1995).
- [90] J-M. Petit B.M. Law and D. Beysens, *Phys. Rev. E* **57**, 5782 (1998).
- [91] J-M. Petit B.M. Law and D. Beysens, *J. Colloid Interface Sci.* **202**, 441 (1998).

- [92] C. Bauer, T. Bieker, and S. Dietrich, *Phys. Rev. E* **62**, 5324 (2000).
- [93] H. Löwen, *Phys. Rev. Lett.* **74**, 1028 (1995).
- [94] H.T. Dobbs and J.M. Yeomans, *J. Phys.: Condens. Matter* **4**, 10133 (1992).
- [95] H.T. Dobbs, G.A. Darbellay, and J.M. Yeomans, *Europhys. Lett.* **18**, 439 (1992).
- [96] T. Gil, M.C. Sabra, J.H. Ipsen, and O.G. Mouritsen, *Biophys. J.* **73**, 1728 (1997).
- [97] T. Gil and J.H. Ipsen, *Phys. Rev. E* **55**, 1713 (1997).
- [98] T. Gil, J.H. Ipsen, and C.F. Tejero, *Phys. Rev. E* **57**, 3123 (1998).
- [99] S. Amokrane and J.G. Malherbe, *J. Phys.: Condens. Matter* **13**, 7199 (2001).
- [100] J.R. Henderson, *Mol. Phys.* **50**, 741 (1983).
- [101] B. Widom, *J. Chem. Phys.* **39**, 2808 (1963).
- [102] B. Widom, *J. Chem. Phys.* **86**, 869 (1982).
- [103] Y. Rosenfeld, *Phys. Rev. Lett.* **63**, 980 (1989).
- [104] T.L. Hill, *An Introduction to Statistical Thermodynamics* (Dover, New York, 1986).
- [105] T.L. Hill, *J. Chem. Phys.* **30**, 1521 (1959).
- [106] D. Chandler, *Introduction to Modern Statistical Mechanics* (Oxford University Press, New York, 1987).
- [107] J.R. Henderson, *J. Chem. Phys.* **116**, 5039 (2002).
- [108] A.J. Archer, R. Evans, and R. Roth, *Europhys. Lett.* **59**, 526 (2002).
- [109] T. Bieker and S. Dietrich, *Physica A* **252**, 85 (1998).
- [110] M.P. Gelfand and R. Lipowsky, *Phys. Rev. B* **36**, 8725 (1987).
- [111] P.J. Upton, J.O. Indekeu, and J.M. Yeomans, *Phys. Rev. B* **40**, 666 (1989).
- [112] H. Shinto, K. Uranishi, M. Miyahara, and K. Higashitani, *J. Chem. Phys.* **116**, 9500 (2002).

- [113] J.E. Molloy and M.J. Padgett, *Contemporary Phys.* **43**, 241 (2002).
- [114] H. de Hek and A. Vrij, *J. Colloid Int. Sci.* **88**, 258 (1982).
- [115] A.M. Kulkarni, A.P. Chatterjee, K.S. Schweizer, and C.F. Zukoski, *Phys. Rev. Lett.* **83**, 4554 (1999).
- [116] S.R. Kline and E.W. Kaler, *Langmuir* **13**, 412 (1994).
- [117] Y. Jayalakshimi and E.W. Kaler, *Phys. Rev. Lett.* **78**, 1379 (1997).
- [118] T.J. Sluckin, *Phys. Rev. A* **41**, 960 (1990).
- [119] A. Parola, D. Pini, L. Reato, and M. Tau, *J. Phys.: Condens. Matter* **15**, S381 (2003).
- [120] M. Dijkstra, R. van Roij, and R. Evans, *J. Chem. Phys.* **113**, 4799 (2000).
- [121] K. Lum, D. Chandler, and J.D. Weeks, *J. Phys. Chem. B* **103**, 4570 (1999).
- [122] J.D. Weeks, K. Katsov, and K. Vollmayer, *Phys. Rev. Lett.* **81**, 4400 (1998).
- [123] J.D. Weeks, *Annu. Rev. Phys. Chem.* **53**, 533 (2002).
- [124] S.X. Sun, *Phys. Rev. E* **64**, 021512 (2001).
- [125] D.M. Huang and D. Chandler, *Phys. Rev. E* **61**, 1501 (2000).
- [126] G.S. Grest, L.H. Fetters, J.S. Huang, and D. Richter, *Adv. Chem. Phys.* **94**, 67 (1996).
- [127] C.N. Likos, H. Löwen, M. Watzlawek, B. Abbas, O. Jucknischke, J. Allgaier, and D. Richter, *Phys. Rev. Lett.* **80**, 4450 (1998).
- [128] M. Watzlawek, C.N. Likos, and H. Löwen, *Phys. Rev. Lett.* **82**, 5289 (1999).
- [129] C.N. Likos and H.M. Harreis, *Condens. Matter Phys.* **5**, 173 (2002).
- [130] T.A. Witten and P.A. Pincus, *Macromolecules* **19**, 2509 (1986).
- [131] M. Watzlawek, H. Löwen, and C.N. Likos, *J. Phys.: Condens. Matter* **10**, 8189 (1998).

- [132] A. Jusufi, J. Dzubiella, C.N. Likos, C. von Ferber, and H. Löwen, *J. Phys.: Condens. Matter* **13**, 6177 (2001).
- [133] J. Dzubiella, A. Jusufi, C.N. Likos, C. von Ferber, H. Löwen, J. Stellbrink, J. Allgaier, D. Richter, A.B. Schofield, P.A. Smith, W.C.K. Poon, and P.N. Pusey, *Phys. Rev. E* **64**, 010401(R) (2001).
- [134] A.B. Bhatia and D.E. Thornton, *Phys. Rev. B* **2**, 3004 (1970).
- [135] T. Biben and J-P. Hansen, *Phys. Rev. Lett.* **66**, 2215 (1991).
- [136] C.N. Likos, N. Hoffmann, H. Löwen, and A.A. Louis, *J. Phys.: Condens. Matter* **14**, 7681 (2002).
- [137] A.A. Louis, *Phil. Trans. Roy. Soc. A* **359**, 939 (2001).
- [138] A. Jusufi, M. Watzlawek, and H. Löwen, *Macromolecules* **32**, 4470 (1999).
- [139] S. Fishman and M.E. Fisher, *Physica A* **108**, 1 (1981).
- [140] L. Belloni, *J. Chem. Phys.* **98**, 8080 (1993).
- [141] L. Verlet and D. Levesque, *Physica* **28**, 1124 (1962).
- [142] G. Gompper and M. Schick, *Phys. Rev. B* **41**, 9148 (1990).
- [143] R.M. Hornreich, R. Liebmann, H.G. Schuster, and W. Selke, *Z. Phys. B* **35**, 91 (1979).
- [144] J. Stephenson, *J. Math. Phys.* **11**, 420 (1970).
- [145] J. Stephenson, *Can. J. Phys.* **48**, 1724 (1970).
- [146] T. Garel and J.M. Maillard, *J. Phys. C* **19**, L505 (1986).
- [147] D. Broseta, L. Leibler, and J-F. Joanny, *Macromolecules* **20**, 1935 (1987).
- [148] A. Sariban and K. Binder, *Colloid Polym. Sci.* **272**, 1474 (1994).
- [149] U. Marini Bettolo Marconi and P. Tarazona, *J. Chem. Phys.* **110**, 8032 (1999).
- [150] U. Marini Bettolo Marconi and P. Tarazona, *J. Phys.: Condens. Matter* **12**, A413 (2000).

- [151] J. Dzubiella and C.N. Likos, *J. Phys.: Condens. Matter* **15**, L147 (2003).
- [152] E. Helfand and F.H. Stillinger, *J. Chem. Phys.* **49**, 1232 (1968).
- [153] A. Baram, M.W. Maddox, and J.S. Rowlinson, *Molec. Phys.* **76**, 1093 (1992).
- [154] Y. Rosenfeld, M. Schmidt, H. Löwen, and P. Tarazona, *Phys. Rev. E* **55**, 4245 (1997).
- [155] W.A Curtin and N.W. Ashcroft, *Phys. Rev. Lett.* **56**, 2773 (1986).
- [156] W.A Curtin and N.W. Ashcroft, *Phys. Rev. A* **32**, 2909 (1985).
- [157] R. Evans, R. Roth, and P. Bryk, *Europhys. Lett.* **62**, 815 (2003).
- [158] M. Abramowitz and I.A. Segun, *Handbook of Mathematical Functions* (Dover, New York, 1965).